The global impact of stellar winds and supernovae on the interstellar medium

Inaugural-Dissertation
zur
Erlangung des Doktorgrades
der Mathematisch-Naturwissenschaftlichen Fakultät
der Universität zu Köln

vorgelegt von

Andrea Gatto
aus Cogoleto, Italien

Köln, 2016

Berichterstatter: Prof. Dr. Stefanie Walch-Gassner
Prof. Dr. Jürgen Stutzki

Tag der mündlichen Prüfung: 13. Januar 2016

Abstract

English version
The interstellar medium is an extremely heterogeneous mixture of gas and dust which fills the space between stars in galaxies. The life-cycle of stars is deeply connected with the presence of this medium. Massive stars form from very high density/low temperature gas and evolve for millions of years. They emit ionising radiation, blow powerful winds from their surface and, at the end of their lifetime, explode as supernovae, thereby heating up and compressing the surrounding material. These stellar feedback processes are fundamental, since they are able to influence the evolution of the interstellar medium at different scales and eventually to promote or deter further star formation events. In this thesis, we investigate the impact of stellar winds and supernovae on the interstellar medium by performing three-dimensional, Adaptive-Mesh-Refinement, hydrodynamic simulations at intermediate (pc-kpc) scales. We study how different assumptions on the position of supernova explosions drive completely different properties of the gas within disc galaxies. Supernovae are placed either at random positions, in density peaks, or both. Explosions located in density peaks do not produce hot gas due to large radiative losses and atomic hydrogen dominates the mass. Random supernovae create a large volume filling hot phase that compresses the gas into small clumps and the majority of the mass is in the form of molecular hydrogen. We then show how the combination of stellar winds and supernovae is able to regulate the otherwise over-efficient star formation process. We model star formation self-consistently via sink particles and we demonstrate how stellar winds are able to reduce the amount of gas converted into stars both at local and global scales. The inclusion of supernovae produce a hot, over-pressurised phase responsible for outflows launching.

German version
Das interstellare Medium ist ein extrem heterogenes Gemisch aus Gas und Staub, das den Raum zwischen den Sternen einer Galaxie ausfüllt. Der Lebenszyklus der Sterne ist stark mit der Struktur und der Entwicklung des interstallaren Mediums verbunden. Massereiche Sterne entstehen aus

den dichten und kalten Kondensationen des interstallaren Mediums und beeinflussen dieses in vielerlei Hinsicht: Sie emittieren ionisierende Strahlung, treiben starke stellare Winde von deren Oberfläche und explodieren am Ende ihres Lebens als Supernovae, die das umgebende Gas aufheizen und komprimieren. Diese stellaren Rückkopplungsprozesse sind von fundamentaler Bedeutung, da sie das interstellare Medium auf vielen Größenskalen beeinflussen und die Entstehung neuer Sterne beschleunigen oder verzögern. In der vorliegenden Arbeit wird der Einfluss von stellaren Winden und Supernovae auf das interstellare Medium auf Skalen von Parsec bis Kiloparsec mit Hilfe von dreidimensionalen, hydrodynamischen Simulationen auf einem adaptiven Gitter untersucht. Dabei wird insbesondere überprüft, wie sich die Position der Supernovae auf die Eigenschaften des umgebenden Gases auswirkt. Die Supernovae werden in den verschiedenen Simulationen entweder in den Regionen größter Dichte oder an zufälligen Stellen platziert. Zudem werden Mischungen aus der ersten und zweiten Verteilungsmethode untersucht. Die Supernovae, die im dichten Gas explodieren, heizen das umgebende Gas aufgrund der starken Strahlungsverluste nicht auf, was zur Folge hat, dass das Medium überwiegend aus atomarem Wasserstoff besteht. Zufällig verteilte Supernovae führen zu großen Volumenanteilen von heißem Gas, das das übrige Medium in kleine, kalte Klumpen komprimiert. Zudem wird gezeigt, wie die Kombination aus stellaren Winden und Supernovae in der Lage ist, den ansonsten zu effizienten Sternentstehungsprozess zu regulieren. Sterngruppen werden selbstkonsistent mit Sinkeilchen modelliert, mit Hilfe derer demonstriert wird wie stellare Winde in der Lage sind, die Kondensation von Gas in Sterne auf lokalen sowie globalen Skalen zu reduzieren. Die Supernovae produzieren heißes Gas mit starkem Überdruck im Vergleich zur Umgebung, das Ausflüsse treibt.

Contents

Contents **1**

1 Introduction **3**

2 The interstellar medium in the Milky Way: a multi-scale journey **7**

2.1 The Milky Way system: a global overview 7
2.2 Components of the interstellar medium 10
2.2.1 Gas 10
Molecular gas 10
Atomic gas 11
Warm Ionised gas 13
Hot Ionised gas 14
2.2.2 Dust 15
2.2.3 Interstellar radiation field 16
2.2.4 Magnetic fields 17
2.2.5 Cosmic rays 18
2.3 Heating and cooling 18
2.3.1 Radiative cooling 18
2.3.2 Heating 21
2.4 The phases of the interstellar medium: a theoretical approach 22
2.5 Stellar feedback 26
2.5.1 Protostellar jets and outflows 26
2.5.2 Ionising radiation and radiation pressure 27
2.5.3 Stellar winds 29
2.5.4 Supernovae 30

3 Stellar winds, supernovae and star cluster sink particles in the FLASH code **33**

3.1 The FLASH code 33
3.1.1 Magneto-hydrodynamics 34
3.1.2 Cooling, heating and chemistry 35
3.1.3 Gravity 35

3.1.4 Sink particles 36
3.2 Supernova feedback 38
3.3 Stellar winds 42
3.4 Sub-grid model for sink particles 46
3.4.1 A simple test for star cluster sink particles 50

4 The impact of supernova positioning on the insterstellar medium 55
4.1 Motivations and goals 55
4.2 Method 57
4.2.1 Initial turbulent stirring 57
4.2.2 Supernova driving 58
4.2.3 Simulations 59
4.2.4 Simulation analysis 59
4.3 Results 62
4.3.1 Energy input 62
4.3.2 Impact of supernova positioning 63
4.3.3 Thermal runaway 69
4.3.4 Random driving at different supernova rates 71
4.3.5 Peak driving vs. random driving 75
Discussion: Is peak driving realistic? 78
4.3.6 Mixed driving 78
Discussion: the transition between the peak and random driving regime. 82
4.3.7 Combined thermal energy and momentum injection . 82
4.3.8 Higher resolution 87
4.4 Conclusions 89

5 Regulation of star formation by stellar winds and supernovae 93
5.1 Motivations and goals 93
5.2 Method 94
5.2.1 Simulation setup 95
List of simulations 95
Initial conditions 97
Refinement criteria 98
5.3 Results 98
5.3.1 The relative importance of stellar winds and supernovae 98
Regulation of star formation at local scales 98
Energies 101
5.3.2 Global evolution and properties of the interstellar medium 108

Global overview 108
Mass fractions 117
Volume filling fractions 123
5.3.3 Star formation 126
5.3.4 Comparison with observations 133
5.4 Conclusions 135

6 Summary **139**

Bibliography **152**

CHAPTER 1

Introduction

The interstellar medium (ISM) is known to be "an entirely chaotic mass [...] of all possible shapes and sizes [...] broken up into numerous irregular details" (Minkowski, 1955), where many different physical processes play a crucial role in shaping its morphology and energy budget.

The life cycle of the ISM is strongly connected with the star formation activity within galaxies. Cold and dense molecular gas undergoes gravitational collapse, forming massive stars which in turn ionise, heat and compress the surrounding medium via stellar feedback. This powerful injection of energy and momentum disperses the gas locally and eventually triggers new star formation events. After some time, hot and cold gas cool down to the molecular phase, and the cycle starts again. This continuous loop between interstellar matter and stars involves several physical processes acting on spatial and temporal scales that span several orders of magnitude. For this reason, a detailed modelling of the ISM is required to better understand the origin of the observed properties of gas, dust and stars in galaxies.

Massive stars (with mass $> 8\,\mathrm{M}_\odot$) are one of the main drivers of galaxies evolution. They influence the surrounding medium at different scales by injecting feedback under the form of protostellar outflows (e.g. Matzner, 2007; Frank et al., 2014), radiation pressure (e.g. Krumholz & Matzner, 2009; Murray et al., 2010), UV radiation (e.g. Churchwell, 2002; Dale et al., 2012; Walch et al., 2012, 2013), stellar winds (e.g. Puls et al., 1996; Toalá & Arthur, 2011; Rogers & Pittard, 2013) and supernova (SN) explosions (e.g. Mac Low et al., 2005; Kiewe et al., 2012; Walch & Naab, 2015).

Due to their ubiquitous presence within star-forming galaxies, massive stars represent a continuous source of turbulence in the ISM. Observations of broad HI and CO emission lines show that warm, cold and molecular gas are shaped by supersonic turbulent motions with a typical one-dimensional velocity dispersion from few to $\approx 10\,\mathrm{km\,s^{-1}}$ (Larson, 1981; Goodman et al., 1998; Heiles & Troland, 2003; Petric & Rupen, 2007; Tamburro et al., 2009; Caldú-Primo et al., 2013). This turbulence should decay quickly in the absence of any continuous source (Stone et al., 1998; Mac Low, 1999). For this reason, massive stars are believed to be the origin of the intermediate and small scale turbulent flows observed in spiral galaxies (Mac Low & Klessen, 2004, but see also Walch et al. 2012; Boneberg et al. 2015), although other processes, such as ambipolar diffusion, magnetic fields, gravitational instabilities, accretion, mergers, galactic shear, etc., could also provide non-negligible contributions (see, e.g., Mestel & Spitzer, 1956; Sellwood & Balbus, 1999; Kritsuk & Norman, 2002; Wada et al., 2002; Aumer et al., 2010; Elmegreen & Burkert, 2010; Karl et al., 2010; Klessen & Hennebelle, 2010; Teyssier et al., 2010).

Feedback from massive stars, responsible for cloud dispersal and turbulence injection, might explain the low star formation efficiency inferred within the Galaxy (Zuckerman & Evans, 1974; Mac Low & Klessen, 2004), although other processes, such as large scale shear flows around spiral arms (Dobbs & Pringle, 2013), can significantly contribute. On the other hand, stellar feedback influences the thermal and kinetic pressures of the gas at large scales (Ostriker et al., 2010), creating a hot ionised medium (Cox & Smith, 1974; McKee & Ostriker, 1977) with high volume filling factor (Ferrière, 2001; Kalberla & Dedes, 2008) and launching powerful outflows from the disc (e.g. Oppenheimer et al., 2010; Creasey et al., 2013; Marinacci et al., 2014).

Despite the large number of previous studies investigating the impact of stellar feedback on the ISM, a complete picture of the mutual dependence between massive stars and interstellar gas is still missing. We improve on these earlier studies by performing three-dimensional (3D), Adaptive-Mesh-Refinement (AMR), (magneto-)hydrodynamic (MHD) simulations with the FLASH code including stellar winds and SN feedback in the ISM. We run different simulations of a $(256\,\mathrm{pc})^3$ periodic box with different initial densities, driving SNe at a fixed rate. We investigate how the ISM properties differ when varying the amount of SNe exploding within the medium, as well as when assuming different positions for the explosions. Subsequently, we include stellar winds, magnetic fields and self-consistent star formation using sink particles and we study how stellar winds and SNe are able to regulate star formation in a representative piece of a galactic disc.

The thesis is organised as follows: in chapter 2 we give a broad and general overview of the ISM properties. In chapter 3 we describe the numerical implementation of stellar winds, SNe and a sub-grid model for star cluster sink particles in the FLASH code. We study the impact of SN explosions alone on the ISM in chapter 4. In chapter 5 we investigate the importance of stellar winds and SNe in regulating the star formation process at galactic scales. We present a summary of the thesis in chapter 6.

CHAPTER 2

The interstellar medium in the Milky Way: a multi-scale journey

In this chapter, we give a brief overview of the main properties of the Galactic ISM at different scales. We focus our attention on the Galaxy alone due to our deeper understanding of its ISM properties with respect to other systems.

2.1 The Milky Way system: a global overview

The Milky Way (MW) is a Sb (spiral-barred) galaxy located close to the centre of mass of the Local Group. This is a group of 54 (3 spirals and 51 dwarfs) galaxies with radius ≈ 1.5 Mpc that is part of the Local Supercluster. The Galaxy is embedded in a halo of dark matter (DM), with radius $\sim 200-400\,\mathrm{kpc}$ and mass $1-2\times 10^{12}\,\mathrm{M}_\odot$ (e.g. Wilkinson & Evans, 1999). The stellar distribution can be described as a combination of an exponential thin disc, with radius $25-30\,\mathrm{kpc}$ and thickness $400-600\,\mathrm{pc}$, a central barred bulge with radius $\sim 2-3\,\mathrm{kpc}$ and an extended halo composed by old stars and globular clusters that extends up to $\approx 30\,\mathrm{kpc}$ from the Galactic centre (Binney & Merrifield, 1998). Stars dominate the mass budget close to the mid-plane of the galaxy, with a total mass of $\sim 5\times 10^{10}\,\mathrm{M}_\odot$ (Dehnen & Binney, 1998).

The gas component reaches similar outer radii, but its vertical distribution is remarkably different, with cold gas being concentrated towards the mid-plane and hotter gas having larger scale heights (see sec. 2.2.1). It is globally organised in two main and three minor spiral arms separated by inter-arm regions with smaller mass/densities. Fig. 2.1 shows an artistic

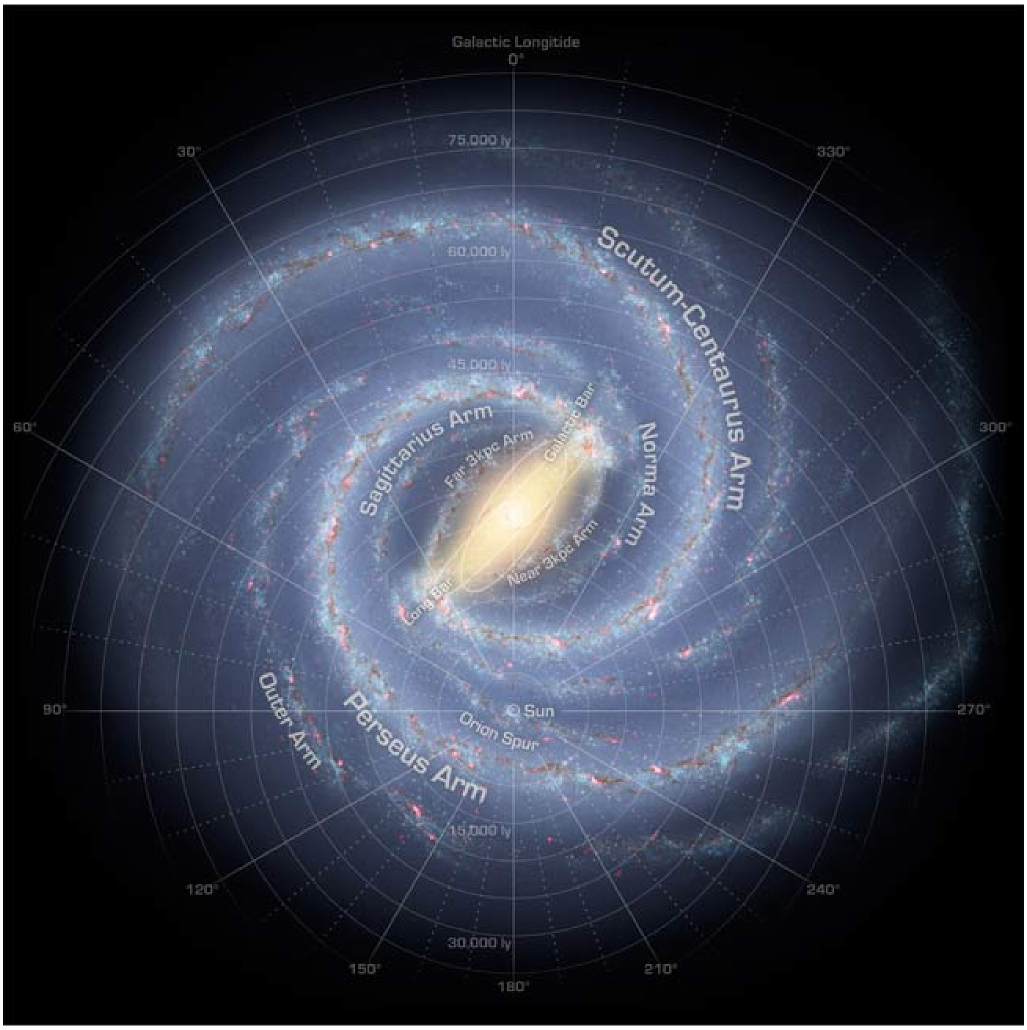
Galactic Longitide
0°
75,000 ly
30°
330°
60,000 ly
Scutum-Centaurus Arm
45,000 ly
60°
300°
Sagittarius Arm
Far 3kpc Arm
Galactic Bar
Norma Arm
Near 3kpc Arm
Long Bar
90°
Sun
270°
Outer Arm
Perseus Arm
Orion Spur
15,000 ly
120°
240°
30,000 ly
150°
210°
180°

Figure 2.1: *Artistic impression of the spiral arms of the Galaxy, as seen in face-on view. Credit: R. Hurt, SSC.*

impression of such a distribution. The gas in the ISM is composed by 70.4% of hydrogen, 28.1% of helium and the remaining 1.5% in metals (Ferrière, 2001), with densities spanning over a range of $n = 10^{-4} - 10^{6}\,\mathrm{cm}^{-3}$ and with temperatures $T = 10 - 10^{8}$ K. The total mass is $M_{\mathrm{gas}} \lesssim 10^{10}\,\mathrm{M}_{\odot}$ (Nakanishi & Sofue, 2006; Kalberla & Kerp, 2009) and it is dominated by atomic (H or H I) and molecular (H_2) hydrogen, with $M_{\mathrm{H}} \approx 0.5 - 0.75 \times M_{\mathrm{gas}}$. The ionised component (H^{+} or H II) does not contribute significantly to the total gas mass. The molecular gas distribution shows two separated peaks within 500 pc (Central Molecular Zone) and at $4 - 6$ kpc (Molecular Ring) from the Galactic centre. It declines exponentially outside the Molecular Ring, and atomic hydrogen dominates the mass at large radii (e.g. Klessen & Glover, 2014). While at large scales the majority of the mass tends to be

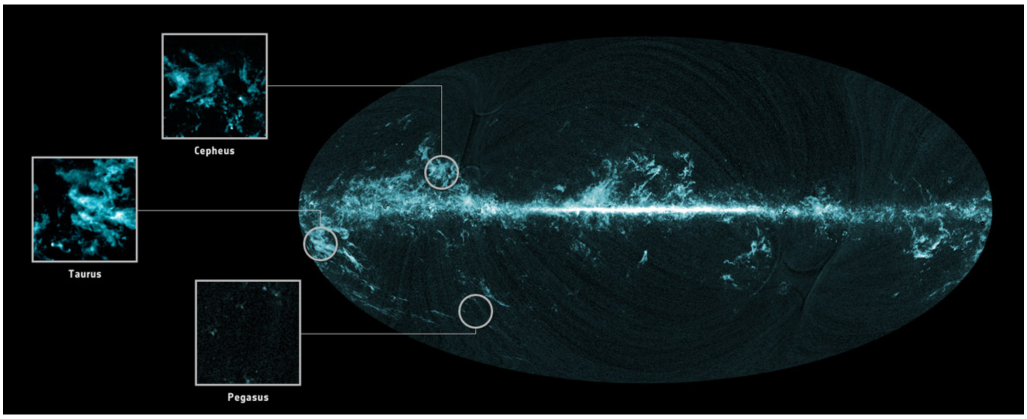

Figure 2.2: *Planck CO maps of Milky Way and three molecular cloud complexes (Cepheus, Taurus, Pegasus). Credit: Planck Collaboration.*

concentrated in large, coherent spiral arms close to the Galactic plane, at small scales its distribution is quite inhomogeneous, with about half of the mass locked up into small, irregular clouds that occupy $1-2\%$ of the total volume (Ferrière, 2001). These clouds can be divided into three main types: i) dark, starlight-absorbing molecular clouds (MCs), mostly composed by H_2, dust and other molecules, with densities $10^2-10^6\,\mathrm{cm}^{-3}$ and temperatures $T=10-30$ K; ii) diffuse clouds, consisting of atomic ($n \lesssim 100\,\mathrm{cm}^{-3}$) and cold ($T \gtrsim 100$ K) gas almost completely transparent to the background interstellar radiation field (ISRF) and iii) translucent clouds, which show intermediate properties. As an example, in Fig. 2.2 we show the all-sky molecular (CO) map of the MW and three representative molecular cloud complexes (Cepheus, Taurus, Pegasus) observed by the Planck satellite. While most of the emission comes from the mid-plane, especially close to the Galactic centre, one can notice how the distribution of molecular gas at small scales is quite clumpy and irregular.

Interstellar dust, with typical temperatures $T=10-100$ K, is also an important component of the ISM. Its total mass is roughly the same as the gas mass in metals, i.e. $\sim 0.01 \times M_{\mathrm{gas}}$. Its distribution follows the one of the densest gas component, as dust is formed more rapidly in this phase (e.g. Zhukovska et al., 2008). Despite its negligible contribution to the total mass of the ISM, we will see in sec. 2.2.2 that its presence within the MW, and in general within star-forming galaxies, is of fundamental importance.

Globally, gas contributes to only $\sim 1\%$ of the total mass of the Galaxy. Its mass is also 5 times smaller than the one enclosed in stars. Applying the cosmological baryon fraction to the virial mass of the MW, one would expect $2-3\times10^{11}\,\mathrm{M}_\odot$ of total baryonic mass of the Galaxy, 3-5 times larger than the one observed. Therefore, 70-80% of the MW's baryons are missing, a problem referred to as the missing baryons problem. A commonly accepted solution is that the MW is embedded in a corona of hot gas at temperatures of a few 10^6 K which contains most of the baryons associated with its potential well (Fukugita & Peebles, 2006) and that extends up to a few hundreds of kpc. However, no convincing detection of such a phase has been presented to date (see e.g. Gatto et al., 2013).

2.2 Components of the ISM

2.2.1 Gas

Molecular gas

MCs are mostly composed by H_2, a molecule difficult to observe, since it does not possess a permanent dipole moment. Direct detection of H_2 is possible by observing absorption lines via space-based UV telescopes and rotational-rovibrational emission in IR. These two methods, however, trace a very small fraction of the total molecular gas content owing to dust absorption of UV light and due to the fact that transitions in IR are mostly produced by "hot" H_2 heated by shocks and radiation. For these reasons, CO (^{12}CO,^{12}C^{16}O), the second most abundant molecule in space, is the most common tracer employed to observe molecular gas. This isotopologue, however, does not completely track the molecular gas distribution. At high densities, ^{12}CO emission becomes optically thick due to its high abundance and other isotopologues, such as ^{13}C^{16}O, ^{12}C^{18}O, ought to be employed. At even higher density, such as the ones typical of prestellar cores ($10^4\,\mathrm{cm}^{-3}$), the relative emissivity of CO drops due to its small critical densities (see also sec. 2.3.1) and efficient condensation onto dust grains. Therefore, other (complex) molecules with higher dipole moments, such as HCN and N^2H^+, need to be used to infer the physical conditions of very high density substructures. On the other hand, low mass MCs have too low density to produce enough CO, leading to the formation of "dark molecular gas". In this case, C^+ is employed to trace complexes with high H_2 fractions but little CO.

Molecular hydrogen mostly forms by means of H atoms adsorption on dust grains. In general, we can approximate MCs as self-gravitating objects with $n = 10^2 - 10^6\,\mathrm{cm}^{-3}$, $T = 10 - 30$ K and with typical sizes of a few tens of pc and masses from 10^4 to $10^6\,\mathrm{M}_\odot$. The scale height of the global molecular gas distribution is 75 pc (Tielens, 2005). The clouds are shaped and supported against gravity by supersonic turbulent motions. Rather than being symmetrical, well-defined spherical clouds, MCs exhibit complicated morphologies. Their internal structure, which can be described by a

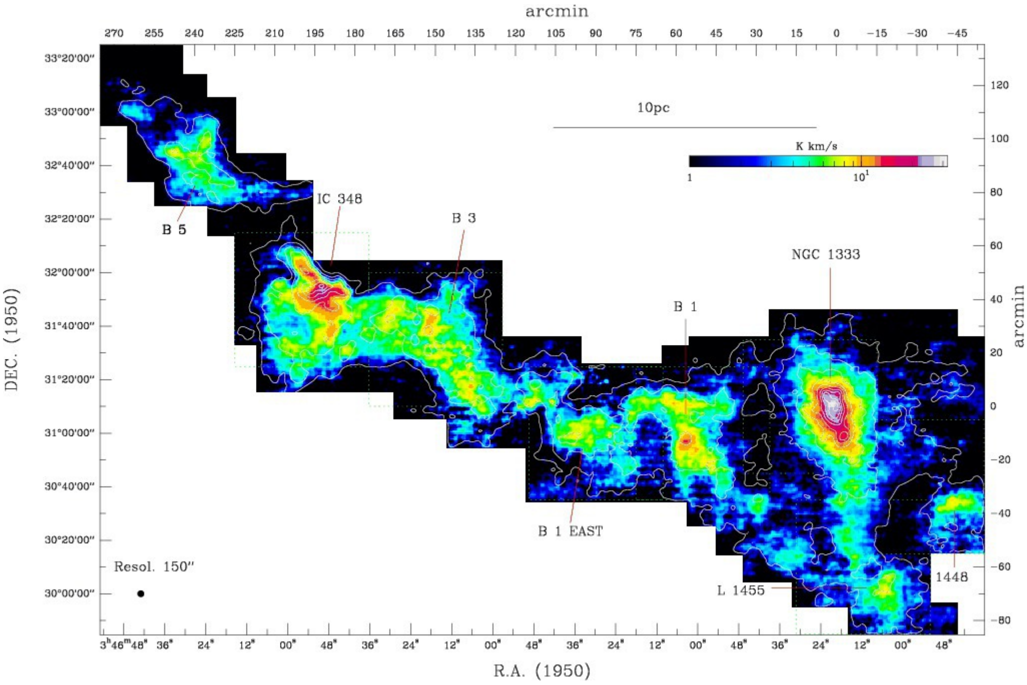
arcmin
270 255 240 225 210 195 180 165 150 135 120 105 90 75 60 45 30 15 0 −15 −30 −45
10pc
K km/s
1
10^1
IC 348
B 5
B 3
NGC 1333
B 1
B 1 EAST
L 1455
1448
Resol. 150″
DEC. (1950)
33°20′00″
33°00′00″
32°40′00″
32°20′00″
32°00′00″
31°40′00″
31°20′00″
31°00′00″
30°40′00″
30°20′00″
30°00′00″
arcmin
120 100 80 60 40 20 0 −20 −40 −60 −80
3h46m48s 36s 24s 12s 00s 48s 36s 24s 12s 00s 48s 36s 24s 12s 00s 48s 36s 24s 12s 00s 48s
R.A. (1950)

Figure 2.3: *^{13}CO (colours) and ^{12}CO (contours) maps of the Perseus cloud from Sun et al. (2006).*

fractal distribution (e.g. Stutzki et al., 1998), is a heterogeneous mixture of filaments and clumps of many different sizes and shapes. The smallest and densest cores, with size $\sim 0.1\,\mathrm{pc}$ and densities $n > 10^4\,\mathrm{cm}^{-3}$ (and masses $0.1 - 10^3\,\mathrm{M}_\odot$), are the building blocks from which stars are assembled. In Fig. 2.3 we show an example of such morphology by plotting the ^{13}CO (colours) and ^{12}CO (contours) maps of the Perseus cloud from Sun et al. (2006). As discussed in the previous paragraph, ^{12}CO traces a more extended (and in general less dense) molecular component. The CO structure significantly differs from a spherical distribution. It is composed by large filaments extending few pc and several density peaks shaped by internal turbulent motions (e.g. André et al., 2010).

Atomic gas

The distribution of atomic hydrogen can be probed by performing radio observations of the 21-cm line from the hyperfine structure of the hydrogen atom, or by observing Lyα absorption lines of hot stars. This component is classically divided into a Cold Neutral Medium (CNM), with typical densities of $n = 20 - 50\,\mathrm{cm}^{-3}$ and temperatures $T = 50 - 100$ K, and a Warm Neutral Medium (WNM) phase (see sec. 2.4), with $n = 0.2 - 0.5\,\mathrm{cm}^{-3}$ and temperatures $T = 6000 - 10000$ K (Ferrière, 2001). While the WNM repre-

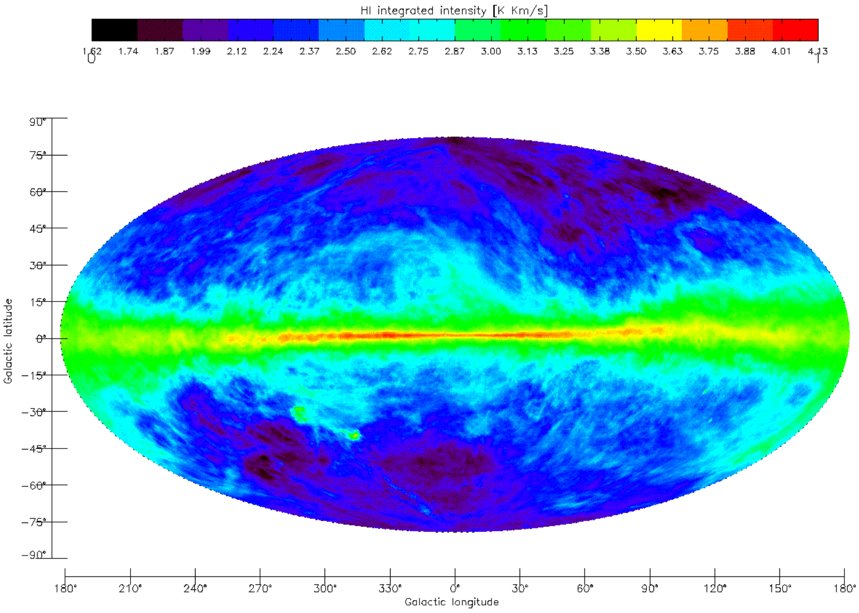
HI integrated intensity [K Km/s]
1.62
1.74
1.87
1.99
2.12
2.24
2.37
2.50
2.62
2.75
2.87
3.00
3.13
3.25
3.38
3.50
3.63
3.75
3.88
4.01
4.13
Galactic latitude
90°
75°
60°
45°
30°
15°
0°
−15°
−30°
−45°
−60°
−75°
−90°
180°
210°
240°
270°
300°
330°
0°
30°
60°
90°
120°
150°
180°
Galactic longitude

Figure 2.4: *H 21-cm integrated emission of the MW from Kalberla et al. (2005).*

sents a diffuse component that fills the majority of the Galactic plane, with typical scale heights of $200 - 400\,\mathrm{pc}$ (Tielens, 2005), the CNM dominates the total mass in H and is mostly positioned in small clouds at or in the vicinity of the mid-plane (with scale height of $\approx 100\,\mathrm{pc}$, Tielens, 2005). As for MCs, CNM clouds are more sheet-like or filamentary, rather than being perfect spheres. While most of them are likely to have formed by condensation of WNM via thermal instability (Hennebelle & Pérault, 1999), a non-negligible fraction of these clouds are part of H shells and super-shells (with radii $50 - 10^3$ pc, Palouš & Ehlerová, 2000). Cold, neutral and atomic gas can also be found at the edge of MCs, where powerful UV radiation from young and massive stars can dissociate the outer layers of molecular complexes.

In Fig. 2.4 we show the integrated atomic hydrogen 21-cm emission map of the MW from Kalberla et al. (2005). A simple visual comparison of this map with Fig. 2.2 show that atomic and molecular gas are mostly spatially correlated (although the scales are different). The bulk of H emission comes again from the inner central region at low altitudes. The atomic hydrogen distribution, however, is more extended both in longitude and in latitude.

Warm atomic hydrogen can also be found at large (few to 100 kpc) distances from the Galactic plane in the form of High Velocity Clouds (HVCs), diffuse clouds with masses $10^7 - 10^8\,\mathrm{M}_\odot$ that travel through the Galactic halo. Contrary to dwarf satellite galaxies, these clouds do not belong to any particular DM substructure and their origin is still unclear[1].

Warm Ionised gas

Observations of free-free absorption of the Galaxy's synchrotron background, high dispersion measures of pulsar signals and faint optical emission lines of weakly ionised metals show that a diffuse, warm ($T \sim 8000$ K) ionised phase (WIM), at similar densities of its neutral counterpart, is present throughout the Galaxy[2], with a vertical scale height of $\sim 1\,\mathrm{kpc}$ (Ferrière, 2001; Klessen & Glover, 2014, and references therein). In Fig. 2.5 we show the integrated Hα emission from the Galactic northern hemisphere from Haffner et al. (2003). The emission is clearly dominated by HII regions close or in the Galactic plane, while the diffuse component is representative of the WIM.

The origin of the WIM is still a matter of debate. UV photons from massive stars are in principle able to create and sustain a diffuse, ionised phase by leaking-out from HII regions through holes in the gas distribution at small scales. The fraction of ionising photons that can to escape to large scale heights through a porous, turbulent medium is, however, quite uncertain (see e.g. Dijkstra et al., 2014, for a study in the high-redshift universe). Mechanisms other than photoionisation, such as photoelectric effect, weak shock-heating, turbulence dissipation, cosmic rays and magnetic fields may also provide non-negligible contributions (see Ferrière, 2001, and references therein).

---

[1] The common belief that these structures originated via thermal instability of hot coronal gas has been proved wrong by Binney et al. (2009), who instead propose that HVCs are perhaps produced by condensation of large quantities of gas expelled to high altitudes from the disc by stellar feedback and, to a minor extent, by accretion from dwarf satellites.

[2] HII regions are usually not considered to be part of this phase.

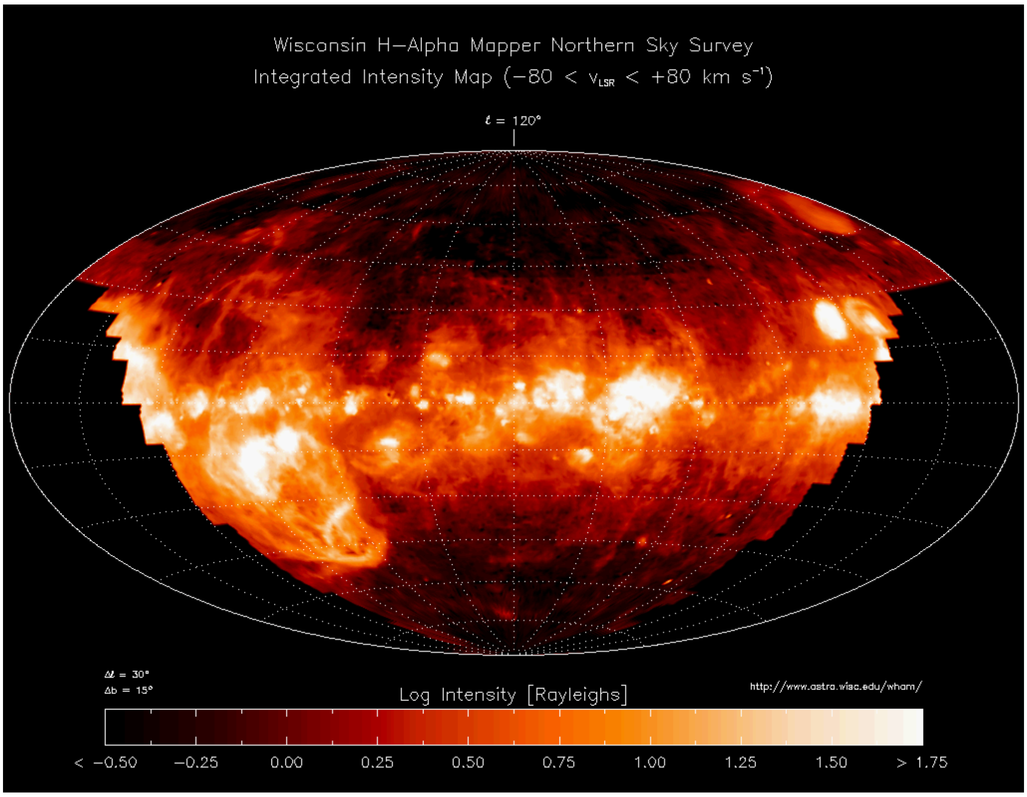
Wisconsin H–Alpha Mapper Northern Sky Survey
Integrated Intensity Map (−80 < v_LSR < +80 km s⁻¹)
ℓ = 120°
Δℓ = 30°
Δb = 15°
Log Intensity [Rayleighs]
http://www.astro.wisc.edu/wham/
< −0.50
−0.25
0.00
0.25
0.50
0.75
1.00
1.25
1.50
> 1.75

Figure 2.5: *Hα integrated emission of the Galactic northern hemisphere from Haffner et al. (2003).*

Hot Ionised gas

The ISM also consists of a diffuse, hot ionised medium (HIM) with densities $n \sim 10^{-3}\,\mathrm{cm}^{-3}$ and temperatures $T \sim 10^6$ K. This phase is rather elusive to detections due to its low densities and high temperatures. This is particularly true for the primordial, low metallicity coronal gas that fills the outer tens-hundreds kpc of the Galaxy (see sec. 2.1). Soft X-ray excess at ~ 0.25 keV can in principle be used to probe the presence of hot gas at low latitudes, but the contamination from the Local Bubble, as well as considerable absorption from cold gas, do not allow us to draw definitive conclusions on the properties of this phase. On the other hand, few individual regions emitting at higher energies (0.5-1 keV) have confirmed the presence of hot plasma close to the Galactic plane in correspondence to supernova remnants (SNRs) and superbubbles (see sec. 2.5). The large scale distribution of the HIM can be inferred from looking at gas at $T \sim$ few 10^5 K via absorption of highly ionised metal lines, since this component is likely to be collisionally, rather than photo, ionised and therefore related to the hotter plasma. The

Component	Density (cm^{-3})	Temperature (K)	Scale height (pc)
Molecular	> 100	10-20	75
CNM	20-50	50-100	100
WNM	0.2-0.5	6000-10000	200-400
WIM	0.2-0.5	8000	1000
HIM	$10^{-2} - 10^{-3}$	10^6	3000

Table 2.1: *Main properties of the ISM gas phases. From left to right: name of the phase, typical number density, typical temperature, estimated scale height. From Tielens (2005); Klessen & Glover (2014).*

(quite uncertain) scale height of the hot phase is between 1.5 and 5 kpc (Ferrière, 2001, and references therein).

It is now widely accepted that the HIM is generated by stellar feedback, especially SN explosions (Cox & Smith, 1974; McKee & Ostriker, 1977, but see also Spitzer 1956, for theoretical arguments in favour of the presence of coronal gas at large heights). This powerful injection of energy is able to create large, over-pressurised bubbles of hot and tenuous gas that sweep up, heat and ionise the surrounding medium. The combined action of several massive stars fills significant fractions of the Galactic plane volume with hot gas, which in turn may power vigorous outflows from the disc (see sec. 2.5 and next chapters).

Table 2.1 gives a summary of the different gas components described so far, along with their main properties. The scale heights presented here, i.e. the typical scales at which each phase operates, should be considered as very crude estimates.

2.2.2 Dust

Despite having negligible mass (mostly composed by metals) with respect to the total gas mass, interstellar dust is a key player in the star formation process and, in general, in setting the thermodynamical properties of the gas within galaxies (see next sections). Dust is in general able to absorb, scatter and polarise light at different frequencies. Its most important observational signature is thermal continuum emission in mid and far-IR bands due to absorption of UV photons from massive stars. It is estimated that 30% or more of the energy emitted as starlight is absorbed and re-emitted by dust throughout the Universe (Bernstein et al., 2002).

Dust grains can be divided into different types: silicates, graphite, polycyclic aromatic hydrocarbons (PAHs), hydrogenated amorphous carbon and grains composed by a various mixtures of silicates, organic material and water ice (Zubko et al., 2004). The size distribution of dust grains is described by a power law, with scaling exponent of -3.5 (Mathis et al., 1977). The total mass is dominated by large grains, while small grains give the most important contribution to the total surface area.

The physical processes that regulate the formation of dust grains in the ISM are not completely understood yet. Dust is believed to be produced in the cool atmospheres of red giant/supergiant stars and in planetary nebulae and then expelled into the ISM by radiation pressure (e.g. Draine, 1990). However, theoretical estimates suggest that dust is destroyed by shocks from SNe at a faster rate than the injection rate from cold stars and observations of dense clouds show that the depletion rate of metals (e.g. silicon and iron) in these structures is higher than in more diffuse media. These considerations evoke a second channel for dust formation via condensation in dense and cold gas (Ferrière, 2001, and references therein).

2.2.3 Interstellar radiation field

Other than gas and dust, the space between stars is filled by additional components, namely photons, magnetic fields and cosmic rays (CRs), that are crucial in regulating the evolution and properties of the interstellar matter. The ISRF can be separated into different components: synchrotron emission from relativistic electrons, the cosmic microwave background (CMB), IR and far-IR emission from dust, bound-bound, bound-free and free-free emission from ionized gas at $T = 10^4$ K (nebular emission), starlight and X-ray from the hot and warm-hot phases ($T > 10^5$ K).

Fig. 2.6 shows the estimated energy density of the ISRF at different frequencies from Klessen & Glover (2014). The CMB, old and young stars contributions are taken to be perfect blackbodies with $T = 2.73, 3500, 18000$ K, respectively. At radio frequencies, synchrotron emission dominates the energy budget of the ISRF. Its contribution to the total bolometric energy is, however, quite low. In the microwave band, the CMB gives the highest contribution, with a peak at $\lesssim 10^{-13}$ erg cm^{-3}. Dust thermal emission dominates in the IR, while starlight from old, low-mass stars produces a maximum in the optical band. At higher frequencies young, massive and hot stars produce UV photons that give rise to a second, less extended peak. Finally, X-rays give a much smaller contribution at high energies. By integrating the contribution of each component listed in the previous paragraph, Klessen & Glover (2014) find that the bolometric energy densities of CMB, IR dust emission and starlight are of similar amplitude, while synchrotron, X-ray and nebular emissions are smaller by 5, 4 and 2 orders of magnitude, respectively.

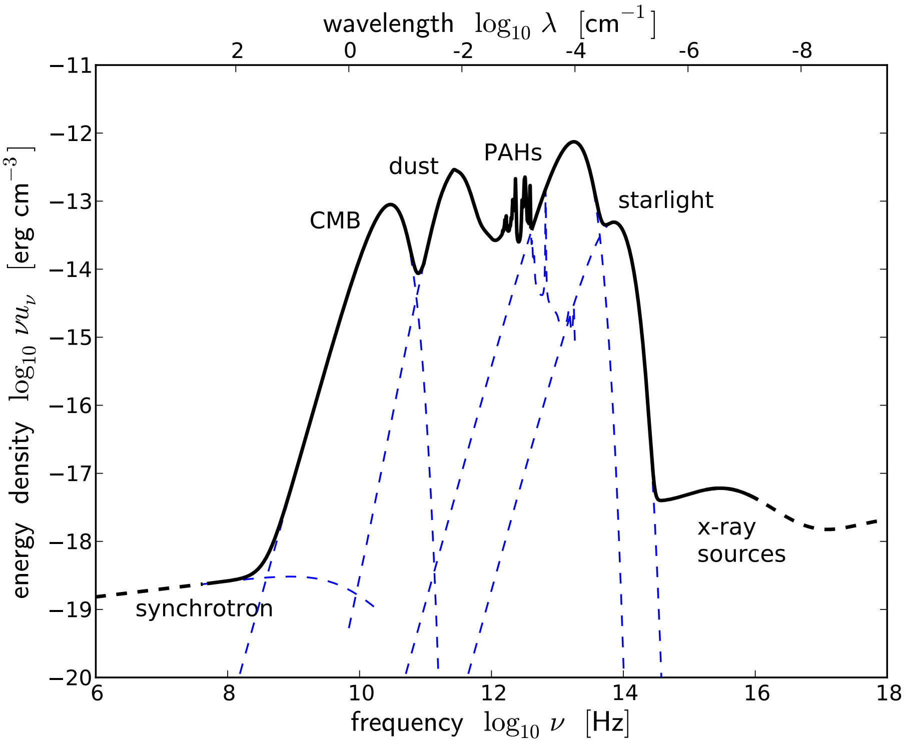

Figure 2.6: *ISRF energy density at different frequencies from Klessen & Glover (2014).*

2.2.4 Magnetic fields

Large and small scale magnetic fields are present throughout the Galaxy, influencing the dynamics of gas and dust and providing moderate contributions to the total energy budget of the ISM. Different observational techniques can be employed to infer the strength and orientation of the magnetic field, from observations of starlight linearly polarised by elongated dust grains partially aligned with the magnetic field, Zeeman-splitting of the H 21-cm line (or other radio lines), Faraday rotation of linearly polarised radio emission[3] to synchrotron emission from relativistic electrons.

In general the strength of the magnetic field is $\gtrsim 1\ \mu$G in the diffuse, ionised gas and it varies from a few μG within regions composed by atomic hydrogen (Troland & Heiles, 1986) to $10^2 - 10^3\mu$G in high density gas (e.g. Crutcher, 1999). The magnetic field distribution in the Galaxy is rather complex, showing tangled, "turbulent" substructures. The details are still a matter of debate.

---

[3] Rotation measures need independent estimates of the free electron column density along the line of sight, such as the dispersion measure, in order to provide a measure of the magnetic field strength. Same as for synchrotron emission, where the spectrum of relativistic electrons has to be assumed or estimated independently.

2.2.5 Cosmic rays

Observations in γ-ray band show that CRs are relativistic particles (protons, helium nuclei, electrons and metal nuclei) traveling close to the speed of light and having energies that span from 100 MeV to more than 1 TeV. Their energy power spectrum can be described by a power-law, with scaling exponent between -2 and -3.

The most energetic particles are probably of extra-Galactic origin, while the majority of CRs residing at low energies are produced in SN shocks via Fermi acceleration (Ackermann et al., 2013). CRs diffuse through magnetic field lines and scatter with the gas component, therefore providing an additional large-scale pressure that can launch outflows from the disc (e.g. Hanasz et al., 2013; Girichidis et al., 2015). Unlike UV and soft X-ray photons, CRs can penetrate inside MCs, partially heating and ionising molecular hydrogen.

2.3 Heating and cooling

2.3.1 Radiative cooling

Cooling of the ISM is a fundamental mechanism that has to be taken into account when studying the thermal and dynamical distribution of gas and dust in galaxies. Cooling of gas can be achieved either adiabatically, i.e. by expanding and doing work on the surrounding medium, or radiatively, i.e. by emitting photons. Here, we focus on the second and by far most dominant process.

The simplest case of radiative cooling can be described by considering a static population (without chemical reactions) of atoms in the optically-thin regime, where photons emitted by the population or by an incident radiation field are not absorbed by the atoms. Therefore, stimulated emission and absorption can be neglected and the cooling process can solely be described by collisional excitation, de-excitation and spontaneous emission. Collisions between atoms can move electrons from an initial, generic level to an excited state. These electrons cascade down towards smaller energy levels either by collisional de-excitation or by emitting photons. The probability for an atom in an excited state to remove its energy via photon emission is given by the critical density of the electron transition, n_{crit}, that is proportional to the ratio between the Einstein's coefficient for spontaneous emission and the collisional de-excitation rate.

Typically, the density of the gas within galaxies is well below the critical densities for the corresponding electron transitions. Therefore, electrons in excited states are more prone to remove energy by emitting photons and gas can cool efficiently. Most of the atoms settle to their ground states. Radiative cooling is able to remove substantial fractions of energy from the system via photon emission. The amount of energy radiated away is dependent on the number of emitters as well as on the number of collisional partners that are required to move electrons to excited levels in the first place. Therefore, the radiative cooling rate scales with density squared.

In few cases, such as for the CO(J=1-0) transition in very dense ($n > 10^3\,\mathrm{cm}^{-3}$) gas, the density is higher than n_crit and a very large number of collisional partners are available. Hence, energy is removed via collisional de-excitation, cooling is inefficient, and the gas approaches local thermodynamical equilibrium (LTE). The level populations tend to their LTE values following the Boltzmann distribution. When the system approaches LTE, collisional de-excitations dominate and radiative cooling is less probable. In these conditions the fraction of atoms in excited states is set by the temperature, rather than by the collisional excitation rate. Hence, on average the amount of energy radiated away solely depends on the number of emitters, making the radiative cooling rate linearly, rather than quadratically, proportional to the density.

In the opthically-thick limit, local absorption of photons emitted by neighbouring atoms has the important effect of lowering the critical density at which LTE is reached, since it decreases the rate of spontaneous emission (see Klessen & Glover, 2014, for details.). The higher is the optical depth, i.e. the higher is the amount of photons trapped by the atoms population, the lower is n_crit. This picture is simplified, as the ISM is composed by many different atoms and molecules with their own specific transitions and therefore critical densities.

For a prototypical ISM, at high temperatures ($T \gtrsim 3\times10^4$ K) the cooling rate of the gas is dominated by free-free and ionised metals line emission. In these conditions the cooling function (or cooling efficiency) Λ, related to the cooling rate via $\dot{\epsilon} = n_\mathrm{e} n \Lambda$ (with n_e number density of free electrons and n number density of H nuclei), can be computed assuming collisional ionisation equilibrium (CIE). This allows to compute the fractional abundances of each element by considering equilibrium between collisional ionisation and radiative recombination, making the cooling function dependent only on temperature and metallicity.

In Fig. 2.7 we show the cooling function for $10^4 < T < 10^8$ K from Gnat & Ferland (2012) assuming CIE and solar metallicity. For $3\times10^4 < T < 10^6$ K hydrogen is ionised and the cooling efficiency has its maximum, with most of the contribution from line emission of weakly ionised metals, such as C, O

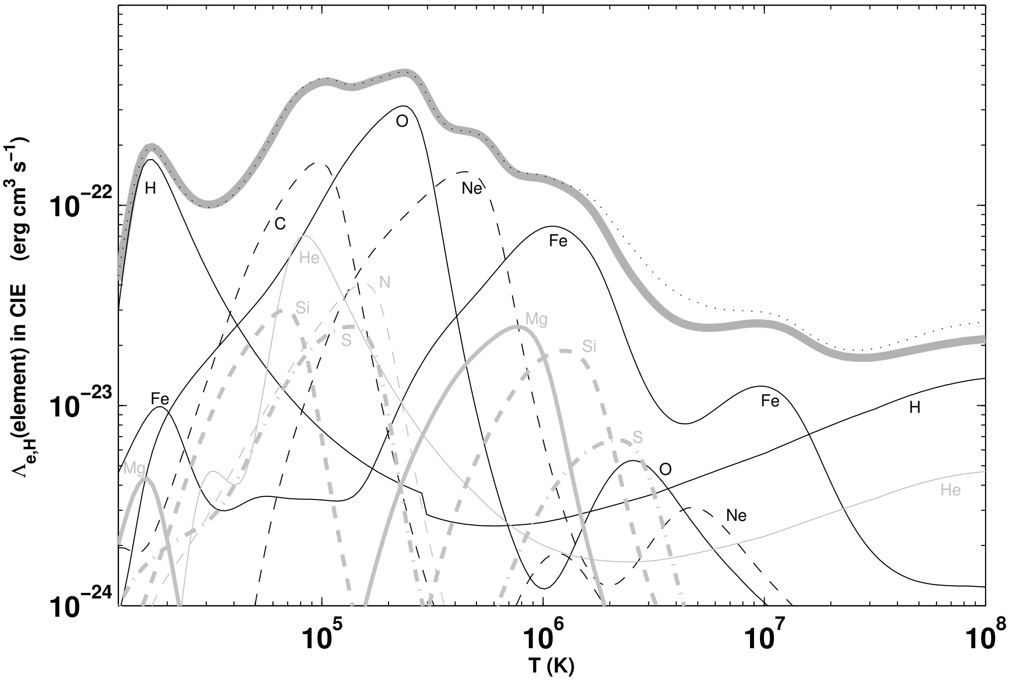

Figure 2.7: *Cooling function (with contributions from each coolant) for* $10^4 < T < 10^8$ *K from Gnat & Ferland (2012).*

and Ne. At higher temperatures most of the metals become fully ionised and Fe is the most important coolant up to $T \sim 10^7$ K. At extremely high T, iron becomes fully ionised as well and free-free bremsstrahlung emission, mostly due to protons and electrons from hydrogen and, to a minor extent, helium, is the main cooling mechanism. At $10^4 \lesssim T \lesssim 3 \times 10^4$ K atomic hydrogen is the main coolant, with a secondary peak in Λ caused by excitation of the Lyman (mostly Lyα) series.

Below $\approx 10^4$ K, the cooling efficiency drops dramatically due to an increasingly small number (and energy) of free electrons. Fine-structure line emission from C^+ and O are the most important coolants in the diffuse ISM (i.e. $10^3 < T < 10^4$ K). At $10^2 < T < 10^3$ K cooling from neutral oxygen is less efficient and C^+ dominates. In denser and colder regions, where dust can provide enough shielding, ionised carbon recombines and atomic carbon fine-structure cooling becomes the most effective process. For densities ($n \sim 1000\,\mathrm{cm}^{-3}$) and temperatures ($T \sim 20$ K) typical of MCs, atomic carbon and oxygen produce large quantities of carbon monoxyde. In this regime rotational transitions of CO are the most important cooling mechanisms. For extremely high densities ($n > 10^5 - 10^6\,\mathrm{cm}^{-3}$) most of the coolants approaches LTE and the cooling rate scale with n, rather than n^2.

After this point, gas-dust grain energy transfer becomes the most efficient cooling process (with cooling rate $\propto n^2$).

2.3.2 Heating

Radiative and adiabatic cooling are balanced by several heating mechanisms. Below, we give a brief description of the main heating processes in the ISM.

Photoelectric heating is one of the most important heating mechanisms for the warm and cold phases. Electrons stripped from dust grains by incident radiation via the photoelectric effect can share a substantial amount of kinetic energy with the surrounding medium via collisions. The amount of kinetic energy carried by a single photo-electron, which can be as high as 1 eV or more (Klessen & Glover, 2014), is equal to the difference in energy between the incident photon and the ionisation potential of the grain. Typically, incident photons are required to have energies > 6 eV (mid/far-UV band) in order to remove electrons from dust grains. Negatively charged grain are easier to photoionise due to their lower energy barrier. At high visual extinctions, such as for MCs, dust is well shielded from UV photons and photoelectric heating does not play a major role.

Dissociation of H_2 molecules by UV photons produces H atoms with kinetic energies sufficiently high to heat the surrounding gas. On average, this mechanism provides a heating rate of 0.4 eV per dissociation (Black & Dalgarno, 1977). The absorption of UV photons by H_2, however, leads to photodissociation only $\sim 15\%$ of the time (Draine & Bertoldi, 1996), while in the other cases it simply moves electrons to excited states. The latter can lead to heating via UV-pumping. While at low H_2 densities the excited electrons cascade down to lower energy levels by emitting a number of near-IR photons (with a non-zero probability of directly re-emitting a single UV photon), at densities higher than $1000\,\mathrm{cm}^{-3}$ the number of collisional partners is high and the excited molecule can heat the surrounding medium via collisional de-excitations. The average heating rate per pumping event is 2 eV (Klessen & Glover, 2014, and references therein). UV pumping is not a dominant heating mechanism in normal ISM conditions, but can become important in dense protostellar cores irradiated by (most likely internal) UV sources.

CRs represent the main heating process in dense gas, where shielding is able to significantly reduce the flux of UV photons and therefore heating from photoelectric effect, as well as from H_2 photodissociation and UV pumping. CRs are able to create ions and free electrons via collisions with H and He atoms or H_2 molecules, which in turn can eventually produce secondary ionisations. These particles have large kinetic energies and heat the surrounding gas via collisions. The amount of energy transferred to the medium for each CR ionisation event is typically between 10 and 20 eV (Klessen & Glover, 2014, and references therein).

X-ray ionisation heats the ISM in a similar way. Absorption of an X-ray photon by an atom or molecule produces an energetic free electron that causes a chain of secondary ionisations. Some of the kinetic energy of these particles are transferred to the medium via collisions. Unlike CRs, however, X-ray are usually absorbed before penetrating deep inside MCs. Therefore, despite being less important than the photoelectric effect, this heating mechanism is more effective in the diffuse, rather than dense, ISM.

Chemical reactions can also release energy into the surrounding gas. In particular, the formation of H_2 from two hydrogen atoms produces a molecule that is initially in an excited rotational and/or vibrational state. As for the UV pumping case, this energy is promptly radiated away in the moment when the ambient medium density is low. For high densities, however, this energy is shared with other particles via collisions. In principle this mechanism might be as important (if not more) as CRs heating in the dense ISM. The rate at which H_2 formation transfers energy to the medium is, however, rather uncertain and different studies have led to opposite conclusions (Klessen & Glover, 2014, and references therein).

Many other mechanisms, such as photionisation of carbon atoms or grain-gas heating, can contribute to the thermal balance of the ISM. Their role, however, is likely to be negligible.

Finally, dynamical process, such as turbulence, gravity, etc., can lead to significant heating. Their contribution can be significantly more important than any other diffuse heating process. The determination of the relative importance of these mechanisms is, however, not straightforward and ought to be investigated via numerical modelling (e.g. Glover & Clark, 2012b).

2.4 The phases of the ISM: a theoretical approach

The existence of two separated atomic phases at $T \sim 100$ (CNM) and 10^4 K (WNM), the so-called two-phase model for the ISM, was theoretically demonstrated by Field et al. (1969, see also Spitzer 1968). The basic principle of this model is that two separate gas phases with different densities and temperatures can coexist in pressure equilibrium due to the balance between cooling and heating.

We can define a net cooling (or heating) rate $\mathcal{L}$ as the difference between the cooling ($n^2\Lambda$) and the heating rates ($n\Gamma$) at different densities and temperatures (or pressures P), $\mathcal{L} = n^2\Lambda - n\Gamma$. The condition $\mathcal{L} = 0$ defines a thermal equilibrium curve in the density-pressure (or, equiva-

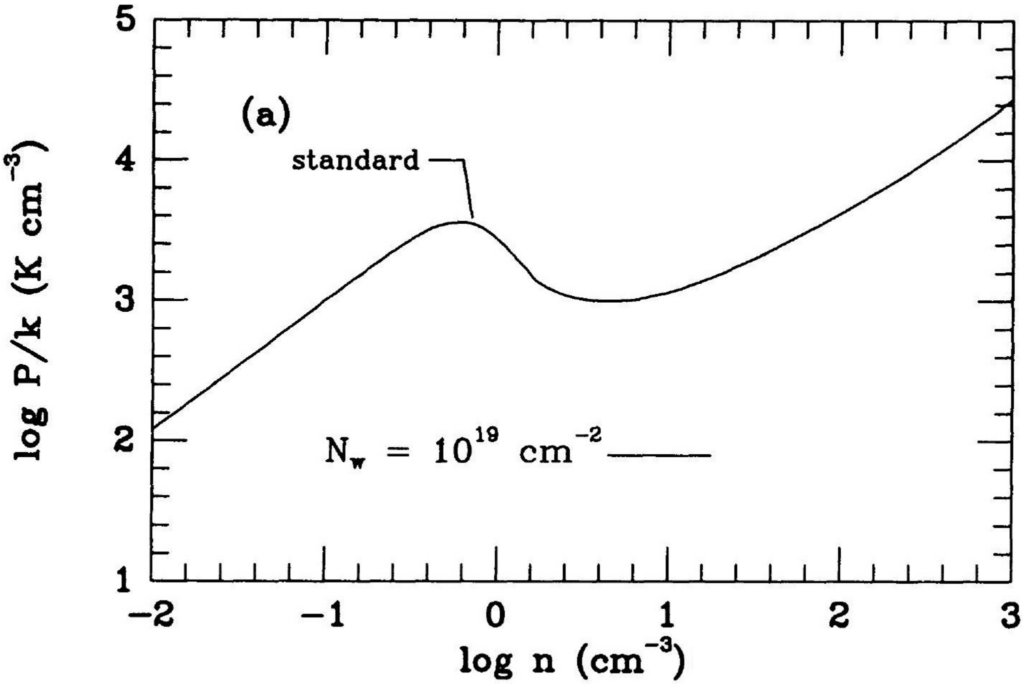

Figure 2.8: *Equilibrium curve in the density-pressure space from Wolfire et al. (1995).*

lently, in the density-temperature, temperature-pressure) space. In Fig. 2.8 we show the equilibrium curve in the density-pressure space computed by Wolfire et al. (1995) by equating several heating and cooling processes. Gas parcels sitting on this curve are in net thermal equilibrium, as heating and cooling balance each other. Gas that resides above the equilibrium curve is dominated by heating, while cooling is more important for points below the curve. Phases in net thermal equilibrium with different densities (and temperatures) can coexist in pressure equilibrium for a pressure range $P/k_{\rm B} = 990 - 3600$ K cm^{-3}, with $k_{\rm B}$ being the Boltzmann's constant. A horizontal line with $P/k_{\rm B} = 3000$ K cm^{-3} intersects the equilibrium curve in three points. The first point is representative of the WNM, with $T \sim 8000$ K and $n \sim 0.1\,{\rm cm}^{-3}$, while the one at highest density is the CNM, with $T \sim 50$ K and $n \sim 50\,{\rm cm}^{-3}$ (see Wolfire et al., 1995, for details). The second intersection at $n \approx 1\,{\rm cm}^{-3}$ is an unstable phase that is not allowed to exist in thermal equilibrium. In fact, by linearly perturbing the equilibrium equation $\mathcal{L} = 0$ it can be shown that thermal stability holds only when $\partial {\rm ln} P/\partial {\rm ln}\rho > 0$ for perturbations at constant $\mathcal{L}$. This condition is satisfied for the WNM and CNM phases, but not in the range $n = 0.2 - 6\,{\rm cm}^{-3}$, where the pressure decreases for increasing density at $\mathcal{L} = 0$. Therefore, gas parcels sitting in this pressure-density range, once perturbed, are forced

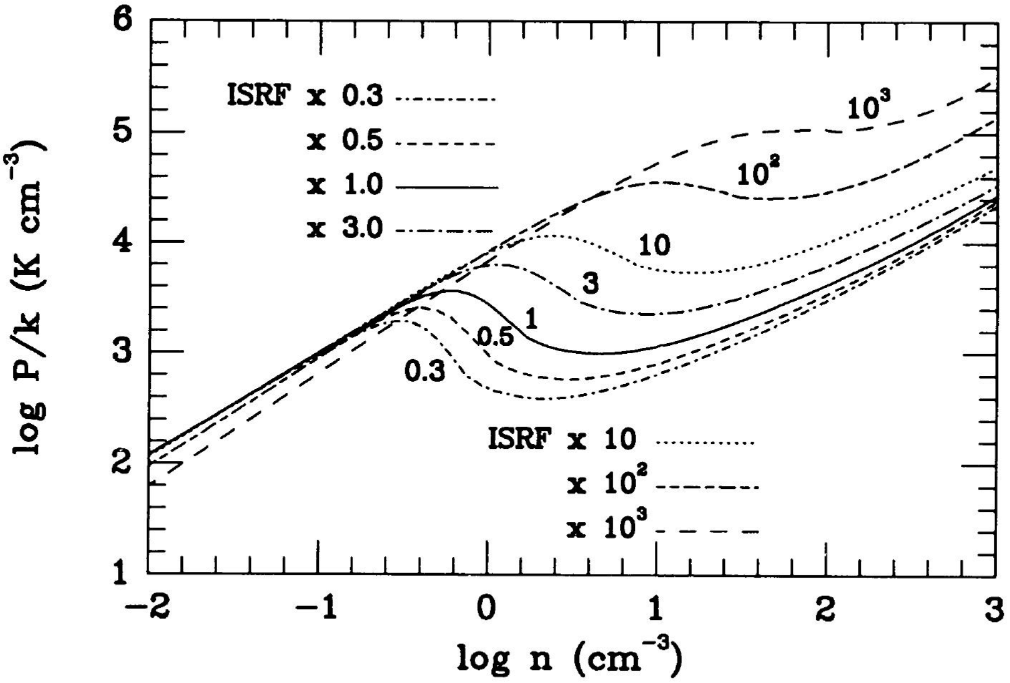

Figure 2.9: Equilibrium curves in the density-pressure space for different values of the ISRF (G_0) from Wolfire et al. (1995).

to move towards the WNM and CNM stable phases via thermal instability, i.e. via heating or cooling.

The exact conditions for which the WNM and CNM can coexist in pressure equilibrium are set by numerous details on the micro-processes that regulate the balance between heating and cooling. Changes in the main properties of the heating and cooling mechanisms have a remarkable effect on the equilibrium curve. As an example, in Fig. 2.9 we show the equilibrium curves computed for the same heating and cooling processes as Fig. 2.8 but varying the intensity of the ISRF. The latter is simply taken as the far-UV interstellar radiation field, G_0, and it varies from 0.3 to 1000 times the value used to compute the equilibrium curve in Fig. 2.8 ($G_0 = 1.7$, Habing, 1968; Draine, 1978). For low ISRF intensities, the curve moves to smaller densities and pressures. Smaller G_0 reduces the amount of photoelectric heating and equilibrium can be achieved at smaller pressure and densities, since less cooling is necessary for reaching $\mathcal{L} = 0$. Increasing the ISRF, on the other hand, moves the equilibrium curves to higher densities and pressures, as the heating rate is higher and stronger cooling is needed. For $G_0 > 100$ only one single stable phase is possible.

The two-phase equilibrium model represents a powerful, although incomplete, description of the ISM thermodynamical state. In the late 70s,

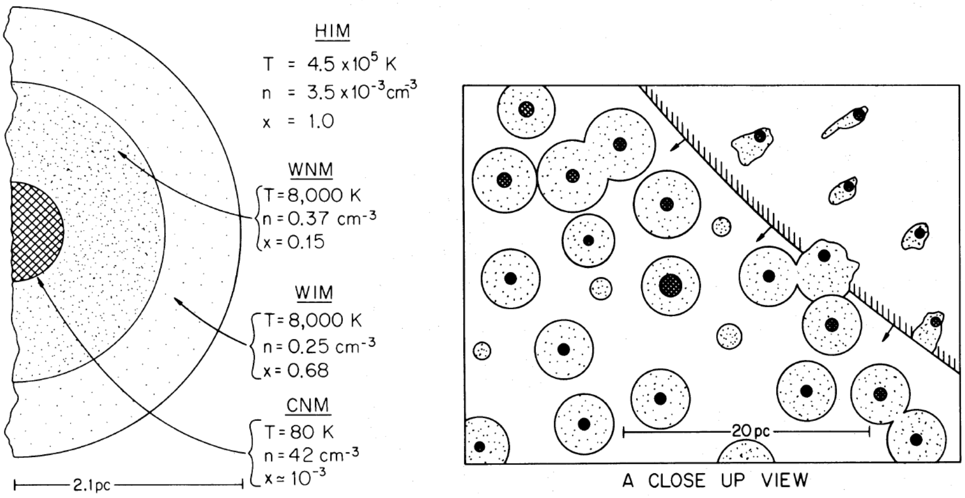

Fig. 1

Fig. 2

Figure 2.10: *Schematic representation of the three-phase ISM from McKee & Ostriker (1977). Left: spatial distribution of the CNM, WNM/WIM and HIM. Right: Small scale structure of the three-phase ISM with a SN blast wave sweeping through the cold and warm phases.*

McKee & Ostriker (1977) proposed a new paradigm, where an additional third phase, i.e. the HIM, resides in pressure equilibrium with the WNM and CNM: the three-phase model. SN explosions are able to inject large amounts of energy into the ISM by creating hot ($T \gtrsim 10^6$ K) and tenuous ($n \sim 10^{-3}\,\mathrm{cm}^{-3}$) bubbles that expand and sweep-up the surrounding material via powerful blast waves. The combined action of many explosions from massive stars produces a HIM in pressure equilibrium with the warm and cold phases that fills from 20 to 80% of the volume of the MW with increasing height above the disc (Ferrière, 2001; Kalberla & Dedes, 2008).

In Fig. 2.10 we show a schematic representation of the three-phase ISM from McKee & Ostriker (1977). The cold and warm phases are assumed to be organised in spherical clouds of few pc size in pressure equilibrium with the hot component (left). Each cloud has a warm, ionised layer (WIM) maintained by the interstellar UV field and, partially, by thermal conduction between the HIM and the WNM. The influence of a SN explosion on the ISM small scale structure is shown on the right panel. A powerful blast wave expands into the medium, heating and partially destroying the outer warm layers of the clouds. Eventually, the cold core of each cloud (CNM) can be destroyed later on via thermal conduction with the hot plasma that fills the SN bubble interior. At late times, the blast wave looses power via radiative (and adiabatic) cooling, the bubble stops expanding and cools, forming new cold/warm clouds via condensation and dynamical processes.

Although the evolution and impact of a single SN bubble on the ISM is clearly not representative of an equilibrium configuration, statistically the synergy between different SN explosions is able to produce an extended hot phase that, averaging on time and space, is in pressure equilibrium with the other components.

The picture of a medium composed by three phases in equilibrium is not fully representative of the thermodynamical properties of the ISM within galaxies. Observations of the 21-cm line reveal that the distribution of atomic hydrogen is far from being described as an ensemble of spherically symmetric clouds (e.g. Heiles, 1967). Moreover, both simulations and observations show that significant fractions of gas lie in the thermally unstable regimes ($10^2 \lesssim T \lesssim 10^4$ K, $10^4 \lesssim T \lesssim 10^6$ K) (e.g. Heiles, 2001; Heiles & Troland, 2003; Savage et al., 2003; de Avillez & Breitschwerdt, 2004; Walch et al., 2011), suggesting that dynamical, other than thermal, processes play a key role in determining the state of the gas within galaxies. The interplay between the different mechanisms that set the thermodynamical properties of the ISM is extremely complex and ought to be investigated via numerical, rather than analytical, modelling.

2.5 Stellar feedback

2.5.1 Protostellar jets and outflows

Accretion of gas by low, intermediate and high-mass protostars can produce bi-polar jets and outflows along the rotation axis of the star. These are likely driven by magneto-centrifugal forces (e.g. Pudritz et al., 2007; Seifried et al., 2012), although their origin is still a matter of debate.

Collimated jets have an onion-like velocity structure, with typical velocities of $100 - 1000\,\mathrm{km\,s^{-1}}$, and are composed by atomic and molecular gas. They propagate through the ambient gas and produce bow-shocks that sweep-up the ambient medium, leading to the creation of protostellar outflows, which are less collimated, slower and mostly composed by molecular hydrogen. These have typical velocities of $1 - 30\,\mathrm{km\,s^{-1}}$ and expands into the parent MC up to a few pc from the protostar (e.g. Frank et al., 2014). As an example, in Fig. 2.11 we show the CO, dust and H_2 maps of the molecular outflows from the Herbig-Haro object HH 211 by Gueth & Guilloteau (1999).

Most of protostellar jets and outflows are confined within their parent MCs, but some of them have been observed extending up to few pc outside (Bally et al., 1997). In general, the temporal and spatial scales over which these feedback mechanisms operate are small. Therefore, they are not ex-

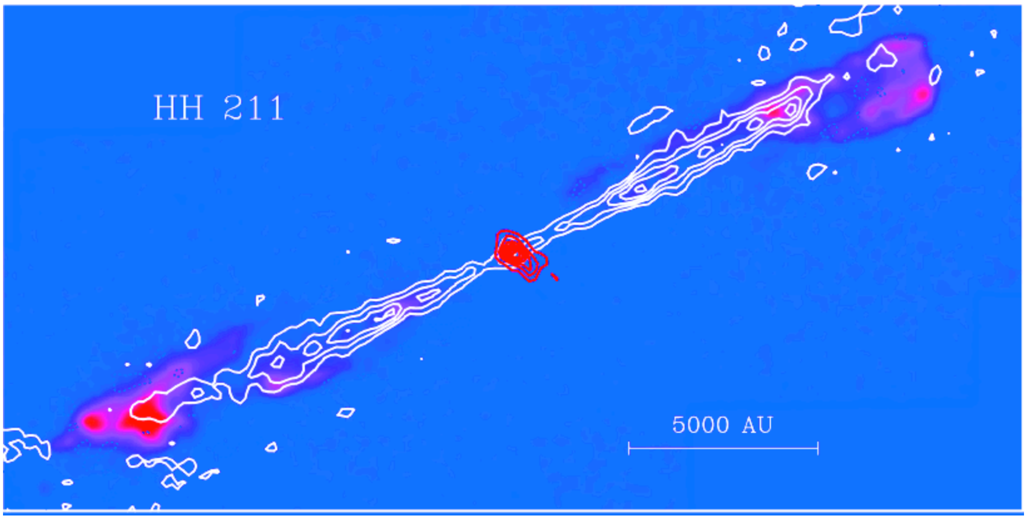

Figure 2.11: *Observations of protostellar molecular outflows from the Herbig-Haro object HH 211 by Gueth & Guilloteau (1999). The white and red contours show the CO and dust continuum emission, respectively, superimposed on* H_2 *emission (colours).*

pected to play a major role in influencing the ISM on scales from tens to thousands of pc (Mac Low & Klessen, 2004; Klessen & Glover, 2014).

2.5.2 Ionising radiation and radiation pressure

Powerful injection of energetic photons from massive stars can also influence the thermodynamical properties of the ISM. UV photons from OB stars ionise the ambient medium and produce free electrons with relatively high velocities, which in turn heat the surrounding medium to $T \sim 8000 - 10^4$ K (for solar metallicities). Each massive star is then embedded into a HII region mainly composed by ionised hydrogen that continuously recombines and is ionised by the UV radiation field.

The radius at which the recombination rate equals the ionisation rate defines the Strömgren sphere, i.e. a sphere of ionised gas in thermal equilibrium whose size is primarily set by the ratio between the flux of ionising photons and the ambient medium density. In the first phase of the HII region evolution, the so-called R-type expansion, the ionisation front expands up to the Strömgren radius within a time-scale of the order of the recombination time. Shortly after, the large pressure gradient between the Strömgren sphere and the ambient medium causes the HII region to expand supersonically. This D-type expansion forms an outer shell that sweeps-up and shocks the surrounding material.

At small scales, HII regions expand into the parent MC with typical velocities $\lesssim 10\,\mathrm{km\,s^{-1}}$, dispersing the cloud and eventually triggering new star formation events (Dale et al., 2012; Walch et al., 2012, 2013; Dale et al., 2014). The combined action of many massive stars belonging to star clusters and OB associations form giant HII regions that can influence the ISM at scales of hundreds of pc (see Fig. 2.5). Analytical estimates suggest that the impact on the ISM at large scales of HII regions is limited, as the majority of the energy emitted by massive stars is employed to maintain the gas ionised inside the bubble, rather than being injected into the medium (Klessen & Glover, 2014, see also Walch et al. 2012 for the case of a single O star embedded into a dense environment). Ionising radiation can also influence the ISM at galactic scales by lowering the ambient medium density of subsequent SN explosions. As we will see below and in the next chapters, explosion of massive stars in tenuous media reduces the fraction of SN energy radiated away by cooling and therefore increases the amount of energy and momentum transferred to the medium. For a single SN exploding within a pre-existing HII region, however, Walch & Naab (2015) show that the amount of energy injected into the medium increases by a modest 50% with respect to the case where ionising radiation is not included.

Radiation pressure can also play an important role. Absorption of radiation from massive stars by dust can drive the expansion of a bubble into the surrounding medium via collisions between excited grains and the neighbouring gas. The impact of radiation pressure on the ISM at both small and large scales is still a matter of debate, as its effectiveness is extremely dependent on how many and for how long IR photons are trapped in the vicinity of massive stars before escaping.

Using analytical estimates Krumholz & Matzner (2009, but see also Murray et al. 2010; Krumholz & Thompson 2012) show that for high ambient medium densities radiation pressure can drive the expansion of the bubble significantly faster than ionising radiation (at least in the initial phases), making this process one of the, if not the, most important star formation regulation mechanisms. Nevertheless, further and less idealised modelling is needed to confirm this hypothesis.

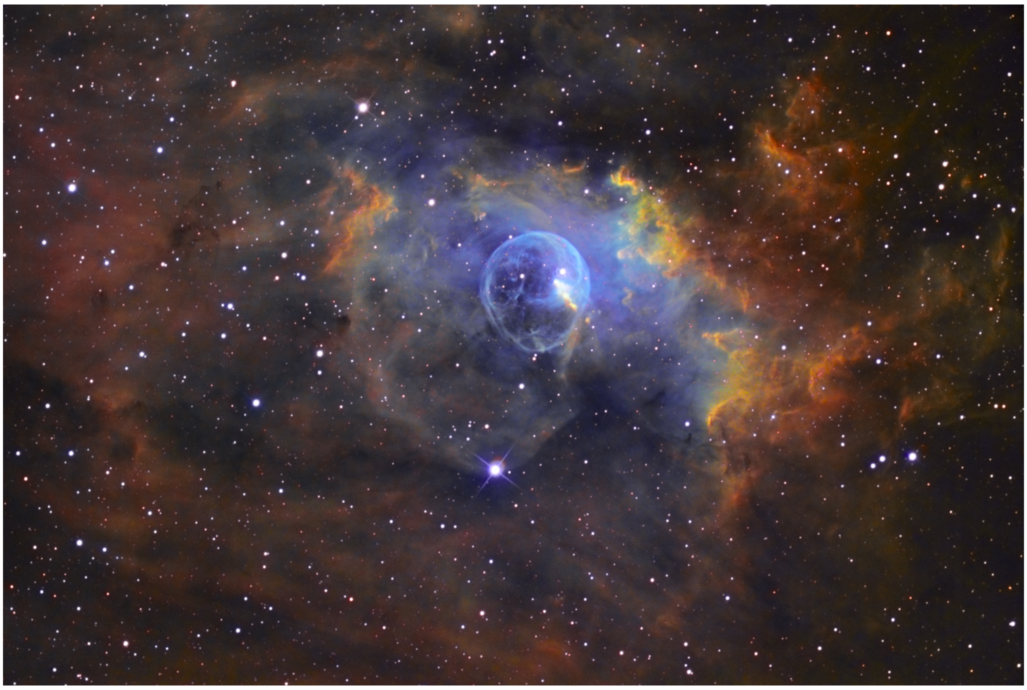

Figure 2.12: *The "Bubble Nebula" NGC 7635 as seen in* S II *(red),* Hα *(green) and* O III *(blue). The bubble is blown by stellar winds from the massive central O star BD+602522. Credit: Russel Croman.*

2.5.3 Stellar winds

Line-driven stellar winds produced in the atmospheres of massive stars can inject significant quantities of energy into the ISM. Once a stellar wind develops from the star surface, it expands supersonically into the ambient medium, creating a shock that travels slower than the winds behind it. Therefore, stellar wind particles that move past this inner shocks are shock-heated. This creates an outer large hot bubble that is over-pressurised with respect to the ambient medium. The expansion of this hot component produces a second, outer shock that sweeps-up and compress the surrounding material. In a star cluster or OB association, single stellar wind bubbles merge into a superbubble that can reach radii of the order of several hundreds of pc. In Fig. 2.12 we show an example of stellar wind bubble blown by a massive O star in the "Bubble Nebula" NGC 7635.

Little is known about the impact of stellar winds at both small and large scales. From a theoretical point of view, numerical simulations of stellar winds feedback within structured MCs by Dale et al. (2014, see also Freyer et al. 2003, 2006) show that this process has a modest impact on the gas, with ionising radiation being the most dominant feedback mechanism between the two. These simulations, however, underestimate the impact of stellar winds (both within the model itself and due to the choice of performing particle-based simulations). Using more adequate grid-based simulations, Rogers & Pittard (2013) show that both stellar winds and SNe couple weakly to the molecular gas. Large fractions of hot gas vent out of the cloud through low-density channels instead of destroying the molecular material (an effect also seen for UV photons when modelling HII regions within MCs, Walch et al., 2012). Despite injecting less energy, they find that stellar winds, rather than SNe, are more effective in removing cold and dense gas. Recent cosmological simulations by Hopkins et al. (2014) suggest that stellar winds have the smallest impact out of the different feedback processes (excluding protostellar jets and outflows) at large scales. However, the limited mass resolution of these models, as well as the employment of a particle-based scheme, raise concerns about the soundness of such a conclusion. Generally, stellar winds can also increase the heating efficiency of SNe by lowering their ambient medium densities, similarly to HII regions (see previous section). We will discuss this point in more detail in chapter 5.

Observational studies also do not provide any definitive answer to the importance of stellar winds. Analysis of multi-wavelength observations of the 30 Doradus star-forming region by different authors provide diametrically opposed conclusions. Lopez et al. (2011) find that stellar winds are unimportant and that radiation pressure dominates within the inner 75 pc, with photoionisation being the most important mechanism at larger radii. On the other hand, Pellegrini et al. (2011) infer that radiation pressure is negligible and that X-ray emitting gas from stellar winds sets the dynamics and structure of the region.

2.5.4 Supernovae

Powerful SN explosions are most likely the dominant feedback process at galactic scales. Massive stars explode as SNe at the end of their lifetime, releasing 10^{51} erg of energy in the ISM and creating a hot, powerful, overpressurised bubble that expands into the surrounding medium. The bubble produces a shock that sweeps-up and compresses the ISM.

Generally, the combined action of many SNe appears to be powerful enough to maintain the observed level of turbulence at intermediate and small scales (e.g. Mac Low & Klessen, 2004; Padoan et al., 2015), as well as powering vigorous outflows from galactic discs (e.g. Creasey et al., 2013; Girichidis et al., 2015) and in general producing a hot, tenuous gas component, i.e. the third phase of the ISM (e.g. McKee & Ostriker, 1977; de Avillez & Breitschwerdt, 2007). At MC scales, SNe can also destroy the parent cloud by injecting energy and momentum directly into the dense

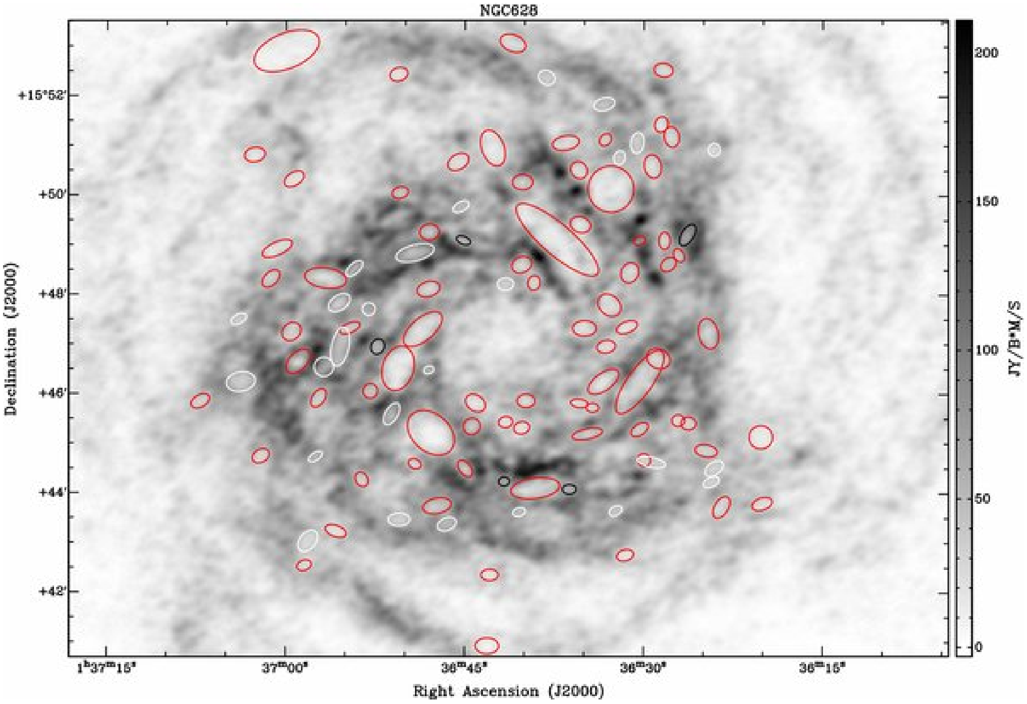

Figure 2.13: *H map and holes of NGC 628 from Bagetakos et al. (2011).*

phase (Iffrig & Hennebelle, 2015, but see also chapter 4,Gatto et al. 2015; Walch et al. 2015).

In Fig. 2.13 we show an example of the large scale impact of SNe on the ISM. The H map of the spiral galaxy NGC 628 shows large holes whose size spans from 0.2 to 2 kpc. Although their origin is still a matter of debate, these are likely to be driven by stellar feedback, especially SNe. SN feedback is also thought to be at the origin of the large scale flows that drive cold gas from the mid-plane to large heights and viceversa, the so-called galactic fountain model (Shapiro & Field, 1976). Fig. 2.14 shows an example of such a process, where a very large mass of extra-planar atomic hydrogen extending well beyond the stellar disc (up to $\sim$ 10 kpc) has been observed by Oosterloo et al. (2007).

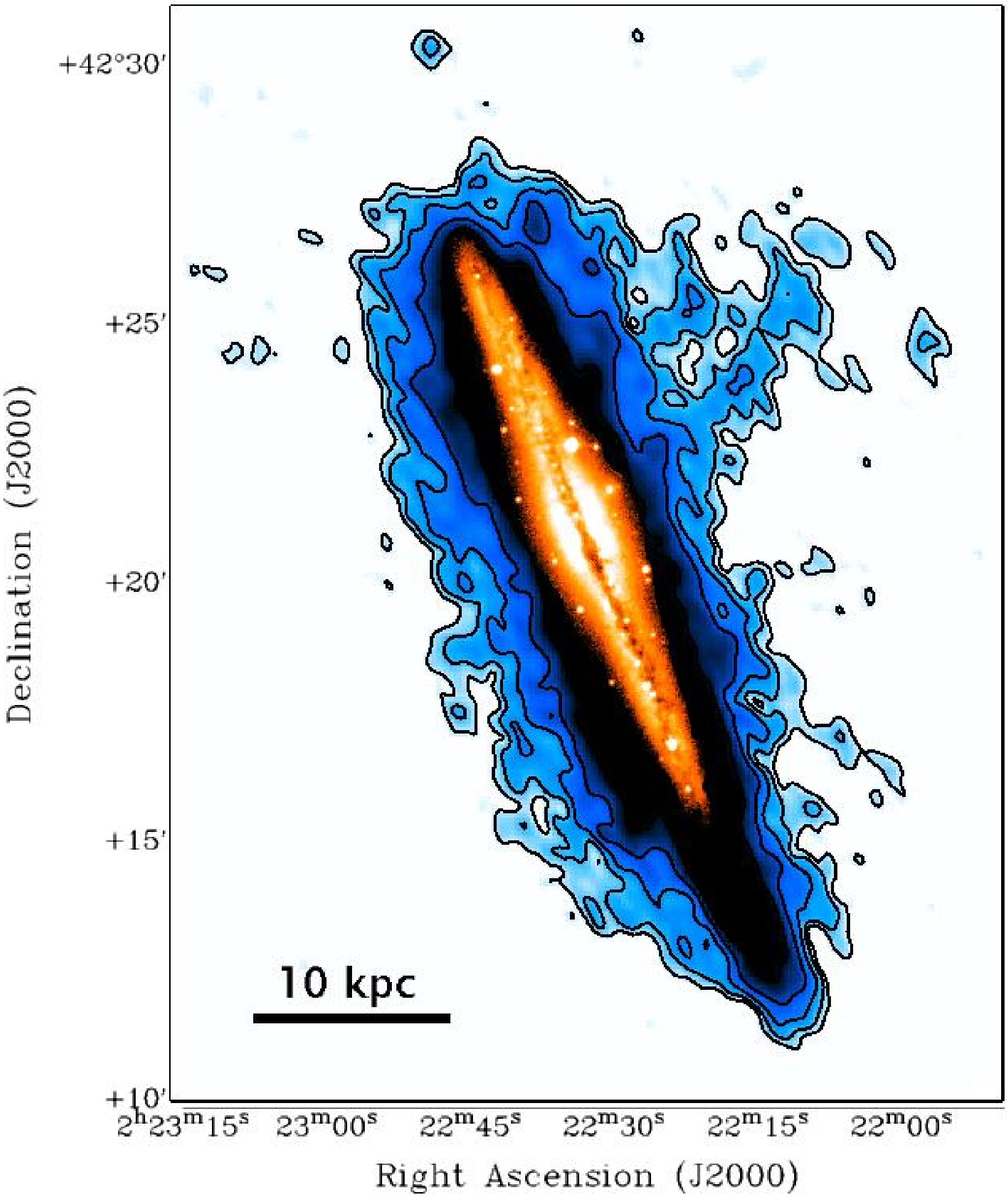

Figure 2.14: *H map (blue and contours) overlaid on the optical image (orange) of NGC 891 from Oosterloo et al. (2007).*

CHAPTER 3

Stellar winds, supernovae and star cluster sink particles in the FLASH code

We give a brief overview on the implementation of stellar winds, SNe and a sub-grid model for sink particles in the FLASH code.

3.1 The FLASH code

The Flash code is a multi-modular, 3D, Eulerian, AMR, MHD code developed by Fryxell et al. (2000, but see also Dubey et al. 2008; Dubey et al. 2013). It is parallelised using domain decomposition via the Message Passing Interface (MPI). It employs a finite-volume scheme, where the physical variables are represented as zone averages. The AMR is handled by the PARAMESH library. We refer to Walch et al. (2015) for a more detailed picture of the code described in this section.

3.1.1 Magneto-hydrodynamics

For all the tests and simulations presented in this and following chapters, we employ 3D, cartesian coordinates and we include diffuse heating and radiative cooling (see next section). We use the directionally split, Bouchut HLL5R solver (Bouchut et al., 2007; Waagan, 2009; Bouchut et al., 2010; Waagan et al., 2011) to solve the following set of ideal MHD equations (here shown including gravity, magnetic fields and source terms, such as heating, cooling, SNe and stellar winds)

$$\frac{\partial \rho}{\partial t} + \nabla \cdot (\rho \mathbf{v}) = 0 \ , \tag{3.1}$$

$$\frac{\partial \rho \mathbf{v}}{\partial t} + \nabla \cdot \left[\rho \mathbf{v}\mathbf{v}^T + \left(P + \frac{\mathbf{B}^2}{8\pi}\right)\mathbf{I} - \frac{\mathbf{B}\mathbf{B}^T}{4\pi}\right] = \rho \mathbf{g} + \dot{q}_{\mathrm{inj}} \ , \tag{3.2}$$

$$\frac{\partial \epsilon}{\partial t} + \nabla \cdot \left[\left(\epsilon + P + \frac{\mathbf{B}^2}{8\pi}\right)\mathbf{v} - \frac{(\mathbf{B} \cdot \mathbf{v})\mathbf{B}}{8\pi}\right] = \rho \mathbf{v}\mathbf{g} + \dot{u}_{\mathrm{chem}} + \dot{u}_{\mathrm{inj}} \ , \tag{3.3}$$

$$\frac{\partial \mathbf{B}}{\partial t} - \nabla \times (\mathbf{v} \times \mathbf{B}) = 0 \ , \tag{3.4}$$

$$\nabla \cdot \mathbf{B} = 0 \ , \tag{3.5}$$

$$\epsilon = u + \frac{\rho \mathbf{v}^2}{2} + \frac{\mathbf{B}^2}{8\pi} \ . \tag{3.6}$$

Here, ρ is the mass volume density, t the time, $\mathbf{v}$ the velocity. $\mathbf{B}$ is the magnetic field and $P = (\gamma - 1)u$ is the thermal pressure, with u being the internal energy per unit of volume and γ the adiabatic index, assumed to be 5/3 in our setups. $\mathbf{I}$ is the 3×3 identity matrix, while $\mathbf{B}\mathbf{B}^T$ and $\mathbf{v}\mathbf{v}^T$ are the outer products of $\mathbf{B}$ and $\mathbf{v}$ with themselves, $\mathbf{g}$ denotes the gravitational acceleration, ϵ is the total energy per unit of volume, $\dot{u}_{\mathrm{chem}}$ represents the net rate of change in internal energy volume density due to diffuse heating and radiative cooling (computed through a chemical network, see below) and n is the gas number density, while $\dot{q}_{\mathrm{inj}}$ and $\dot{u}_{\mathrm{inj}}$ are the momentum and internal energy per unit of volume and per unit of time injected by stellar winds and/or SNe.

3.1.2 Cooling, heating and chemistry

We include heating and cooling processes using a simplified version of the chemical network implemented by Glover & Mac Low (2007a,b), Glover et al. (2010) and Glover & Clark (2012a), which allows us to follow the abundances of five chemical species: $\mathrm{H}, \mathrm{H}^+, \mathrm{H}_2, \mathrm{CO}$ and C^+. We model the formation of H_2 and CO considering also the effects of dust shielding and molecular (self-)shielding with the TreeCol algorithm of Clark et al. (2012, see Walch et al. 2015, for more details).

Gas cooling of the hot ($T > 10^4$ K) phase is modelled using the cooling rates of Gnat & Ferland (2012), who assume that the atoms and ions are in CIE. For the warm and cold components, we use the cooling function developed in Glover et al. (2010) and Glover & Clark (2012a), which computes (non-equilibrium) cooling rates from the chemical abundances of the gas.

We include the heating processes following the prescriptions used in Glover et al. (2010) and Glover & Clark (2012a). We include heating from photoelectric effect, CRs and X-rays. We take the diffuse FUV interstellar radiation field to be $G_0 = 1.7$ (Habing, 1968; Draine, 1978). We set the CR ionisation rate of H to $\zeta = 3 \times 10^{-17}\ \mathrm{s}^{-1}$, while for the X-ray ionisation and heating rates we use the values of Wolfire et al. (1995).

The metallicity is set to solar with abundances $x_{\mathrm{O,tot}} = 3.16 \times 10^{-4}$, $x_{\mathrm{Si}^+} = 1.5 \times 10^{-5}$ (Sembach et al., 2000), and $x_{\mathrm{C,tot}} = 1.41 \times 10^{-4}$. The (constant) dust-to-gas mass ratio is set to 10^{-2}.

3.1.3 Gravity

For some of our simulations (see chapter 5), we include gravity. The gravitational acceleration of the gas is set by three different components: self-gravity, a background static potential and sink particles (see below), so that $\mathbf{g}_{\mathrm{gas}} = \mathbf{g}_{\mathrm{sg}} + \mathbf{g}_{\mathrm{ext}} + \mathbf{g}_{\mathrm{sinks}}$.

Self-gravity is computed by solving Poisson's equation for the gas in three dimensions using a tree-based method described in detail in Walch et al. (2015),

$$\Delta\Phi = 4\pi G \rho_{\mathrm{gas}} \ , \tag{3.7}$$

with Φ being the gravitational potential and G Newton's constant.

We neglect any dark matter contribution and we consider an external potential generated by the stellar component close to the galactic disc. The stellar distribution is assumed to be isothermal in the form of (Spitzer, 1942)

$$\rho_*(R, z) = \rho_*(R, 0)\ \mathrm{sech}^2(z/2z_{\mathrm{d}}) \ , \tag{3.8}$$

where ρ_* is the density of stars at radius R and height z. We compute $\rho_*(R, 0)$ by assuming a stellar surface density of $30\,\mathrm{M}_\odot\ \mathrm{pc}^{-2}$ and a scale height $z_\mathrm{d} = 100\,\mathrm{pc}$. We then integrate the one-dimensional Poisson's equation along the z-direction for ρ_* and we apply the recovered acceleration so that $\mathbf{g}_\mathrm{ext} = g_*(z)\hat{z}$.

3.1.4 Sink particles

In chapter 5, we make use of sink particles to model star formation and feedback self-consistently at intermediate scales. Here, we briefly describe the sink particles unit from the FLASH 4 public release, described in Federrath et al. (2010, see also Bate et al. 1995; Krumholz et al. 2004; Jappsen et al. 2005; Hubber et al. 2013; Bleuler & Teyssier 2014 for details on the implementation of sink particles in other codes).

Collisionless sink particles provide the framework to represent the star formation process in dense regions undergoing local gravitational collapse. Following Federrath et al. (2010), a sink particle is created at a certain position if

- the gas density is larger than a user-defined density threshold ρ_thr;
- all cells within the accretion sphere, centred on the local density maximum and with radius r_accr, are at the highest refinement level;
- the gas within r_accr is in a converging flow ($\nabla \cdot \mathbf{v} < 0$)
- there is a central gravitational potential minimum;
- the gas within r_accr is Jeans unstable;
- the gas within r_accr is gravitationally bound
- the accretion sphere does not overlap with one of an existing particle.

Once a sink particle is formed, it can accrete gas within r_accr if its density is greater than ρ_thr. Additional checks are performed within this radius to verify that only bound, collapsing matter is removed from the gas distribution and added to the particle (see Federrath et al., 2010, for details).

The contribution of sink particles to the gravitational acceleration of the gas is also taken into account, both within and outside the sinks' accretion radii. Following Federrath et al. (2010), outside the accretion radius this involves a direct summation for all computational cells and all particles.

For a given gas parcel, the acceleration due to sink particles can be written as

$$\mathbf{g}_{\mathrm{sinks}} = -\sum_{\mathrm{p}=0}^{N_{\mathrm{p}}} \frac{GM_{\mathrm{p}}}{\mathbf{r}_{\mathrm{p}}^{3}} \hat{r}_{\mathrm{p}} \ , \tag{3.9}$$

with N_{p} total number of sink particles, M_{p} mass of the particle p, and $\mathbf{r}_{\mathrm{p}}$ distance between the cell and particle p. Within the accretion radius, the gas acceleration due to the gravitational attraction from a close particle computed via eq. (3.9) can become artificially large. For this reason, a cubic spline gravitational softening scheme is applied to compute gas accelerations within r_{accr}.

The motion of a sink particle is affected by the gravitational pull generated by the gas, as well as by other particles and by the presence of an external potential. The gravitational acceleration due to the gas (outside r_{accr}) is computed by linearly interpolating eq. (3.7), while for the sink - sink contribution a direct summation over all particles is employed. Finally, the acceleration from the external potential $\mathbf{g}_{\mathrm{ext}}$ is applied along the z-direction depending on the height of the particle (see section 3.1.3). Sink particles are advanced using a leapfrog integration method. A sub-cycling scheme is employed in order to guarantee stable and accurate results.

The formation and evolution of sink particles in hydrodynamic simulations is governed by two important parameters: r_{accr} and ρ_{thr}. We set the accretion radius to four cells at the maximum refinement level (a typical value, see e.g. Krumholz et al., 2004; Hennebelle & Iffrig, 2014). This choice satisfies the Truelove criterion, where the Jeans length of the gravitationally bound, free-falling isothermal gas must be resolved by at least four cells at a given resolution in order to prevent artificial fragmentation (Truelove et al., 1997). For MHD free-fall isothermal collapse, however, Heitsch et al. (2001) show that at least eight cells are required. The value $r_{\mathrm{accr}} = 4 \times \Delta x$ fulfills both criteria while minimising the volume around sink particles within which the gas distribution is not well described. The choice of r_{accr} also sets the maximum density below which the gas can be considered Jeans-stable at a given resolution, i.e. ρ_{thr}. The Jeans length can be expressed as

$$\lambda_{\mathrm{J}} = \left(\frac{\pi c_{\mathrm{s}}^{2}}{G\rho} \right)^{\frac{1}{2}} \ , \tag{3.10}$$

with c_{s} sound speed of the gas. By considering that λ_{J} is at most resolved by $2 \times r_{\mathrm{accr}}$ and that $c_{\mathrm{s}}^{2} \sim k_{\mathrm{B}}T/\mu m_{\mathrm{p}}$, we can rearrange eq. (3.10) and write

$$\rho_{\mathrm{thr}} = \frac{\pi k_{\mathrm{B}}}{m_{\mathrm{p}}G} \frac{T}{\mu (2 \times r_{\mathrm{accr}})^{2}} \ . \tag{3.11}$$

For our simulations, however, the gas temperature T (and to some extent the chemical composition) covers over more than seven orders of magnitude. Considering the range $T = 10^2 - 10^4$ K, one can find a density threshold that varies between ≈ 10 and $1000\,\mathrm{cm}^{-3}$ for a spatial resolution of ~ 4 pc (see chapter 5). Therefore, we set its value in the middle of this range, $\rho_{\rm thr} = 2 \times 10^{-22}$ g cm^{-3} ($n \sim 100\,\mathrm{cm}^{-3}$).

3.2 Supernova feedback

Classically, the evolution of a SNR can be divided into four different stages (neglecting gravity and magnetic fields, e.g. Slavin & Cox, 1992):

- Free expansion phase: shortly after the explosion, namely shortly after having released 10^{51} erg of energy and $\gtrsim 1$ M$_\odot$ of matter in $\sim$ one day, the velocity of the ejecta is so high (10^4 km s^{-1}) that the bubble expansion is not affected by the presence of the external ambient medium. This phase ends when the mass swept up during the expansion is of the same order of the mass ejected and this occurs typically after a few hundreds of years after the explosion. In this stage, the outer radius of the bubble goes as $r_{\rm s} \propto t$.

- Adiabatic (or Sedov-Taylor) phase: when the edge of the bubble feels the presence of the ambient medium, a shock is formed. Due to its high velocity, the gas encompassed by the shock is heated to extreme temperatures (more than 10^7 K at the initial stage) and the shock can be treated as adiabatic. During this phase, the SN bubble is composed by a hot, tenuous interior, which constitutes most of the structure and expands adiabatically pushing the exterior part, a denser and cooler shell made up by the ambient medium compressed by the external shock. The shock radius in this phase follows $r_{\rm s} \propto t^{2/5}$.

- Pressure-driven radiative phase: when the shock velocity drops to some hundreds of km s^{-1}, corresponding to a bubble radius of a few tens of pc, the cooling time within the outer shell becomes comparable with the age of the bubble. The dense material within the shell can cool down efficiently and the shock becomes radiative. This means that, while the internal part remains hot and adiabatic, the shell collapses, increasing its density and reaching $T \sim 10^4$ K. In this regime, $r_{\rm s} \propto t^{2/7}$.

- Momentum-driven radiative phase: once the pressure of the internal part drops to low values (of the same order of the ambient medium pressure) via a mixture of adiabatic and radiative cooling, it stops

> pushing the shell outwards. The shock remains radiative but looses the support from the interior, therefore simply expanding by means of momentum conservation, with $r_{\mathrm{s}} \propto t^{1/4}$. The velocity of the shock continuously decreases up to the point where it reaches the sound speed of the ambient medium. This defines the end of the SNR lifetime. At this point $\sim$ 90-95% of the initial energy has been radiated away, while the remaining part is transferred to the ambient medium in the form of kinetic energy.

Due to our limited spatial resolution (of the order of a few pc), we are unable to model the free expansion phase of each SN bubble. Therefore, for a given position at a given time, we mimic the explosion of a massive star as SN by injecting 10^{51} erg of energy into the surrounding medium. This over-pressurised region expands supersonically into the ambient medium, creating a hot bubble that develops an outer shock traveling at few hundreds of $\mathrm{km\,s^{-1}}$.

We inject thermal or kinetic energy in a spherical volume of radius r_{inj}. This injection radius can either be fixed, i.e. can be set a priori by selecting the number of cells over which the energy is deposited, or variable. In the latter case, r_{inj} is determined as the radius that encloses a fixed gas mass, M_{inj}, which is set as initial parameter of the simulation. Nevertheless, we require r_{inj} to be sampled by at least four cells in order to preserve the spherical geometry of the bubble. Therefore, for variable injection radius, r_{inj} is determined in the following way:

$$r_{\mathrm{inj}} = \begin{cases} \left(\frac{3}{4\pi}\frac{M_{\mathrm{inj}}}{\overline{\rho}}\right)^{\frac{1}{3}} & \text{if } r_{\mathrm{inj}} \geqslant 4\Delta x \\ 4\Delta x & \text{if } r_{\mathrm{inj}} < 4\Delta x \ , \end{cases} \tag{3.12}$$

where $\overline{\rho}$ is the mean density within the injection region and Δx is the resolution element.

Once r_{inj} is defined, the SN energy is deposited into the medium by adding $E_{\mathrm{SN}} = 10^{51}$ erg to the gas distribution. Here, we do not consider any injection of mass (see next section). For thermal energy injection, for each cell i within the injection sphere the thermal and total specific energies are updated as

$$e_{\mathrm{i,th,new}} = e_{\mathrm{i,th,old}} + \frac{E_{\mathrm{SN}}}{M_{\mathrm{inj}}} \ , \tag{3.13}$$

$$e_{\mathrm{i,tot,new}} = e_{\mathrm{i,tot,old}} + \frac{E_{\mathrm{SN}}}{M_{\mathrm{inj}}} \ . \tag{3.14}$$

In this case, the material within the injection region experiences a sudden rise in temperature (thermal pressure/energy), which in turn causes the gas to expand into the surrounding medium by means of pressure-gradient force. The bubble expands supersonically and enters its Sedov-Taylor phase by creating a shock that sweeps up the ambient medium. After some time, the shell starts to cool efficiently and the SNR evolves into its radiative phases.

Kinetic energy injection modifies the total energy and velocity field in the following way. The velocity field (here shown only for the x-component) is modified as

$$v_{\rm i,x,new} = \sqrt{|v^2_{\rm i,x,old} \pm v^2_{\rm x,SN}|}\ , \tag{3.15}$$

with $v_{\rm x,SN}$ x-component of the radial velocity $v_{\rm SN} = \sqrt{2E_{\rm SN}/M_{\rm inj}}$, which is always directed radially outwards from the centre of the explosion. The high velocities imprinted in the injection sphere causes the gas to travel supersonically outwards through the ambient medium. This process creates an outer shock that heats the surrounding gas to very high temperatures, producing a hot bubble with an outer shock as for the thermal energy case[4]. Here, the plus-minus sign represents a net kinetic energy injection. If the pre-existing velocity field $v_{\rm i,x,old}$ has same sign of $v_{\rm x,SN}$, then the two velocities are added together, while they are subtracted to each other when having opposite sign. Therefore, while for thermal energy injection formally 10^{51} erg of energy are deposited into the gas distribution, for kinetic energy injection it may be lower. The amount of energy deployed into the system in this case depends on the orientation of the pre-existing velocity field within the injection sphere. Therefore, this methods provides a way to inject net kinetic energy, as the final total specific energy reads

$$e_{\rm i,tot,new} = e_{\rm i,tot,old} + \frac{1}{2}(v^2_{\rm i,x,new} + v^2_{\rm i,y,new} + v^2_{\rm i,z,new}) \leqslant e_{\rm i,tot,old} + \frac{E_{\rm SN}}{M_{\rm inj}}\ . \tag{3.16}$$

In Fig. 3.1 we show the evolution of the shock radius for a test of a single SN exploding in an uniform medium (crosses). This is compared with the analytic solutions for the Sedov-Taylor (dashed line) and pressure-driven radiative (solide line) phases. The latter is plotted with a different normalisation with respect to its real solution in order to highlight the difference with respect to the adiabatic evolution. At early times, the position of the shock matches perfectly the expected behaviour for the Sedov-Taylor phase. For $t > 0.05$ Myr, the bubble departs from the adiabatic solution and starts

---

[4] Thermal and kinetic energy injection produce the same result only in the case of ambient medium with zero initial velocities.

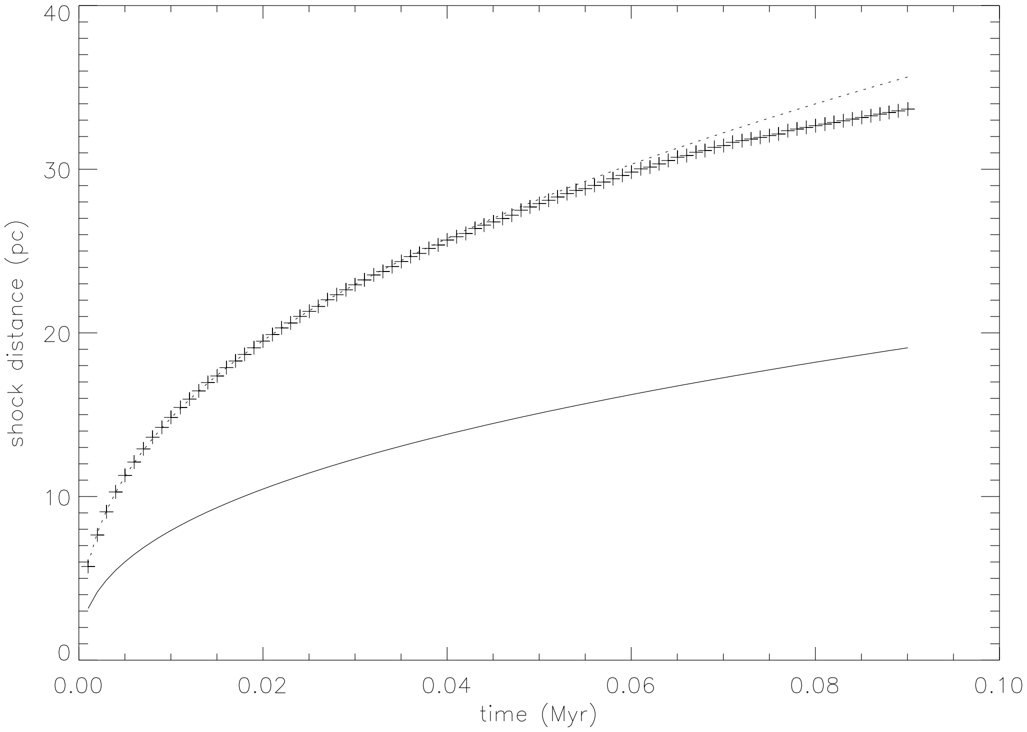

Figure 3.1: *Evolution of the shock position for a single SN exploding in an uniform medium (crosses) compared with the analytic solutions for the Sedov-Taylor (dashed line) and pressure-driven radiative (solide line) phases.*

loosing energy via radiative cooling. After this time, the shock radius becomes smaller than the one predicted by the dashed line and starts following the solution for the pressure-driven radiative phase, as can be noticed by comparing the slopes of the numerical solution with the one of the solid line.

In case of high densities and/or low mass resolution within the injection region, the Sedov-Taylor phase of the SN bubble is unresolved. In this case, the correct evolution of the SNR is not captured. For instance, in case of thermal energy injection the energy input would result in an effective temperature below 10^6 K:

$$T_{\mathrm{i,SN}} = (\gamma - 1)\frac{E_{\mathrm{SN}}}{M_{\mathrm{inj}}}\frac{\mu m_{\mathrm{p}}}{k_{\mathrm{B}}} < 10^6 \text{ K} , \tag{3.17}$$

where γ is the polytropic index, μ the mean molecular weight, m_{p} the proton mass and k_{B} the Boltzmann constant. The cooling rate is a non-linear function of the gas temperature. At $T < 10^6$ K the injected energy is almost instantaneously lost due to strong radiative cooling. This leads to over-cooling, which is a well-known problem in galaxy simulations (e.g. Stinson et al., 2006; Creasey et al., 2011; Gatto et al., 2013). Many different solutions have been put forward to address the problem of unresolved SNe: switching off cooling for a certain time after the explosion (e.g. Thacker & Couchman, 2000); clustering of massive stars to develop superbubbles (e.g. Shull & Saken, 1995; Krause et al., 2013; Keller et al., 2014; Sharma et al., 2014); or momentum rather than energy input (e.g. Kim et al., 2011; Shetty & Ostriker, 2012; Kim & Ostriker, 2015). Of course one could just increase the resolution. Therefore, we further implement a momentum input scheme for unresolved SNe, which is based on Blondin et al. (1998). We first calculate the radius of the bubble at the end of the Sedov-Taylor phase (Blondin et al., 1998)

$$r_{\mathrm{ST}} = 19.1 \left(\frac{E_{\mathrm{SN}}}{10^{51}\ \mathrm{erg}}\right)^{\frac{5}{17}} \left(\frac{\overline{n}}{\mathrm{cm}^{-3}}\right)^{-\frac{7}{17}}\ \mathrm{pc}, \tag{3.18}$$

where $\overline{n}$ is the mean number density within the injection region. We define a SN as unresolved if its $r_{\mathrm{ST}} < 4\Delta x$. The momentum is computed from (Blondin et al., 1998)

$$p_{\mathrm{ST}} = 2.6 \times 10^5 \left(\frac{E_{\mathrm{SN}}}{10^{51}\ \mathrm{erg}}\right)^{\frac{16}{17}} \left(\frac{\overline{n}}{\mathrm{cm}^{-3}}\right)^{-\frac{2}{17}}\ \mathrm{M}_{\odot}\ \mathrm{km\ s}^{-1}. \tag{3.19}$$

We deposit this momentum to the flattened density distribution within the injection region by adding the corresponding velocity of

$$v_{\mathrm{SN}} = \frac{p_{\mathrm{ST}}}{M_{\mathrm{inj}}}\ , \tag{3.20}$$

where v_{SN} points radially outwards, similarly to the case for kinetic energy injection. In addition, we increase the temperature of the injection region to 10^4 K. This guarantees that, despite the significant energy losses, the momentum input is accounted for. This method has two caveats. i) The momentum of a SN bubble can still increase during the pressure-driven snowplough phase (Cioffi et al., 1988), which is not included in this model. ii) Due to the injection of transonic or subsonic motions, high Mach number shocks are not created and little to no hot gas is produced. Therefore, the momentum input given in equation (3.19) is a lower limit.

3.3 Stellar winds

Stellar winds bubbles from massive stars have different structure and evolution with respect to their SN counterparts (once again neglecting gravity and magnetic fields, e.g. Weaver et al., 1977). At first, a powerful wind expelled from the surface of a hot stars travels at supersonic speed, creating an inner shock. The shock is slower with respect to the wind behind it, and wind particles are shocked once they get past this inner shock. This process produces an outer, extended region of hot and tenuous gas that, similarly to the SN case, is over-pressurised with respect to the ambient medium. This hot bubble expands supersonically and creates an outer shock that sweeps up and heat the surrounding material. As a consequence, the bubble rapidly evolves into a well-defined structure composed by an inner free-wind region, an inner shock, where the wind is shocked and most of its kinetic energy is converted into thermal energy, a large, volume-filling hot bubble, composed by hot and low-density gas, and an outer shock. The evolution of a stellar wind bubble can be divided into three different stages:

- Adiabatic phase: in this regime, both the hot interior and the shell behind the outer shock do not loose energy via radiative cooling and expands adiabatically. In this case, the outer shock evolves as $r_\mathrm{s} \propto t^{3/5}$.
- Shell radiative phase: the outer shell starts radiating away energy and becomes thin, as for the SN case. In this stage, the outer shock still has the same evolution as in the adiabatic phase, $r_\mathrm{s} \propto t^{3/5}$, but with a slightly smaller normalization of the $r_\mathrm{s} - t$ relation. This is because, unlike SNe, stellar winds are a continuous energy source in time. The motion of the outer shock is driven by the hot interior, that is loosing energy via expansion but that is also continuously replenished with new (thermal) energy via the inner shock. As a consequence, the evolution of the bubble remains the same as long as the internal hot region stays adiabatic. The change in the normalization is simply due to the fact that the shell becomes thinner once it starts radiating away part of its energy.
- Radiative phase: at late times, both the outer shell and the hot interior loose energy via radiation. Similarly to the case for the SN bubble, the expansion of the bubble slows down as a fraction of hot gas energy is lost rather than employed to push the outer shock. This regime, however, is usually never reached as the explosion of the central massive stars occurs before the end of the shell radiative phase.

We simulate stellar wind feedback by injecting mass end energy or momentum in a spherical volume centered around the massive star position. Knowing the star's mass-loss rate $\dot{M}_\mathrm{wind}$ and wind terminal velocity v_wind (see next section), at a given time-step Δt we uniformly add the total mass injected by winds, $M_\mathrm{wind} = \sum \dot{M}_\mathrm{wind} \times \Delta t$, to the pre-existing density distribution ρ_old within the injection sphere. For each cell i in the accretion volume $V_\mathrm{inj} = 4/3 \pi r_\mathrm{inj}^3$

$$\rho_\mathrm{i,new} = \rho_\mathrm{i,old} + \rho_\mathrm{wind} \ , \tag{3.21}$$

with $\rho_{\rm wind} = M_{\rm wind}/V_{\rm inj}$. Before increasing the energy/momentum within $V_{\rm inj}$, we scale the velocity field according to the change in mass to conserve momentum and we then change the internal energy to conserve the total one[5]

$$v_{\rm i,x,1} = v_{\rm i,x,old} \frac{\rho_{\rm i,new}}{\rho_{\rm i,old}} \ , \tag{3.22}$$

$$e_{\rm i,k,1} = \frac{1}{2}(v_{\rm i,x,1}^2 + v_{\rm i,y,1}^2 + v_{\rm i,z,1}^2) \ , \tag{3.23}$$

$$e_{\rm i,tot,1} = e_{\rm i,tot,old} \frac{\rho_{\rm i,old}}{\rho_{\rm i,new}} \ , \tag{3.24}$$

$$e_{\rm i,th,1} = e_{\rm i,tot,1} - e_{\rm i,k,1} \ . \tag{3.25}$$

These operations are also performed when simulating a SN explosion with mass injection (see next section). In this case, $\rho_{\rm i,new} = \rho_{\rm i,old} + \rho_{\rm SN}$, with $\rho_{\rm SN}$ defined as the injected mass divided by the injection volume. Subsequently, the SN energy is injected following eq. (3.13) to (3.16) but using the updated variables (e.g. $e_{\rm i,th,1}$) instead of the old ones (e.g. $e_{\rm i,th,old}$).

As a second step, we inject the corresponding wind energy under the form of either thermal energy, kinetic energy or momentum. For thermal energy injection, we update the specific thermal energy within $r_{\rm inj}$ as for the SN case. The mechanical luminosity of the wind per unit volume can be written as

$$L_{\rm wind} = \frac{1}{2} \frac{\dot{M}_{\rm wind} v_{\rm wind}^2}{V_{\rm inj}} \ . \tag{3.26}$$

The wind energy is injected as thermal energy following

$$e_{\rm i,th,2} = e_{\rm i,th,1} + \frac{L_{\rm wind}}{\rho_{\rm i,new}} \Delta t \ , \tag{3.27}$$

$$e_{\rm i,tot,2} = e_{\rm i,tot,1} + \frac{L_{\rm wind}}{\rho_{\rm i,new}} \Delta t \ . \tag{3.28}$$

---

[5] These quantities can be scaled using density, instead of mass, since all the cells within the injection sphere are at the same spatial resolution.

For kinetic energy injection, we compute the 3D wind velocity[6] as

$$v_{\mathrm{i,3D,wind}} = \left(\frac{2L_{\mathrm{wind}}\Delta t}{\rho_{\mathrm{i,new}}} \right)^{\frac{1}{2}} , \tag{3.29}$$

and we split it into its x, y and z-components, i.e. $v_{\mathrm{i,x,wind}}$. For each directional component of the cell cell i, we quadratically add or remove the wind velocity to the pre-existing velocity field, depending on the their relative sign, as for the SN case (see previous section)

$$v_{\mathrm{i,x,2}} = \sqrt{|v^2_{\mathrm{i,x,1}} \pm v^2_{\mathrm{i,x,wind}}|} , \tag{3.30}$$

$$e_{\mathrm{i,tot,2}} = e_{\mathrm{i,th,1}} + \frac{1}{2}(v^2_{\mathrm{i,x,2}} + v^2_{\mathrm{i,y,2}} + v^2_{\mathrm{i,z,2}}) . \tag{3.31}$$

Finally, stellar winds can also be simulated via momentum, rather than energy, injection. In this case, we still compute the directional components of the 3D wind velocity from eq. (3.29) but we add/subtract them linearly, instead of quadratically, to the pre-existing velocity field

$$v_{\mathrm{i,x,2}} = v_{\mathrm{i,x,1}} \pm v_{\mathrm{i,x,wind}} . \tag{3.32}$$

The remaining amount of energy is injected as thermal energy

$$e_{\mathrm{i,th,2}} = e_{\mathrm{i,th,1}} + \frac{1}{2}\frac{\rho_{\mathrm{old}}}{\rho_{\mathrm{wind}}} v^2_{\mathrm{i,3D,wind}} - (v^2_{\mathrm{i,x,1}} + v^2_{\mathrm{i,y,1}} + v^2_{\mathrm{i,z,1}})^{\frac{1}{2}} v_{\mathrm{i,3D,wind}} , \tag{3.33}$$

$$e_{\mathrm{i,tot,2}} = e_{\mathrm{i,th,2}} + \frac{1}{2}(v^2_{\mathrm{i,x,2}} + v^2_{\mathrm{i,y,2}} + v^2_{\mathrm{i,z,2}}) . \tag{3.34}$$

In Fig. 3.2 we show the evolution of the outer shock position from a test of a single wind bubble expanding in an uniform medium. We compare the evolution of the bubble with the one predicted for the shell radiative phase from the analytic calculations by Weaver et al. (1977). In this case the crosses do not match perfectly the analytic prediction due to a combination of hydrodynamic instabilities in presence of radiative cooling and the definition of the outer shock position itself (i.e. point of maximum density). The differences are well within the expected error and we can consider the numerical results in agreement with the analytic solution.

---

[6] Note that this is not the terminal velocity of the wind, v_{wind}, discussed in the previous paragraphs.

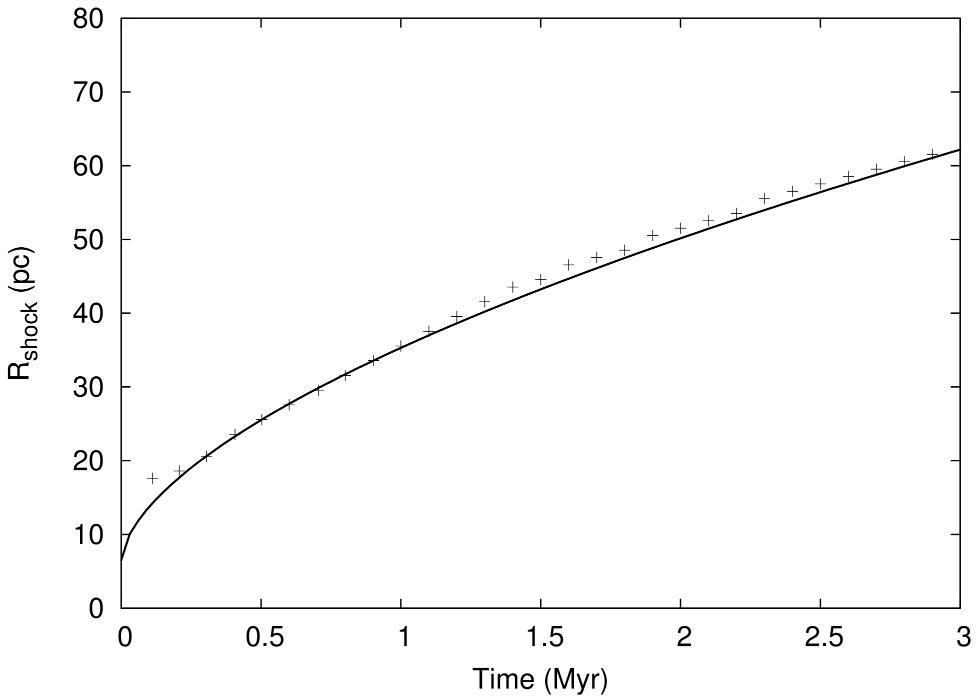

Figure 3.2: *Evolution of the outer shock position for a single wind bubble expanding in an uniform medium (crosses) compared with the analytic solution for the shell radiative phase from Weaver et al. (1977) (solid line).*

3.4 Sub-grid model for sink particles

For the chosen values of ρ_{thr} and r_{accr}, sink particles formed in our simulations, with typical masses $\approx 10^3 - 10^4\,\mathrm{M}_{\odot}$ and radii of $\approx 16\,\mathrm{pc}$, represent groups, associations and clusters of stars. Therefore, we implement a simple sub-grid prescription to model the formation and evolution of massive stars within sink particles.

For each sink particle, we assume that a fraction of all the initial and accreted mass is converted into stars, i.e. $\dot{M}_* = \epsilon_{\mathrm{SF}} \times \dot{\mathrm{M}}_{\mathrm{p}}$, where ϵ_{SF} is the star formation efficiency parameter and $\dot{M}_{\mathrm{p}}$ represents either the initial mass of the sink or its accreted mass per unit time. We explore a star formation efficiency parameter of $\epsilon_{\mathrm{SF}} = 0.1, 1$. Using a Salpeter initial mass function (IMF) (Salpeter, 1955) we set the number of massive stars of the cluster by considering that one massive star forms for every $120\,\mathrm{M}_{\odot}$ of gas converted into stars. Once a massive star has formed, we set its initial mass in the range $9 - 120\,\mathrm{M}_{\odot}$ by drawing a random number weighted by the assumed IMF. We do not model any formation delay or proto-stellar phase, so that stars are assumed to assemble and shift into the zero-age main sequence (ZAMS) instantly.

The parameter $\epsilon_{\rm SF}$ governs the rate at which stars form within sinks. The sink particle formation efficiency, $\epsilon_{\rm CF}$, is determined self-consistently during the simulations. The "true" star formation efficiency in our simulations is the combination of the two, $\epsilon_{\rm SF,true} = \epsilon_{\rm SF} \times \epsilon_{\rm CF}$. Setting $\epsilon_{\rm SF}$ to different values has profound consequences for the impact of stellar feedback in the ISM. Assigning $\epsilon_{\rm SF} = 1$ has the advantage of not having to deal with sub-grid models for the spatial and thermodynamical properties of gas within sink particles. However, given the scales considered in this work, this comes at a price of overestimating the star formation rate (SFR). On the other hand, assuming $\epsilon_{\rm SF} = 0.1$ gives a more reasonable estimate of the number of massive stars formed within a sink. Due to our choice of the density threshold, it is reasonable to assume that the remaining 64.3% of the sink's mass is in the form of H_2 (with 25.7% in neutral helium and ignoring dust and metals, e.g. Ferrière, 2001; Klessen & Glover, 2014). One disadvantage in this case is that this gas is locked-up within sinks. Magnetic fields suffer from the same problem, since they are stronger in denser gas. Gas locked-up in sink particles is not able to take part in the global gas dynamics, and we effectively create everlasting MCs.

We follow the evolution of each single massive star in the simulations using the latest Geneva stellar evolution tracks by Ekström et al. (2012), and we inject stellar feedback accordingly. These are 112 individual tracks separated in intervals of $1\,{\rm M}_\odot$, from the ZAMS to the Wolf-Rayet (WR)/pre-SN phase, for different stars with initial masses from 9 to $120\,{\rm M}_\odot$. The age and initial mass of each star are used at every time-step as inputs for the sub-grid model. We use the mass-loss rate and terminal velocity of each star to inject stellar winds within the injection radius $r_{\rm inj} = r_{\rm accr}$.

While the mass-loss rates can be directly taken from the tracks by Ekström et al. (2012), we estimate terminal velocities ($v_{\rm wind}$), which are absent in the tracks, according to their evolutionary status (defined from the surface abundances of the models, see Georgy et al. 2012): (i) for OB-stars and A-supergiants, we use a slightly modified version of the scaling relations provided by Kudritzki & Puls (2000) and Markova & Puls (2008), namely $v_{\rm wind} = 2.45\ v_{\rm esc}$ for $T_{\rm eff} > 2.3 \times 10^4$ K, $v_{\rm wind} = 1.3\ v_{\rm esc}$ for $T_{\rm eff} < 1.8 \times 10^4$ K, and a linear interpolation in between (the so-called bi-stability jump, see Puls et al. 2008 and references therein). Here, $v_{\rm esc}$ is the photospheric escape velocity corrected for the radiative acceleration by electron-scattering and $T_{\rm eff}$ corresponds to the "corrected" effective temperature as provided by the tracks. (ii) For WR stars, we adapt observational data compiled by Crowther (2007), using linear interpolations. In particular, for WNL and WNE stars, we use $v_{\rm wind} = 700\ {\rm km\,s^{-1}}$ for $T_{\rm eff} < 2 \times 10^4$ K, and a linear inter/extrapolation between 700 and 2100 $\mathrm{km\,s^{-1}}$ for $2 \times 10^4 < T_{\mathrm{eff}} < 5 \times 10^4$ K, whilst for WC stars we use again $v_{\mathrm{wind}} = 700$ $\mathrm{km\,s^{-1}}$ for $T_{\mathrm{eff}} < 2 \times 10^4$ K, and a linear inter/extrapolation between 700 and 2800 $\mathrm{km\,s^{-1}}$ for 2×10^4 K $< T_{\mathrm{eff}} < 8 \times 10^4$ K. (iii) For red supergiants, we follow van Loon (2006), with $v_{\mathrm{wind}} \propto L^{0.25}$, normalised to $v_{\mathrm{wind}} = 10$ $\mathrm{km\,s^{-1}}$at luminosity of $L = 30000$ $L_{\odot}$. (iv) Finally, the terminal velocities for objects in between blue and red supergiants (rather insecure) have been approximated by the geometric mean of the v_{wind}values for the "neighbouring" blue and red supergiants, resulting in typical values of $v_{\mathrm{wind}} \approx 50$ $\mathrm{km\,s^{-1}}$ for yellow supergiants.

Fig. 3.3 shows the stellar evolution tracks used in this work for four representative stars with initial masses of $9, 12, 20$ and $85\,\mathrm{M_{\odot}}$. Depending on the mass, different stars show marked differences in the values and trends of mass-loss rate, wind terminal velocity, energy injected and lifetime. Therefore, the coupling of our sub-grid prescription with these tracks not only allows us to model the mass-dependent influence of clustered massive stars, but it also introduces a natural delay between the formation and the explosion of massive stars as SNe.

We inject the mechanical luminosities of stellar winds in the form of kinetic energy by summing up the contribution of every massive star in a cluster (i.e. sink particle). The mass of the star, as well as that of the corresponding sink particle, is updated at every injection event according to its mass-loss rate. Once the star has reached the end of its lifetime, it explodes as a SN. SN energy is injected by increasing the thermal energy of the injection region by 10^{51} erg for each explosion. For simplicity, we do not take into account remnants, and the residual mass of the star is injected within r_{inj} along with the explosion energy. As a last step, the sink particle mass is updated and the star is removed from the stellar population. When stellar winds are not included, we still follow the evolution of each star, but we do not inject any energy from winds, nor do we lower the sink particle mass. Instead, massive stars are "frozen" within the sink up to the end of their corresponding stellar track. At the end of the star's lifetime, we simply inject all the (initial) mass and the related SN energy within r_{inj}.

We centre each feedback event on the sink position and we do not consider ejection of runaway stars from clusters and associations, i.e. we do not spawn single stellar sink particles from clusters. Moreover, we do not consider any feedback mechanism from stars with $M \leqslant 8\,\mathrm{M_{\odot}}$. With their slow stellar winds and long life times, they provide a negligible effect on the spatial and temporal scales we are interested in. Type Ia SNe are also not included in our model.

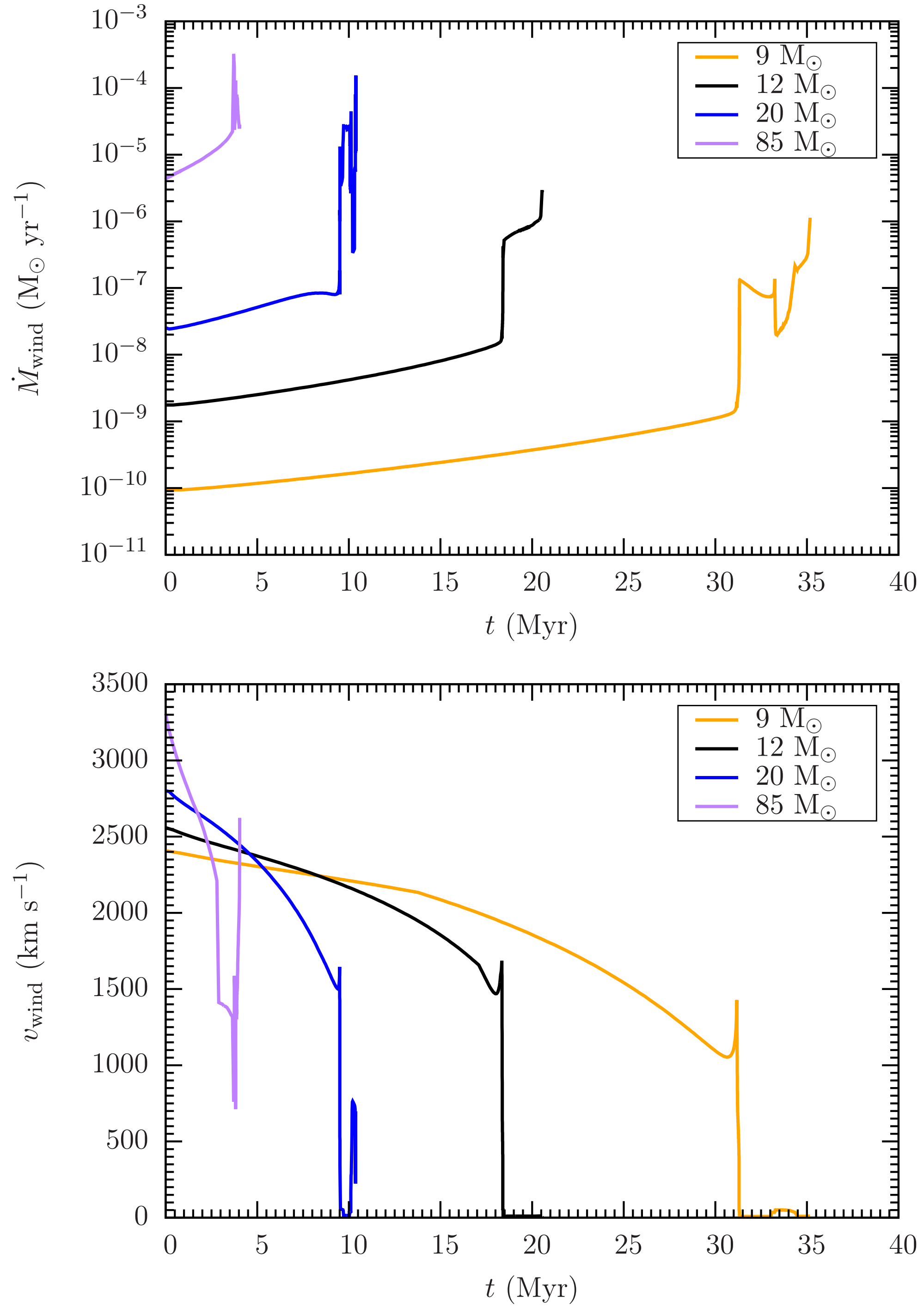

Figure 3.3: *Mass-loss rates and wind terminal velocities injected via stellar winds from the Geneva stellar evolution tracks for four representative stars with initial masses 9 (orange), 12 (black), 20 (blue) and 85 (purple)* $M_\odot$.

3.4.1 A simple test for star cluster sink particles

We show a simple test case for the cluster sink particles sub-grid model. We set up a cubic box of side 500 pc with outflow (“diode”) boundary conditions in all directions at $\Delta x \sim 4$ pc resolution (see chapter 5). The test includes radiative cooling, diffuse heating and self-gravity, but not the external static potential and magnetic fields. We set up an initial density distribution in the form of a truncated power law

$$\rho = \begin{cases} \dfrac{\rho_0}{(r/r_0)^2} & \text{if } r < r_{\rm trunc} \\ \dfrac{\rho_0}{(r_{\rm trunc}/r_0)^2} & \text{if } r \geqslant r_{\rm trunc}\ , \end{cases} \tag{3.35}$$

with $\rho_0 = \rho_{\rm thr} = 2 \times 10^{-22}$ g cm^{-3}, $r_0 = 4\,$pc, $r_{\rm trunc} = 50\,$pc and with an initial sound speed of $1\,{\rm km\,s^{-1}}$. The star formation efficiency is set to $\epsilon_{\rm SF} = 1$. We run three simulations with different combinations of feedback, i.e. without feedback, with SNe alone, and with winds and SNe. We let the gas collapse under the influence of self-gravity and we form a cluster sink particle close to, but not exactly at, the centre of the box after $\sim 3\,$Myr with an initial mass of $\sim 750\,{\rm M_\odot}$. Fig. 3.4 shows the density slices at $z = 0$ for three different times, while Fig. 3.5 shows the sink’s mass (top) and gas mass within $r_{\rm accr}$ (bottom) evolution for the different simulations. SN explosions at different times are indicated by arrows.

Without the inclusion of any feedback mechanism, no low density - high temperature gas is present and the particle continues to accrete material from outside, leading to a final mass of $\sim 10^4\,{\rm M_\odot}$. After $\sim 20\,$Myr the sink has consumed a considerable amount of the mass available within the box and accretion slows down. Similarly, the gas mass within $r_{\rm accr}$ is constant up to this point due to the continuous flow of matter driven by self-gravity, and it decreases when the mass available outside the accretion volume has been reduced significantly. Averaging over 30 Myr we find a mean SFR of $\sim 7 \times 10^{-4}\,{\rm M_\odot\ yr^{-1}}$. We note also that the cluster sink formation efficiency, defined as $\varepsilon_{\rm CF} = M_{\rm sink}/M_{\rm gas}(r_{\rm accr})$ at the creation time $t_{\rm c}$, is ≈ 9 %.

Drastically different features are present when SN feedback is included. Due to the absence of earlier feedback, the cluster continues to accrete mass from outside as in the case without feedback. During this phase, as well as at the creation time, new massive stars have formed. Star formation stops after $\sim 10\,$Myr, when the first SN goes off. This and the subsequent explosions remove gas from the accretion volume and form a hot, tenuous bubble which expands into and sweeps up the ambient medium. After $\sim 30\,$Myr the bubble has been powered by many SNe and it almost reaches the box boundaries. In contrast with the case without feedback, where the sink particle is able to accrete and form stars continuously during the entire

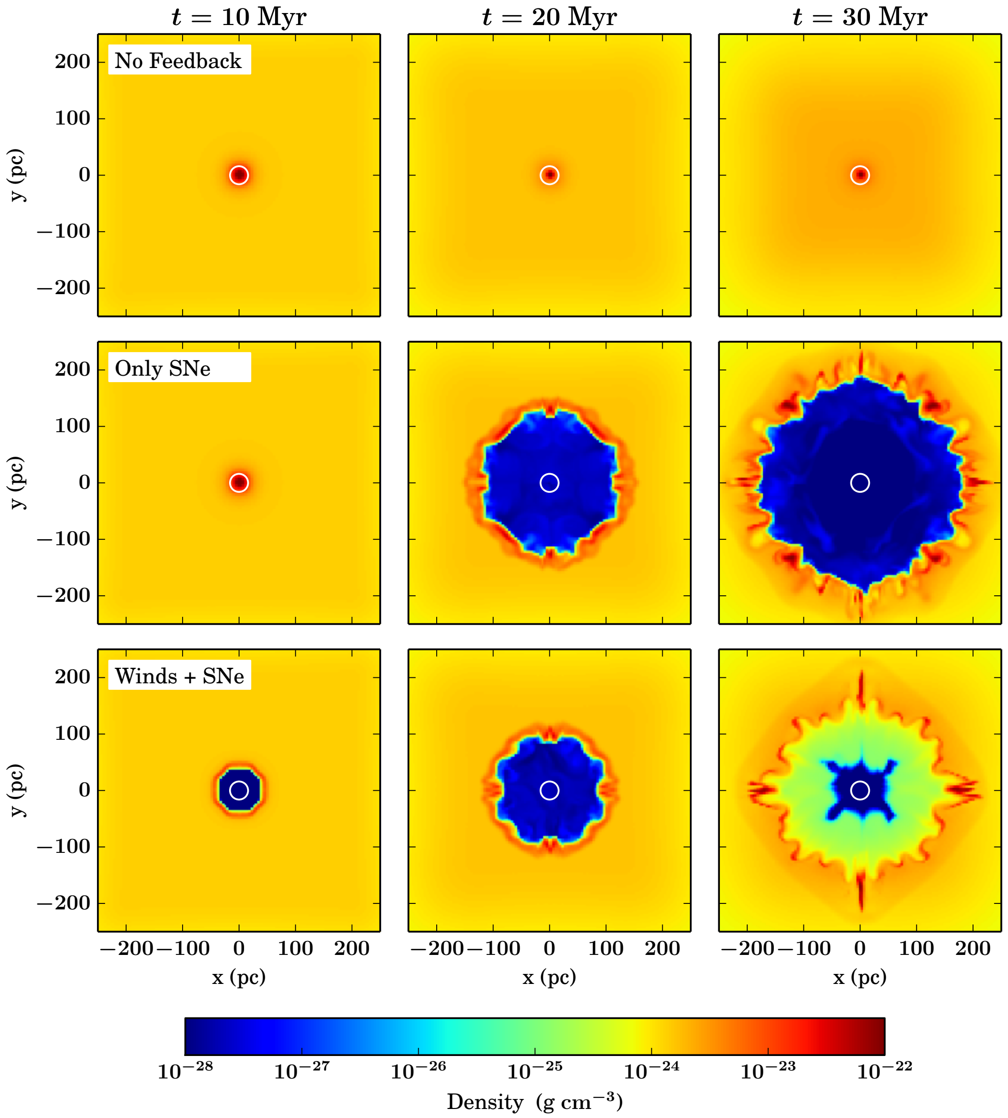

Figure 3.4: *Density slices at $z = 0$ for three different combinations of feedback, without feedback (first row), with SNe (second row) and with winds and SNe (third row). Each column represents a different snapshot at $t = 10\,\mathrm{Myr}$ (first column), $t = 20\,\mathrm{Myr}$ (second column) and $t = 30\,\mathrm{Myr}$ (third column). The white circles represents the accretion/injection radius.*

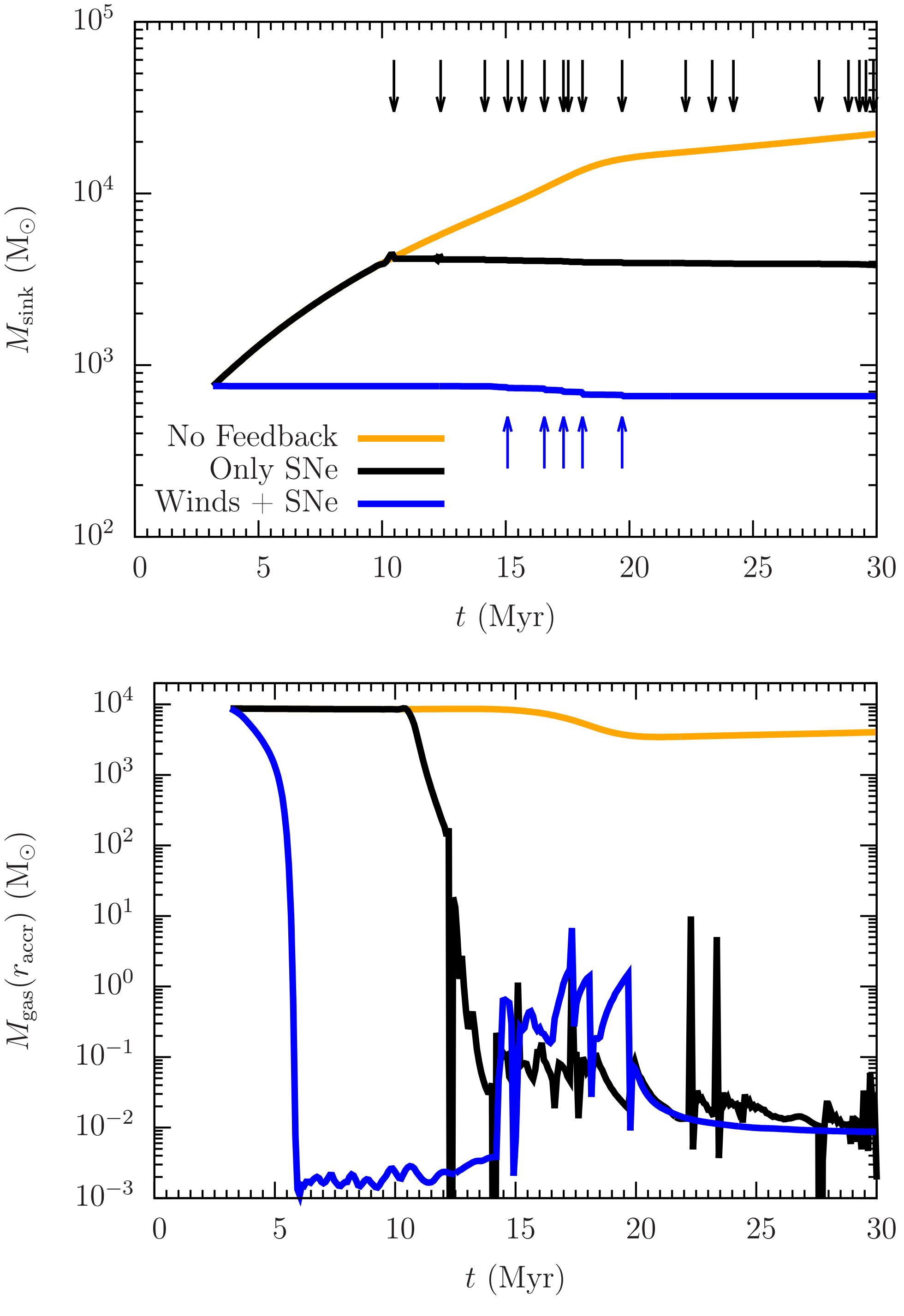

Figure 3.5: *Evolution of sink mass (top panel) and gas mass within the accretion/injection radius (bottom panel). Each line represents a different simulation, without feedback (orange line), with SNe (black line) and with winds and SNe (blue line). Each arrow, with same colour as the respective simulation, denotes the time at which one or more SNe have exploded.*

simulation, the star formation process is restricted to the first $\sim 8\,\mathrm{Myr}$. Within this time, the cluster forms 27 massive stars. Averaging through the whole simulation time, this gives SFR $\sim 10^{-4}\,\mathrm{M}_\odot\ \mathrm{yr}^{-1}$, 7 times lower than the one recovered without feedback.

The picture is again different for the simulation with stellar winds and SNe. At $t = t_\mathrm{c}$, six massive stars have formed. They start injecting stellar winds instantly and prevent any further star formation event. Accretion is quenched outright and the gas mass within r_accr drops by seven orders of magnitude in $\sim 3\,\mathrm{Myr}$. As a result, the sink mass remains almost constant up to the pre-SN phase of the most massive star. Contrary to the other simulations, at early times ($\sim 10\,\mathrm{Myr}$) hot and low-density gas fills a fraction of the box's volume due to the development of a wind bubble. Due to the monolithic nature of their formation process and similar initial masses, massive stars explode as SNe within the pre-existing wind bubble in a short time range (between 15 and $20\,\mathrm{Myr}$). After the final explosion, the bubble expands within the ambient medium, lowering its pressure up to the point where it starts collapsing on itself, as shown in the bottom right panel of Fig. 3.4 for $t = 30\,\mathrm{Myr}$. At the final time, as well as shortly after the explosion of the last SN ($t = 20\,\mathrm{Myr}$), the bubble produced by the combined effect of stellar winds and SNe is much less extended with respect to the case where only SNe are included. Stellar winds are able to shut down accretion and subsequent star formation at early times, therefore injecting much less energy into the ambient medium and reducing the average SFR to $2 \times 10^{-5}\,\mathrm{M}_\odot\ \mathrm{yr}^{-1}$, 5 times lower than the case with only SNe and 35 times less than the simulation without feedback.

We note some grid effects on the bubble's shape, especially at late times. These are also present when not including stellar winds and are an unavoidable spurious effect due to a combination of hydrodynamic instabilities and the limited resolution employed. For the simulations presented in chapter 5, however, superbubbles produced by the combined effects of stellar winds and SNe or by SNe alone interact with a highly inhomogeneous medium shaped by a number of shocks, rarefaction waves, and turbulent motions in general. This minimises the grid effects shown here by generating anisotropic expansion of the bubbles, as well as by creating intermittent asymmetries in the ambient medium on different time scales.

These simple tests show the importance stellar winds and SNe when simulating star formation at intermediate scales. SNe alone are able to lower the SFR of a cluster sink particle by a factor of 7. When including stellar winds, the SFR is reduced by a factor of 35 and star formation is efficiently quenched in short time scales. However, it would be a mistake to extrapolate these results of a single, isolated star cluster embedded into an idealised ambient medium to the case of a realistic environment, where multiple clusters affect and are affected by a number of different physical processes. For this reason, in chapter 5 we make use of this sub-grid model to study the interplay between massive stars and the ISM in a realistic stratified medium shaped by turbulent motions.

CHAPTER 4

The impact of supernova positioning on the insterstellar medium

4.1 Motivations and goals

Type II SN progenitors are massive OB stars with typically low space velocities of ≈ 15 km s^{-1} (Stone, 1991). Due to these velocities, they can only travel tens to hundreds of parsecs away from their birthplaces during their lifetimes. However, 10–30% of O stars and 5–10% of B stars in the Galaxy are runaway stars, which have large velocities (from 30 to a few hundred km s^{-1}; Blaauw, 1961; Gies, 1987; Gies & Bolton, 1986; Stone, 1991) and are therefore found far from associations (from several hundred parsecs to a kiloparsec away from their birthplaces). Runaway stars are produced by dynamical ejection by means of gravitational scattering (Gies & Bolton, 1986; Fujii & Portegies Zwart, 2011; Perets & Šubr, 2012), by massive binary systems where one of the two stars explodes as a SN, which leads to the ejection of the unbound companion (Blaauw, 1961; Portegies Zwart, 2000; Eldridge et al., 2011), or both mechanisms (Pflamm-Altenburg & Kroupa, 2010).

Runaway massive stars typically explode in the diffuse ISM, i.e. in random positions, which are not correlated with the dense molecular clouds within which massive star formation takes place. This also applies to Type Ia SNe, which add an additional random component of SN explosions due to the long lifetimes of their progenitors.

A high fraction of massive stars (70–90 %; Lada & Lada 2003) also form in clusters and associations, rather than in isolation. Despite being initially embedded in high density environments, the high degree of clustering and multiplicity of Type II SN progenitors causes the majority of SN explosions to happen within low density gas that has previously been processed by the combined effect of stellar winds (Tenorio-Tagle et al., 1990, 1991; Brighenti & D'Ercole, 1994; Rogers & Pittard, 2013) and HII regions (Gritschneder et al., 2009; Walch et al., 2012, 2013; Dale et al., 2014), as well as earlier SNe in superbubbles (McCray & Kafatos, 1987; Mac Low & McCray, 1988; Tenorio-Tagle & Bodenheimer, 1988). However, there is evidence that SNe are also interacting with the dense gas. In the inner Galaxy, around 15% of identified SN remnants show clear signs of interaction with molecular gas, including water maser emission (Hewitt & Yusef-Zadeh, 2009) and TeV γ-ray emission (Fukui et al., 2003). Overall, SNe that explode in any of the above low density environments can be approximated by explosions at random positions in an ISM with a significant VFF of hot gas. The remaining fraction of SNe interacting with dense gas can be modelled via explosions within the densest gas parcels (Walch & Naab, 2015).

Several studies of the SN-driven ISM have been carried out in the past, assuming clustered, random or density peak positions for the explosions. For instance, de Avillez & Breitschwerdt (2004) studied a representative piece of a stratified galactic disc, shaped by SNe going off at fixed rate and mostly placed in regions with highest density. Joung & Mac Low (2006) performed similar simulations but chose random positions for their explosion locations. In a recent paper, Hennebelle & Iffrig (2014) perform magneto-hydrodynamical simulations of a stratified Galactic disc modelling star formation via star cluster sink particles. They show that SN explosions correlated in space and time with the particles' position and accretion can significantly inhibit further star formation. Similar conclusions have been drawn in Iffrig & Hennebelle (2015). A massive star exploding outside of the dense gas has a limited effect with respect to the case where the explosion is located within the cloud. In the latter case, a higher fraction of momentum is transferred to the cold gas and up to half of the cloud's mass can be removed by the SN. Despite the number of previous works investigating the effect of SNe on both stratified (e.g. Shetty & Ostriker, 2012; Hill et al., 2012; Gent et al., 2013; Kim et al., 2013) and unstratified ISM (see, e.g., Balsara et al., 2004; Kim, 2004; Slyz et al., 2005; Mac Low et al., 2005; Dib et al., 2006, for modelling in periodic boxes), a systematic study is missing of the impact of different assumed SN positions, as well as the consequences of varying the SN rate with the gas density.

In this chapter, we study the turbulent, multi-phase ISM in regions of different mean density over a timescale of $\sim$ 100 Myr with fixed (Type II) SN rates, which are informed by the Kennicutt-Schmidt (KS) relation (Schmidt, 1959; Kennicutt, 1998). We focus on three different scientific questions:

1. Given a certain initial gas density, how do the properties of the ISM depend on the assumed SN rate?
2. What are the differences between a medium shaped by SNe placed randomly or at density peaks?
3. How does the ISM change as a function of the ratio between SNe that explode randomly or at density peaks?

4.2 Method

We simulate a volume of (256 pc)^3 with periodic boundary conditions. For the majority of the simulations the resolution is fixed to 128^3 cells ($\Delta x = 2$ pc), but we run a few setups at higher resolution (see sec. 4.3.8). In different simulations, we change the initial total number density of the box from $n_\mathrm{i} = 0.5$ cm^{-3} to $n_\mathrm{i} = 30$ cm^{-3} (see Table 4.1) and the initial temperature is 6000 K. We include a chemical network to treat radiative cooling and diffuse heating as well as molecule formation (see sec. 3.1.2) and we do not model the effects of gravity and magnetic fields nor we include sink particles.

4.2.1 Initial turbulent stirring

At first, the gas is stirred with an Ornstein-Uhlenbeck random process (Eswaran & Pope, 1988) with dimensionless wavenumbers $k = 1$–2, where $k = 1$ corresponds to the box side, L. The phase turnover time is $t_\mathrm{drive} = 25$ Myr, which corresponds to one crossing time for the warm gas. We distribute the turbulent energy onto solenoidal and compressive modes, using a 2:1 ratio. At every time step the total energy input is adjusted such that we obtain a global, mass-weighted, 3D root-mean-square (rms) velocity that is roughly constant at $v_\mathrm{3D,rms} = 10\,\mathrm{km\,s^{-1}}$. We stir the gas for one crossing time (25 Myr) in order to generate a turbulent two-phase medium before the onset of SN driving (see also Walch et al., 2011).

n_i (cm^{-3})	Σ_gas (M$_\odot$ pc^{-2})	$\dot{N}_\mathrm{SN,-}$ (Myr^{-1})	$\dot{N}_\mathrm{SN,KS}$ (Myr^{-1})	$\dot{N}_\mathrm{SN,+}$ (Myr^{-1})
0.5	4.1	-	1.2	-
1	8.1	1.5	3	6
3	24.3	7	14	28
10	81.2	38.5	77	154
30	243	180	360	720

Table 4.1: *Parameters of the simulations. Column 1 gives the mean volume density* n_i *and column 2 gives the corresponding gas surface density. In column 3 to 5 we list the simulated SN rates, where* $\dot{N}_\mathrm{SN,KS}$ *is derived from eq. (4.2).*

4.2.2 Supernova driving

After 25 Myr, the artificial turbulent driving is stopped. Instead, we initialise SN explosions at a fixed rate, which we adjust to the mean box mass density ρ_i. We compute the gas surface density of the box as $\Sigma_\mathrm{gas} = \rho_\mathrm{i} L$. The Kennicutt-Schmidt relation (Kennicutt, 1998):

$$\frac{\Sigma_\mathrm{SFR}}{\mathrm{M_\odot yr^{-1} kpc^{-2}}} = 2.5 \times 10^{-4} \left(\frac{\Sigma_\mathrm{gas}}{\mathrm{M_\odot pc^{-2}}}\right)^{1.4} , \tag{4.1}$$

relates the total gas surface density $\Sigma_\mathrm{gas} = \Sigma_\mathrm{HI+H_2}$ to a typical SFR surface density. For a conventional stellar initial mass function (e.g. Salpeter, 1955), approximately 100 M$_\odot$ of gas that collapses into stars produces on average only one massive star, which will explode as a SN Type II at the end of its lifetime. Hence, we only consider Type II SNe and neglect the additional contribution from Type Ia SNe, which is $\sim 15\%$ of the total SN rate in the Galaxy (Tammann et al., 1994). With this information we compute the SN rate (SNR), $\dot{N}_\mathrm{SN,KS}$, for every n_i as

$$\frac{\dot{N}_\mathrm{SN,KS}}{\mathrm{Myr}} = \frac{\Sigma_\mathrm{SFR}}{\mathrm{M_\odot Myr^{-1} pc^{-2}}} \times 10^{-2} \frac{L^2}{\mathrm{pc^2}} . \tag{4.2}$$

The SN rate derived in this way is afflicted with uncertainties of at least a factor of 2. For this reason we vary the SN rate by a factor of 2 for a number of initial densities. We list $\dot{N}_\mathrm{SN}$ for each density in Table 4.1.

For the majority of our simulations, each SN injects $E_\mathrm{SN} = 10^{51}$ erg of thermal energy into the ISM. The injection radius is defined as the radius that encompasses 10^3 M$_\odot$ of gas. For two runs we use a combined scheme in which we inject all of the SN energy in the form of thermal energy if the SN is resolved. If $R_\mathrm{ST} < 4\Delta x$, then we inject momentum rather than thermal energy (see sec. 3.2). In both cases, we do not inject any mass along with the explosion energy/momentum.

4.2.3 Simulations

We will show that the positioning of the SNe relative to the gas density distribution changes the structure of the ISM. Therefore, we choose three different schemes to place the SNe: (i) random driving (runs R-$\mathrm{n_i}$), (ii) peak driving (runs P-$\mathrm{n_i}$), i.e. the current SN is placed on the global density maximum at the time, and (iii) a mixture of the two, i.e. mixed driving (runs Mf-$\mathrm{n_i}$), with a fixed ratio f_{peak} of peak to total SNe.

We carry out a number of simulations with different driving schemes and densities, which we summarise in Table 4.2. By default, we choose random driving. For this driving scheme, we run five simulations with $\dot{N}_{\mathrm{SN,KS}}$ for $n_{\mathrm{i}} = 0.5, 1, 3, 10, 30\,\mathrm{cm}^{-3}$ and eight for $n_{\mathrm{i}} = 1, 3, 10, 30\,\mathrm{cm}^{-3}$ with half ($\dot{N}_{\mathrm{SN},-}$) and twice the KS SN rate ($\dot{N}_{\mathrm{SN},+}$). In addition, we perform four simulations ($n_{\mathrm{i}} = 0.5, 1, 3, 10\,\mathrm{cm}^{-3}$) with peak driving. For $n_{\mathrm{i}} = 3\,\mathrm{cm}^{-3}$, we carry out 9 simulations using mixed driving with different values of f_{peak}.

We investigate the applicability of the combined model of thermal energy and momentum injection using two simulations with $n_{\mathrm{i}} = 3\,\mathrm{cm}^{-3}$ and $f_{\mathrm{peak}} = 100\%$ (P-C-$\mathrm{n_3}$) and 50% (M50-C-$\mathrm{n_3}$). Finally, we run two simulations for $n_{\mathrm{i}} = 3\,\mathrm{cm}^{-3}$ at a higher resolution (with $\Delta x = 1$ pc). These runs are called R-HR-$\mathrm{n_3}$ for random and P-HR-$\mathrm{n_3}$ for peak driving.

4.2.4 Simulation analysis

The simulations are stopped once an approximate chemo-dynamical equilibrium is reached, i.e. the mass distribution of the different chemical species stays roughly constant. This is typically the case after 100–200 Myr (note that 25 Myr was the initial crossing time), depending on the initial box density and SN rate. We discuss the properties of the resulting ISM for different initial densities, driving schemes, and resolution towards the end of the simulations. In particular, we focus on four quantities:

1. the distribution of gas mass among ionised, neutral, and molecular hydrogen;
2. the gas pressure in different temperature regimes;
3. the VFFs of gas within the different temperature regimes; and
4. the observable velocity dispersion.

We compute every quantity by averaging over the final 5 Myr of each simulation in order to reduce statistical errors.

To compare with velocity dispersions observed in HI and H_{α}, we compute the mass-weighted, one-dimensional velocity dispersion, $\sigma_{\mathrm{avg\,1D}}$. We first

name	n_i (cm^{-3})	$\dot{N}_\mathrm{SN}$ (Myr^{-1})	Driving	Note
R-n$_{0.5}$	0.5	1.2	R	
R-n$_1$	1	3	R	
R-n$_{1-}$	1	1.5	R	
R-n$_{1+}$	1	6	R	
R-n$_3$	3	14	R	
R-n$_{3-}$	3	7	R	
R-n$_{3+}$	3	28	R	
R-n$_{10}$	10	77	R	
R-n$_{10-}$	10	38.5	R	
R-n$_{10+}$	10	154	R	
R-n$_{30}$	30	360	R	
R-n$_{30-}$	30	180	R	
R-n$_{30+}$	30	720	R	
P-n$_{0.5}$	0.5	1.2	P	
P-n$_1$	1	3	P	
P-n$_3$	3	14	P	
P-n$_{10}$	10	77	P	
M10-n$_3$	3	14	M	$f_\mathrm{peak} = 10$
M20-n$_3$	3	14	M	$f_\mathrm{peak} = 20$
M30-n$_3$	3	14	M	$f_\mathrm{peak} = 30$
M40-n$_3$	3	14	M	$f_\mathrm{peak} = 40$
M50-n$_3$	3	14	M	$f_\mathrm{peak} = 50$
M60-n$_3$	3	14	M	$f_\mathrm{peak} = 60$
M70-n$_3$	3	14	M	$f_\mathrm{peak} = 70$
M80-n$_3$	3	14	M	$f_\mathrm{peak} = 80$
M90-n$_3$	3	14	M	$f_\mathrm{peak} = 90$
P-C-n$_3$	3	14	P	CM
M50-C-n$_3$	3	14	M	CM $f_\mathrm{peak} = 50$
R-HR-n$_3$	3	14	R	$\Delta x = 1$ pc
P-HR-n$_3$	3	14	P	$\Delta x = 1$ pc

Table 4.2: *List of all simulations. From left to right: name of the simulation; initial number density of the box* n_i*; supernova rate* $\dot{N}_\mathrm{SN}$*; Driving mode: pure random (R), pure peak (P) or mixed (M); Note: combined model with thermal energy and momentum input (CM).*

compute the 1D dispersion for HI and H_α along the x-, y-, and z-directions for each simulation:

$$\sigma_{j,k,\mathrm{turb}} = \left(\frac{\sum_i (v_{i,k} - \overline{v}_k)^2 \ m_{i,j}}{M_{j,\mathrm{tot}}} \right)^{1/2} , \tag{4.3}$$

where j indicates the chemical species (HI or H_α), i is the cell index, v_i is the velocity of the cell, and $\overline{v}$ is the average velocity in the respective direction k. m_j is the mass of species j in cell i, and $M_{j,\mathrm{tot}}$ is the total mass of species j. We then average over all three directions and receive a mean, one-dimensional velocity dispersion:

$$\sigma_{j,\mathrm{turb}} = \frac{1}{3} \sum_{k=1}^{3} \sigma_{j,k,\mathrm{turb}}. \tag{4.4}$$

HI VELOCITY DISPERSION: For HI the intensity is proportional to the number of emitters (e.g. Rohlfs & Wilson, 1996). Therefore the HI mass is a good proxy for the total radiation flux, i.e. $M_j \propto L_j$, and the resulting velocity dispersion, $\sigma_{\mathrm{HI,turb}}$, can be considered as an intensity-weighted velocity dispersion.

H_α VELOCITY DISPERSION: For H_α, the mass of ionised hydrogen is not a good estimate of the H_α intensity, since the emission decreases with increasing temperature. Here, we compute the H_α flux from two contributions, namely the recombination of ionised hydrogen and collisional excitation from the ground state to level $n = 3$. We have to neglect the contribution from HII regions around young massive stars since these are not treated in the simulations. Collisional excitations to $n > 3$ represent a negligible contribution to the total H_α emission since transitions to these levels are significantly less likely (Anderson et al., 2000, 2002, but see also Péquignot & Tsamis (2005) and references therein). We compute $m_{\mathrm{H}\alpha}$ ($dL_{\mathrm{H}\alpha}$) and $M_{\mathrm{tot,H}\alpha}$ ($L_{\mathrm{tot,H}\alpha}$), required in eq. (4.3), following the emissivity calculations for recombination and collisional excitation of Draine (2011); Dong & Draine (2011), and Kim et al. (2013) (but see also Aggarwal, 1983):

$$dL_{\mathrm{H}\alpha,\mathrm{R}} \propto T_4^{-0.942-0.031\ln(T_4)} n_\mathrm{e} n_\mathrm{HII} dV \ , \tag{4.5}$$

$$dL_{\mathrm{H}\alpha,\mathrm{C}} \propto \frac{\Gamma_{13}(T_\mathrm{e})}{\sqrt{T_\mathrm{e}}} e^{\frac{-12.1\mathrm{eV}}{k_\mathrm{B} T_\mathrm{e}}} n_\mathrm{e} n_\mathrm{HI} dV \ , \tag{4.6}$$

where $T_4 = T/10^4$ K, T_e is the electron temperature, n_j is the number density of species j in cm^{-3}, dV is the zone volume, and

$$\Gamma_{13}(T_\mathrm{e}) = 0.35 - 2.62 \times 10^{-7} T_\mathrm{e} - 8.15 \times 10^{-11} T_\mathrm{e}^2 + 6.19 \times 10^{-15} T_\mathrm{e}^3. \tag{4.7}$$

We apply equation (4.6) only for cells with temperatures $4000 < T < 25\,000$ K assuming $T_{\mathrm{e}} = T$. We only consider this temperature range because emission at $T < 4000$ K will be negligible, while we expect to find very little atomic hydrogen at $T > 25\,000$ K. We also assume $n_{\mathrm{e}} = n_{\mathrm{H\,II}}$, which results in a $\sim 10\%$ error at most in regions where helium is ionised.

We approximate the gas to be optically thin to the H_α and HI emission. Although this assumption might lead to a poor estimate of the line intensities, we do not expect major absorption features except in cold and dense HI clouds. In this case HI self-absorption could also play a non-negligible role. However, as we will see in the next sections, most of the dense clumps in our models are composed of H_2, with only a small mass fraction of atomic gas in the outer shells.

THERMAL COMPONENT: We include thermal broadening by adding a mass-weighted thermal velocity

$$\sigma_{j,\mathrm{therm}} = \left(\frac{\sum_i v_{i,\mathrm{therm}}^2 \; m_{i,j}}{M_{j,\mathrm{tot}}} \right)^{1/2} , \tag{4.8}$$

where $v_{i,\mathrm{therm}} = (2k_B T_i/\mu_i)^{1/2}$ with T_i being the temperature and μ_i the mean mass per particle in cell i. We assume that all species within a cell have the same temperature, which can cause small errors in the thermal velocity estimate. The resulting total velocity dispersion is

$$\sigma_{\mathrm{avg\ 1D},j} = \left(\sigma_{j,\mathrm{turb}}^2 + \sigma_{j,\mathrm{therm}}^2 \right)^{1/2} . \tag{4.9}$$

4.3 Results

4.3.1 Energy input

In Figure 4.1 we show the cumulative energy input as a function of time for artificial turbulent driving (solid lines) and SN driving (dashed lines) with a SN rate derived from the KS relation, for initial densities $n_{\mathrm{i}} = 0.5, 3$ and $10\,\mathrm{cm}^{-3}$. We point out that the energy input from artificial driving necessary to maintain a constant 3D, mass-weighted, rms velocity of $v_{\mathrm{3D,rms}} = 10\,\mathrm{km\,s}^{-1}$ (corresponding to a one-dimensional velocity dispersion of $\sim 5 - 6\,\mathrm{km\,s}^{-1}$) is always about two orders of magnitude lower than the energy input in the corresponding SN-driven box. Nevertheless, we will see that SN driving is inefficient in terms of turbulence driving. Therefore, even though the energy input is high, the resulting, average, one-dimensional velocity dispersions in cold HI gas stay below $10\,\mathrm{km\,s}^{-1}$.

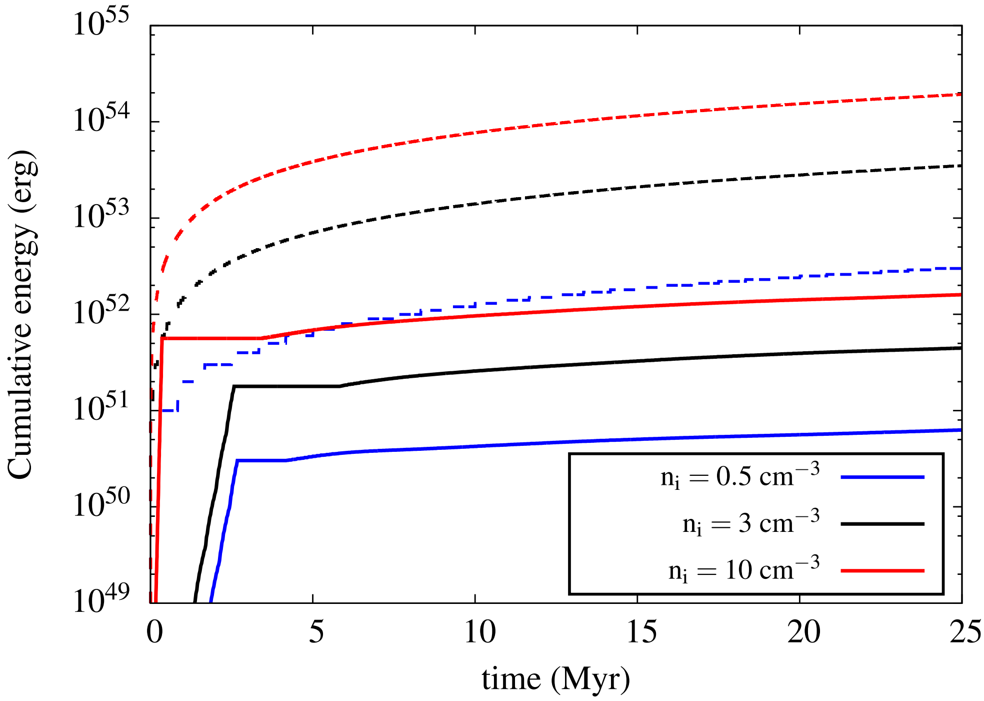

Figure 4.1: *Cumulative energy injected in the first 25 Myr of artificial (solid lines, $t = 0 - 25$ Myr) and SN driving (dashed lines, $t = 25 - 50$ Myr) for different n_i.*

4.3.2 Impact of supernova positioning

We start from the artificially stirred, turbulent box at different densities at $t_\mathrm{drive} = 25$ Myr. We then evolve the simulations with SN driving at different rates and positioning of the SNe relative to the dense gas.

Density and temperature distribution: In Figure 4.2, we compare the density and temperature structure of the ISM for three runs with $n_\mathrm{i} = 3\,\mathrm{cm}^{-3}$ and $\dot{N}_\mathrm{SN,KS}$ at $t = 100$ Myr, using peak driving (run P-n$_3$, left column), random driving (run R-n$_3$, middle column), and mixed driving (run M50-n$_3$, i.e. mixed driving with $f_\mathrm{peak} = 50\%$, right column). The SN rate is the same and the huge differences in the ISM structure are solely due to the positioning of the SNe. For peak driving, the box is filled with warm and cold gas, which is distributed in filaments and extended clouds. There is little to no hot gas present. In the case of random driving, on the other hand, most of the box is filled with hot gas, while the cold gas is concentrated in small and dense clumps. The mixed driving case with an equal contribution from random and peak driving lies in between the other two cases. Gas at $T \gtrsim 10^6$ K occupies the majority of the box volume, but

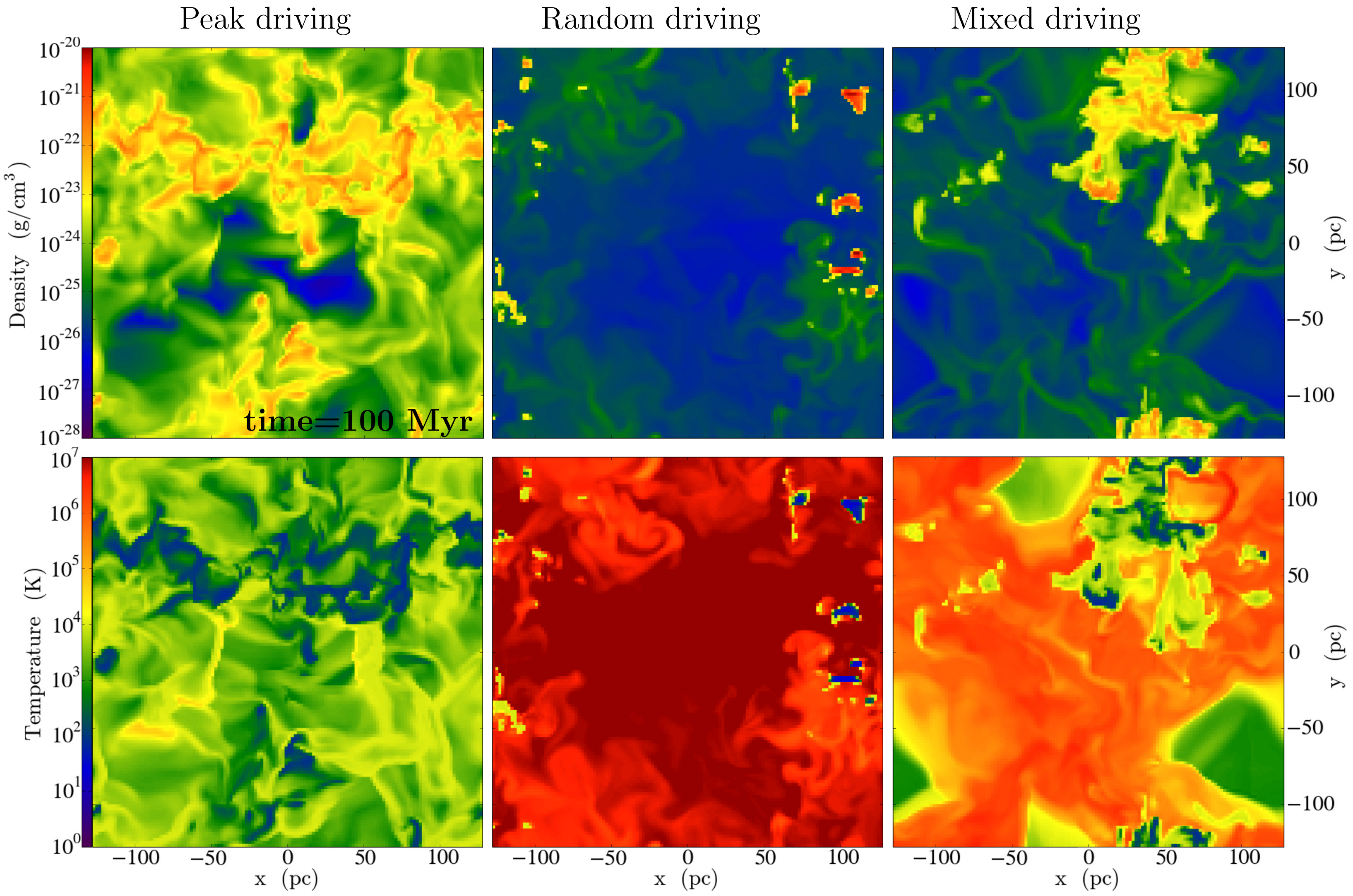

Figure 4.2: *Density (top row) and temperature (bottom row) slices for three runs with initial density* $n_{\mathrm{i}} = 3\,\mathrm{cm}^{-3}$ *and SN rate drawn from the Kennicutt-Schmidt relation* $\dot{N}_{\mathrm{SN,KS}}$. *From left to right, we show runs P-*n_3 *(peak driving), R-*n_3 *(random driving) and M50-*n_3 *(mixed driving with* $f_{\mathrm{peak}} = 50\%$*) at* $t = 100$ *Myr.*

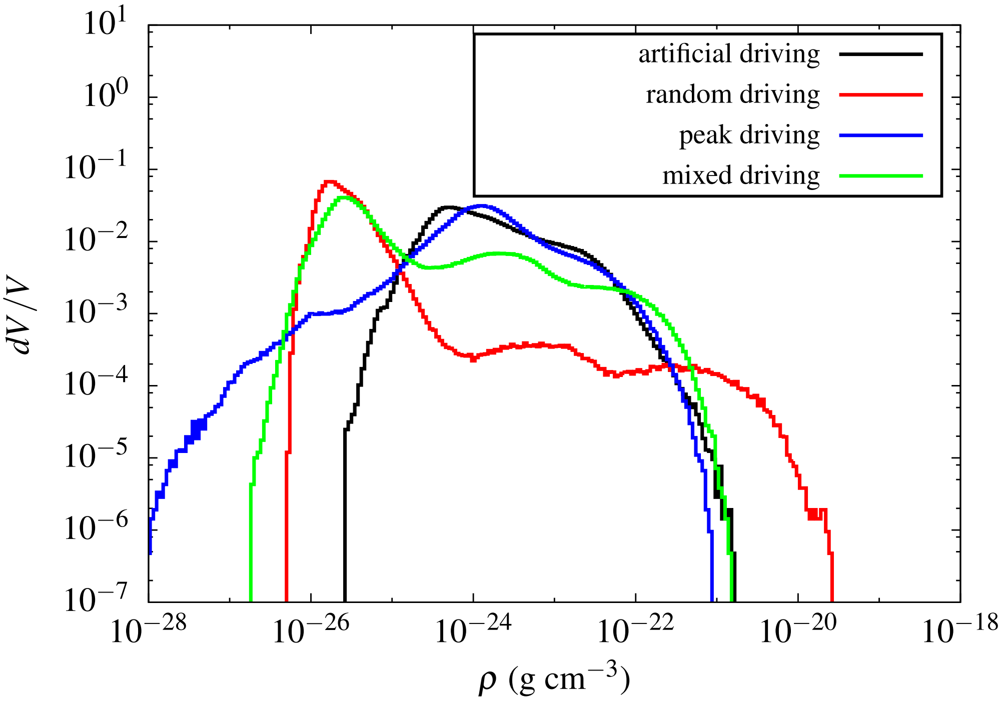

Figure 4.3: *Volume-weighted density PDFs for different driving modes, i.e. random (red line), peak (blue line), and 50% mixed driving (green line), for the* $n_i = 3\,\mathrm{cm}^{-3}$ *runs at* $t = 100$ *Myr. In addition, we show the initial condition from artificial stirring at* $t_{\mathrm{drive}} = 25$ *Myr (black line).*

the cold and warm phases are located not just in massive clumps, but also in extended filamentary complexes.

Density probability distribution functions: In Figure 4.3, we show the volume-weighted probability distribution functions (PDFs) of density for the initial condition derived from artificial turbulence stirring at $t_{\mathrm{drive}} = 25$ Myr (black line) and for the three different driving modes at $t = 100$ Myr. For artificial driving at a rms velocity of 10 $\mathrm{km\,s^{-1}}$, we find a broad PDF which can be interpreted as two overlapping log-normal distributions. The medium does not consist of two distinct warm and cold phases. A significant fraction of the gas lies far from the equilibrium curve due to turbulent motions (e.g. Walch et al., 2011, but see also Vázquez-Semadeni et al. 2000; Micic et al. 2013; Saury et al. 2014). For peak driving (blue line) the PDF roughly coincides with the one for artificial driving at high densities, but with a more extended tail towards low densities. In the case of random driving (red line), the distribution has a strong peak at low densities ($\rho \sim$ few $\times\, 10^{-26}$ g cm^{-3}), which corresponds to the hot, overpressured phase, followed by two subsequent peaks at higher densities. The maximum density reached is well above the ones produced by other driving modes. Since most of the volume is filled with hot gas, the volume-weighted PDF is dominated by a single peak at low densities. Mixed driving (green line) displays an intermediate distribution between random and peak driving with three broad peaks. This is typical for a turbulent three-phase ISM consisting of cold, warm and hot gas, with significant contributions from each component (e.g. Gent et al., 2013).

PHASE DIAGRAMS: In Figure 4.4, we show exemplary $\rho - T$ and $\rho - P$ phase diagrams for random and peak driving, where the mass distribution is colour-coded. In the random driving case (first two plots) the gas is moved to high pressures $P/k_B \gtrsim 10^4$ K cm^{-3}, which is above the mean pressure in the Milky Way (e.g. Jenkins & Tripp, 2011). A small fraction of the gas reaches high temperatures $T > 10^6$ K; this gas occupies virtually all of the volume, as shown in Figure 4.3. This hot, high-pressure gas pushes the majority of the mass into the cold, dense phase (see section 4.3.3). The cold, high density tail lies slightly below the equilibrium curve. A likely explanation is that at high density, the cold gas is efficiently shielded against the far-UV interstellar radiation field. Since the equilibrium values are computed without considering this mechanism, the densest component has a lower equilibrium pressure and temperature in this density range.

On the other hand in the peak driving case (last two plots) a two-phase medium, with warm and cold gas in approximate pressure equilibrium, is formed. The densest component actually lies slightly above the equilibrium curve due to the continuous heating of the densest gas parcels by SN shocks. However, these simulations contain little to no hot gas, as the SNe, which explode only in dense environments, fail to effectively heat the gas (see section 4.3.5). The maximum densities reached in simulations with peak driving are 1–2 orders of magnitude smaller than in the random driving case since, by construction, peak driving removes the densest component of the medium and highly over-pressured hot regions are not present in this case.

SUMMARY: We may summarise the impact of the different SN positioning (see Figs. 4.2 and 4.4) as follows: in the case of random driving, most SNe are placed in positions where their energy can be efficiently transferred to the ISM. In the case of peak driving, the SNe explode in dense gas, which may promptly radiate a large fraction of the inserted energy. The higher the fraction of random SNe, the more efficiently energy is injected, which increases the thermal gas pressure and increases the chance to end up in a thermal runaway regime, as discussed in the next section. In section 4.3.6 we explore this transition in simulations with different $f_{\rm peak}$.

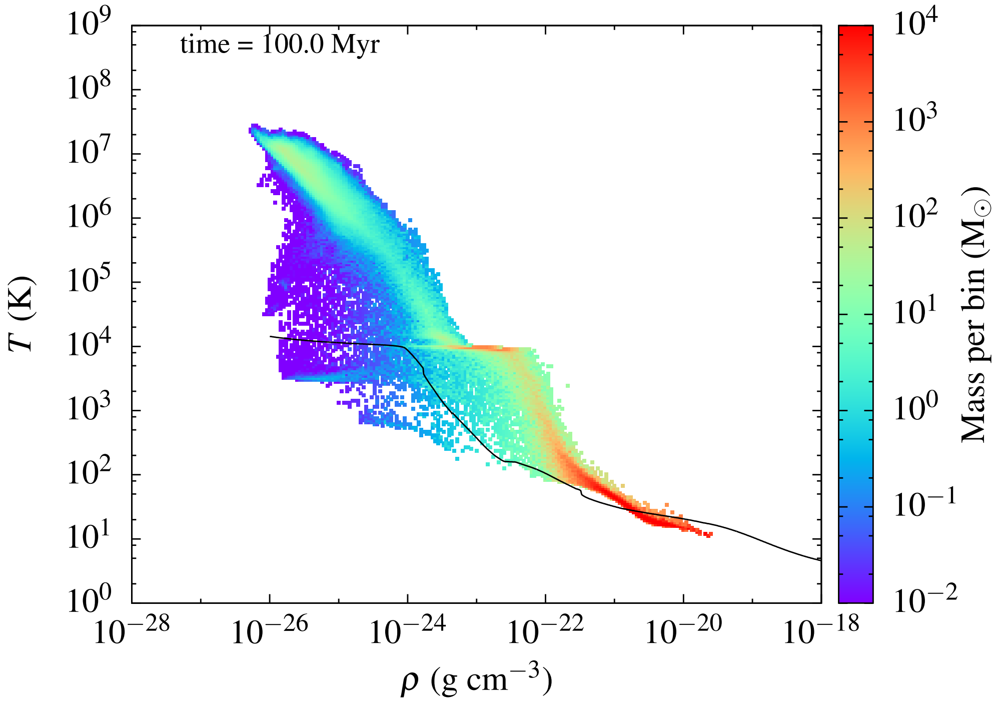
time = 100.0 Myr
T (K)
10^0
10^1
10^2
10^3
10^4
10^5
10^6
10^7
10^8
10^9
10^{-28}
10^{-26}
10^{-24}
10^{-22}
10^{-20}
10^{-18}
ρ (g cm^{-3})
Mass per bin (M$_\odot$)
10^4
10^3
10^2
10^1
10^0
10^{-1}
10^{-2}

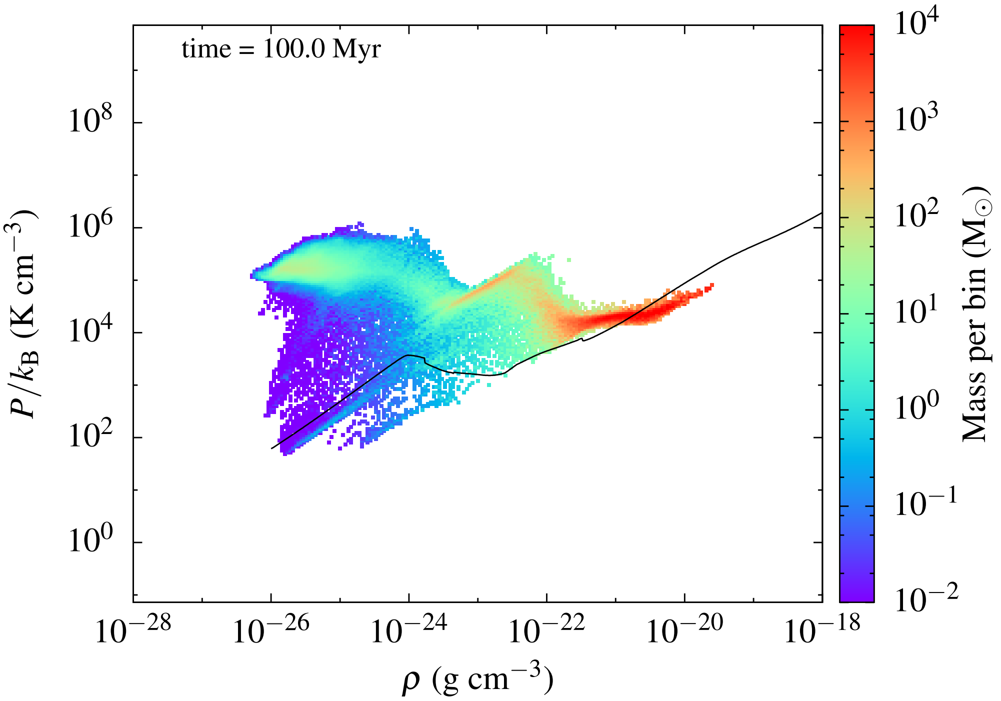
time = 100.0 Myr
P/k_B (K cm^{-3})
10^0
10^2
10^4
10^6
10^8
10^{-28}
10^{-26}
10^{-24}
10^{-22}
10^{-20}
10^{-18}
ρ (g cm^{-3})
Mass per bin (M$_\odot$)
10^4
10^3
10^2
10^1
10^0
10^{-1}
10^{-2}

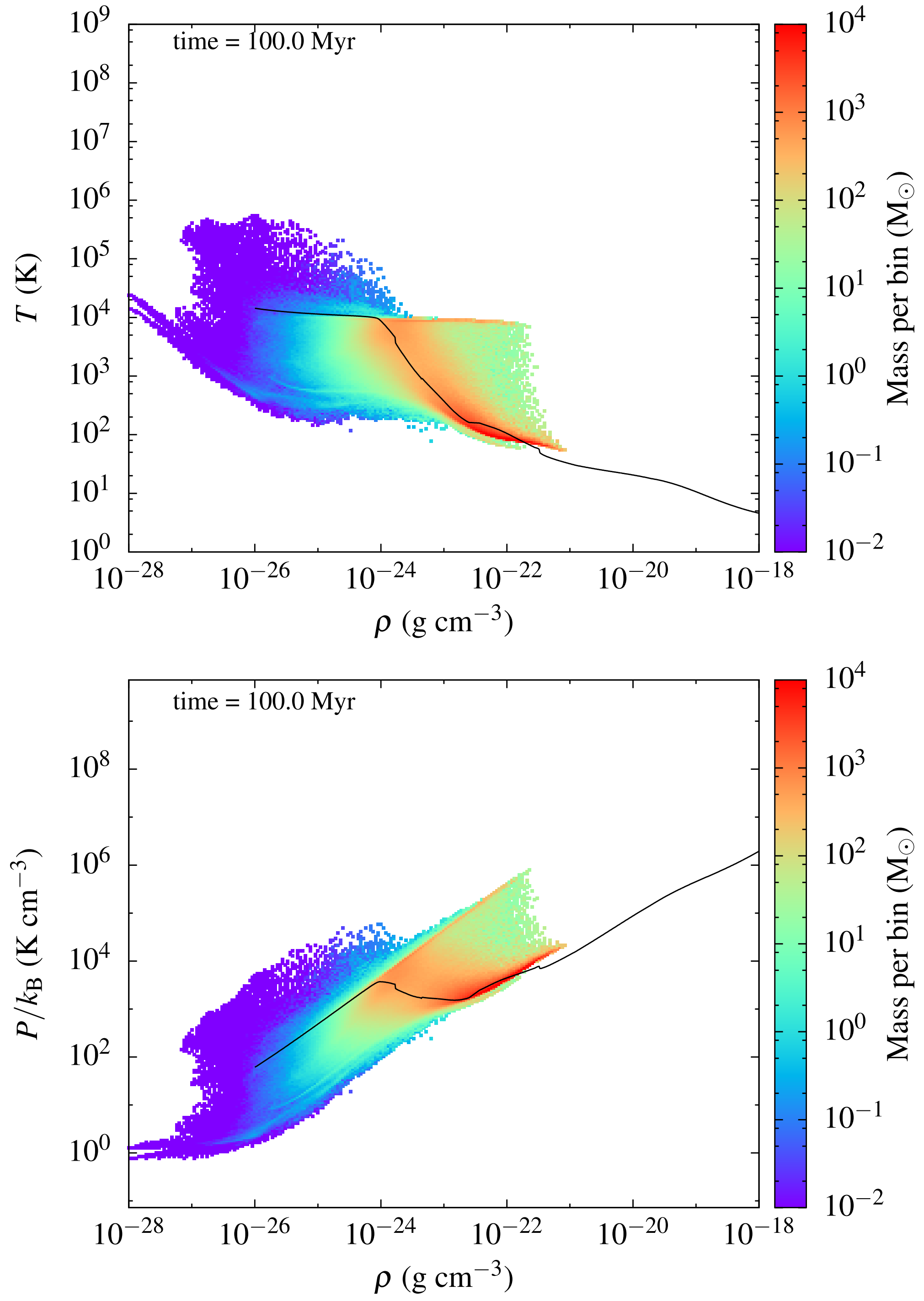

Figure 4.4: *Density-temperature and density-pressure phase diagrams for two simulations with initial density* $n_\mathrm{i} = 3\,\mathrm{cm}^{-3}$ *and* $\dot{N}_\mathrm{SN,KS}$ *at* $t = 100$ *Myr. We colour-code the mass distribution. The first two plots show run R-*n_3 *(random driving), while the last two show run P-*n_3 *(peak driving). The solid lines show the equilibrium curve.*

4.3.3 Thermal runaway

The high pressure reached in our models results in the equilibrium between heating and cooling lying not in the regime near $P/k_B \sim 10^3$ K cm^{-3} where a two-phase medium is possible, but rather on the cold branch of the equilibrium curve, where balance between heating and cooling can only be reached at low temperatures and high densities. This explains why virtually all the mass lies at high density ($n > 100$ cm^{-3}) and low temperature ($T < 200$ K). As a result, we move from the classic paradigm of a two-phase medium in pressure equilibrium towards a scenario in which only the cold phase survives, consistent with the picture of Wolfire et al. (1995) for high heating (far-UV interstellar field) rates. The cooling times in the remaining rarefied gas are long, since radiative cooling is proportional to n^2 and drops significantly for temperatures above 10^6 K (Raymond et al., 1976). As a result, almost all of the volume is occupied by gas with low density and $T > 10^6$ K, whose cooling time far exceeds the dynamical time of the system: the third phase of the three-phase medium (McKee & Ostriker, 1977). This picture is consistent with the findings of Scannapieco et al. (2012), who use hydrodynamical simulations of artificially-driven turbulence in a stratified disc to mimic the impact of stellar feedback. They find that, for turbulent one-dimensional velocity dispersions $\gtrsim 35\,\mathrm{km\,s^{-1}}$, large fractions of gas are continuously heated and unable to cool within a turbulent crossing time. This process leads to powerful outflows and compression of cold gas. In the thermal runaway regime, our simulations behave in a similar way, as energy is directly deposited into a hot, high pressure medium, with a resulting one dimensional velocity dispersion of the hot phase well above the critical value of $35\,\mathrm{km\,s^{-1}}$.

The high pressures reached in the thermal runaway regime marks a clear distinction from the classic picture of McKee & Ostriker (1977). In that model, a SN remnant expands into a medium characterised by the presence of many evenly-distributed, small, two-phase clouds having cold cores surrounded by warm envelopes. The passage of the SN blast wave heats and destroys these clouds, sweeping them up into a dense shell. This dense shell cools and slows down during the radiative phase, and the remnant ceases to exist when it reaches pressure equilibrium with the ambient medium. For thermal runaway, however, SNe go off in a hot, high pressure environment, while isolated cold clouds lie far from the explosion position. Well before the end of the Sedov-Taylor phase, the remnants reach pressure equilibrium with the hot gas and deposit their energy into the medium without any significant radiative loss.

In this environment heating cannot be balanced by radiative cooling. In our periodic box, within which there is no vertical stratification to allow

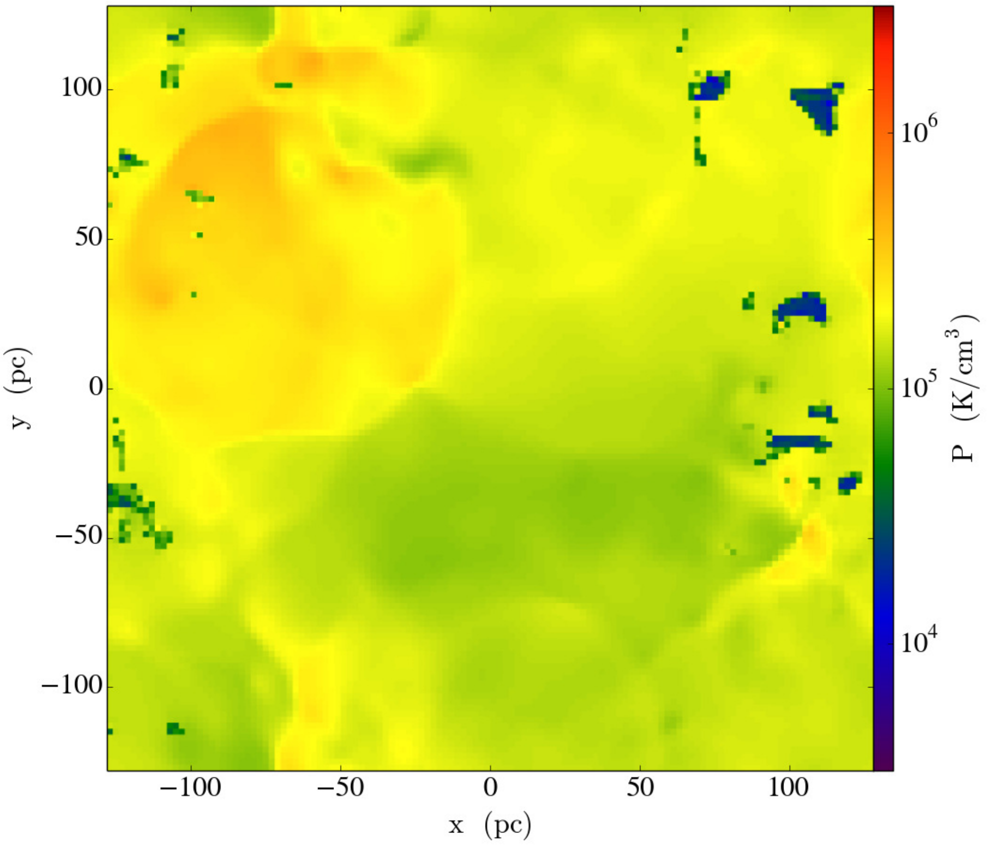

Figure 4.5: *Pressure slice for the random driving run with initial density* $n_{\rm i} = 3\,{\rm cm}^{-3}$ *and* $\dot{N}_{\rm SN,KS}$ *at* $t = 100$ *Myr (see also central column of Fig. 4.2).*

an atmosphere to evolve into hydrostatic equilibrium with a galactic potential, the hot gas pressure can only be set by the balance between cooling and heating. Random driving thus pushes the system towards a thermal runaway regime, where the hot gas contains most of the energy, while the majority of the box mass is stored in the coldest phase without the possibility to return to a system with a significant warm phase ($T \sim 10^4$ K). Cold gas is not formed from a two-phase medium, but instead cools directly to the cold branch of the equilibrium curve, forming high-density clumps with small VFF. The cold clumps are produced by compression waves coming from the hot, high-pressure gas. This mechanism causes an efficient and fast conversion from warm, atomic gas to molecular. These clumps are resolved by so few zones that they cannot reach high enough densities to remain in pressure equilibrium with the background. As a result, cold clouds at low pressures are embedded into a hot, high-pressure environment. This numerically caused jump in pressure can reach about one order of magnitude (see Fig. 4.5 for the pressure distribution in run with $n_\mathrm{i} = 3\,\mathrm{cm}^{-3}$ and $\dot{N}_\mathrm{SN,KS}$). Therefore, we must treat the interior properties of the clouds as limits at low density and velocity dispersion, rather than converged values.

4.3.4 Random driving at different supernova rates

In this section we discuss the properties of the ISM forming in runs R-$\mathrm{n_i}$ with randomly placed SNe and different initial densities n_i. The SN rates are adjusted to the given n_i (see section 4.2.2). We perform three simulations with different SN rates for almost every n_i using $\dot{N}_\mathrm{SN,KS}$, and $\dot{N}_\mathrm{SN,-}$ and $\dot{N}_\mathrm{SN,+}$, where the SN rate is decreased/increased by a factor of two, respectively (see also Table 4.1). In Figure 4.6 we compare the different simulations. We plot the mass in ionised, atomic, and molecular hydrogen (first plot), the pressure in three different temperature regimes, which are representative for the cold, warm ionised, and hot phase of the ISM (second plot), the VFF in different temperature phases (third plot), and the velocity dispersion of the gas in HI and H_α (fourth plot) towards the end of each simulation. To guide the eye we connect the simulations with equal n_i but different SN rate.

CHEMICAL COMPOSITION: We follow the chemical evolution of the gas, including the formation of molecular hydrogen, taking into account the effects of dust shielding and molecular (self-)shielding. We find that the mass in ionised hydrogen is always below 10% and decreasing for increasing box density. For low densities ($n_\mathrm{i} \lesssim 3\,\mathrm{cm}^{-3}$) most of the total mass is in atomic hydrogen. At higher densities ($n_\mathrm{i} \gtrsim 3\,\mathrm{cm}^{-3}$) less than 50% of the mass is in HI and the rest is in molecular hydrogen. Molecular hydrogen, which is organised in small, dense clumps (see Fig. 4.2), dominates the mass budget at high densities and SN rates (up to 80% of the total mass is in form of H_2 at $n_\mathrm{i} = 30\,\mathrm{cm}^{-3}$).

GAS PRESSURE: We compute the average pressure in three different temperature regimes: (i) for the stable cold phase at $T \leqslant 300$ K; (ii) for the stable warm phase at $8000 \leqslant T \leqslant 12000$ K; and (iii) for the hot phase at $T \geqslant 3 \cdot 10^5$ K. For $n_\mathrm{i} \leqslant 1\,\mathrm{cm}^{-3}$ the medium is roughly in pressure equilibrium, but for higher densities and SN rates the pressures of the three phases diverge slowly as we get into the thermal runaway regime.

VOLUME FILLING FRACTIONS: We show the VFFs of the gas in the third plot of Figure 4.6. We distinguish four different temperature regimes: the cold phase at $30 \leqslant T < 300$ K; the warm atomic ISM at $300 \leqslant T < 8000$ K; the warm ionised medium at $8000 \leqslant T < 3 \times 10^5$ K; and the hot ionised medium at $T \geqslant 3 \times 10^5$ K. Only for two simulations (R-$\mathrm{n}_{0.5}$ and R-n_{1-}), are

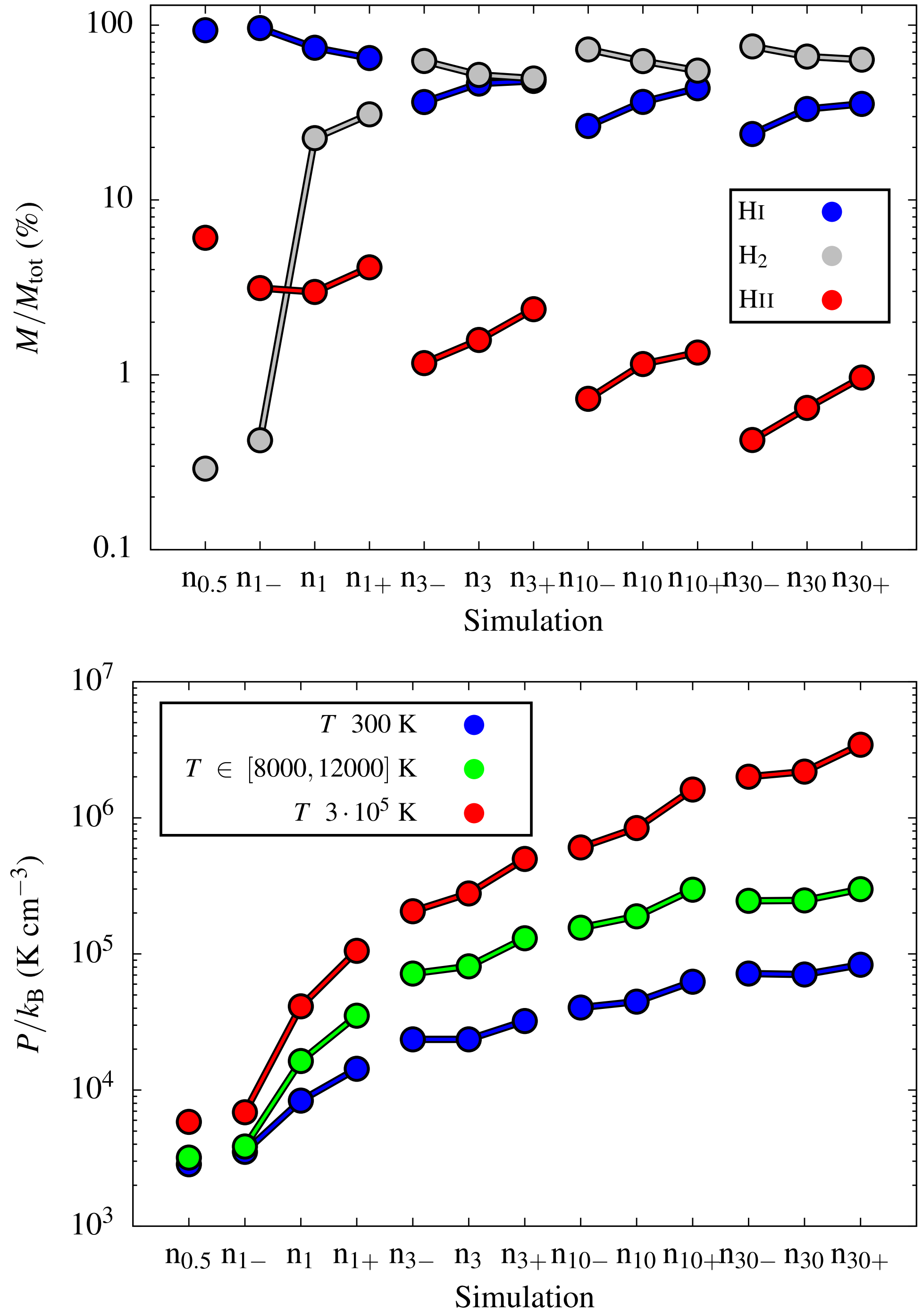
M/M_{tot} (%)
100
10
1
0.1
HI
H_2
HII
$n_{0.5}$ n_{1-} n_1 n_{1+} n_{3-} n_3 n_{3+} n_{10-} n_{10} n_{10+} n_{30-} n_{30} n_{30+}
Simulation
P/k_B (K cm^{-3})
10^7
10^6
10^5
10^4
10^3
T 300 K
$T \in [8000, 12000]$ K
T $3 \cdot 10^5$ K
$n_{0.5}$ n_{1-} n_1 n_{1+} n_{3-} n_3 n_{3+} n_{10-} n_{10} n_{10+} n_{30-} n_{30} n_{30+}
Simulation

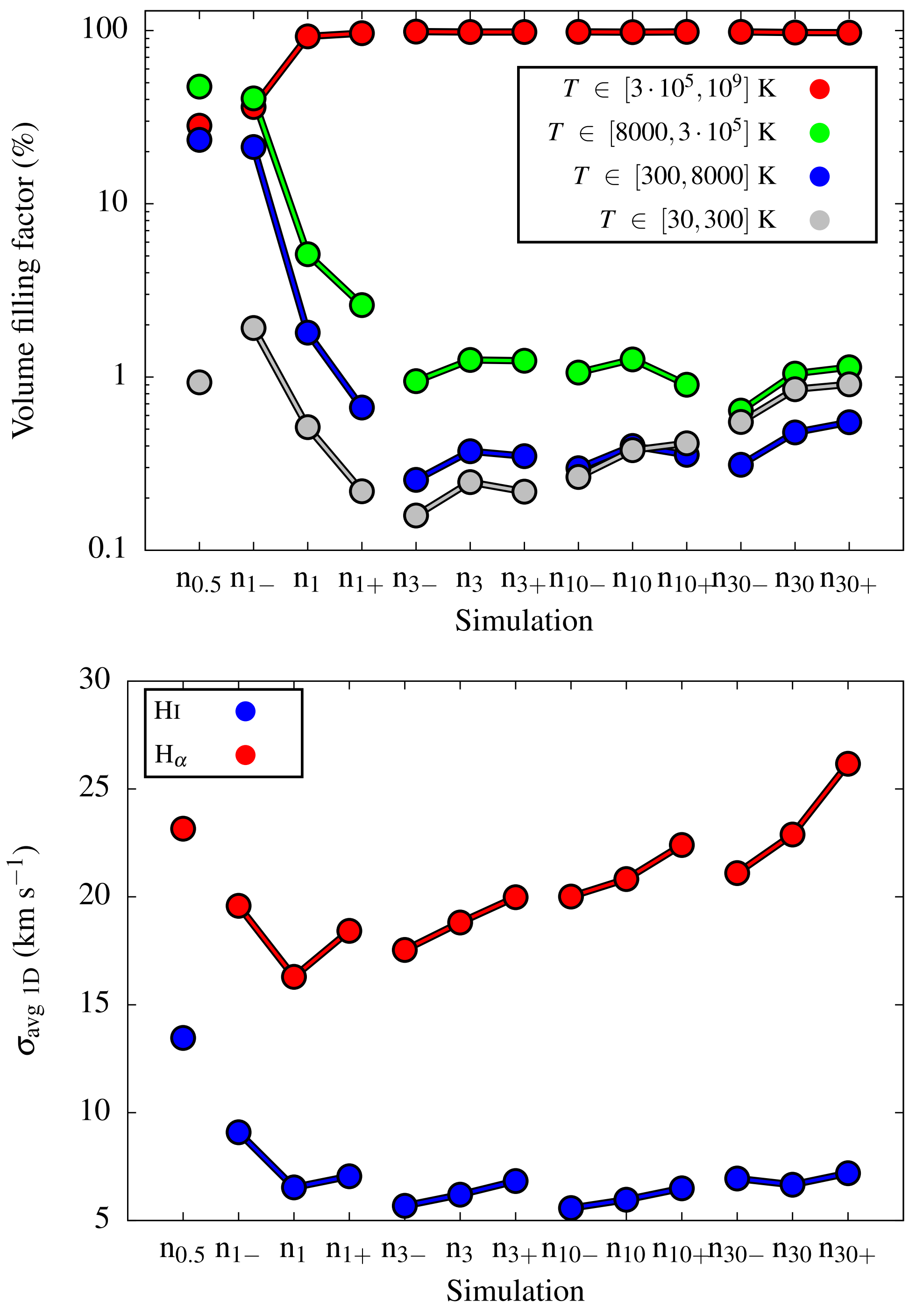

Figure 4.6: *Average mass fractions (first plot), pressures (second plot), VFFs (third plot) and 1D velocity dispersions (fourth plot) with random driving for different initial densities* n_{i} *and SN rates. The index i represents the initial number density, while the + and − signs give the SN rate (*$\dot{N}_{\mathrm{SN},+}$ *and* $\dot{N}_{\mathrm{SN},-}$*). The values are averaged over the last 5 Myr (section 4.2.4). The different lines connect simulations with same* n_{i} *but different SN rate.*

the VFFs close to what we expect for a Milky Way-type galaxy near the mid-plane (e.g. Kalberla & Dedes, 2008; Kalberla & Kerp, 2009), whereas the hot gas fills most of the volume at higher densities and/or SN rates.

We compare the VFFs of the hot ionised medium with the analytic prediction of McKee & Ostriker (1977). The volume occupied by SN remnants at random locations in a uniform medium, f, can be written as

$$f = 1 - e^{-Q} \ , \tag{4.10}$$

with porosity Q defined as

$$Q = 10^{-0.29} E_{51}^{1.28} S_{-13} \bar{n}^{-0.14} \tilde{P}_{04}^{-1.3} \ , \tag{4.11}$$

where E_{51} is the SN energy normalised to 10^{51} erg, S_{-13} is the SN rate in units of 10^{-13} pc^{-3} yr^{-1}, $\bar{n}$ is the number density of the ambient medium in cm^{-3}, and $\tilde{P}_{04} = 10^{-4} P_0 / k_{\rm B}$, with P_0 and $k_{\rm B}$ ambient medium pressure and Boltzmann constant, respectively.

We find a reasonable agreement of the VFF for models R-n$_{0.5}$ and R-n$_{1-}$, where $f \sim 30\%$ - 40%. However, the analytic model predicts lower hot gas VFFs for higher densities and SN rates such than the ones found in our higher SN rate simulations. Since $Q \propto \bar{n}^{1.26} \tilde{P}_{04}^{-1.3}$, f as derived from eq. (4.10) and (4.11) is roughly constant, whereas the simulation shows it increasing towards unity in the thermal runaway regime.

Hi and H$_\alpha$ velocity dispersion: In the fourth plot of Figure 4.6, we show the velocity dispersions in Hi, $\sigma_{\rm avg\ 1D}$(Hi), and H$_\alpha$, $\sigma_{\rm avg\ 1D}({\rm H}_\alpha)$. For $n_{\rm i} \leq 1\,{\rm cm}^{-3}$ and, in particular, for low SN rates ($\dot{N}_{\rm SN} \lesssim 2$ Myr^{-1}), SNe are able to inject the observed level of turbulence in the Hi gas, while $\sigma_{\rm avg\ 1D}$(Hi) $\sim 5 - 7\,{\rm km\,s}^{-1}$ for $n_{\rm i} > 1\,{\rm cm}^{-3}$. Due to the small size of most cold clumps, these values are a mixture of the clump-to-clump velocity dispersion and thermal broadening, rather than being a measure of the disordered motions within these clouds. For the H$_\alpha$ dispersion, we find a similar trend going from SN rates of $\dot{N}_{\rm SN} \lesssim 2$ Myr^{-1} to slightly higher ones. First $\sigma_{\rm avg\ 1D}({\rm H}_\alpha)$ drops from ~ 24 km s^{-1} to ~ 17 km s^{-1}, but then it increases slowly with increasing box density and SN rate and is ~ 26 km s^{-1} for $n_{\rm i} = 30$ cm^{-3} and high SN rates.

4.3.5 Peak driving vs. random driving

We perform simulations using peak driving (runs P-n_i) at the same box densities and SN rates as in the corresponding runs with random driving (see Table 4.2). In Figure 4.7 we show the resulting ISM properties with respect to the random driving case.

CHEMICAL COMPOSITION: The peak driving runs are dominated by atomic rather than molecular gas. The H_2 mass fraction is low for two reasons: (i) the densest peaks are dispersed by SNe and, therefore, H_2 is locally dissociated; and (ii) the strong compressive SN shocks, which are widespread in the case of random driving, are localised in the immediate neighbourhood of the SN for peak driving. The destruction of molecular gas from peak SNe is broadly consistent with the findings of Hennebelle & Iffrig (2014) and Iffrig & Hennebelle (2015), where SNe exploding close to or within star formation sites can disperse cold and dense gas. In addition, the inefficient heating by peak SNe further reduces the small fraction of mass in the form of thermally ionised hydrogen.

GAS PRESSURE: We find lower pressures for peak driving, in particular for the warm and cold gas components. However, the pressure of the hot phase ($T \geq 3 \times 10^5$ K) appears to be significantly higher (by a factor of ~ 10) in case of peak driving at $n_\mathrm{i} \geq 3$ cm^{-3}. This increase has to be interpreted in conjunction with the decreasing VFF of the hot gas at these densities. Since the SNe, which explode in high density environments, are subject to strong radiative cooling, the high pressure reflects the young age of the SN remnants that do contribute to the hot phase.

VOLUME FILLING FRACTIONS: Peak driving does not produce a predominantly hot ISM. Instead, the VFF is highest for the warm and cold atomic phases. In particular for low densities, a non-negligible contribution is also produced by the warm ionised medium, but the VFF of this component decreases with increasing density, similar to the case of random driving. In general, the absence of a significant hot phase reflects the small sphere of influence of each peak SN, whose expansion is stopped early on due to strong radiative cooling.

HI AND H_α VELOCITY DISPERSION: In the case of peak driving, the HI velocity dispersion is slightly higher than for random driving. This is reasonable since the SNe deposit momentum into the cold gas. The velocity dispersion of the warm ionised gas as seen in H_α grows even more significantly up to $50-70$ km s^{-1} for $n_\mathrm{i} \geq 3$ cm^{-3}. As we have seen, the hot and warm ionised gas are found in the earliest stages of the SN remnants, which otherwise cool efficiently. Thus, the apparent high values of the H_α velocity dispersion stem from the integration over a number of isolated, compact, young SN remnants.

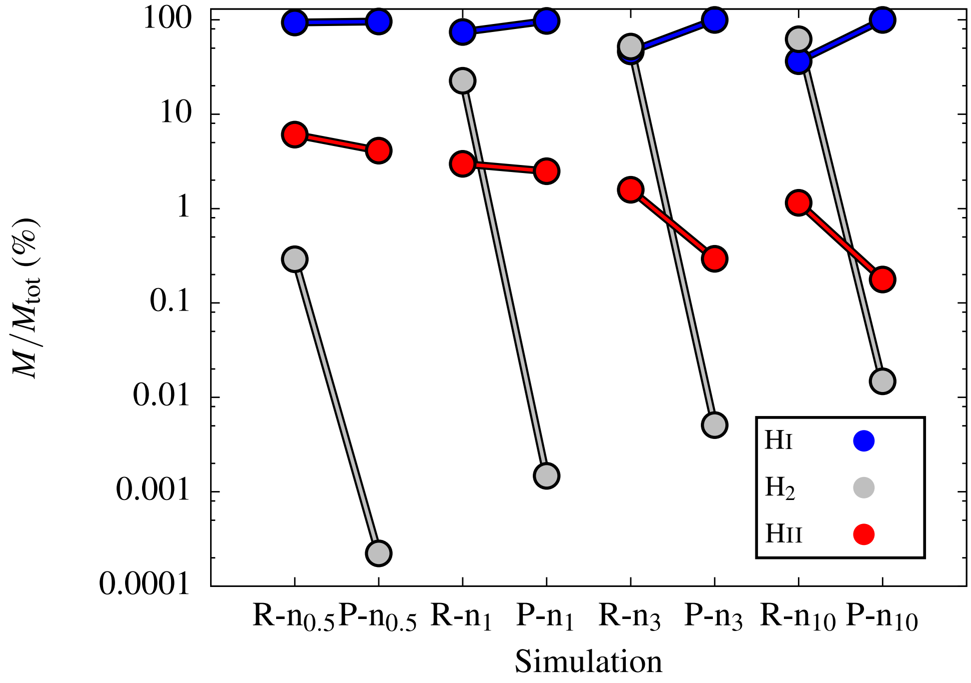
M/M_{tot} (%)
100
10
1
0.1
0.01
0.001
0.0001
R-n$_{0.5}$
P-n$_{0.5}$
R-n$_1$
P-n$_1$
R-n$_3$
P-n$_3$
R-n$_{10}$
P-n$_{10}$
Simulation
HI ●
H_2 ●
HII ●

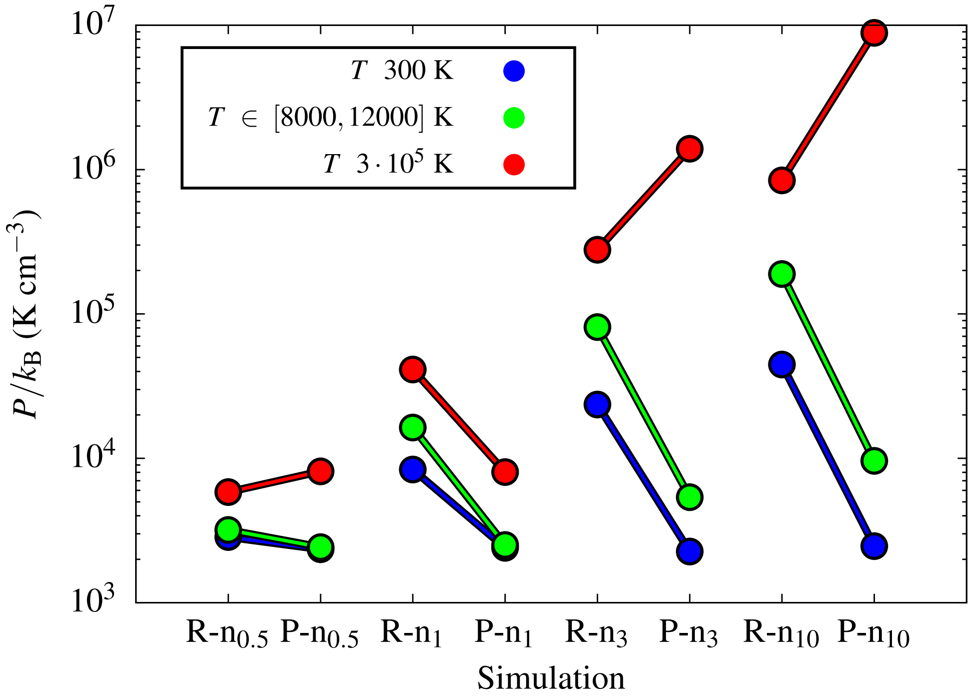
P/k_B (K cm^{-3})
10^7
10^6
10^5
10^4
10^3
T 300 K ●
$T \in [8000, 12000]$ K ●
T $3 \cdot 10^5$ K ●
R-n$_{0.5}$
P-n$_{0.5}$
R-n$_1$
P-n$_1$
R-n$_3$
P-n$_3$
R-n$_{10}$
P-n$_{10}$
Simulation

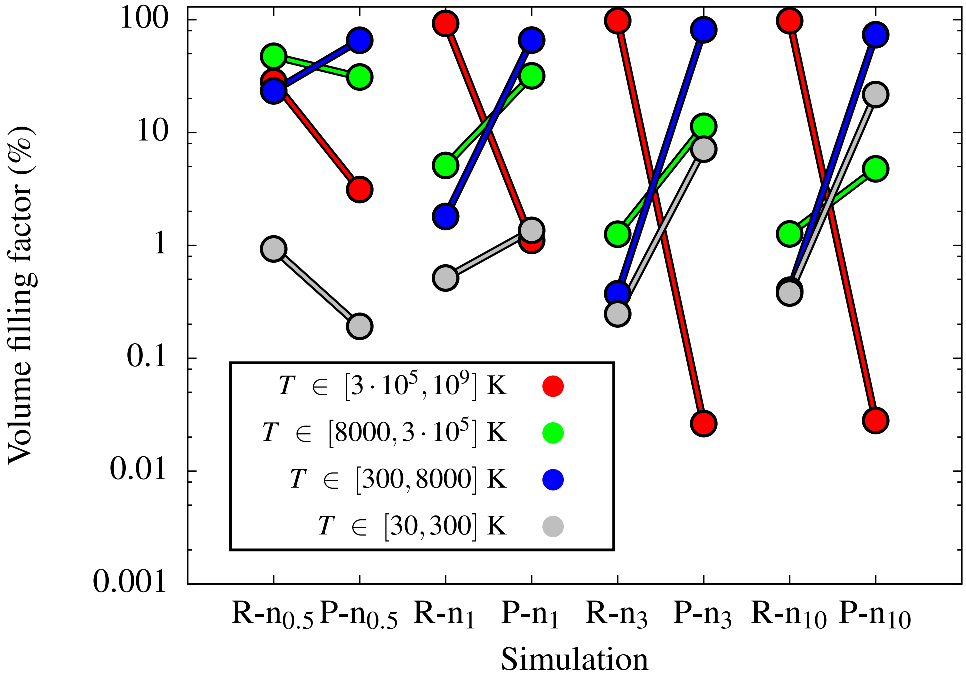

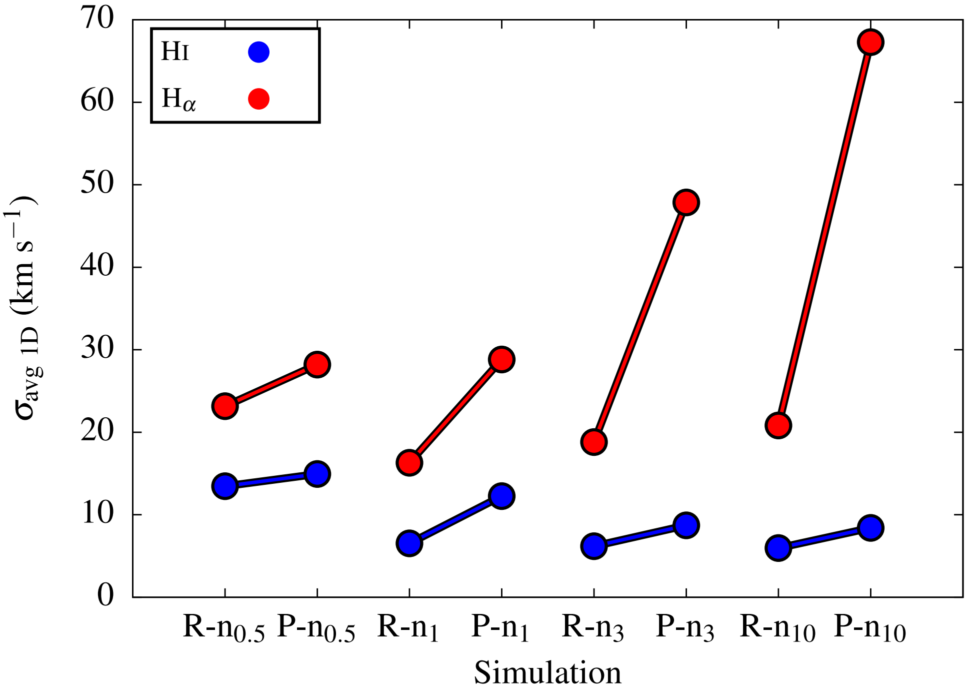

Figure 4.7: *Average mass fractions (first plot), pressures (second plot), VFFs (third plot) and 1D velocity dispersions (fourth plot) with random (R) and peak (P) driving for different initial densities n_i, using the corresponding $\dot{N}_{\mathrm{SN,KS}}$. The lines connect simulations with equal n_i and SN rate but different driving modes (R or P).*

Discussion: Is peak driving realistic?

Figure 4.7 shows that peak driving efficiently disperses cold gas. The SNe which, by choice, explode in the densest environments, are subject to strong radiative cooling. For this reason, peak driving fails to reproduce both the VFF of hot gas and the large molecular gas mass fractions characteristic of the Milky Way (Ferrière, 2001). The absence of hot gas is also inconsistent with the expectation of SNe being responsible for the creation of a hot phase (McKee & Ostriker, 1977).

We can conclude that pure peak driving does not reproduce realistic ISM conditions – probably because we neglect other important physical ingredients, such as clustering and stellar feedback mechanisms, i.e. pre-SN feedback like stellar winds and ionising radiation (Walch et al., 2012). However, one has to be cautious not to over-estimate the effect of radiative cooling due to the finite numerical resolution of our models. Numerical over-cooling acting at the interface between the cold shell and the hot interior of a SN bubble may reduce the amount of hot gas. More importantly, the density and, therefore, the mass within the SN injection region is high in case of peak driving. Since we always inject a SN energy of 10^{51} erg per explosion, the effective temperature within the injection region can drop below 10^6 K in a dense environment. This is an unfavourable temperature regime, the cooling curve is steep and the heated SN gas can be cooled efficiently.

Figure 4.8 shows the approximate initial temperatures (from eq. 3.17) of all SNe in case of $n_\mathrm{i} = 3\,\mathrm{cm}^{-3}$ and $\dot{N}_\mathrm{SN,KS}$ for run R-n_3 with random and run P-n_3 with peak driving. The temperature within the injection region, $T_\mathrm{i,SN}$, depends on the density. Typically, the temperature is $T_\mathrm{i,SN} > 2 \times 10^6$ K in case of random driving. For peak driving we find $T_\mathrm{i,SN} \gtrsim 10^6$ K, and for $\sim$35% of all explosions the temperature is below 10^6 K, leading to immediate strong cooling. For this reason, we explore a combined energy and momentum input model in section 4.3.7.

4.3.6 Mixed driving

Peak and random driving represent two extreme cases of what we expect for the spatial distribution of SNe. To examine intermediate cases, we perform 9 additional simulations with $n_\mathrm{i} = 3\,\mathrm{cm}^{-3}$ and $\dot{N}_\mathrm{SN,KS}$ and different values of f_peak, the fraction of SNe going off in dense gas. Here, $f_\mathrm{peak} = 0\%$ corresponds to random driving and $f_\mathrm{peak} = 100\%$ corresponds to peak driving. In Figure 4.9 we show the mass fractions (first plot), pressures (second plot), VFFs (third plot) and 1D velocity dispersions (fourth plot) as a function of f_peak.

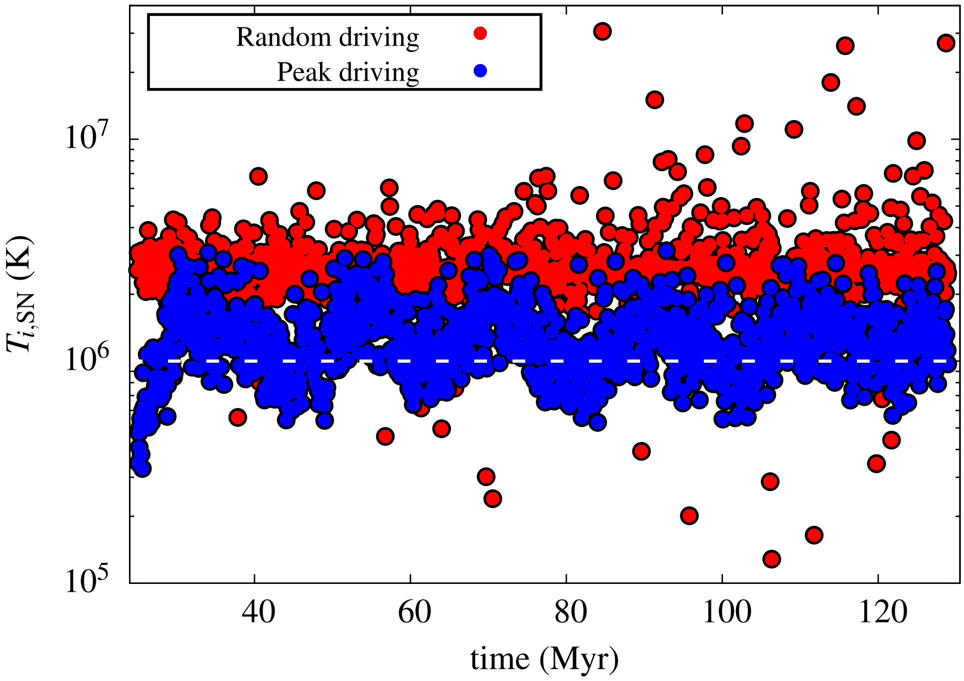

Figure 4.8: *Initial temperature of SNe estimated from equation (3.17) for pure peak and random driving with* $n_\mathrm{i} = 3\,\mathrm{cm}^{-3}$ *and* $\dot{N}_\mathrm{SN,KS}$.

CHEMICAL COMPOSITION: The ratio of atomic to molecular gas has a steep transition at $f_\mathrm{peak} \approx 50\%$. For $f_\mathrm{peak} > 50\%$ the box is HI-dominated, which is typical for an ISM where the coldest component is removed by SN explosions within the dense gas. On the other hand, for $f_\mathrm{peak} < 50\%$, we find large amounts of molecular hydrogen since (i) a smaller f_peak disperses fewer dense clumps, and (ii) the larger number of uncorrelated SNe heat up the gas around the dense and cold medium and compress it (see section 4.3.3).

GAS PRESSURE: We find that all three phases are out of pressure equilibrium, although the pressures of the cold and warm phases decrease with increasing f_peak and these phases become close to isobaric for $f_\mathrm{peak} > 50\%$. However, the hot gas pressure diverges for $f_\mathrm{peak} > 50\%$ as the SN remnants which contribute to this phase become younger and occupy smaller volumes. This has already been discussed for the case of pure peak driving (see section 4.3.5).

VOLUME FILLING FRACTIONS: A sharp transition at $f_\mathrm{peak} \approx 50\%$ can also be found for the VFFs of the different gas phases. For $f_\mathrm{peak} \gtrsim 50\%$, the hot gas VFF drastically decreases while the VFFs of the warm and cold components are increasing. For small $f_\mathrm{peak} < 50\%$ the number of random

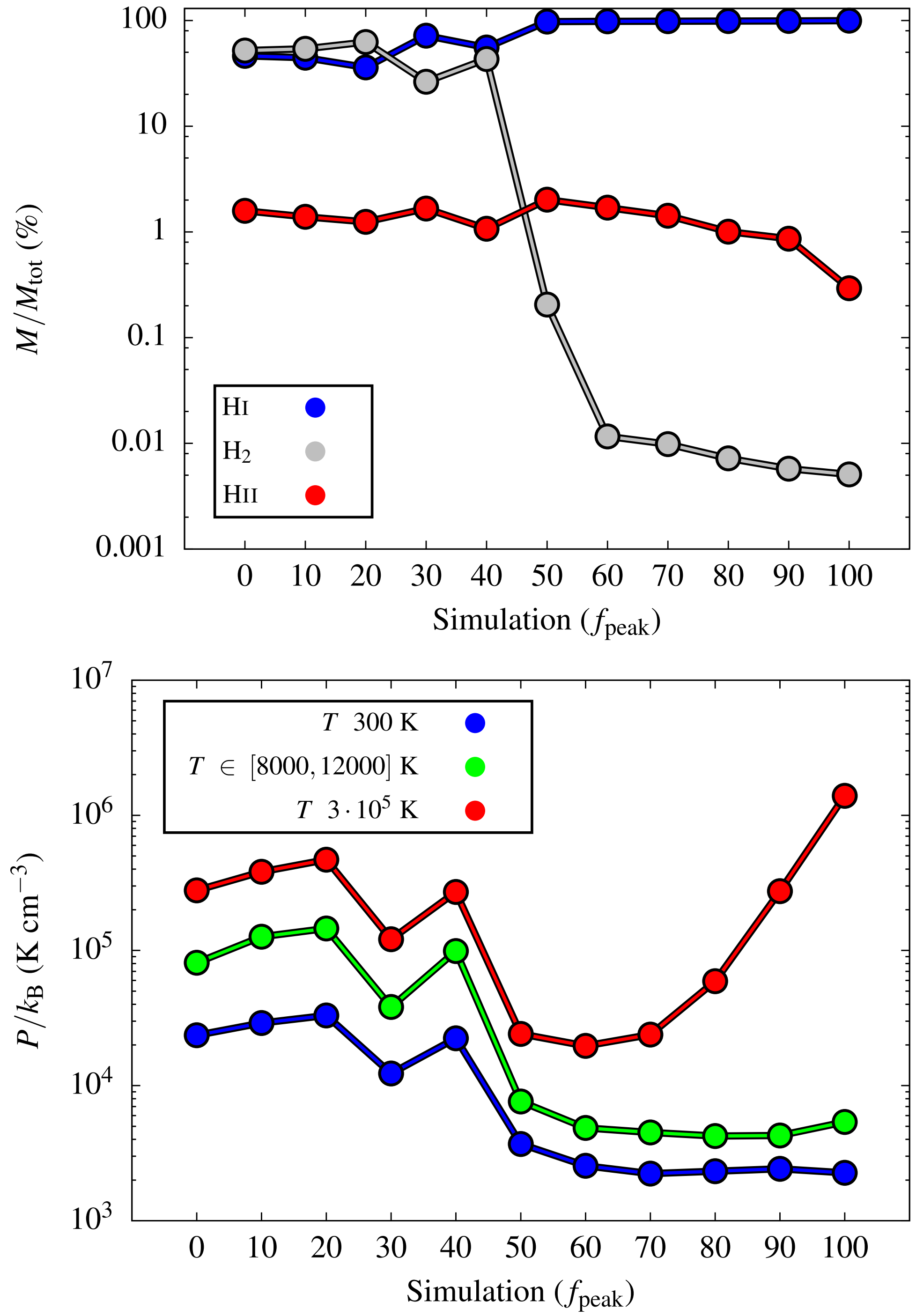
$M/M_{\rm tot}$ (%)
100
10
1
0.1
0.01
0.001
HI ●
H_2 ●
HII ●
0
10
20
30
40
50
60
70
80
90
100
Simulation ($f_{\rm peak}$)
P/k_B (K cm^{-3})
10^7
10^6
10^5
10^4
10^3
T 300 K ●
$T \in [8000, 12000]$ K ●
T $3 \cdot 10^5$ K ●
0
10
20
30
40
50
60
70
80
90
100
Simulation ($f_{\rm peak}$)

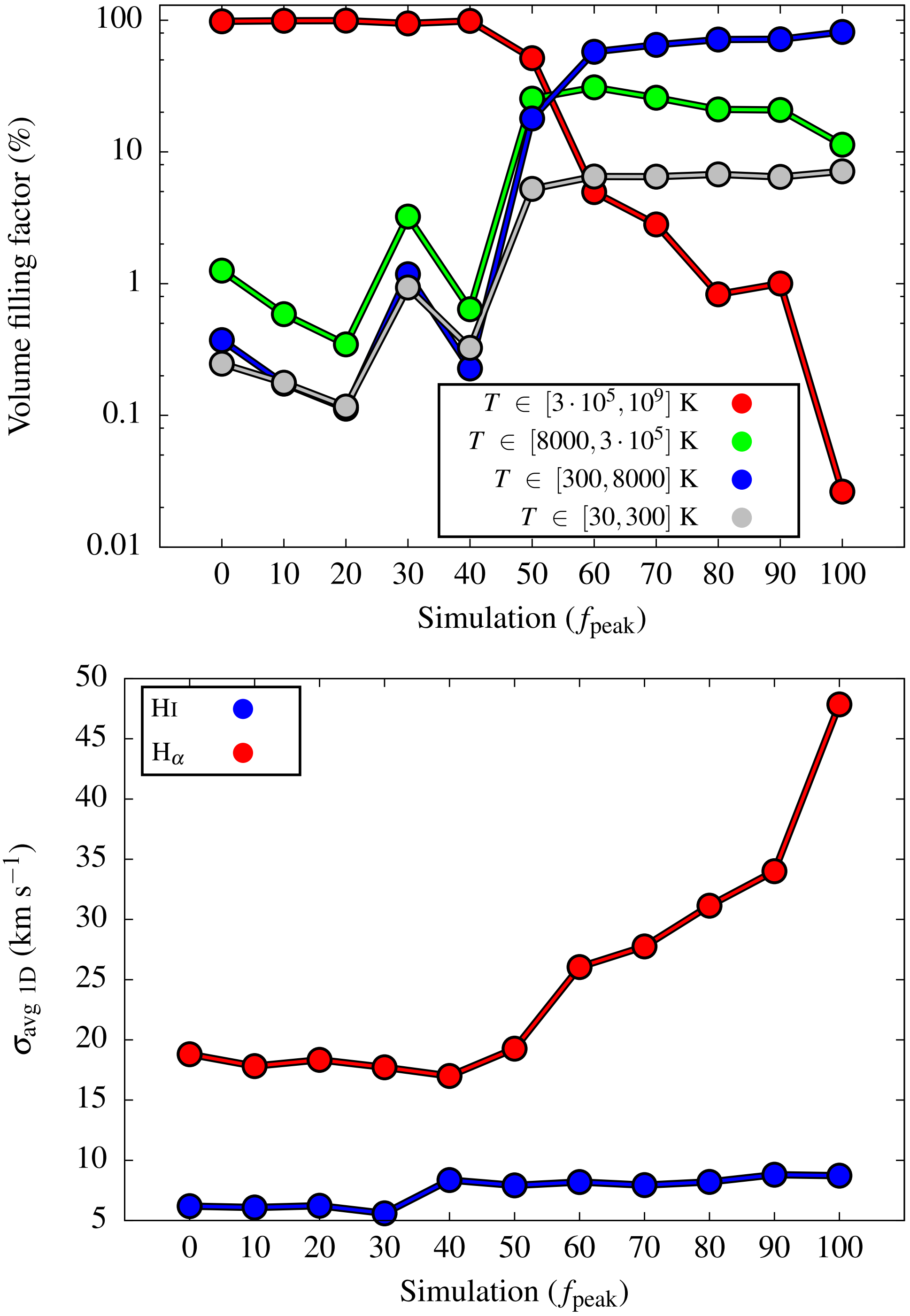

Figure 4.9: *Average mass fractions (first plot), pressures (second plot), VFFs (third plot) and 1D velocity dispersions (fourth plot) as a function of* $f_{\rm peak}$ *for simulations using* $n_{\rm i} = 3\,{\rm cm}^{-3}$ *and* $\dot{N}_{\rm SN,KS}$.

SN explosions is high enough to fill most of the box with hot gas and drive the box towards the thermal runaway regime.

HI AND H_α VELOCITY DISPERSION: With increasing peak fraction, the HI velocity dispersion increases from $\sim 5-6\ \mathrm{km\,s^{-1}}$ to $\sim 8-9\ \mathrm{km\,s^{-1}}$ at $f_{\mathrm{peak}} \approx 40\%$. Also the H_α velocity dispersion increases for $f_{\mathrm{peak}} \gtrsim 40\%$, from $\sim 18\ \mathrm{km\,s^{-1}}$ to $\sim 48\ \mathrm{km\,s^{-1}}$ for $f_{\mathrm{peak}} = 100\%$. For high f_{peak}, most of the H_α-emitting gas comes from young SN remnants (see section 4.3.5).

Discussion: the transition between the peak and random driving regime.

Mixed driving, i.e. a combination of peak and random driving at different ratios, shows a relatively sharp transition in most ISM properties at a critical ratio of $f_{\mathrm{peak,crit}} \approx 50\%$. It is likely that $f_{\mathrm{peak,crit}}$ depends on the box density and SN rates. For instance, we expect $f_{\mathrm{peak,crit}}$ to shift to higher values for higher average densities. It is also likely that $f_{\mathrm{peak,crit}}$ shifts towards lower values if the periodic boundary conditions are relaxed and the box is allowed to 'breathe' (i.e. to adjust to local pressure equilibrium as gas is allowed to escape the box). In this case the thermal runaway can also be delayed, leading to small $f_{\mathrm{peak,crit}}$, or even avoided altogether. Thus, rather than being interested in extrapolating detailed physical conclusions, we are more keen on stressing once again that there are major differences in the properties of the ISM, which results from implementations of either peak or random driving.

4.3.7 Combined thermal energy and momentum injection

Due to our finite numerical resolution, the injection of thermal energy alone might lead to over-cooling in dense regions (see section 4.3.5 and Figure 4.8). Therefore, we introduce a SN model, which allows us to switch from thermal energy to momentum input when the density in the vicinity of the SN is high and the Sedov-Taylor phase is unresolved (see section 3.2). Using two simulations, we discuss how the combined model performs with respect to the thermal energy injection scheme. In particular, we redo run P-n_3, i.e. peak driving at $n_{\mathrm{i}} = 3\,\mathrm{cm^{-3}}$, and run M50-$n_3$, i.e. mixed driving with $f_{\mathrm{peak}} = 50\%$ and $n_{\mathrm{i}} = 3\,\mathrm{cm^{-3}}$. The corresponding new runs, which use the combined model, are called P-C-n_3 and M50-C-n_3.

The comparison between runs with and without momentum input suffers from uncertainties in the resolution of peak SNe with thermal energy injection. If unresolved, these SNe are prone to cool too quickly and the resulting momentum input could be underestimated (see section 3.2 and 4.3.8). On the other hand, the momentum injection method only takes into account the momentum-generating Sedov-Taylor phase and neglects the additional contribution from the pressure-driven snowplough phase (section 3.2). Due to these intrinsic differences, a very detailed comparison is not possible at the moment.

In Figure 4.10 (top) we show that the Sedov-Taylor radius (eq. 3.18) is unresolved, i.e. $R_{\rm ST} < 4\Delta x$ as indicated by the green dashed line, for all SNe in run P-C-n_3 and for 63% of the SNe in M50-C-n_3. In the latter case, the percentage of unresolved SNe being > 50 % reflects the fact that most random SNe explode in a low density environment, but not all of them. For the unresolved SNe, the injected momentum varies between $1-2\times 10^5\,{\rm M}_\odot$ km s^{-1}, as shown in the bottom plot of Figure 4.10. On a side note, if we instead require that the temperature within the injection region is higher than 10^6 K, we find that $R_{\rm ST}$ as given in eq. (3.18) is somewhat conservative and could safely be increased by a factor of ~ 1.6.

In Figure 4.11 we compare the properties of the resulting ISM for runs with pure thermal energy injection and the new combined SN scheme. Here, the lines connect the models with the old and the new combined model.

Chemical composition: For both cases (peak and mixed driving), the two SN injection schemes give comparable mass fractions in all species. There are small differences, but these are well within the statistical fluctuations in the time evolution of each component.

Gas pressure: The main difference between the thermal energy injection and the combined SN injection scheme is that there is no hot gas present in case of the combined model, if all the SNe are using the momentum input scheme. This is the case for run P-C-n$_3$ (see also Fig. 4.10) and therefore we cannot compare the pressures of the hot phase between the two approaches in case of peak driving. If there is a random component (run M50-n$_3$), then the pressures of the hot phase are the same for thermal energy injection and combined model. The reason is that, in case of thermal energy injection, SNe which explode in dense gas cool on short time scales and do not contribute to the hot gas phase.

Furthermore, both mixed and peak driving show a slightly reduced pressure of the warm phase when the combined scheme is applied. For the mixed driving case (run M50-n$_3$), this brings the warm and the cold phase into pressure equilibrium. For the peak driving case (run P-C-n$_3$), the pressure of the warm phase appears to be smaller than the pressure of the cold phase. This is an artefact. Since the young SN bubbles themselves contribute significantly to the warm phase (because we set the temperature within the injection region to 10^4 K when momentum is injected), the warm phase is not formed self-consistently in this simulation. However, the thermal energy injected in this way is between $1-9$ % $E_{\rm SN}$, with the majority of SNe lying in the range $1-5$ %, in very good agreement with Kim & Ostriker (2015), Martizzi et al. (2015) and Walch & Naab (2015).

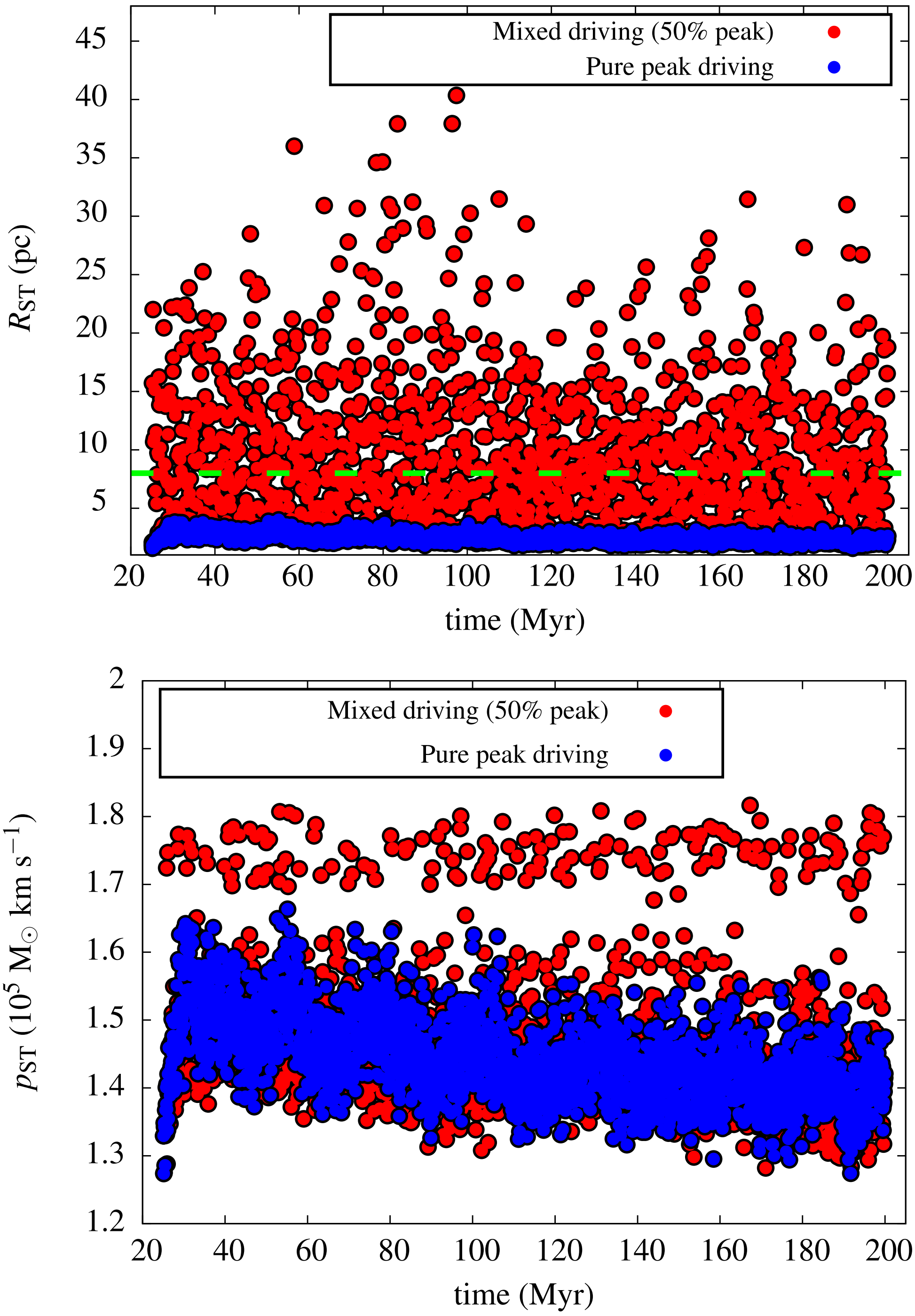

Figure 4.10: *Radius at the end of the Sedov-Taylor phase (eq. 3.18; top) and injected momentum (eq. 3.19; bottom) for runs with pure peak driving (run P-C-n3) and mixed driving with* $f_{\mathrm{peak}} = 50\,\%$ *(run M50-C-n3). The dashed lines shows the resolution limit of* $4\Delta x$*, below which SNe are modelled via momentum input.*

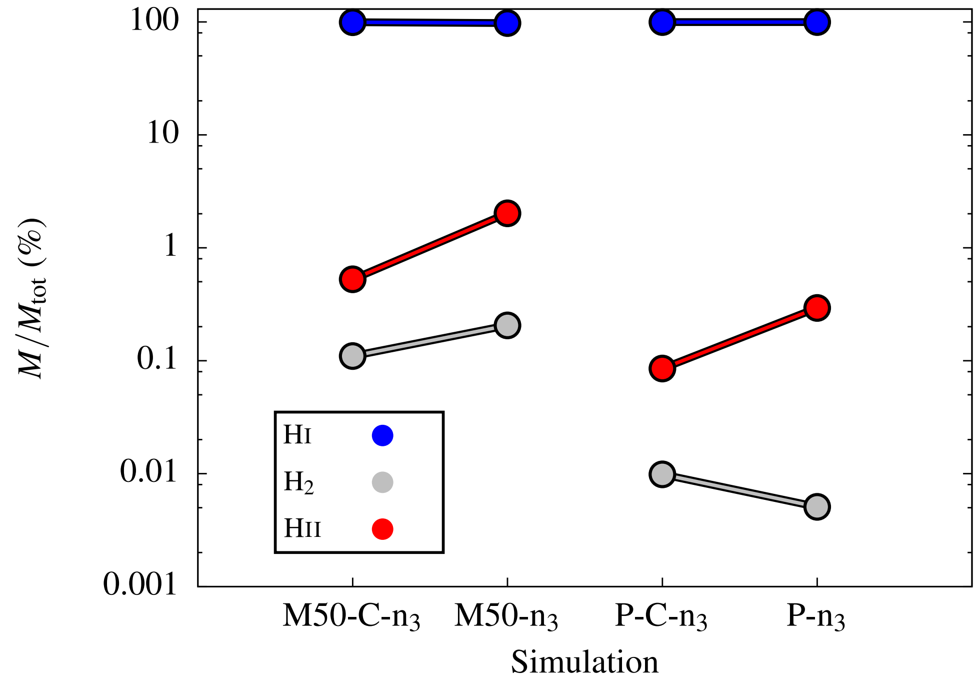
100
10
1
0.1
0.01
0.001
M/M_{tot} (%)
HI ●
H_2 ●
HII ●
M50-C-n_3
M50-n_3
P-C-n_3
P-n_3
Simulation

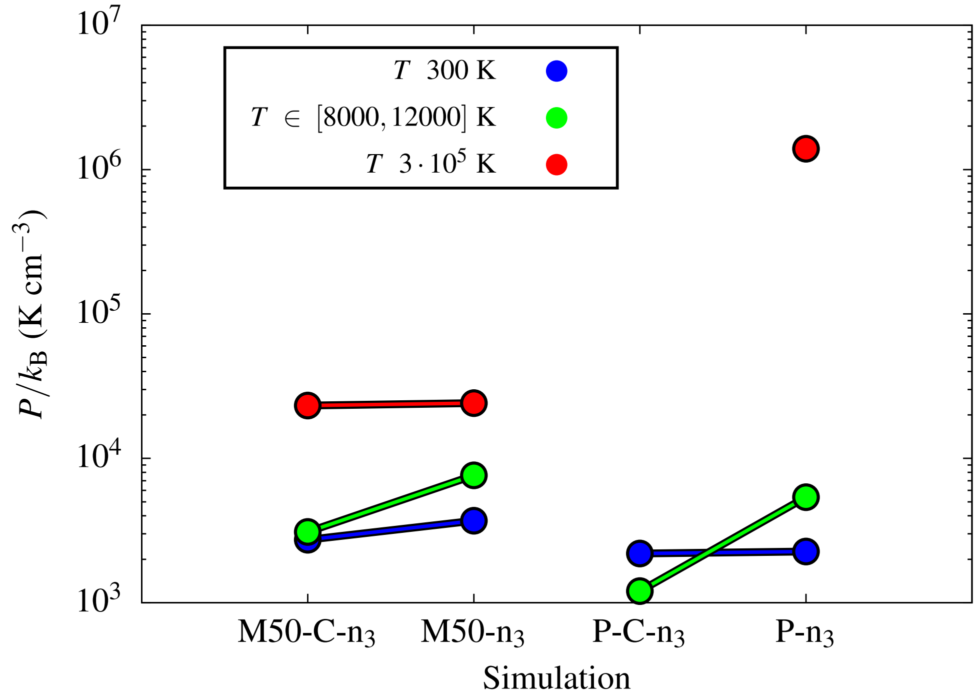
10^7
10^6
10^5
10^4
10^3
P/k_B (K cm^{-3})
T 300 K ●
$T \in [8000, 12000]$ K ●
T $3 \cdot 10^5$ K ●
M50-C-n_3
M50-n_3
P-C-n_3
P-n_3
Simulation

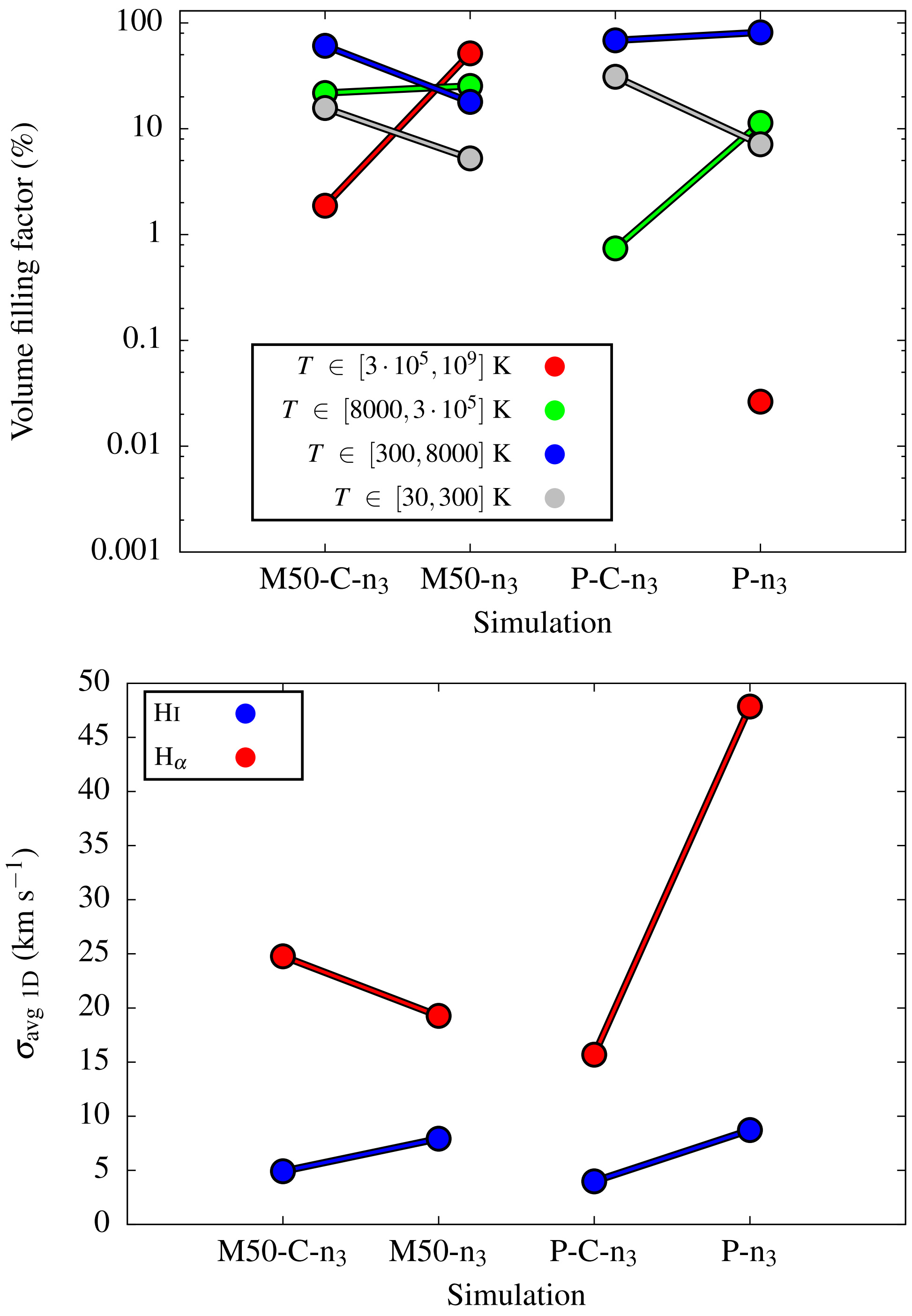

Figure 4.11: *Average mass fractions (first plot), pressures (second plot), VFFs (third plot) and 1D velocity dispersions (fourth plot) for the momentum input simulations with* $n_\mathrm{i} = 3\,\mathrm{cm}^{-3}$ *and* $\dot{N}_\mathrm{SN,KS}$. *The points are: mixed driving with 50% peak with combined thermal and momentum injection (M50-C-n*$_3$*); mixed driving with 50% peak with thermal energy injection (M50-n*$_3$*); pure peak driving with combined injection (P-C-n*$_3$*); pure peak driving with thermal energy injection (P-n*$_3$*). The values are the average over the last 5 Myr of each simulation. The different lines connect simulations with same* n_i*, SN rates, and driving modes, but different injection methods.*

Volume Filling Fractions: The VFFs of the cold gas increase when using the momentum input scheme, which is more efficient in dispersing dense gas than the thermal injection method. As described above, the hot phase is missing or negligible when modelling SNe with momentum injection.

Hi and H_α velocity dispersion: The derived one dimensional Hi velocity dispersion is slightly lower for the combined model. The H_α emission is sensitive to the actual physical state of the warm component. Setting an upper temperature value of 10^4 K within the SN remnants strongly influences the derived H_α velocity dispersion. We do not recommend to trust the H_α velocity dispersion if the thermal state of the gas within the injection region has not been derived in a self-consistent way.

4.3.8 Higher resolution

As an alternative one may avoid having $T_{\mathrm{i,SN}} < 10^6$ K in the SN injection region by going to a higher numerical resolution. We run two additional simulations with resolution $\Delta x = 1$ pc with pure peak and random driving (with pure thermal injection) for our fiducial setup ($n_{\mathrm{i}} = 3\,\mathrm{cm}^{-3}$ and $\dot{N}_{\mathrm{SN,KS}}$). For peak driving, this increase of a factor of two in resolution shifts the fraction of SNe having an estimated $T_{\mathrm{i,SN}} > 10^6$ K from 65% to 96%, while for random driving this value is close to unity in both cases.

In Figure 4.12 we compare the mass-weighted density PDFs for the fiducial and high resolution simulations for random (top) and peak driving (bottom). We plot the mass-weighted PDF as this emphasises differences in the high density regime, which is most critical. The density PDFs also show good convergence between fiducial and higher resolution, with an increase in density of rather less than a factor of two.

Kim & Ostriker (2015) show that the conditions $R_{\mathrm{ST}} > 3\ \Delta x$ and $R_{\mathrm{ST}} > 3\ R_{\mathrm{inj}}$ should be satisfied in order to recover a final momentum close to the values retrieved from their high resolution, sub-pc simulations. Combining these criteria and having assumed $R_{\mathrm{inj}} \geqslant 4\ \Delta x$ (eq. 3.12), their requirements can be translated into $R_{\mathrm{ST}} > 12\ \Delta x$. This slightly differs from our criterion, where $R_{\mathrm{ST}} \geqslant R_{\mathrm{inj}} > 3\ \Delta x$. From eq. (3.18) (but see also section 4.3.7) $R_{\mathrm{ST}} \approx 30.6\ n^{-0.4}$ pc. Therefore one can show that the critical density of the injection region (ambient medium) below which a SN is considered to be resolved is $n_{\mathrm{crit}} \approx 2\,\mathrm{cm}^{-3}$ from the Kim & Ostriker (2015) criteria and $n_{\mathrm{crit}} \approx 59\,\mathrm{cm}^{-3}$ from ours at our fiducial resolution of 2 pc. For $\Delta x = 1$ pc, $n_{\mathrm{crit}} \approx 10\,\mathrm{cm}^{-3}$ from Kim & Ostriker (2015) and $n_{\mathrm{crit}} \approx 330\,\mathrm{cm}^{-3}$ for us. For an initial density of $3\,\mathrm{cm}^{-3}$, the highest densities reached are $n \sim 100 - 500\,\mathrm{cm}^{-3}$ (see Fig. 4.12, bottom) and, hence, only a fraction of SNe in the high resolution run can be considered to be resolved. At fiducial

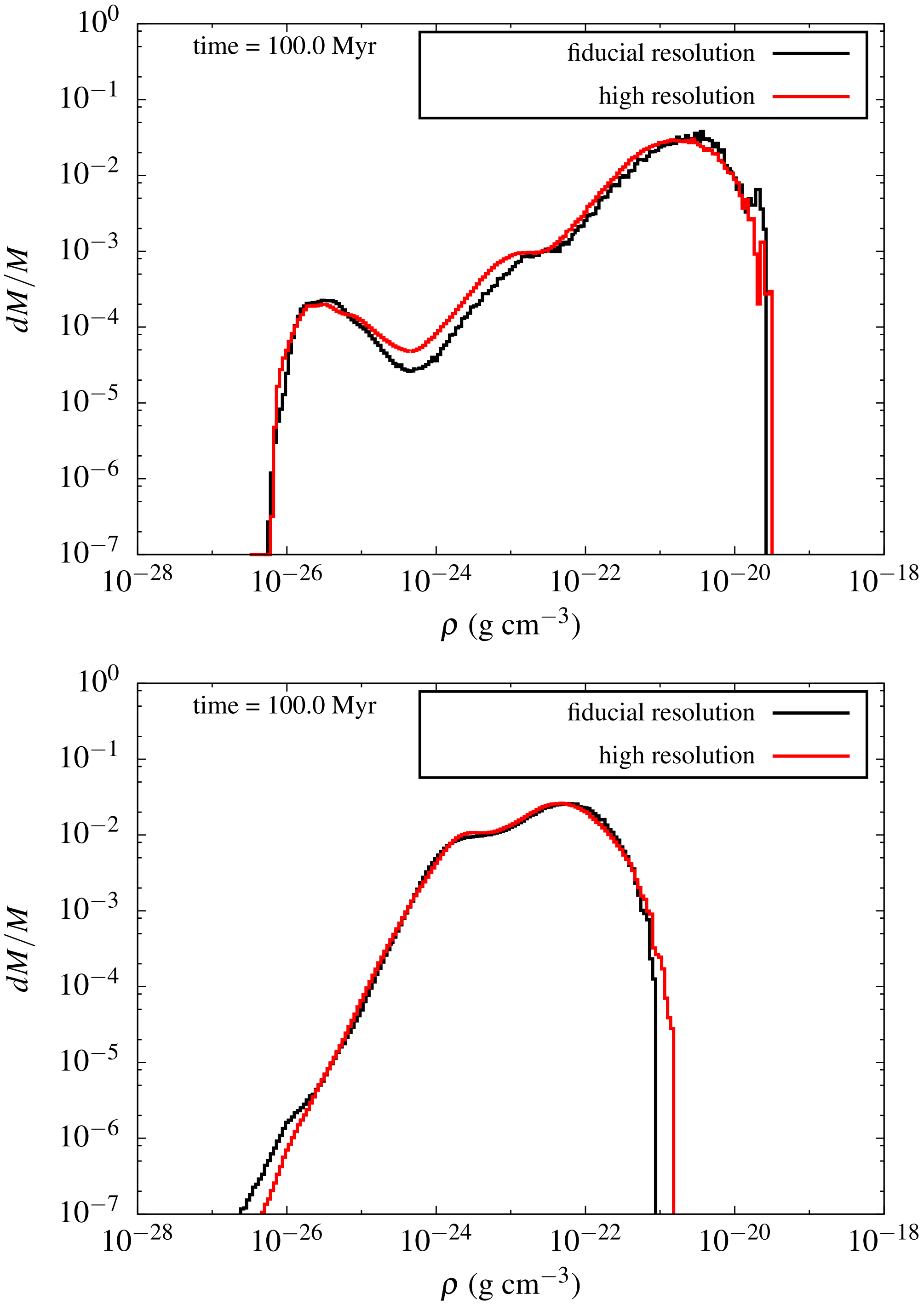

Figure 4.12: *Mass-weighted density PDFs for random (top, runs R-*n_3 *and R-HR-*n_3*) and peak driving (bottom, runs P-*n_3 *and P-HR-*n_3*) for simulations with* $\Delta x = 2$ *pc (fiducial resolution) or 1 pc (higher resolution), and our fiducial parameters* $n_\mathrm{i} = 3\,\mathrm{cm}^{-3}$ *and* $\dot{N}_\mathrm{SN,KS}$.

resolution both ours and Kim & Ostriker (2015) conditions reveal that all of the SNe are not resolved (see also top plot of Fig. 4.10). Therefore, simulations with peak driving and thermal injection with initial density $n_\mathrm{i} \geqslant 3\,\mathrm{cm}^{-3}$ suffer from an underestimate of the momentum input by SNe and hence should be considered representative of a lower limit of the impact of peak SNe.

4.4 Conclusions

SUMMARY: We perform 3D hydrodynamic simulations to study the SN-driven ISM in periodic volumes of size (256 pc)^3. We include radiative cooling and diffuse heating, shielding from dust, and molecular gas (self-)shielding, as well as a chemical network to follow HI, HII, H_2, CO and CII. We study media with different mean gas densities, $n_\mathrm{i} = 0.5,\ 1,\ 3,\ 10,$ and $30\ \mathrm{cm}^{-3}$, which, integrated over the box side, correspond to surface densities of $\Sigma_\mathrm{gas} \approx 4,\ 8,\ 24,\ 81,$ and $243\ \mathrm{M}_\odot \mathrm{pc}^{-2}$. After an initial phase of turbulent stirring at root-mean-square velocity of $10\,\mathrm{km\,s}^{-1}$ for one crossing time (25 Myr), we switch to supernova driving and follow the simulations for more than three additional crossing times.

The SN rates are constant for each simulation, but change with the mean box density according to the Kennicutt-Schmidt relation. We additionally perform models with a factor of two higher and lower SN rates. We explore the impact of the placement of the SNe relative to the dense gas. We distinguish between random positions (random driving), positioning on local density peaks (peak driving), and a mixture of the two (mixed driving). The different SN placements should reflect that SNe could explode (i) mostly in their birthplaces, where they might be deeply embedded (peak driving); (ii) preferentially in low density environments (random driving). Random driving provides a simple way to introduce SNe in evolved, low density environments without including all the necessary extra physics (wind and ionisation feedback from massive stars; clustering of massive stars; runaway stars) acting in between the point of star formation and the SN explosion. For mixed driving, we perform a set of simulations where we explore different ratios of peak to random driving using the fiducial setup ($n_\mathrm{i} = 3\ \mathrm{cm}^{-3}$ and $\dot{N}_\mathrm{SN,KS}$).

RANDOM DRIVING AT DIFFERENT SUPERNOVA RATES: In the case of random driving, most of the mass is in cold, dense atomic and molecular hydrogen, whereas most of the volume is filled with hot, rarefied gas. The ISM is out of pressure equilibrium in all simulations apart from two cases with lowest density and lowest SN rate. The synthetically observed 1D velocity dispersions are $\sim 5-7\ \mathrm{km\,s^{-1}}$ in HI and $\sim 17-25\ \mathrm{km\,s^{-1}}$ in H_α. Increasing the SN rate by a factor of two leads to an increase in the mean gas pressure of the different phases (cold, warm, hot medium), a small increase in the velocity dispersion ($\sim$ few $\mathrm{km\,s^{-1}}$), and higher HI mass fractions, while the H_2 mass fractions decrease. However, the volume is always completely filled with hot gas, unless we consider low densities ($n_\mathrm{i} \leq 1\ \mathrm{cm}^{-3}$) and SN rates of $\dot{N}_\mathrm{SN} \lesssim 2\ \mathrm{Myr}^{-1}$. We attribute this behaviour to a thermal runaway process (see section 4.3.3), which occurs at high pressures, where only the cold branch of the equilibrium cooling curve can be reached, and no two-phase medium can form. In our case, though, the pressures are artificially determined. The boxes are not allowed to reach hydrostatic equilibrium to a larger galactic potential, so the SNe continuously feed energy into the high-pressure, hot medium. Thus, they can push almost all of the gas mass into small, molecular clumps that quickly form molecular hydrogen.

Peak and mixed driving: For peak instead of random driving, the ISM has a completely different structure. It is dominated by a filamentary distribution of warm gas (mostly HI), with little to no hot gas present. SNe that explode in dense gas also disperse the cold medium, and therefore the mass fraction of molecular hydrogen is small. The absence of hot gas (volume filling fraction VFF $\ll 50\%$) is due to the low heating efficiency and strong cooling of the SNe, which interact with dense gas. However, due to our limited resolution, we note that the impact of peak SNe is probably underestimated in high density regions (for $n > 1 - 60\,\mathrm{cm}^{-3}$ with fiducial and $n > 10 - 300\,\mathrm{cm}^{-3}$ with high resolution). In these cases, one should anyway expand the model to include other important physical conditions and processes, such as stellar clustering, stellar winds, and ionising radiation, and non-constant SN rate are critical ingredients, that shape the ISM and have to be taken into account.

For the setup with $n_\mathrm{i} = 3\ \mathrm{cm}^{-3}$ and $\dot{N}_\mathrm{SN,KS}$, we vary the fraction of peak driving to random driving to explore the effect of a mixed SN placement at different fractions f_peak. A relatively sharp transition between the two regimes (peak and random) occurs when $\sim$50% of the SN are located within density peaks. As f_peak increases, the mass fraction in H_2 drops, and the VFF of the warm and cold gas decreases. Interestingly, we find that the pressure of the hot phase as well as the velocity dispersion in H_α increase with increasing peak fraction ($\mathrm{H}_\alpha \sim 50\ \mathrm{km\,s^{-1}}$ for 100% peak driving). This behaviour can be attributed to the younger age of the SN remnants that contribute to these quantities.

Combined energy and momentum input: In low density gas, the SNe are well resolved and we model them with thermal energy input. Explosions within high density regions are eventually unresolved and would be subject to strong radiative (over-)cooling. Therefore, we introduce a new model, which combines thermal energy input for resolved SNe and momentum input for unresolved SNe. The momentum input at the end of the Sedov-Taylor phase is calculated using the relations derived in Blondin et al. (1998). We put the model to work in two of the simulations (peak driving and mixed driving at $f_{\mathrm{peak}} = 50\%$). We find that the momentum input model fails to produce any hot gas because the shock speeds are too small to heat the medium to more than 10^4 K. Otherwise, the combined model gives similar results to the thermal energy injection model and is therefore a viable alternative to model SN in partly unresolved environments – with the limitation that the temperature structure of the gas is no longer self-consistent.

CLUMPY H_2 IN GAS-RICH DISCS: When thermal runaway sets in, hot gas at high pressure pushes the gas into small and dense clouds, leading to a fast and efficient conversion from HI to H_2. Warm gas directly cools towards the cold branch of the equilibrium curve and, similar to the case of a high far-UV interstellar radiation field, a bi-stable equilibrium between the cold and warm phases does not exist anymore. We speculate that the molecular-dominated, very clumpy structure of the ISM in simulations with a high gas surface density $\Sigma_{\mathrm{gas}} \gtrsim 100$ $\mathrm{M}_\odot$ pc^{-2} could be a reasonable representation of systems with high gas surface densities and very high mid-plane pressures like ULIRGs (Downes & Solomon, 1998, but see also Rosolowsky & Blitz 2005) or normal star forming galaxies at high redshift (Genzel et al., 2010) that have high gas fractions and SFRs (e.g. Tacconi et al., 2010, 2013). Their mid-plane pressures are three to four orders of magnitudes higher than for the Milky Way (Bowyer et al., 1995; Berghöfer et al., 1998; Jenkins & Tripp, 2011) and plausibly reach values of $P/k_{\mathrm{B}} \sim 10^{6-7}\ \mathrm{K\,cm^{-3}}$ for surface densities of 100 $\mathrm{M}_\odot$ pc^{-2} and above (Swinbank et al., 2011), very similar to our models for $n_{\mathrm{i}} = 10$ or $30\,\mathrm{cm}^{-3}$ with random driving. Such high mid-plane pressure forces all the gas onto the cold branch of the equilibrium curve, so that it reaches densities that allow quick conversion from atomic to molecular gas. Thus, in high pressure, gas rich environments, the sizes and masses of the collapsing and H_2 forming structures could be regulated by supernova feedback. Our simulations show that the mass budget of the ISM can be dominated by molecular gas while, at the same time, this molecular gas is still found in small dense clumps with low filling factor surrounded by hot rarefied gas, rather than being evenly distributed. However, this picture needs to be refined with simulations of stratified, high-surface density discs (similar to Shetty & Ostriker, 2012) and a more self-consistent treatment of star formation to address the issue of self-regulation in gas-rich environments. On the other hand, for low $\Sigma_{\rm gas} \sim 5$ M$_\odot$ pc^{-2}, where the ISM has reasonable pressures and VFFs, we find too little molecular gas. Here we are probably missing the aid of self-gravity.

LIMITATIONS OF THE MODEL: For peak driving, the limited resolution employed raises concerns about the effectiveness of density peak SNe. Recent results from Kim & Ostriker (2015) suggest that our models with pure thermal injection should be considered to be lower limits on the impact of peak driving on the ISM. For random SNe, in particular for intermediate $\Sigma_{\rm gas} \sim 10 - 100$ M$_\odot$ pc^{-2}, the creation of high pressure, high VFF, hot gas in the random driving case is overestimated due to our choice of periodic boundary conditions in all three dimensions. In a stratified disc, these high pressures would power a galactic fountain or outflow, lowering the ambient pressure in the mid-plane to the hydrostatic equilibrium value within a crossing time (few dozens of Myr) of a scale height for the hot gas. Other key physical ingredients, such as ionising radiation, stellar winds, and stellar clustering, etc. could also play a crucial role in determining the state of the multi-phase ISM. For these reasons, the employment of the simplified setup presented here does not allow us to draw any quantitative conclusions. However, this kind of study clearly shows the qualitative consequences of each model.

CHAPTER 5

Regulation of star formation by stellar winds and supernovae

5.1 Motivations and goals

A great deal of effort has been spent over the past decades on studying the interplay between massive stars and the ISM. Cosmological simulations employing SN feedback alone or a combination of different feedback mechanisms have emphasised the fundamental role of massive stars in regulating the otherwise over-efficient star formation process (e.g. Agertz et al., 2013; Hopkins et al., 2014). These simulations, however, suffer from limited spatial and/or mass resolution and fail to capture the detailed physics which governs the ISM on small and intermediate scales.

To overcome this problem, many authors have focused their attention on the study of the ISM using grid-based, 3D, MHD simulations of a representative piece of an isolated, stratified galactic disc, mainly investigating the impact of SN explosions on the three-phase ISM with or without the employment of self-gravity (e.g. de Avillez & Breitschwerdt, 2007; Joung & Mac Low, 2006; Hill et al., 2012; Shetty & Ostriker, 2012; Gent et al., 2013; Kim et al., 2013).

In a recent paper, Walch et al. (2015) study the impact of the assumed position of SN explosions driven at a fixed rate on a section of a galactic disc using a chemical network to model H_2 formation (see also previous chapter). They show that SNe located at random positions help self-gravity in driving the formation of molecular hydrogen in filaments and clumps. On the other hand, SNe positioned at density maxima have a much smaller heating efficiency and produce lower H_2 mass fractions, as well as no outflows from the disc (Girichidis et al., 2015). As a result, non-clustered density peak SNe modelled without the inclusion of earlier feedback mechanisms, such as ionising radiation and stellar winds, fail in reproducing the observed properties of the ISM (see also Gatto et al., 2015).

These previous studies, however, drive SNe at a fixed rate and lack a self-consistent treatment of star formation, i.e. the employment of sink particles (Bate et al., 1995). A step further in this regard has been taken by Hennebelle & Iffrig (2014), who use MHD simulations of a $(1\ \mathrm{kpc})^3$ slice of a galactic disc including sink particles (but see also Slyz et al., 2005, for a similar study in an unstratified periodic box). They model SN feedback correlated in space and time with sink particles' position and accretion and show that explosions from massive stars can significantly lower the SFR by a factor of 20-30. These values, however, are likely upper limits due to the lack of a time delay between the formation and the explosion of massive stars.

Given these previous results, a more detailed modelling of the physics that regulates the cycling between massive stars and ISM is needed. In this chapter, we improve on these earlier works by studying the mutual influence of the three-phase ISM, star formation, and feedback. We pursue 3D MHD simulations of a representative piece of a galactic disc including diffuse heating and radiative cooling, an external static stellar potential and self-gravity, magnetic fields, self-consistent star formation via sink particles and stellar feedback in the form of stellar winds and SNe. We take into account dust and gas (self-)shielding and we model the formation, evolution and destruction of $\mathrm{H}, \mathrm{H}^+, \mathrm{H}_2, \mathrm{CO}, \mathrm{C}^+$ via a chemical network. We use a sub-grid prescription that allows us to model the formation and evolution of massive stars within sink particles. We follow the complete evolution of each single massive star and inject the corresponding feedback using the latest Geneva stellar evolution tracks by Ekström et al. (2012). We compare the relative impact of magnetic fields, stellar winds and SNe on the multi-phase ISM.

5.2 Method

We simulate an elongated volume of $(500\,\mathrm{pc})^2$ in the x and y directions and $\pm\ 5\,\mathrm{kpc}$ in z. We adopt periodic boundary conditions for x and y and outflow boundary conditions in the z direction. The resolution varies between $\Delta x \simeq 7.8\,\mathrm{pc}$ at high altitudes and $\Delta x \simeq 3.9\,\mathrm{pc}$ close to the mid-plane (see section 5.2.1).

We include (see chapter 3):

- an external, static stellar potential;

- self-gravity;
- diffuse heating and radiative cooling, including non-equilibrium effects;
- dust and gas (self-)shielding;
- a chemical network to follow the distributions of $\mathrm{H}, \mathrm{H}^+, \mathrm{H}_2, \mathrm{CO}, \mathrm{C}^+$;
- magnetic fields;
- sink particles;
- a sub-grid prescription that models the formation and evolution of massive stars using stellar tracks; and
- stellar winds and SN feedback from sink particles.

We do not employ any radiation transport scheme, so we do not model the impact of ionising radiation from massive stars on the ISM. We will include this effect in future studies. We do, however, model the effect of the interstellar radiation field in our heating and cooling prescriptions, approximating it as a homogeneous, static, diffuse field without coupling in space and time with massive stars produced in our simulations.

5.2.1 Simulation setup

List of simulations

We perform nine simulations with different combinations of star formation efficiencies and stellar feedback, with or without magnetic fields. Simulations are stopped at 80 Myr (without magnetic fields) or 88 Myr (with magnetic fields), i.e. after 71 Myr of star formation and feedback activity. After this time, the simulation that produces the largest amount of outflowing gas starts to lose significant mass at the $z = \pm 5\,\mathrm{kpc}$ boundaries, and any comparison with runs without or with smaller mass-loss would be affected by such a difference. We run one simulation with $\epsilon_{\mathrm{SF}} = 1$ and no magnetic fields and without any feedback from sink particles, run e100-NoF-NoMag. We compare this run with other non-magnetic simulations with $\epsilon_{\mathrm{SF}} = 1$, where we permute the feedback processes from sink particles. Run e100-WSN-NoMag includes both stellar winds and SN explosions, while runs e100-W-NoMag and e100-SN-NoMag include exclusively stellar winds and SNe, respectively. In e100-WSN-Mag3 we study the effect of magnetic fields by running one simulation with $\epsilon_{\mathrm{SF}} = 1$, an initial magnetic field of

Name	$\epsilon_{\rm SF}$	Stellar winds	Supernovae	Magnetic field	Notes
e100-NoF-NoMag	1	no	no	no	
e100-SN-NoMag	1	no	yes	no	
e100-W-NoMag	1	yes	no	no	
e100-WSN-NoMag	1	yes	yes	no	
e100-WSN-Mag3	1	yes	yes	yes	$B_{0,\rm x} = 3$ μG, $B_{0,\rm y} = B_{0,\rm z} = 0$ μG
e10-NoF-NoMag	0.1	no	no	no	from run e100-NoF-NoMag with $\epsilon_{\rm SF} = 0.1$
e10-SN-NoMag	0.1	no	yes	no	
e10-WSN-NoMag	0.1	yes	yes	no	
e10-WSN-Mag3	0.1	yes	yes	yes	$B_{0,\rm x} = 3$ μG, $B_{0,\rm y} = B_{0,\rm z} = 0$ μG

Table 5.1: *List of simulations performed. The first column shows the name of simulation, as used in the text. The other columns show the main features of each run, from the star formation efficiency to the employment of stellar winds and SNe from sink particles to the inclusion of magnetic fields.*

3 μG and including both stellar winds and SNe. We also run the same simulations assuming $\epsilon_{\mathrm{SF}} = 0.1$ (e10-SN-NoMag, e10-WSN-NoMag, e10-WSN-Mag3) excluding the model with only winds and without feedback. Note that for run e10-NoF-NoMag, we do not perform a new simulation, but instead simply reanalyze the results of run e100-NoF-NoMag with ϵ_{SF} set to 0.1. Table 5.1 lists all the simulations performed and their main features.

Initial conditions

We set the initial density field as uniform in x and y and with a Gaussian distribution in the z-direction

$$\rho(z) = \rho_0 \exp\left[-\left(\frac{z}{2z_0}\right)^2\right] , \tag{5.1}$$

with scale height $z_0 = 30\,\mathrm{pc}$. In order to recover an initial gas mass surface density of $\Sigma_{\mathrm{gas}} = 10\,\mathrm{M}_{\odot}\ \mathrm{pc}^{-2}$, we set the density in the mid-plane to $\rho_0 = 9 \times 10^{-24}$ g cm^{-3} and we truncate the distribution when its density reaches the chosen background density of $\rho_{\mathrm{bg}} = 10^{-28}$ g cm^{-3}. The disc is initially at rest, with temperature $T = 4500$ K, and it is set to be fully atomic. The hot halo gas is assumed to be in pressure equilibrium with the gas within the disc. For simulations with magnetic fields, we scale the x-component of $\mathbf{B}$ in the z-direction as

$$B_{\mathrm{x}}(z) = B_{0,\mathrm{x}} \left[\frac{\rho(z)}{\rho_0}\right]^{\frac{1}{2}} , \tag{5.2}$$

with $B_{0,\mathrm{x}} = 3\ \mu$G and $B_{\mathrm{y}} = B_{\mathrm{z}} = 0\ \mu$G (see Walch et al., 2015; Girichidis et al., 2015).

We initially drive artificial turbulent motions with an Ornstein–Uhlenbeck random process (Eswaran & Pope, 1988). We do this in order to create some inhomogeneities in the gas distribution while also providing support to the disc, which would otherwise go into free-fall collapse on a short time-scale. We inject turbulence with a power spectrum that is flat between dimensionless wave-numbers $k = 1$ and $k = 2$ (corresponding to scales ranging from $L/2$ to L, where L is the size of the box in the x and y directions), and zero elsewhere. The turbulence is driven using a natural mix of 2/3 solenoidal (divergence-free) and 1/3 compressive (curl-free) modes. The strength of the driving is chosen to ensure that the global, mass-weighted, 3D root-mean-square (rms) velocity remains constant at $v_{\mathrm{3D,rms}} = 10\,\mathrm{km\,s^{-1}}$. The phase turnover time corresponds to the turbulent crossing time in the x and y directions of $\sim 50\,\mathrm{Myr}$. Artificial driving is automatically switched off once the first sink particle forms, which occurs at $\sim 9\,\mathrm{Myr}$ in our non-magnetic runs or at $\sim 17\,\mathrm{Myr}$ in our magnetic runs.

Refinement criteria

We set the base grid to a minimum refinement level $l_{\rm ref,min} = 4$, corresponding to a spatial resolution of $\Delta x \simeq 7.8\,{\rm pc}$ in each direction. We let the AMR routines refine on density discontinuities up to a maximum level $l_{\rm ref,max} = 5$, or $\Delta x \simeq 3.9\,{\rm pc}$, using a second derivative-based criterion. Moreover, we require the blocks that contain sink particles to be at the maximum refinement level. We refine up to $l_{\rm ref,max} = 5$ blocks that have Jeans length sampled by less than five cells, while we let them derefine (according also to the previous criteria) if the Jeans' length is resolved by at least ten cells. Finally, in order to evolve the simulations for long time-scales while still being able to capture outflows from the disc, we force a derefinement to the minimum level above and below $\pm\ 1\,{\rm kpc}$.

5.3 Results

5.3.1 The relative importance of stellar winds and supernovae

Regulation of star formation at local scales

In Fig. 5.1 we compare the evolution of the sink mass, gas mass within $r_{\rm accr}$ and sink accretion rate with respect to their relative initial values at the creation time $t_{\rm c}$ for the first sink particle formed in the e100-NoF-NoMag, e100-SN-NoMag, and e100-WSN-NoMag simulations. In all three cases the sink initial properties, i.e. creation time, mass, position, velocity, distribution and thermodynamical properties of the ambient medium within and outside $r_{\rm accr}$, stellar population, etc., are the same. This comparison allows us to understand the differential impact of winds and SN explosions at local scales (see also sec. 3.4.1).

Without any feedback (e100-NoF-NoMag), the sink accretes Jeans–unstable gas from a large reservoir of gas within $r_{\rm accr}$ and increases its mass by more than an order of magnitude during the first $\lesssim 20\,{\rm Myr}$ of evolution. It is continuing to accrete gas rapidly at the end of this period, and would continue to grow. When only SNe are included (e100-SN-NoMag), the first explosion at $\sim 5\,{\rm Myr}$ stops accretion and create a blast wave that removes the gas from within and around the sink. However, due to the lack of earlier energy injection, the sink was able to accrete and form new stars between its formation and the first SN explosions. SNe can only regulate the sink star formation activity on time-scales of the order of the lifespan of the most massive stars. Including stellar winds and SNe (e100-WSN-NoMag) terminates sink growth right after the formation. The accretion rate of the sink falls rapidly to zero and only a few stars are created after $t_{\rm c}$. The

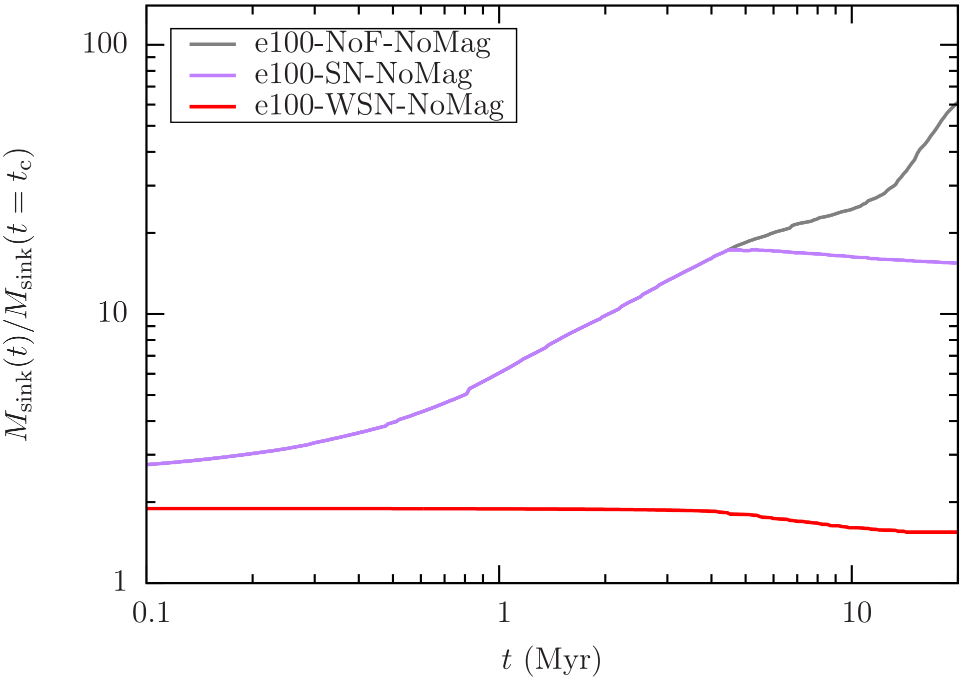
e100-NoF-NoMag
e100-SN-NoMag
e100-WSN-NoMag
$M_{\rm sink}(t)/M_{\rm sink}(t=t_{\rm c})$
100
10
1
0.1
1
10
t (Myr)

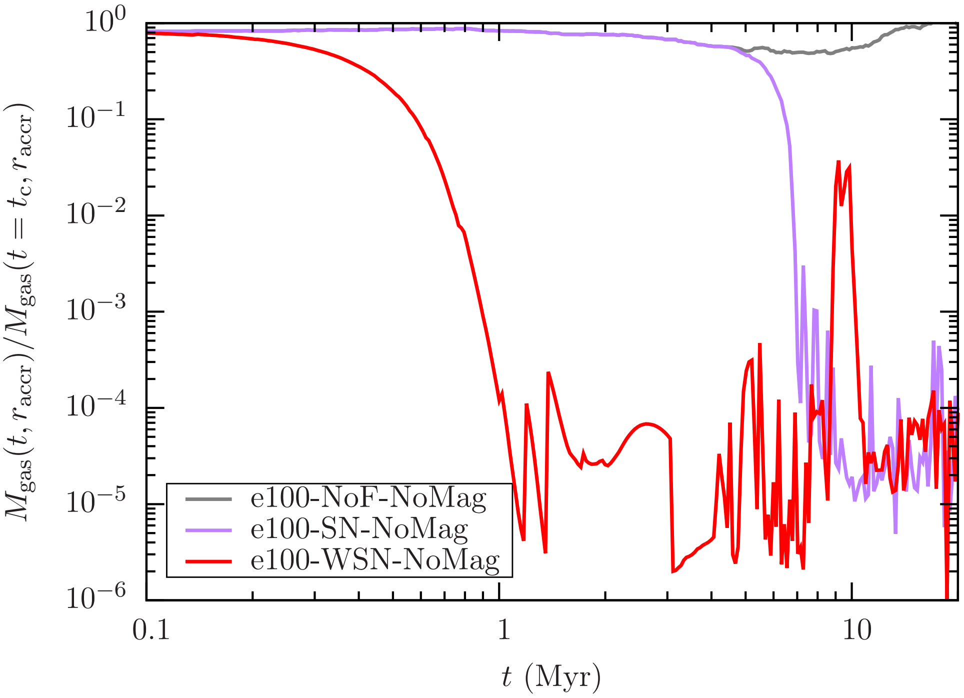
10^0
10^{-1}
10^{-2}
10^{-3}
10^{-4}
10^{-5}
10^{-6}
$M_{\rm gas}(t, r_{\rm accr})/M_{\rm gas}(t=t_{\rm c}, r_{\rm accr})$
e100-NoF-NoMag
e100-SN-NoMag
e100-WSN-NoMag
0.1
1
10
t (Myr)

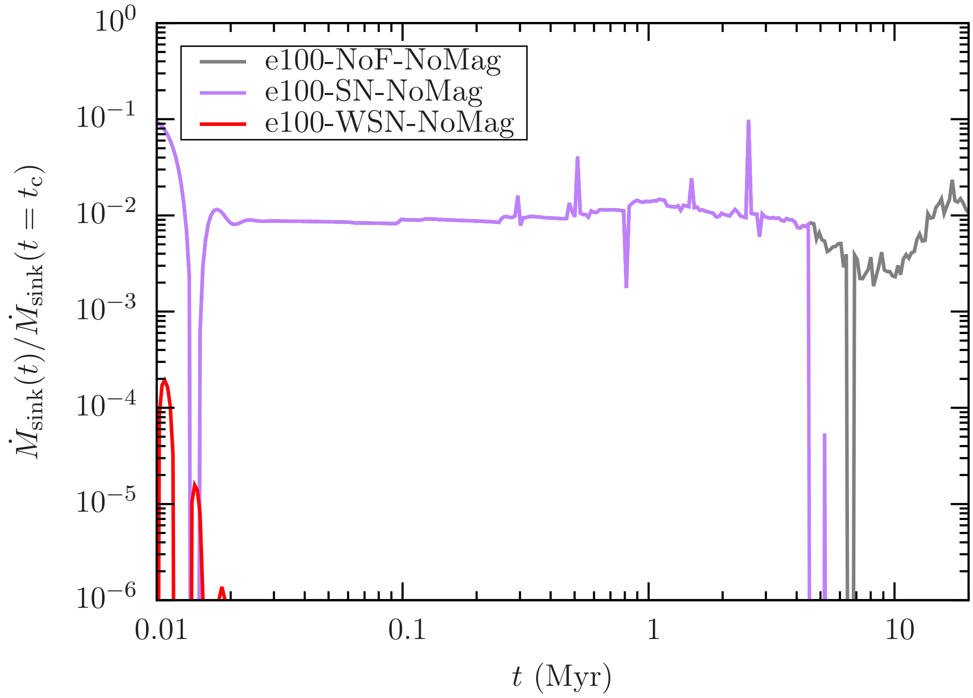

Figure 5.1: *Evolution of the sink particle mass, gas mass within $r_{\rm accr}$ and sink particle accretion rate with respect to the relative initial quantities at the formation time $t_{\rm c}$ for the first sink particle formed in the e100-NoF-NoMag, e100-SN-NoMag, and e100-WSN-NoMag simulations.*

gas mass within $r_{\rm accr}$ is entirely removed in $\sim 1\,$Myr, significantly lowering the density of the ambient medium by the time the first SN explodes at $\sim 5\,$Myr (see next section). As a result, the mass of the sink, and therefore the amount of gas converted into stars, is more than one order of magnitude smaller with respect to the case where only SNe are present.

We conclude that stellar winds are more important than SNe in regulating the star formation activity within sink particles due to the faster onset of energy injection. This result also applies if we set $\epsilon_{\rm SF} = 0.1$, with the difference being the longer time-scale required to stop accretion onto the sink particle due to the smaller amount of energy injected by feedback. While the time-scale required for SNe to regulate the star formation activity is of the order of the lifespan of the most massive stars (or longer, for smaller $\epsilon_{\rm SF}$), it is of the order of the formation time (or longer, for smaller $\epsilon_{\rm SF}$) of the most massive stars for stellar winds.

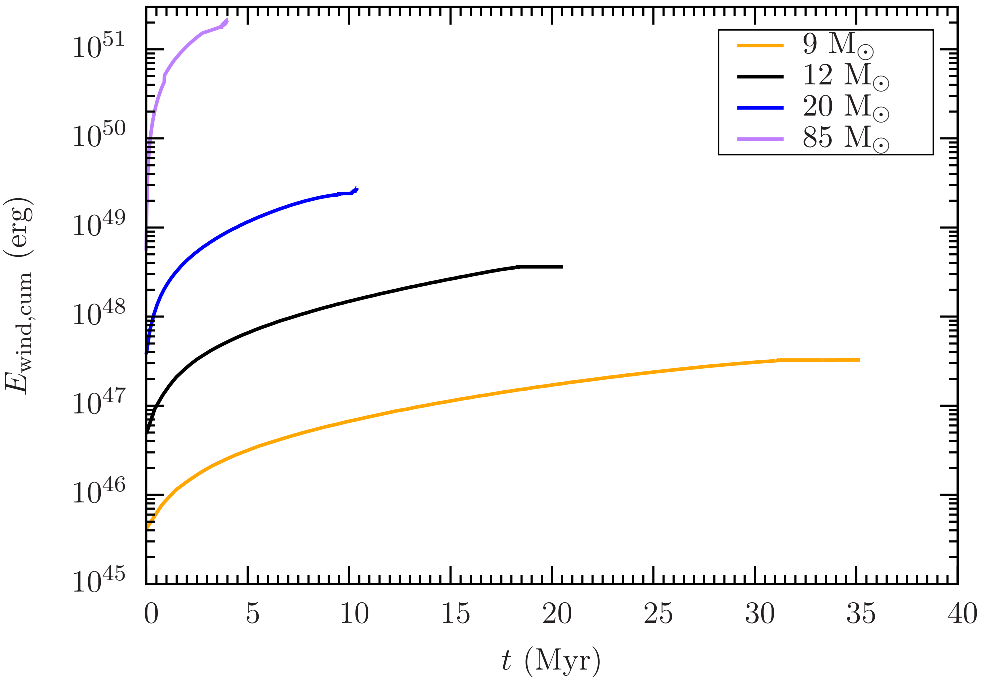

Figure 5.2: *Cumulative energies injected via stellar winds from the Geneva stellar evolution tracks for four representative stars with initial masses 9 (orange), 12 (black), 20 (blue) and 85 (purple) $\mathrm{M}_\odot$ (see also Fig. 3.3).*

Energies

Fig. 5.2 shows the cumulative energies injected by massive stars with different initial masses via stellar winds computed integrating the stellar tracks shown in Fig. 3.3. While for the whole range $9-120\,\mathrm{M}_\odot$ the energy injected by a single SN is fixed at $E_{\rm SN} = 10^{51}$ erg, for stellar winds the amount of energy injected depends strongly on the initial mass of the star. Stars at the lower end of this range inject only very small amounts of energy into the ISM, i.e. $\sim 10^{-2}-10^{-4}\times E_{\rm SN}$, but the most massive stars inject as much or more energy in winds as they do when they die as SNe. For example, if we examine the stellar wind energies shown in Fig. 5.2 for a $9\,\mathrm{M}_\odot$ and an $85\,\mathrm{M}_\odot$ star, we see that we would need around 6600 $9\,\mathrm{M}_\odot$ stars in order to produce the same wind energy as a single $85\,\mathrm{M}_\odot$ star. Moreover, radiative cooling allows stellar winds to transfer only a small fraction of the injected energy into the ISM. Unlike SNe, stellar winds inject energy continuously during the stars' lifetime. Stars with smaller initial masses inject less energy over a more extended period, making cooling more efficient in radiating away substantial fractions of the injected energy at each time. Therefore, most of the influence that stellar winds have on the ISM is due to a small number of very massive O stars.

If we apply the same arguments when considering SN explosions, we find that globally SNe are the most important energy injection mechanism (see also Mac Low & Klessen, 2004; Klessen & Glover, 2014). Most of the energy injected by SNe is produced by stars at the lower end of our considered mass range, i.e. B stars, as these stars are considerably more numerous but have longer lifespans than the massive O stars that produce the strongest stellar winds. Therefore, stellar winds dominate the energy budget during the first phase of the evolution of the stellar population, while SNe take over at later times, typically after $\approx 5-20\,\mathrm{Myr}$.

The amount of energy injected and transferred to the medium by stellar feedback also depends on the temporal and spatial clustering of massive stars and on the presence of stellar winds. Spatial clustering of massive stars has a large impact, as if we increase the number of sources, the energy lost by radiative cooling scales only sub-linearly with the total energy injected (e.g. Kim & Ostriker, 2015), provided that the temporal separation between explosions is less than the cooling time of the first SN remnant. Therefore, the degree to which the formation of massive stars is correlated in time as well as in space, which depends on the star formation history (SFH) and the IMF, also plays a key role in determining the efficiency of the stellar feedback. On the other hand, stellar winds are the only process able to influence the ISM at early times, lowering the ambient medium density and therefore increasing the heating efficiency of SNe (similarly to ionising radiation, see Walch & Naab, 2015).

In Table 5.2 we show, for each of the simulations including SN feedback, the total number of SNe (N_{SN}), the average number of massive stars per sink particle ($\overline{N}_{*,\mathrm{p}}$), defined as the product of the assumed ϵ_{SF} with the average mass of the sink particles at the time when their accretion rate drops to zero, the supernova rate averaged over 71 Myr of star formation activity ($\overline{\mathrm{SNR}}$), the average density of the gas in which the SN explode ($\overline{\rho}_{\mathrm{SN}}$), defined as the average density within the injection region at the moment the SN energy is injected, and the fraction of SNe exploding in regions with density above a density cut of $\rho_{\mathrm{cut}} = 2 \times 10^{-24}$ g cm^{-3} ($N_{\mathrm{SN}}(\rho > \rho_{\mathrm{cut}})$), a value in between the typical cold, dense and warm, diffuse phase densities (e.g. Ferrière, 2001; Klessen & Glover, 2014). In order to estimate how much more energy (momentum) a single SN can inject into the ISM when stellar winds are present, we compute the ratio between the expected momentum from a SN exploding when stellar winds are included with respect to the same quantity for the run with same ϵ_{SF} but including only SNe (SN-NoMag). Since the momentum developed by a single SN is $p_{\mathrm{SN}} \propto \rho^{-0.17}$ (Kim & Ostriker, 2015), then the ratio we compute is simply $\overline{p}_{\mathrm{SN}}/\overline{p}_{\mathrm{SN,SN-NoMag}} =$

Name	$N_{\rm SN}$	$\overline{N}_{*,\rm p}$	$\overline{\rm SNR}$ (Myr^{-1})	$\overline{\rho}_{\rm SN}$ (g cm^{-3})	$N_{\rm SN}(\rho > \rho_{\rm cut})$ (%)	$\frac{\overline{p}_{\rm SN}}{\overline{p}_{\rm SN,SN-NoMag}}$
e100-SN-NoMag	4985	133	70.2	3.9×10^{-24}	14.5	1
e100-WSN-NoMag	2620	65	36.9	2.9×10^{-25}	1.7	1.6
e100-WSN-Mag3	2857	83	40.2	3.1×10^{-25}	2.2	1.5
e10-SN-NoMag	970	15	13.7	7.2×10^{-23}	84.7	1
e10-WSN-NoMag	498	6	7.5	1.6×10^{-24}	9.4	1.9
e10-WSN-Mag3	443	8	6.2	4.5×10^{-24}	23.2	1.6

Table 5.2: *Properties of SNe for different simulations with and without stellar winds. From left to right, we show: name of the model, total number of SNe, average number of massive stars per sink particle, average SNR, average density of the ambient medium in which the SNe explode, fraction of SNe for which this density is above* $\rho_{\rm cut}$*, and the average momentum developed by a single SN with respect to same quantity for the corresponding SN-NoMag model.*

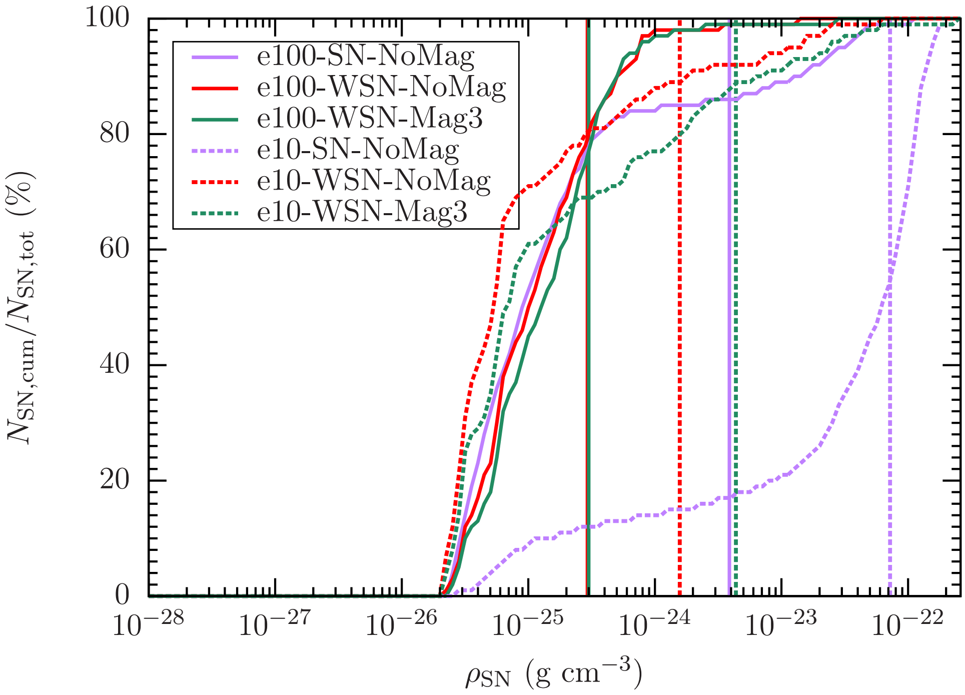

Figure 5.3: *Cumulative distribution of SNe (as a percentage of the total number of explosions) as a function of the density of the gas in which they explode, ρ_{SN}, plotted for a number of different simulations. The vertical lines represent the average value of ρ_{SN} in each model, as listed in Table 5.2. Stellar winds typically reduce the ambient medium density by an order of magnitude.*

$(\overline{\rho}_{\mathrm{SN,SN-NoMag}}/\overline{\rho}_{\mathrm{SN}})^{0.17}$. Note that this computation is largely approximate for two main reasons: i) the average densities we make use of are computed within, rather than outside, the injection region; and ii) it does not take into account clustering. For the same simulations, in Fig. 5.3 we plot the cumulative distribution of SNe (as a percentage of the total number of SNe, N_{SN}) as a function of the density of the gas in which they explode, ρ_{SN}. The vertical lines show the corresponding average densities $\overline{\rho}_{\mathrm{SN}}$.

Models without stellar winds (SN-NoMag) form more massive stars (see also Sec. 5.3.3), and so produce more SNe. The average number of massive stars per sink is also higher in these runs. Due to the higher $\overline{\mathrm{SNR}}$, more energy is injected into the ISM than in the runs that include stellar winds. However, the density of the gas with which the SNe interact is generally an order of magnitude or more higher in runs without winds compared to runs with winds. This is particularly true for run e10-SN-NoMag, where almost 85% of SNe occur in regions with $\rho > \rho_{\mathrm{cut}}$ and the cumulative distribution shows an extended tail at large ambient medium densities. Consequently, when $\epsilon_{\mathrm{SF}} = 0.1$, SNe alone are inefficient at heating the ISM due to the fact that the majority of the explosions interact with high density gas. Although numerical overcooling certainly plays a role, this is consistent with the results shown in the previous chapter (see also Walch et al., 2015; Kim & Ostriker, 2015; Martizzi et al., 2015; Walch & Naab, 2015), who show that (non-clustered) density peak SNe are subject to large radiative losses. Models including stellar winds have smaller clustering and $\overline{\mathrm{SNR}}$ with respect to the runs with SNe alone, but more SNe explode in low density gas. Therefore, while the total energy injected by SNe is smaller, the fraction of energy transferred to the ISM is likely to be higher and the estimated momentum injected by a single SN is larger by a factor of 1.5-2.

In general, the fraction of energy transferred to the ambient medium by stellar feedback is a complex function of the SFR, SFH and degree of clustering, as well as on the structure of the ISM, which in turn depend on several key factors. The arguments presented above can only be used to infer the qualitative behaviour of each different model and the stellar feedback energy transfer efficiency has to be computed numerically, rather than analytically.

In the top two panels of Fig. 5.4 we plot the cumulative energy injected by stellar winds and SNe for different simulations with feedback. As expected, SNe dominate the total energy budget. For simulations including both stellar winds and SNe (e100-WSN-NoMag, e100-WSN-Mag3, e10-WSN-NoMag, e10-WSN-Mag3), we find that during 71 Myr of star formation activity SNe inject around 5 times more energy than stellar winds. Due to the higher number of massive stars (see Table 5.2), runs with only SNe (e100-SN-NoMag, e10-SN-NoMag) have more energy injected with respect to the case where only/also stellar winds are included.

In the third panel, we plot the energy transfer efficiency, defined as $\epsilon_{\mathrm{transf}} = 1 - E_{\mathrm{rad,cum}}/E_{\mathrm{inj,cum}}$, with $E_{\mathrm{rad,cum}}$ cumulative energy radiated away by cooling and $E_{\mathrm{inj,cum}}$ cumulative energy injected by feedback. We integrate E_{rad} starting from the first feedback event. Given that E_{rad} is the total energy lost via cooling, it comprises also cooling events not necessarily related to feedback. For this reason, we only show the evolution for three representative simulations for which stellar feedback dominates the total energy budget.

At early times, $\epsilon_{\mathrm{transf}}$ increases for all simulation due to large quantities of energy injected by stellar feedback. Up to $t \lesssim 30\,\mathrm{Myr}$, e100-WSN-NoMag produces a strong energy coupling due to the early contribution of stellar winds and SNe. At later times, the energy transfer efficiency drops due to a decreasing amount of energy injected per unit of time (see first two panels). At $t = 80\,\mathrm{Myr}$, $\epsilon_{\mathrm{transf}}$ falls to $\approx 1\%$. The model with only SNe (e100-SN-NoMag) shows a stronger peak in transfer efficiency at later times due to more energy injected for $t > 30\,\mathrm{Myr}$. The decrease in efficiency

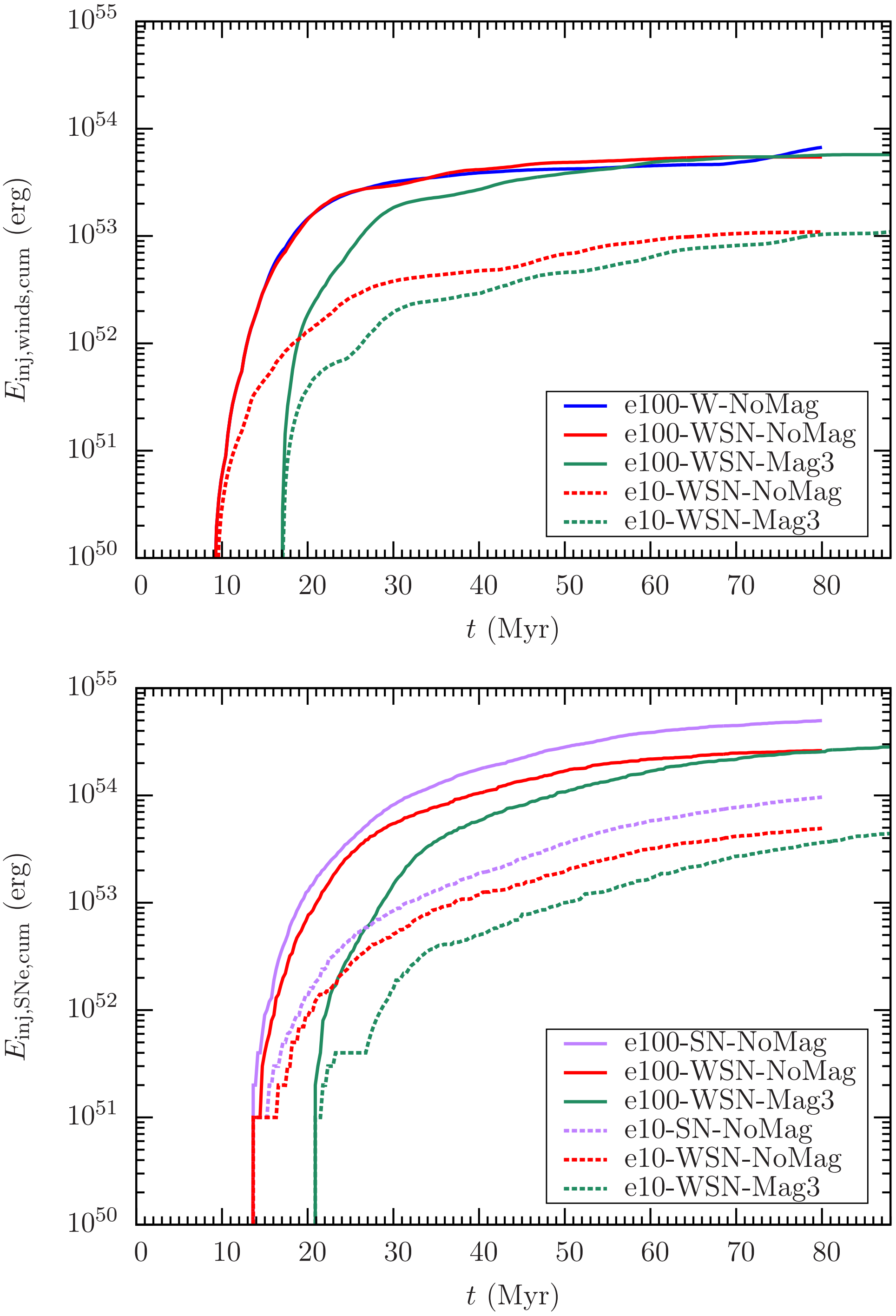
10^{55}
10^{54}
10^{53}
10^{52}
10^{51}
10^{50}
$E_{\mathrm{inj,winds,cum}}$ (erg)
e100-W-NoMag
e100-WSN-NoMag
e100-WSN-Mag3
e10-WSN-NoMag
e10-WSN-Mag3
0
10
20
30
40
50
60
70
80
t (Myr)
10^{55}
10^{54}
10^{53}
10^{52}
10^{51}
10^{50}
$E_{\mathrm{inj,SNe,cum}}$ (erg)
e100-SN-NoMag
e100-WSN-NoMag
e100-WSN-Mag3
e10-SN-NoMag
e10-WSN-NoMag
e10-WSN-Mag3
0
10
20
30
40
50
60
70
80
t (Myr)

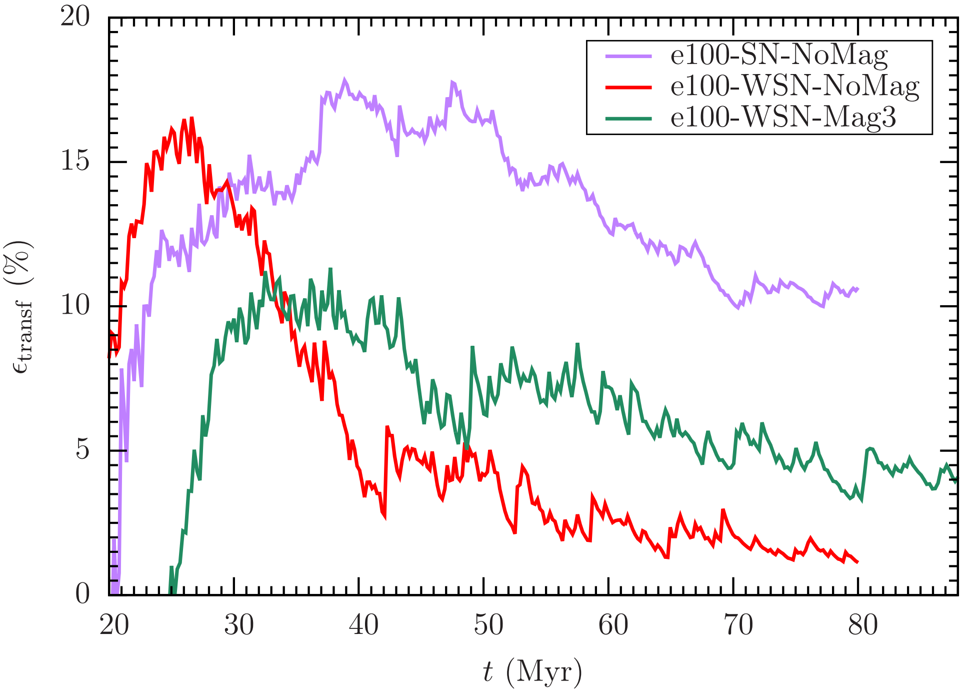

Figure 5.4: *Evolution of the cumulative energy injected by stellar winds, SNe and energy transfer efficiency for different simulations with stellar feedback.*

for $t > 50\,$Myr is less severe as more (and more clustered) SNe are able to explode, producing a final $\epsilon_{\rm transf} \approx 10\%$. The run with both magnetic fields and stellar winds (e100-WSN-Mag3) represents a case in between these two. $\epsilon_{\rm transf}$ reaches a maximum at $t \sim 30-40\,$Myr due to delayed star formation activity in presence of magnetic fields (see Sec. 5.3.3). After this, the efficiency drops due to a decreasing energy injection rate. However, this energy injection rate is higher than in the non-magnetised case. As a result, more (and slightly more clustered, see Table 5.2) energy can be injected at later times, counteracting radiative cooling, and setting the final $\epsilon_{\rm transf}$ to $\approx 3-4\%$. These values should be considered as extremely rough estimates, as the time at which we start integrating $E_{\rm rad}$ and the definition of $E_{\rm rad}$ itself play a major role in setting $\epsilon_{\rm transf}$ for the different models.

5.3.2 Global evolution and properties of the ISM

Global overview

Figs. 5.5, 5.6, 5.7, 5.8, 5.9, 5.10, 5.11 and 5.12 show snapshots of the simulations at $t = 40$ Myr (without magnetic fields) and $t = 48\,\mathrm{Myr}$ (with magnetic fields), i.e. after 31 Myr of star formation activity, cut at $z = \pm 1\,\mathrm{kpc}$.

For the e100-NoF-NoMag run (Fig. 5.5), where stellar feedback is not included, the structure, dynamics and thermodynamical properties of the disc, as well as the star formation process, are solely set by the combination of decaying initial turbulence, gravity, and heating and cooling processes. The lack of pressure support via stellar feedback causes the disc to oscillate around the mid-plane and stars are formed continuously during the entire simulation. The gas distribution is highly filamentary. Due to the continuous conversion process from dense gas to stars, a large fraction of cold gas is accreted onto sink particles, while the warm component is able to survive due to its larger thermal pressure.

The inclusion of SNe at $\epsilon_{\mathrm{SF}} = 1$ (e100-SN-NoMag, Fig. 5.6, e100-WSN-NoMag, Fig. 5.8, e100-WSN-Mag3, Fig. 5.9) causes a large volume of the mid-plane to be occupied by hot gas produced by explosions of massive stars. This hot component creates a pressure gradient that is able to launch outflows of ionised and atomic gas and disrupt the disc. The distribution of cold and warm gas in the disc is more clumpy than e100-NoF-NoMag due to the compression from the hot, high-pressure ambient medium. There is no molecular gas in the outflowing component due to the strong shock-heating provided by SNe. This process efficiently converts the molecular phase into ionised gas. The H_2 is concentrated in the mid-plane, but with a broader distribution over z with respect to the e100-NoF-NoMag run. When stellar winds are included (e100-WSN-NoMag, e100-WSN-Mag3) the outflowing gas is slightly denser and colder and the H_2 distribution reaches larger heights due to the early pressure support provided by stellar winds. In e100-WSN-Mag3, the presence of additional magnetic pressure support causes star formation to be delayed with respect to the non-magnetised case. Therefore, cold and warm gas is kicked out of the mid-plane at later times.

In run e100-W-NoMag (Fig. 5.7), stellar winds are still able to produce a hot component and to compress the cold and warm gas, but their heating efficiency is smaller with respect to SN explosions (see Sec. 5.3.1). Therefore, the ISM close to the the mid-plane is colder, more diffuse and less clumpy with respect to the models where SNe are included. Stellar winds alone are not able to power outflows but significantly increase the scale heights of the ionised, atomic and molecular gas distributions.

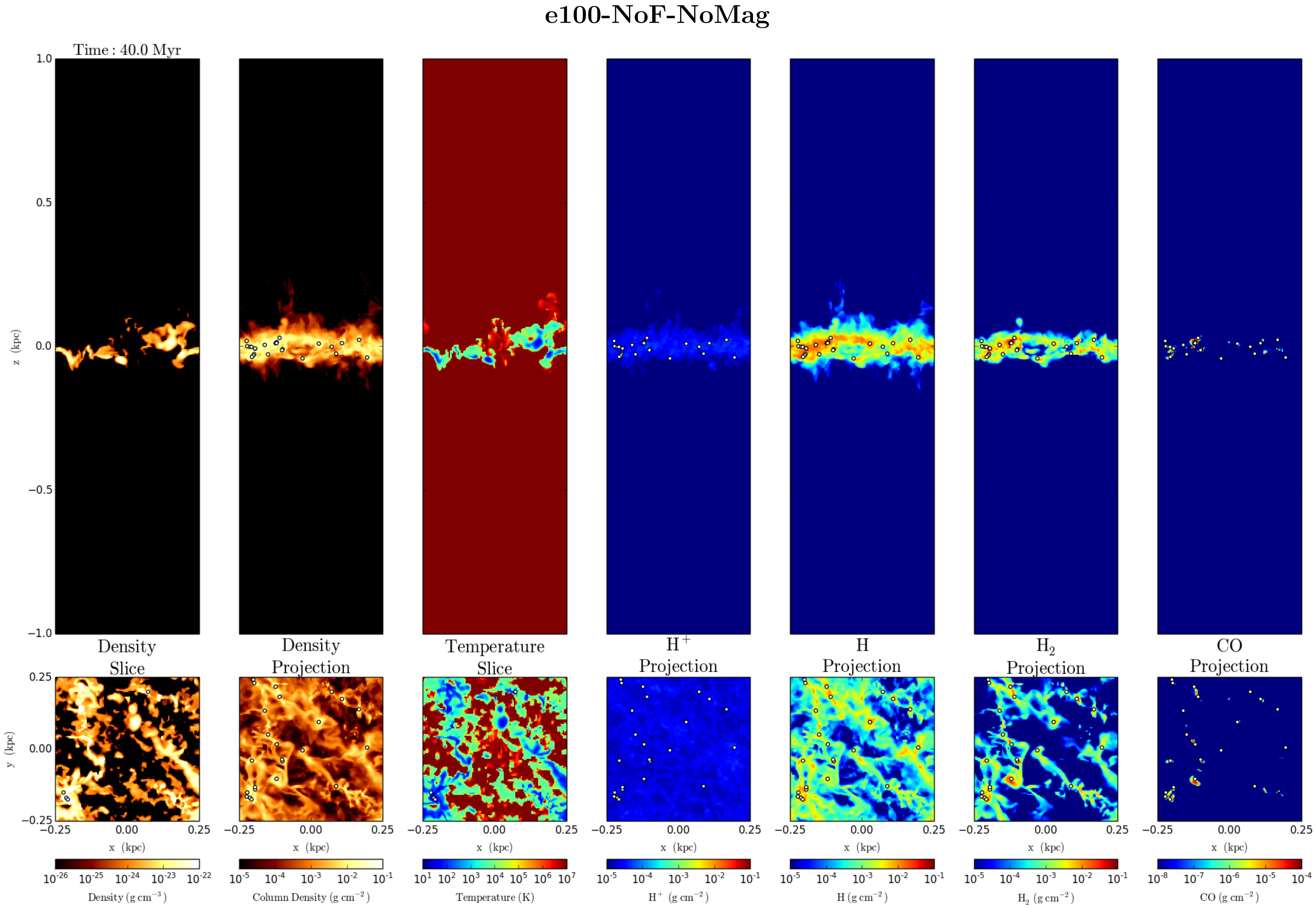

Figure 5.5: *Snapshots at $t = 40\,\mathrm{Myr}$ for the e100-NoF-NoMag simulation. For each plot, the top row shows the edge-on view of the disc in the x-z plane cut at $z = \pm\,1\,\mathrm{kpc}$, while the bottom row is the face-on view in the x-y plane. From left to right, we plot: mass density slice, mass density projection, temperature slice, and the projections of the mass densities of* H^+, H, H_2, CO, *respectively. The white points represent sink particles.*

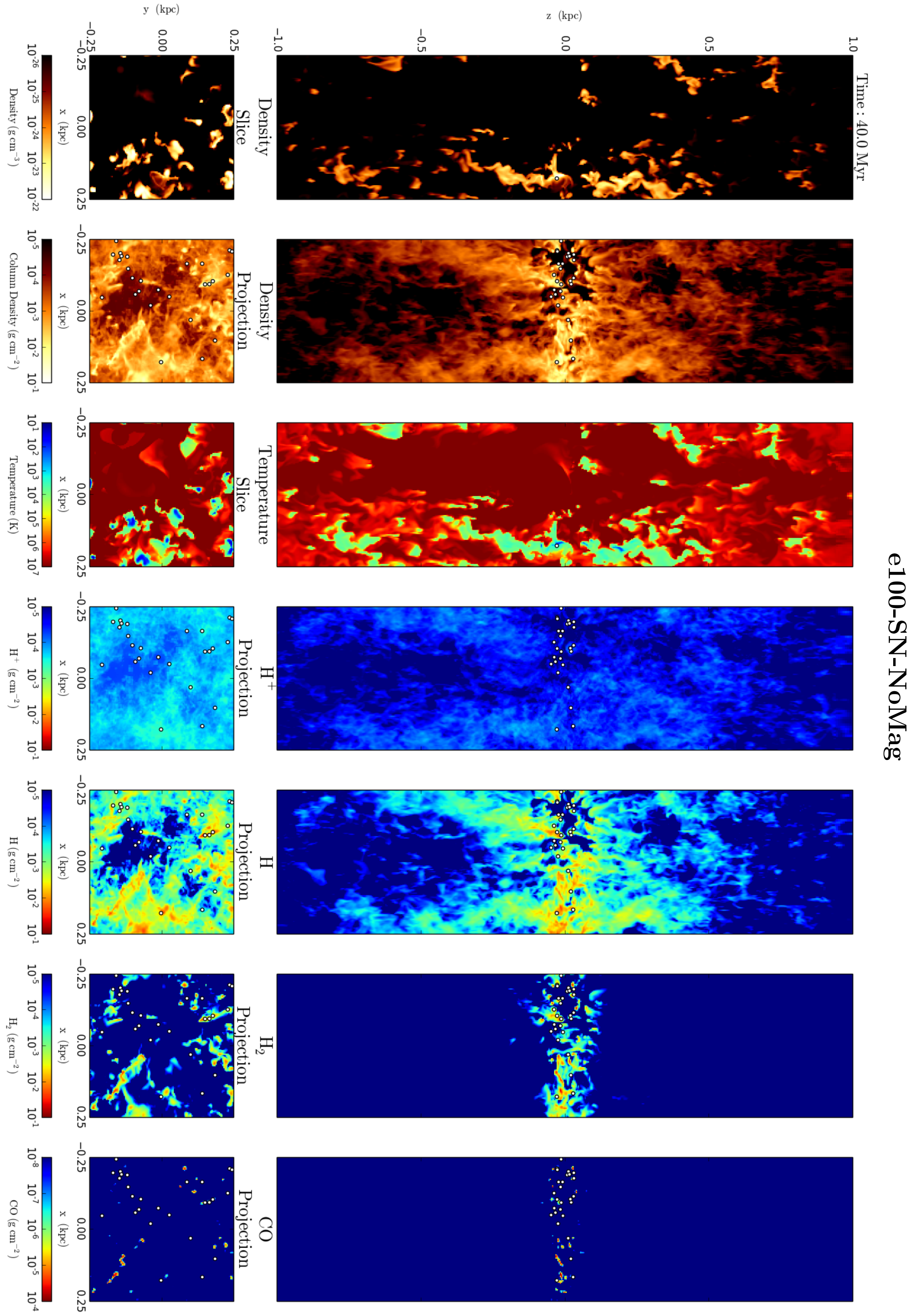

Figure 5.6: *Same as Fig. 5.5 for the e100-SN-NoMag simulation.*

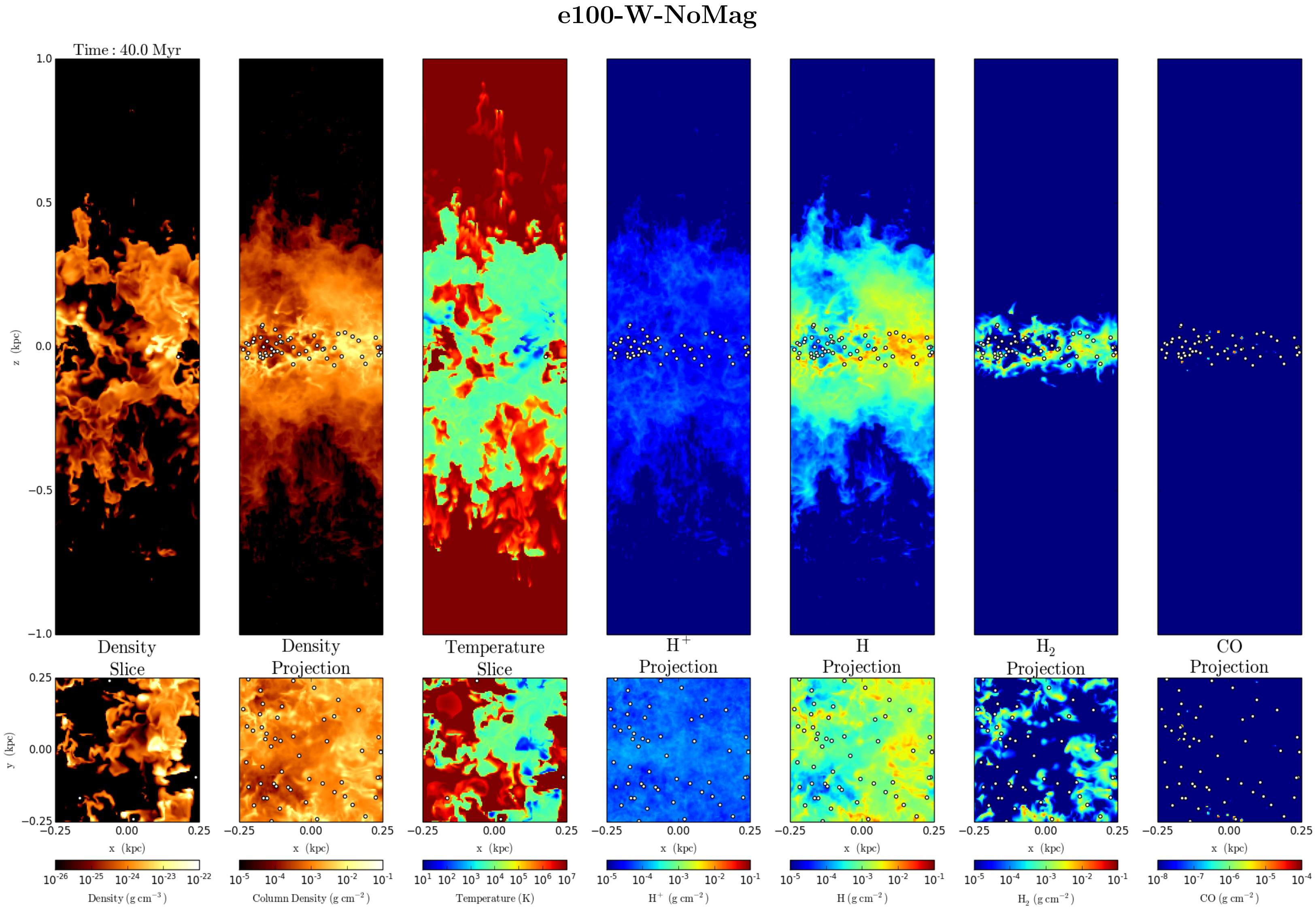

Figure 5.7: *Same as Fig. 5.5 for the e100-W-NoMag simulation.*

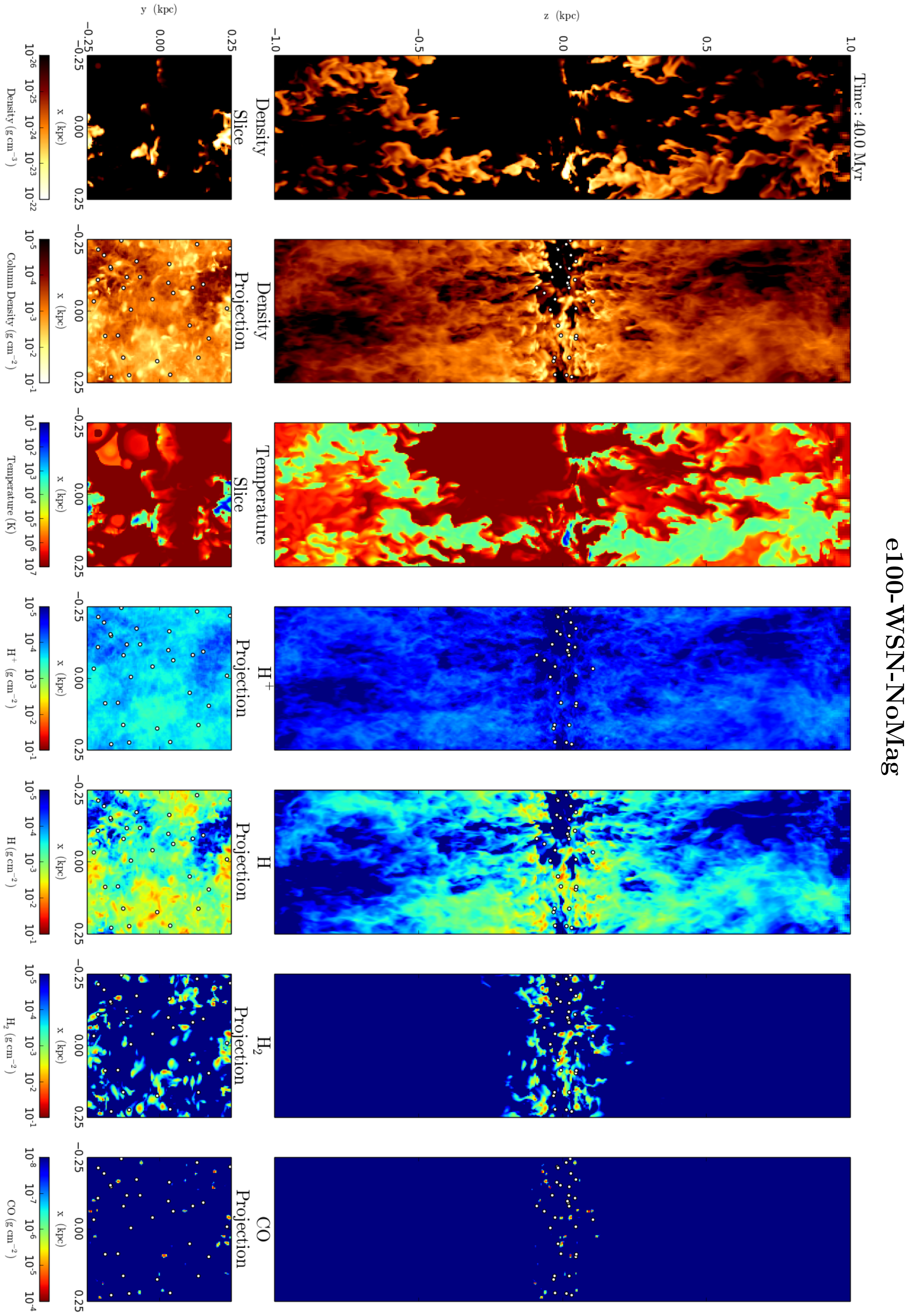

Figure 5.8: Same as Fig. 5.5 for the e100-WSN-NoMag simulation.

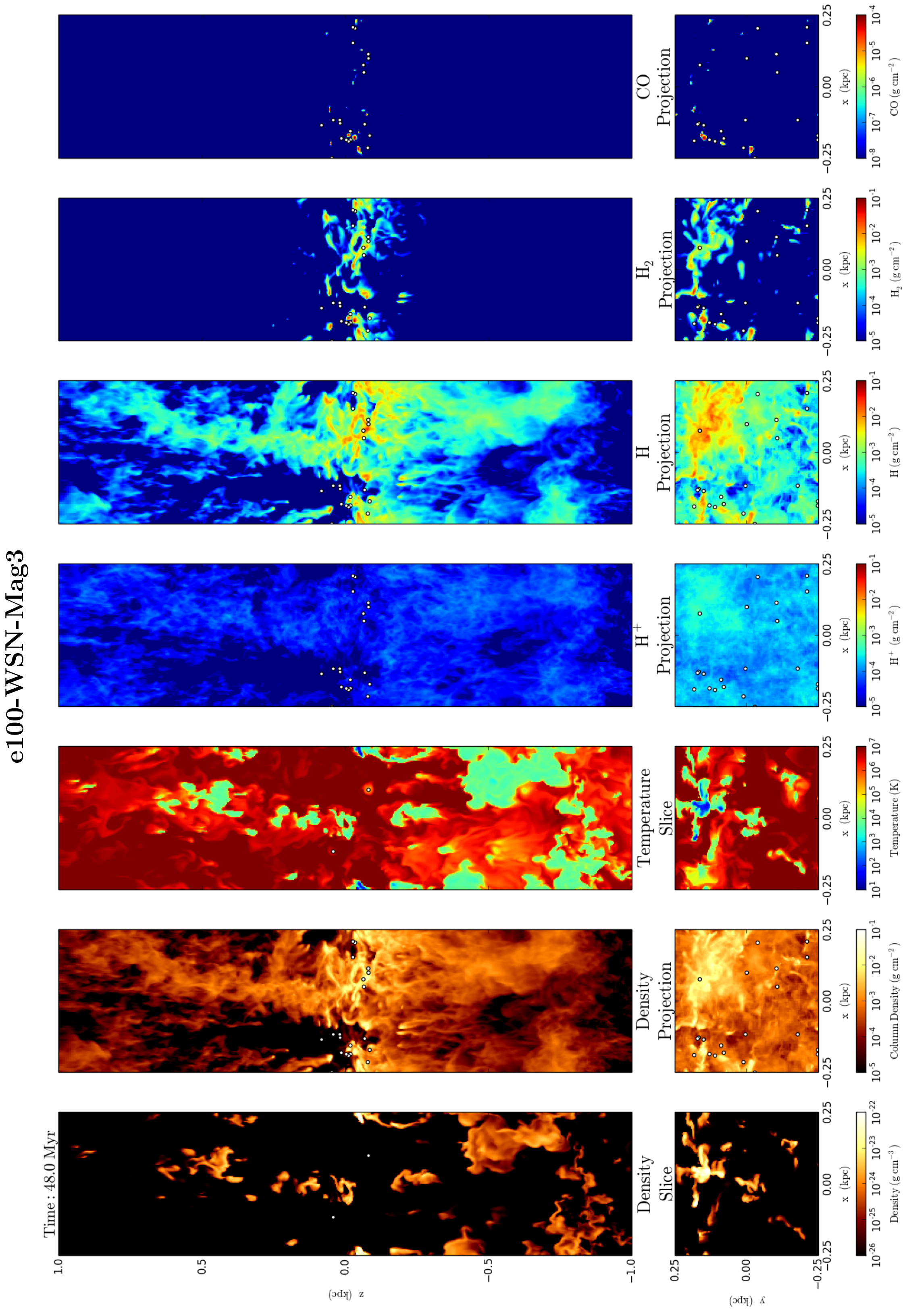

Figure 5.9: *Same as Fig. 5.5 for the e100-WSN-Mag3 simulation at* $t = 48\,\mathrm{Myr}$.

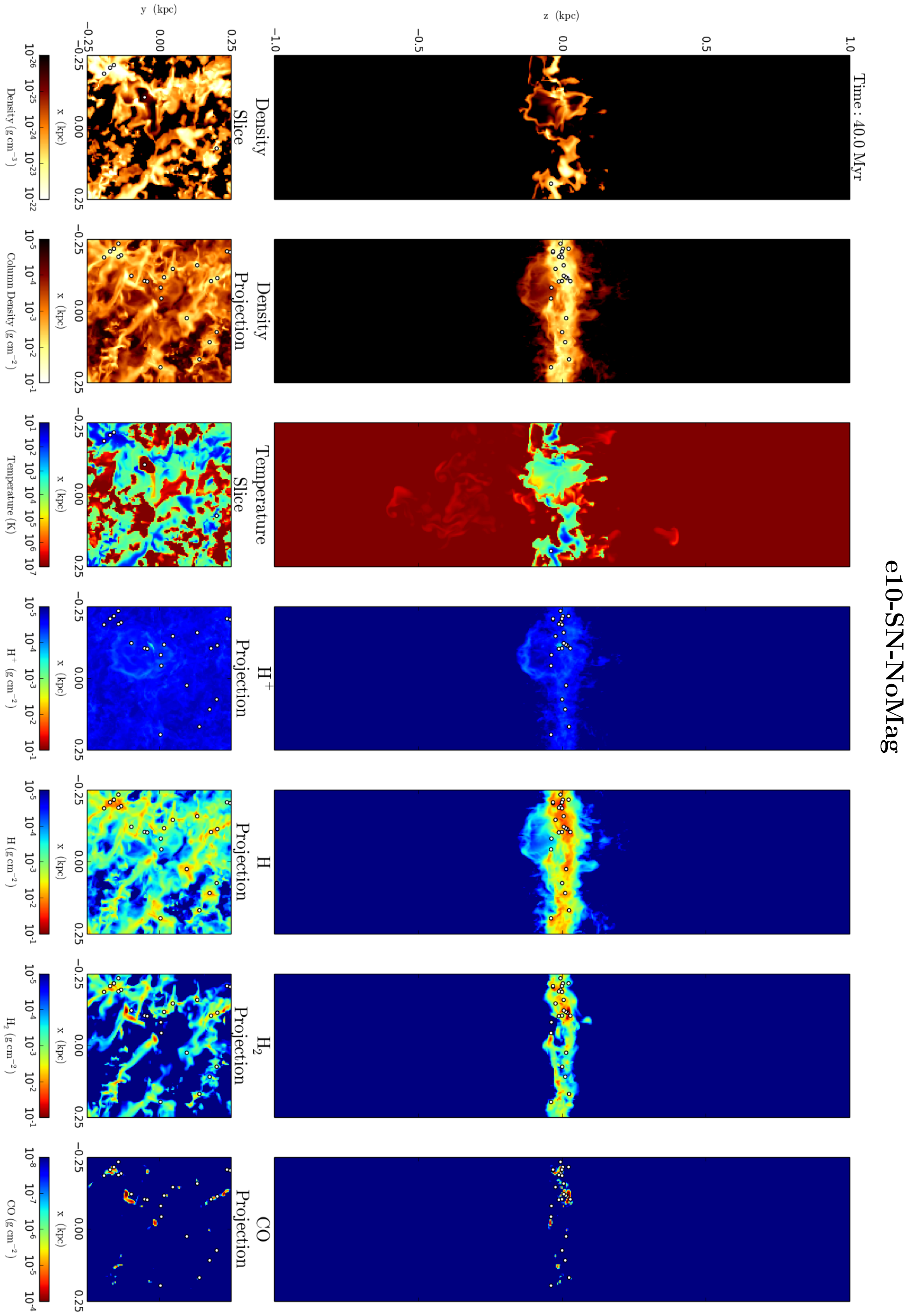

Figure 5.10: Same as Fig. 5.5 for the e10-SN-NoMag simulation.

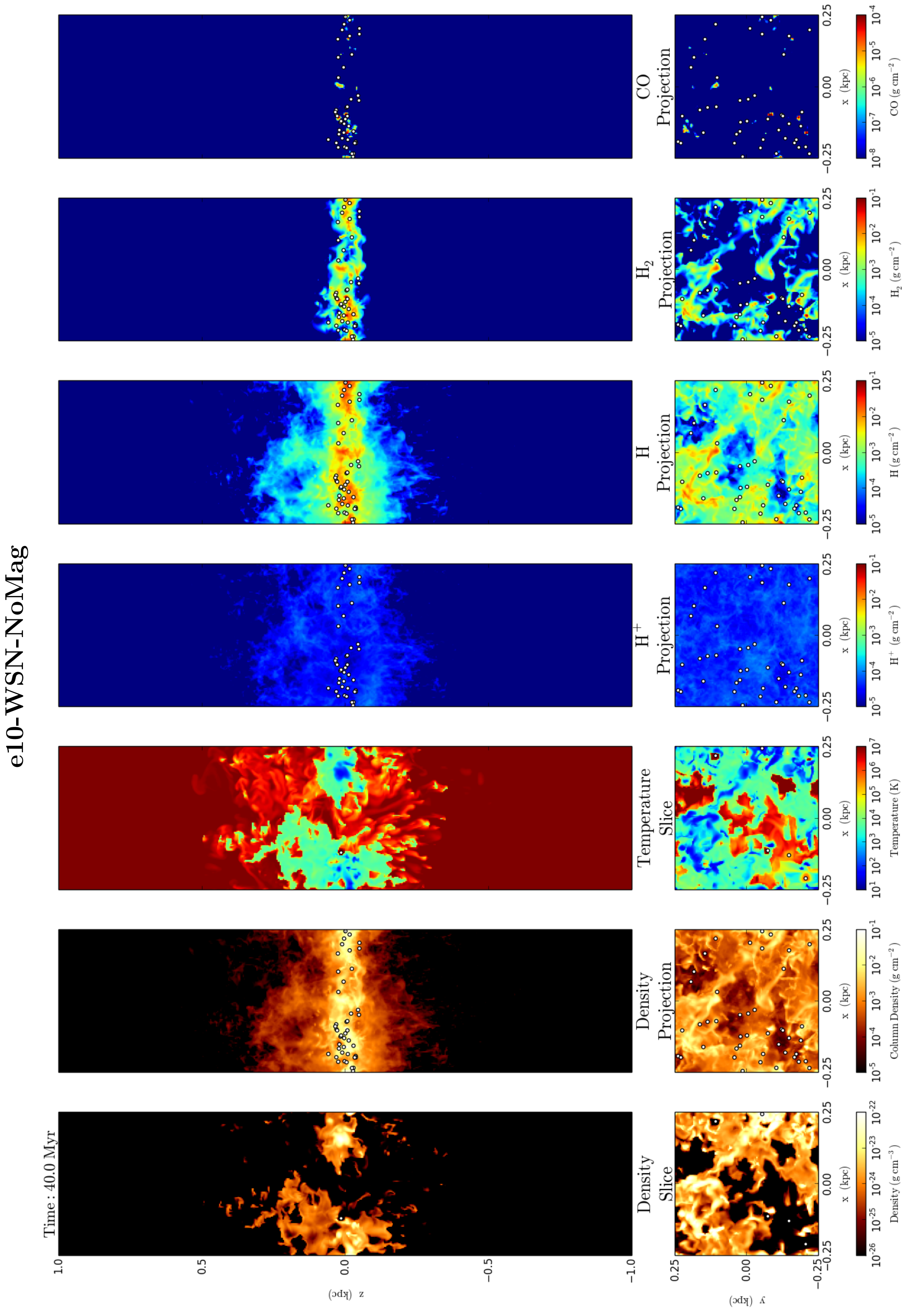

Figure 5.11: *Same as Fig. 5.5 for the e10-WSN-NoMag simulation.*

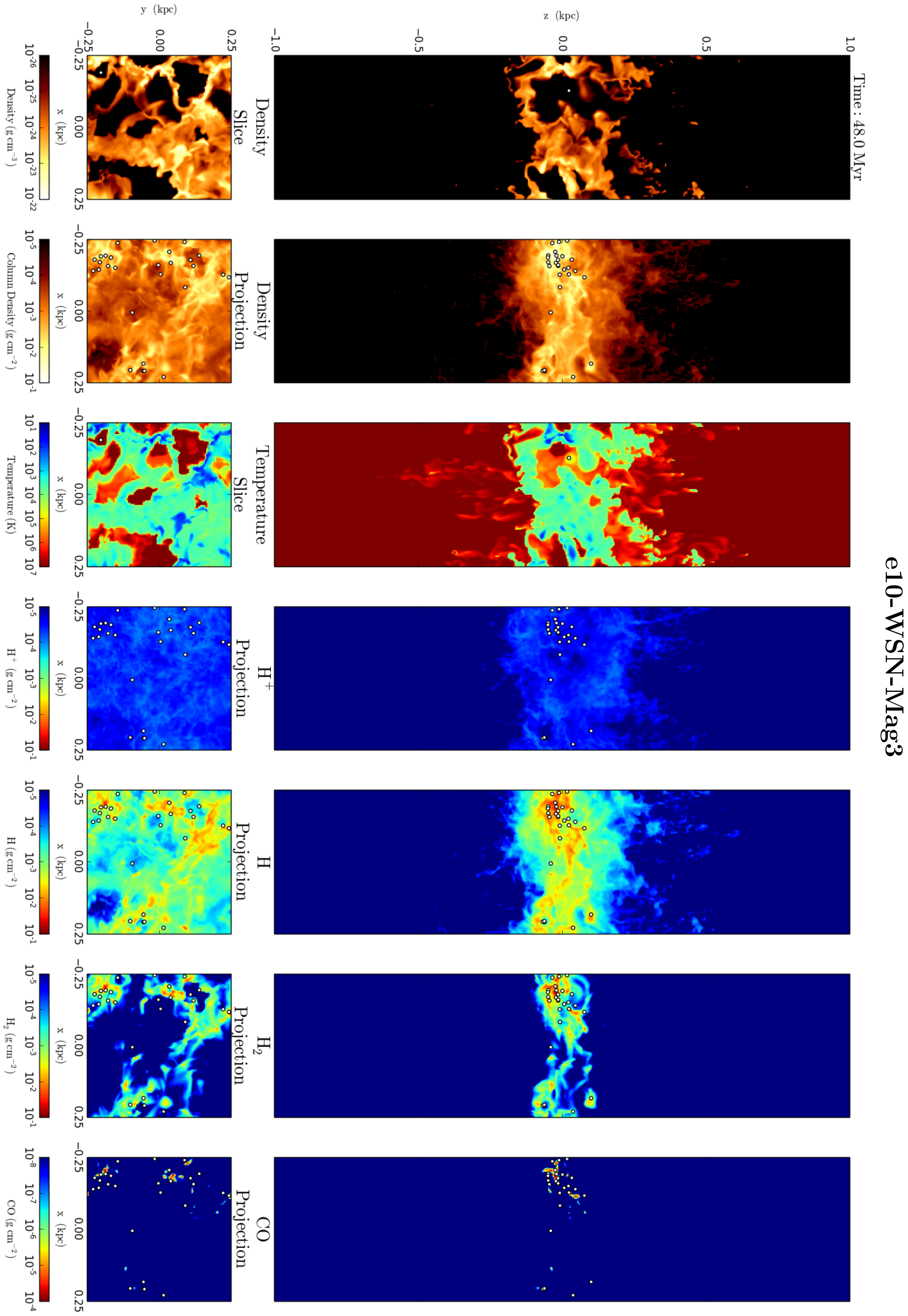

Figure 5.12: *Same as Fig. 5.5 for the e10-WSN-Mag3 simulation at $t = 48$ Myr.*

We find significantly different ISM properties for $\epsilon_{\mathrm{SF}} = 0.1$. When only SNe are included (e10-SN-NoMag, Fig. 5.10), outflows are not present and the disc has a smaller scale height. This is not surprising, as for lower star formation efficiency fewer SNe are produced (see Table 5.2). In this case, explosions from massive stars are inefficient at producing large fractions of hot gas and the mid-plane is filled with warm and cold gas. A large number of massive stars are produced almost constantly throughout the entire simulation due to lack of sufficient pressure support.

If we include both stellar winds and SNe, with or without magnetic fields (e10-WSN-NoMag and e10-WSN-Mag3, Fig. 5.11 and 5.12), we do not produce any outflows and the disc remains bound. The scale heights of the cold and warm distributions are larger due to pressure support from stellar winds and increased heating efficiency of SNe, as discussed in Sec. 5.3.1. As in the case for only SNe feedback, the amount of hot gas is reduced and we find more cold and warm gas concentrated towards the mid-plane with respect to the corresponding models with $\epsilon_{\mathrm{SF}} = 1$.

Globally, these results are in qualitative agreement with the findings of Gatto et al. (2015); Walch et al. (2015); Girichidis et al. (2015). Despite having different SFRs/SNRs and feedback mechanisms, we find that all the models having a significant fraction of the mid-plane volume filled with hot gas show development of large scale outflows. This hot, over-pressurised phase compresses the gas close to the disc into small, cold and dense clumps. On the other hand, a moderate number of SNe interacting with dense gas does not produce significant quantities of hot gas, outflows are not generated and the disc has small scale heights. In this case, compression from the hot component is missing, and the gas is mostly organised in filaments and extended clouds. An initial magnetic field of 3μG does not significantly affect the dynamics of the gas but delays the formation of cold and dense gas.

Mass fractions

In the upper panels of Fig. 5.13, we show how the mass fraction in gas and in sink particles evolves as a function of time in our different simulations. In the remaining panels in this Figure, we show similar plots for the fraction of the total hydrogen mass present in the form of H, H^+ resolved H_2 and "sub-grid" H_2. The latter is defined as the mass in H_2 gas plus the sum of the locked-up H_2 in sink particles for simulations with $\epsilon_{\mathrm{SF}} = 0.1$. In general, due to our limited spatial and mass resolution and therefore the employment of a low density threshold for sink particle formation, our gas-phase H_2 mass fractions are significantly underestimated and should be considered as

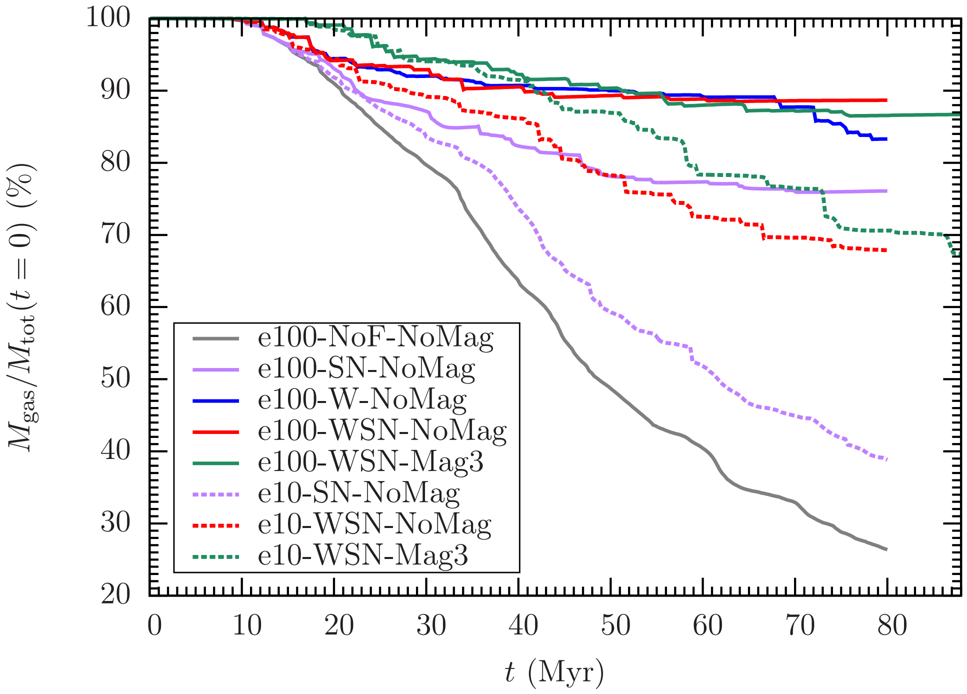
$M_{\rm gas}/M_{\rm tot}(t=0)$ (%)
100
90
80
70
60
50
40
30
20
0
10
20
30
40
50
60
70
80
t (Myr)
e100-NoF-NoMag
e100-SN-NoMag
e100-W-NoMag
e100-WSN-NoMag
e100-WSN-Mag3
e10-SN-NoMag
e10-WSN-NoMag
e10-WSN-Mag3

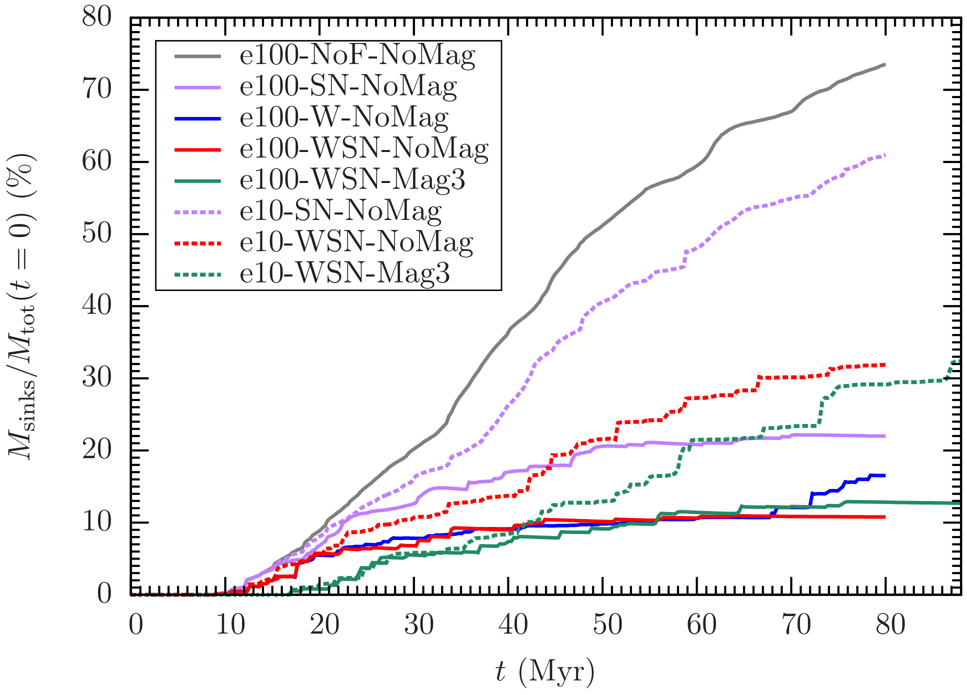
$M_{\rm sinks}/M_{\rm tot}(t=0)$ (%)
80
70
60
50
40
30
20
10
0
0
10
20
30
40
50
60
70
80
t (Myr)
e100-NoF-NoMag
e100-SN-NoMag
e100-W-NoMag
e100-WSN-NoMag
e100-WSN-Mag3
e10-SN-NoMag
e10-WSN-NoMag
e10-WSN-Mag3

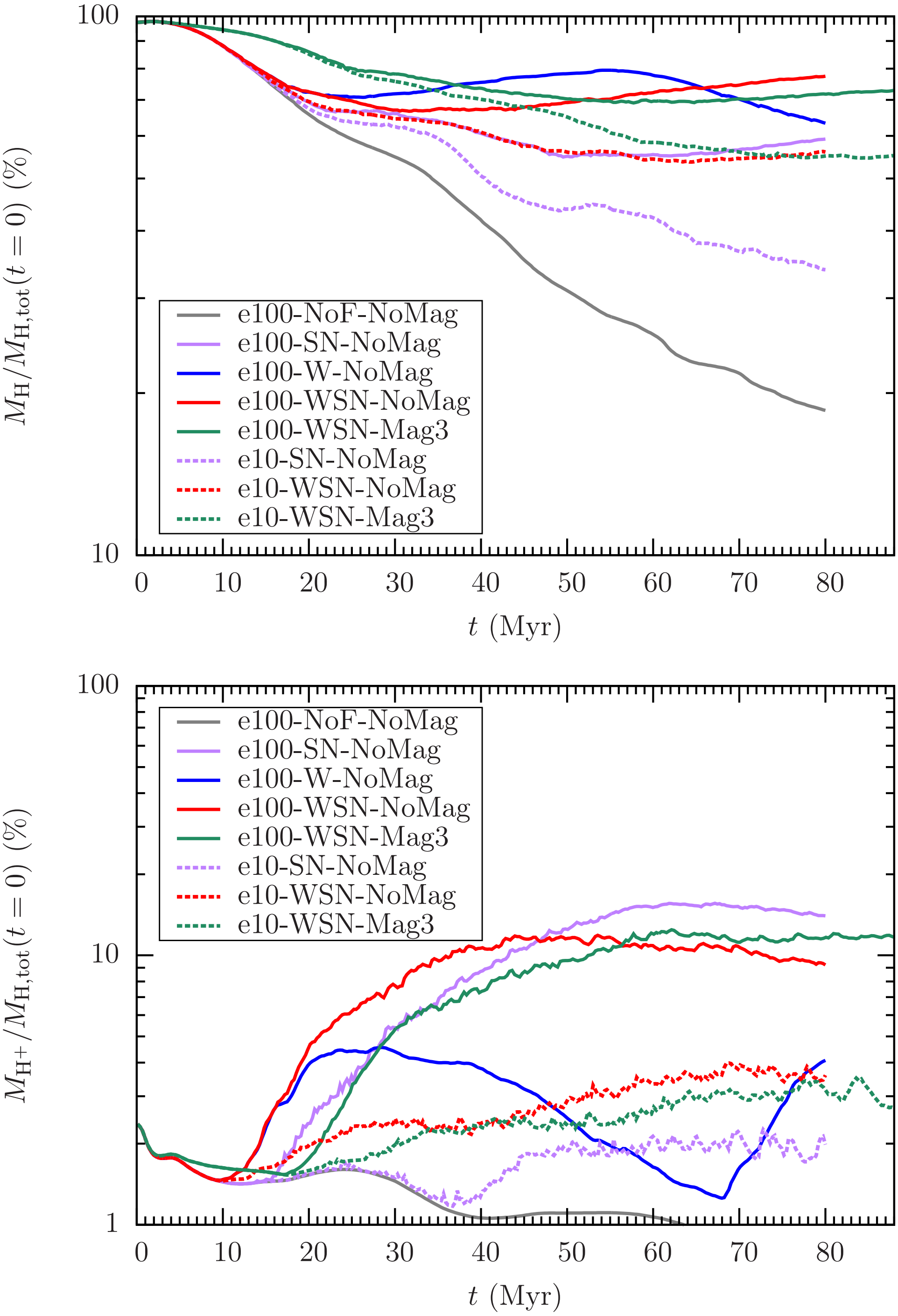
100
10
$M_{\rm H}/M_{\rm H,tot}(t=0)$ (%)
e100-NoF-NoMag
e100-SN-NoMag
e100-W-NoMag
e100-WSN-NoMag
e100-WSN-Mag3
e10-SN-NoMag
e10-WSN-NoMag
e10-WSN-Mag3
0
10
20
30
40
50
60
70
80
t (Myr)
100
10
1
$M_{\rm H^+}/M_{\rm H,tot}(t=0)$ (%)
e100-NoF-NoMag
e100-SN-NoMag
e100-W-NoMag
e100-WSN-NoMag
e100-WSN-Mag3
e10-SN-NoMag
e10-WSN-NoMag
e10-WSN-Mag3
0
10
20
30
40
50
60
70
80
t (Myr)

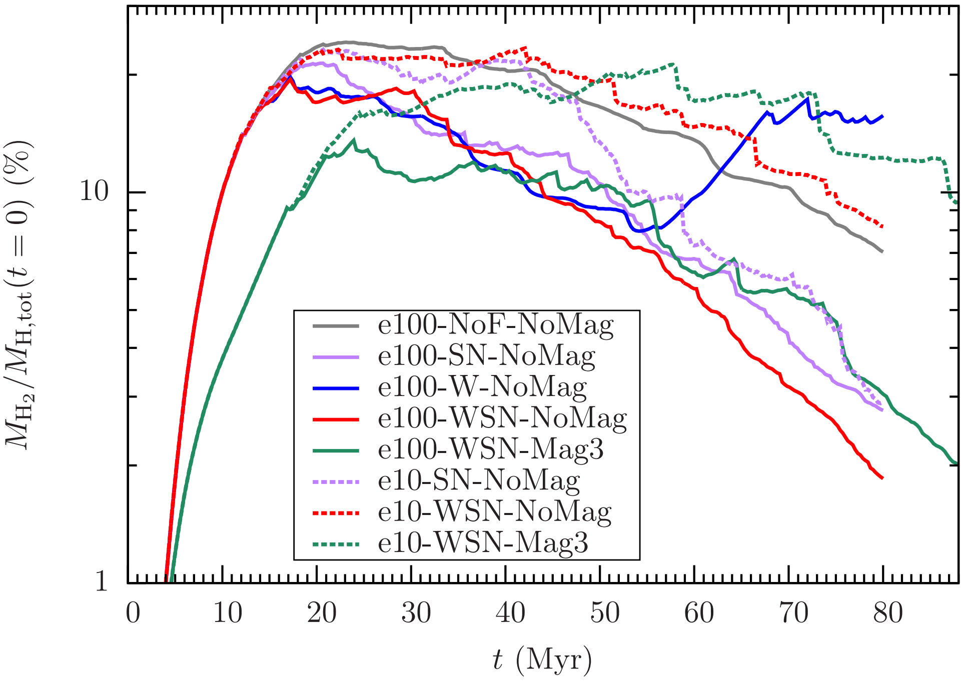

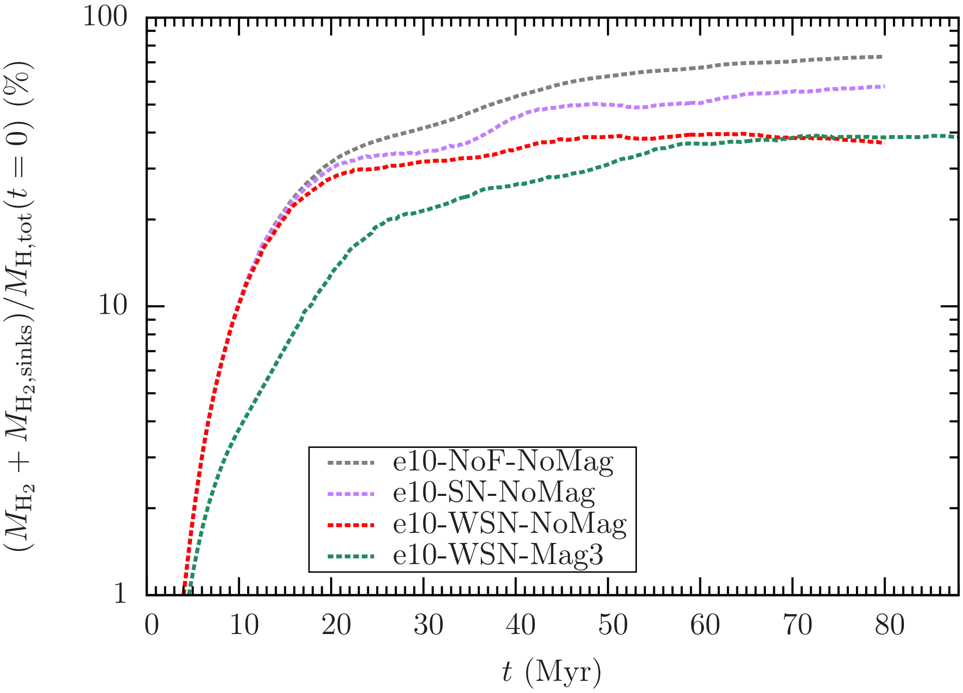

Figure 5.13: *Evolution of the fraction of the total mass in gas (first plot) and in sinks (second plot) and of the total hydrogen mass in* H *(third plot),* H^+ *(fourth plot),* H_2 *(fifth plot) and "sub-grid"* H_2 *(sixth plot) in the different simulations.*

lower limits on the true values. Moreover, the H^+ mass fractions are also underestimated due to the lack of photoionisation feedback.

The final total gas mass is larger than the total mass in sink particles at the final output time in all but two of the simulations. For the run without feedback (e100-NoF-NoMag), we find that at $t = 80\,\mathrm{Myr} \sim 75\%$ of the initial gas mass has been converted into stars. Moreover, this run is still actively forming stars, and so at later times this fraction would be even higher. For instance, running the simulation until $t = 190\,\mathrm{Myr}$ produces a final total mass in sink particles $\sim 97\%$ of the initial mass, i.e. almost all of the initial mass in the disc has been converted into stars. This is clearly not representative of the behaviour of a real disc galaxy and demonstrates the vital role that stellar feedback plays in regulating the star formation rate.

Due to the inefficient energy transfer by SNe alone at $\epsilon_{\mathrm{SF}} = 0.1$, e10-SN-NoMag also shows that a significant fraction of the initial mass ($\sim 60\%$) is locked-up into sink particles at $t = 80\,\mathrm{Myr}$. This is clearly unphysical, as large fractions of gas frozen into sink particles should in principle return to the grid via stellar feedback (as for the e10-WSN models, see Sec. 3.4). In this case, however, we expect this recycled material to collapse and form new sink particles in short time-scales, as SNe alone at low ϵ_{SF} are inefficient in providing sufficient pressure support to the gas (see Sec. 5.3.1).

The same simulation with $\epsilon_{\mathrm{SF}} = 1$ (e100-SN-NoMag) has a much higher number of SN explosions and indeed shows a much smaller final sink particle mass fraction, $\sim 22\%$. After $\sim 40 - 50\,\mathrm{Myr}$ in this run, both the total gas and total sink particles masses flatten due to the development of powerful outflows that reduce further star formation.

Runs with $\epsilon_{\mathrm{SF}} = 1$ and stellar winds (with and without SNe: runs e100-W-NoMag, e100-WSN-NoMag and e100-WSN-Mag3) convert much less gas into sink particles due to the inclusion of this early feedback mechanism, with a final total mass of sink particles between 10 and 20 % of the initial total mass. As in the case with only SNe for $\epsilon_{\mathrm{SF}} = 1$, runs e100-WSN-NoMag and e100-WSN-Mag3 produce outflows that shut down the formation of new stars and the evolution of the gas and sink masses flattens at late times.

A particularly interesting case is the sudden drop (rise) of the gas (sinks) mass at later times for the model with only stellar winds (run e100-W-NoMag). This is related to a burst of star formation caused by the lack of pressure support from feedback. As time goes by, the number of stars injecting significant wind energy decreases as the most massive stars die. As a result, the disc loses pressure support and starts to collapse, ultimately producing a new burst of star formation.

Finally, runs e10-WSN-NoMag and e10-WSN-Mag3 convert more mass into sinks due to the lower pressure support from stellar feedback in comparison to the corresponding runs with $\epsilon_{\mathrm{SF}} = 1$.

The total gas mass is dominated by H at all times for all simulations and the mass fractions in H^+ and H_2 are always below 20%. All models show an initial decrease of atomic hydrogen mass and a corresponding increase in H_2 due to a combination of gravitational collapse and weak compression from initial turbulent motions. Runs with magnetic fields reach a smaller peak H_2 mass fraction due to additional magnetic pressure support of the dense gas that counteracts the effects of gravity.

At $t \gtrsim 20\,\mathrm{Myr}$, run e100-NoF-NoMag does not produce ionised gas due to lack of stellar feedback, and atomic hydrogen is continuously converted into H_2 via gravity. The molecular gas content decreases with time due to continuous accretion onto sink particles.

Simulations with $\epsilon_{\mathrm{SF}} = 1$ and SNe (with and without stellar winds, e100-SN-NoMag, e100-WSN-NoMag, e100-WSN-Mag3) show an even steeper decrease in H_2, and a consequent increase in H and H^+, at the moment where stellar feedback is able to convert significant quantities of molecular into atomic and ionised hydrogen. e100-W-NoMag has a similar behaviour but produces higher H and smaller H^+ mass fractions at early times due to the lack of powerful SN explosions that shock-heat the cold gas directly into the ionised phase. Stellar winds are mostly responsible for converting cold into warm gas through weak shock-heating and ram pressure, while SNe are able to move substantial amounts of cold gas directly into the hot phase. After 55 Myr, atomic and ionised hydrogen are converted into H_2 due to disc collapse. New stars are formed, the H^+ mass fraction increases and the conversion from atomic to molecular hydrogen is slowed down by stellar winds.

Simulations including stellar winds and SNe with $\epsilon_{\mathrm{SF}} = 0.1$ (e10-WSN-NoMag, e10-WSN-Mag3) show smaller H and H^+ mass fractions and larger H_2 masses with respect to their counterparts with $\epsilon_{\mathrm{SF}} = 1$. This is not surprising, as less injected energy corresponds to smaller amounts of cold gas moved to the warm and hot phases.

Run e10-SN-NoMag is similar to the model without feedback. The H_2 mass fraction is smaller with respect to e100-NoF-NoMag due to the combination of large quantities of cold gas converted into stars (see first row) and shock-heating from massive stars. The H mass fraction is still higher due to (limited) pressure support provided by SNe that counteracts the conversion from molecular to atomic hydrogen via gravitational collapse. SNe alone at low ϵ_{SF} have small energy transfer efficiencies and therefore produce less ionised gas than in the case when stellar winds are included.

Assuming that for models with $\epsilon_{\mathrm{SF}} = 0.1$ each sink has 64.3% of its mass in the form H_2, we find final H_2 mass fractions lying in the range $40 - 80\%$, depending if and what feedback mechanism is included. In general, we find that the “sub-grid” H_2 mass fraction decreases for increasing energy transfer efficiency of feedback, as less gas mass is locked-up into sink particles (see first row). As already discussed, this locked-up gas does not take part in the global gas dynamics. Therefore, these mass fractions should be considered as the product of a pure academic exercise, rather than true results of our models.

For models with $\epsilon_{\rm SF} = 0.1$ and stellar winds (e10-WSN-NoMag, e10-WSN-Mag3), we find a gas surface density ratio $\Sigma_{\rm H_2}/\Sigma_{\rm H}$ between 0.1 and 0.4, and up to 0.7 when the “sub-grid” H_2 is included. This is consistent with the molecular to atomic hydrogen surface densities inferred from observations of 33 nearby spiral galaxies by Schruba et al. (2011). They find that, for $\Sigma_{\rm H+H_2} \lesssim 10\,{\rm M_\odot}$ pc^{-2}, this ratio is 0.1-20, with most of the galaxies having $\Sigma_{\rm H_2}/\Sigma_{\rm H} = 0.1 - 1$. Runs e10-SN-NoMag, e10-NoF-NoMag (and therefore e100-NoF-NoMag) also agree with observations, reaching a ratio of molecular to atomic mass greater than 1 when the “sub-grid” H_2 is included. Simulations with $\epsilon_{\rm SF} = 1$ and stellar feedback (e100-SN-NoMag, e100-W-NoMag, e100-WSN-NoMag, e100-WSN-Mag3) have $\Sigma_{\rm H_2}/\Sigma_{\rm H} \sim 0.1 - 0.3$ between 20 and 60 Myr. With the exception of e100-W-NoMag, this ratio falls below 0.1 at late times due to the decrease in H_2 mass.

Volume filling fractions

We define five temperature cuts (see Walch et al., 2015):

- hot: $T > 3 \times 10^5$ K;
- warm-hot: $8000 < T \leqslant 3 \times 10^5$ K;
- warm: $300 < T \leqslant 8000$ K;
- cold: $30 < T \leqslant 300$ K;
- molecular: $T \leqslant 30$ K;

and we plot the evolution of their volume filling fractions within $z = \pm 250\,$pc in Fig. 5.14. We exclude the molecular phase, as its VFF is always negligible.

For e100-NoF-NoMag, the VFF of the hot gas is always very large, as the disc collapses towards $z = 0$ and the hot halo gas fills the rest of the volume. Small fractions of the volume are occupied by warm-hot unstable gas due to partial mixing of the disc with the hot coronal gas. The remaining fraction of the volume is occupied by the warm component, with VFF $\lesssim 10\%$. The cold gas VFF is always negligible and decreases due to continuous star formation.

For the simulation with only stellar winds (e100-W-NoMag), after the first phase of disc contraction the hot gas VFF decreases and the volume is

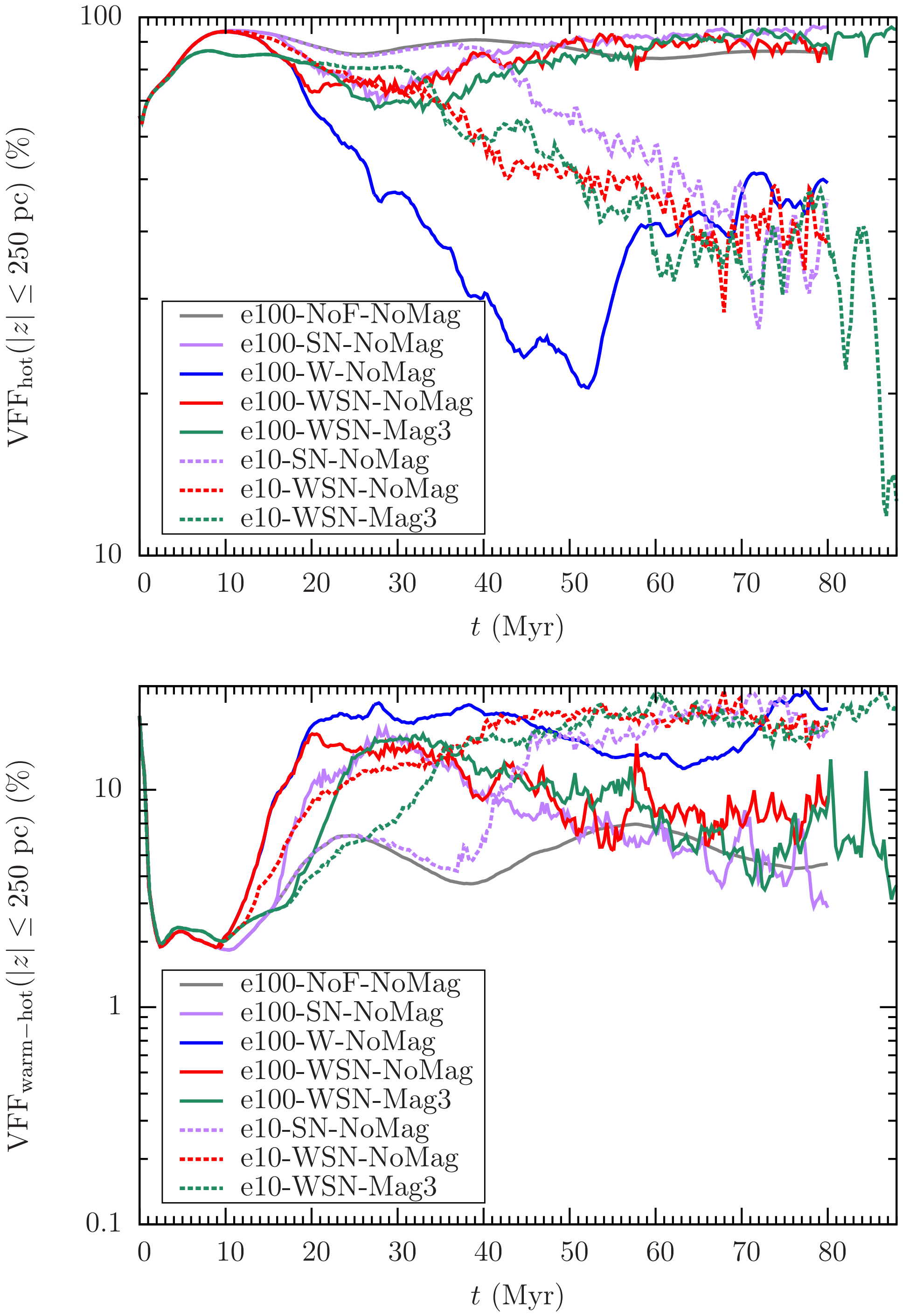
100
10
0
10
20
30
40
50
60
70
80
t (Myr)
$\mathrm{VFF_{hot}}(|z| \leq 250\ \mathrm{pc})$ (%)
e100-NoF-NoMag
e100-SN-NoMag
e100-W-NoMag
e100-WSN-NoMag
e100-WSN-Mag3
e10-SN-NoMag
e10-WSN-NoMag
e10-WSN-Mag3
10
1
0.1
0
10
20
30
40
50
60
70
80
t (Myr)
$\mathrm{VFF_{warm-hot}}(|z| \leq 250\ \mathrm{pc})$ (%)
e100-NoF-NoMag
e100-SN-NoMag
e100-W-NoMag
e100-WSN-NoMag
e100-WSN-Mag3
e10-SN-NoMag
e10-WSN-NoMag
e10-WSN-Mag3

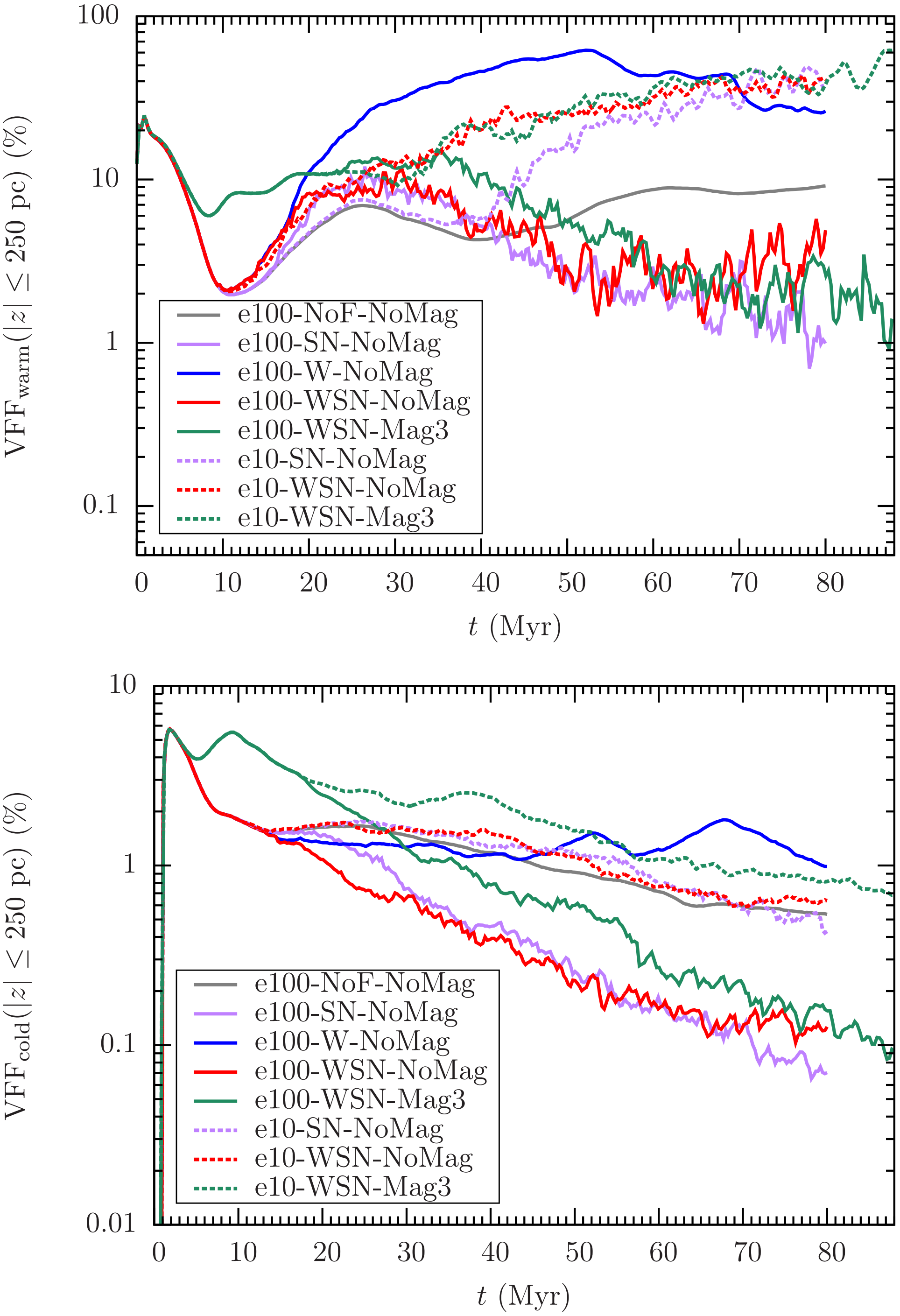

Figure 5.14: *Evolution of the hot ($T > 3 \times 10^5$ K, first plot), warm-hot ($8000 < T \leqslant 3 \times 10^5$ K, second plot), warm ($300 < T \leqslant 8000$ K, third plot) and cold ($30 < T \leqslant 300$ K, fourth plot) volume filling fractions within $z = \pm 250\,\mathrm{pc}$ for different simulations.*

filled by warm gas pushed to large scale heights by stellar winds. Around 20% of the volume is in the form of warm-hot unstable gas, while the cold phase stabilises itself at $\gtrsim 1\%$. Stellar winds are still able to produce hot gas, but their impact is limited with respect to SNe, as cold and warm gas is gently pushed around and mildly heated by their continuous action on the medium. At late times we find an increase in the hot and warm-hot VFFs due to a second main burst of star formation.

When SNe are included, the evolution of the VFFs is bimodal in $\epsilon_{\rm SF}$. For $\epsilon_{\rm SF} = 1$ (e100-SN-NoMag, e100-WSN-NoMag, e100-WSN-Mag3), we find large quantities of hot gas, as SNe are responsible for the conversion from cold gas directly into the hot phase. Hot, high-pressure gas fills $\approx 90\%$ of the mid-plane due to a large number of SNe exploding during the simulation. The warm, warm-hot and cold VFFs decrease rapidly since these phases are efficiently converted into hot gas or launched to $|z| \gg 250\,{\rm pc}$ via outflows.

When $\epsilon_{\rm SF} = 0.1$ (e10-SN-NoMag, e10-WSN-NoMag, e10-WSN-Mag3), we find the opposite trend: less energy is injected by stellar feedback, reducing the hot gas VFF to $\sim 40\%$, while the VFFs of the warm and the warm-hot phases reach $\sim 40\%$ and $\sim 20\%$, respectively. The cold gas VFF is still small, but higher than in the corresponding models with $\epsilon_{\rm SF} = 1$.

Runs with magnetic fields (e100-WSN-Mag3, e10-WSN-Mag3) produce higher VFFs of the cold phase due to additional magnetic pressure support of the dense ISM at all times. This effect, however, is likely to be underestimated due to the continuous loss of magnetic energy via sink particles creation and accretion of cold gas (see Sec. 3.4).

Runs with $\epsilon_{\rm SF} = 0.1$ (and e100-W-NoMag) show a good agreement with the VFFs of the different ISM phases close to the mid-plane of MW-like galaxies predicted by de Avillez (2000); Kalberla & Kerp (2009). Simulations with $\epsilon_{\rm SF} = 1$ (with the exception of e100-W-NoMag) have too large hot gas VFFs and the ISM in these runs is more representative of starbursting systems (see Sec. 5.3.4).

5.3.3 Star formation

We compute the SFR of each simulation by summing the mass in stars within sink particles ($\epsilon_{\rm SF} \times M_{\rm p}$) at their respective $t_{\rm c}$ and the mass accreted and transformed into stars ($\epsilon_{\rm SF} \times \dot{M}_{\rm p} \times \Delta t$) at $t > t_{\rm c}$. This gives us a direct and well defined way to compute the SFR in our simulations. We call this quantity "instantaneous" or "numerical" SFR. We bin this quantity in intervals of $\Delta t_{\rm SFR} = 1\,{\rm Myr}$, so that

$$\mathrm{SFR}_{\rm inst}(t) = \frac{\epsilon_{\rm SF}}{\Delta t_{\rm SFR}} \sum_{\rm p}^{N_{\rm p}} \big(M_{\rm p}(t = t_{\rm c}) + \dot{M}_{\rm p}(t) \times \Delta t \big), \tag{5.3}$$

for $t - \frac{\Delta t_{\rm SFR}}{2} < t < t + \frac{\Delta t_{\rm SFR}}{2}$ and with Δt time-step corresponding to the accretion event, typically ~ 800 yr when feedback is included. The instantaneous SFR has the benefit of providing a rigorous measure of the star formation activity in the simulations. However, it has some disadvantages. First, it has to be binned over some temporal range. Second, especially for low SFR and/or small $\Delta t_{\rm SFR}$, its evolution is quite bursty, with long intervals where $\rm SFR_{inst} = 0$. Third, it cannot be compared with SFRs constrained by observations, where the mass of stars formed is averaged over a certain time-scale dependent on the employed star formation tracer. For these reasons, we also define a "delayed" or "observed" $\rm SFR_{del}$ by smoothing $\rm SFR_{inst}$ in a way similar to observations. Due to our assumed IMF, each massive star tracks $120\,\rm M_\odot$ of gas converted into stars. We smooth the contribution of each massive star i to the SFR by averaging it over its corresponding lifespan, so that the delayed SFR can be written as

$$\mathrm{SFR_{del}}(t) = \sum_{i}^{N_*} \frac{120\,\mathrm{M_\odot}}{t_{\rm ls,i}} \ , \tag{5.4}$$

for $t_{\rm sc,i} < t < t_{\rm sc,i} + t_{\rm ls,i}$, with $t_{\rm sc,i}$ and $t_{\rm ls,i}$ creation time and lifespan of the star i, respectively.

In Fig. 5.15 we plot the evolution of the surface density (in the x-y plane, $(0.5\,\rm kpc)^2$) of $\rm SFR_{inst}$ and $\rm SFR_{del}$, as well as the average value of the latter (that is almost coincident with the average value of $\Sigma_{\rm SFR_{inst}}$).

e100-NoF-NoMag shows a smooth SFH due to the absence of feedback. Gas is continuously converted into stars and the average $\Sigma_{\rm SFR}$ settles to $8.8 \times 10^{-2}\ \rm M_\odot\ yr^{-1}\ kpc^{-2}$.

The run including SNe alone (e100-SN-NoMag) returns a similar SFH in the first ~ 30 Myr due to the inability of SNe to inject significant amount of energy into the ISM at early times (see Sec. 5.3.1). At later times, explosions from low mass progenitors are more frequent. Therefore, large quantities of cold gas are heated and expelled from the disc, decreasing the amount of gas available to form stars and therefore the SFR. Despite this decrease, the SFH of this model is still quite continuous. The average $\Sigma_{\rm SFR}$ is 2.5 times smaller than the one recovered without feedback. As discussed before, the latter has to be interpreted as a lower limit, since for later final times this ratio is likely to increase.

The inclusion of stellar winds (e100-W-NoMag, e100-WSN-NoMag, e100-WSN-Mag3) produces an average SFR ~ 1.75 (4.38) times smaller than for e100-SN-NoMag (e100-NoF-NoMag), regardless of the presence of SNe and/or magnetic fields, making stellar winds the dominant regulating mechanism for star formation *on these time-scales.* Runs with SN explosions show a more bursty SFH with respect to e100-W-NoMag due to a more clumpy

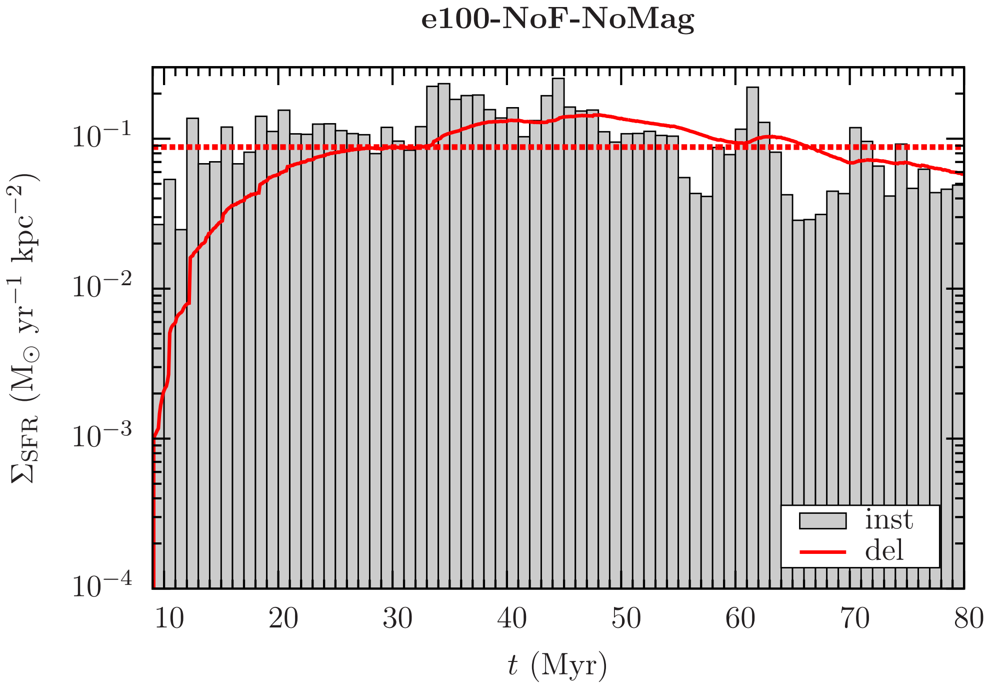
e100-NoF-NoMag

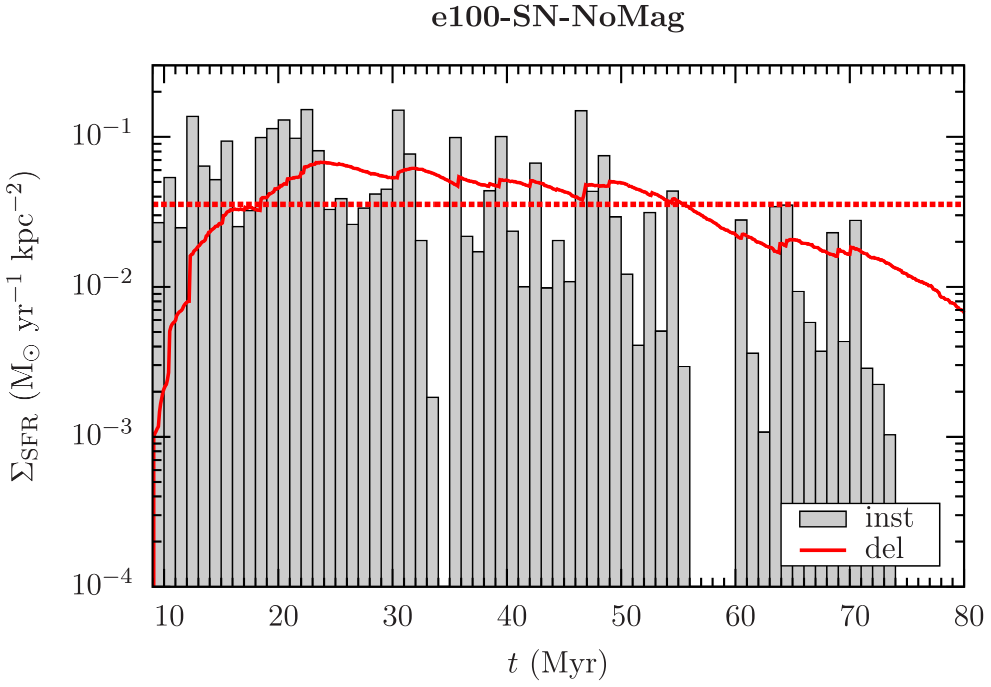
e100-SN-NoMag

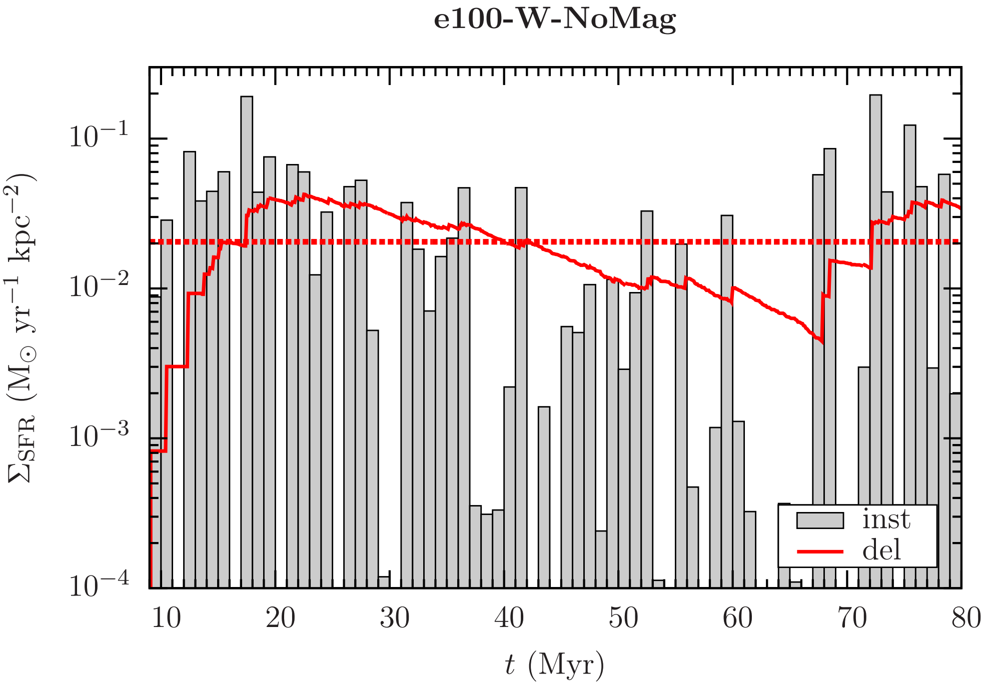
e100-W-NoMag

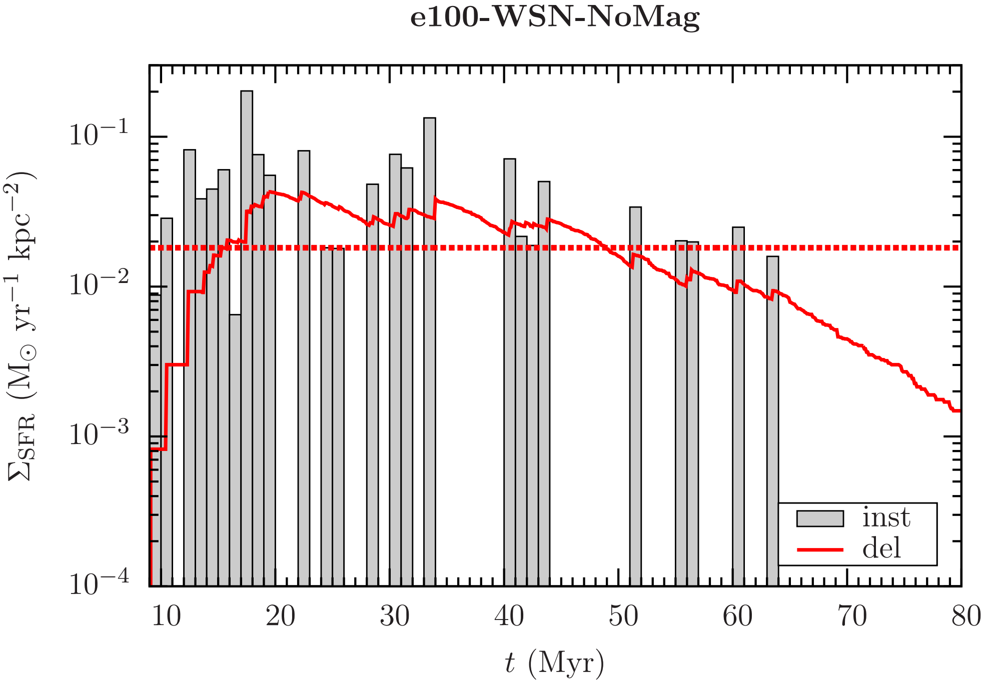
e100-WSN-NoMag

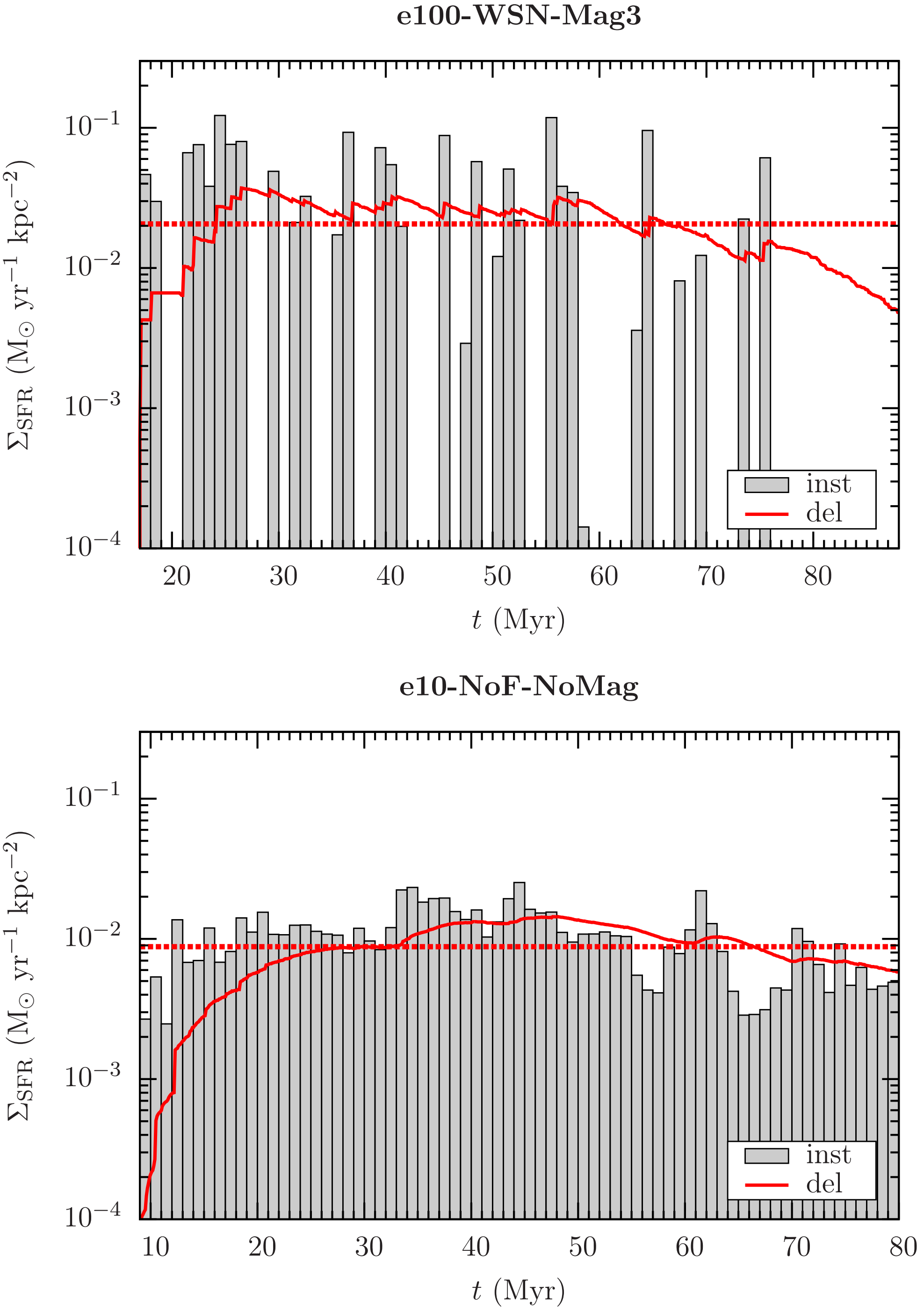
e100-WSN-Mag3
$\Sigma_{\rm SFR}$ (M$_\odot$ yr^{-1} kpc^{-2})
10^{-1}
10^{-2}
10^{-3}
10^{-4}
20
30
40
50
60
70
80
t (Myr)
inst
del
e10-NoF-NoMag
$\Sigma_{\rm SFR}$ (M$_\odot$ yr^{-1} kpc^{-2})
10^{-1}
10^{-2}
10^{-3}
10^{-4}
10
20
30
40
50
60
70
80
t (Myr)
inst
del

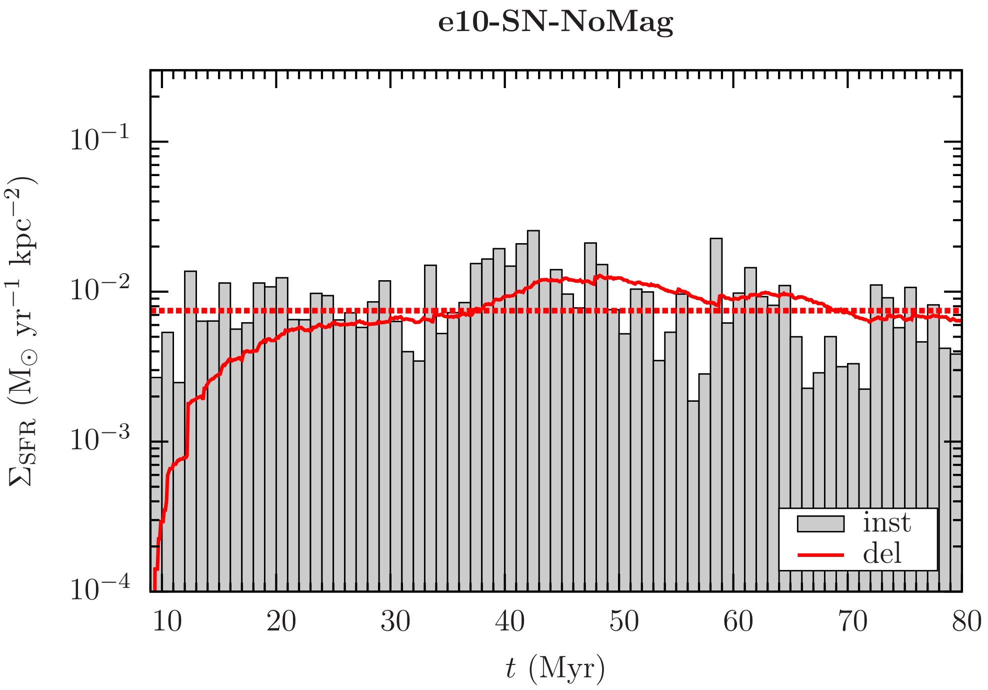
e10-SN-NoMag
$\Sigma_{\rm SFR}$ ($\rm M_\odot$ yr^{-1} kpc^{-2})
10^{-1}
10^{-2}
10^{-3}
10^{-4}
10
20
30
40
50
60
70
80
t (Myr)
inst
del

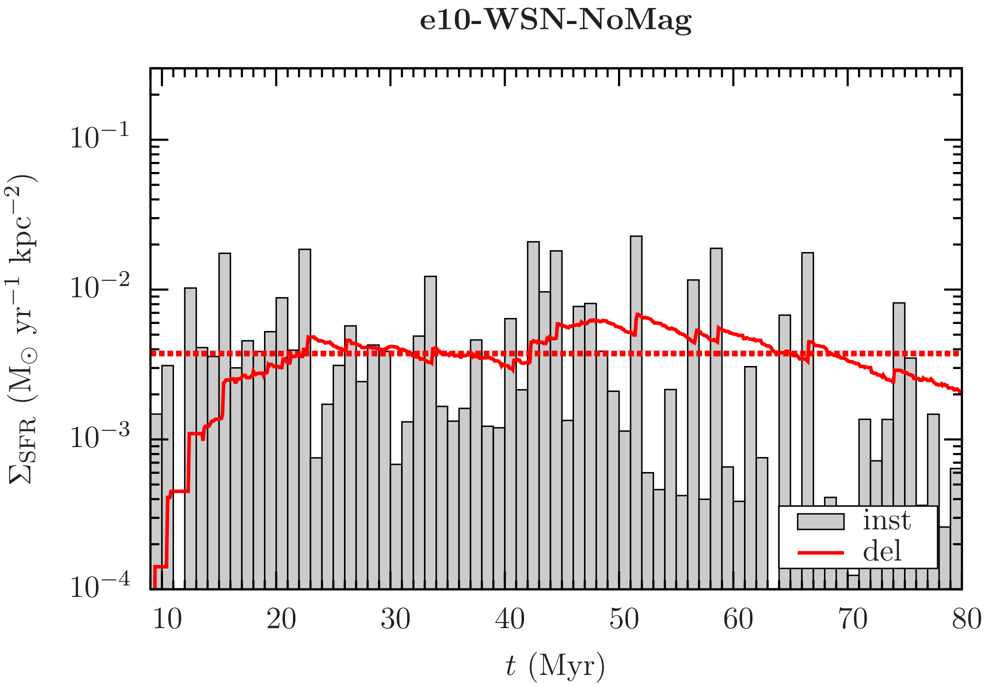
e10-WSN-NoMag
$\Sigma_{\rm SFR}$ ($\rm M_\odot$ yr^{-1} kpc^{-2})
10^{-1}
10^{-2}
10^{-3}
10^{-4}
10
20
30
40
50
60
70
80
t (Myr)
inst
del

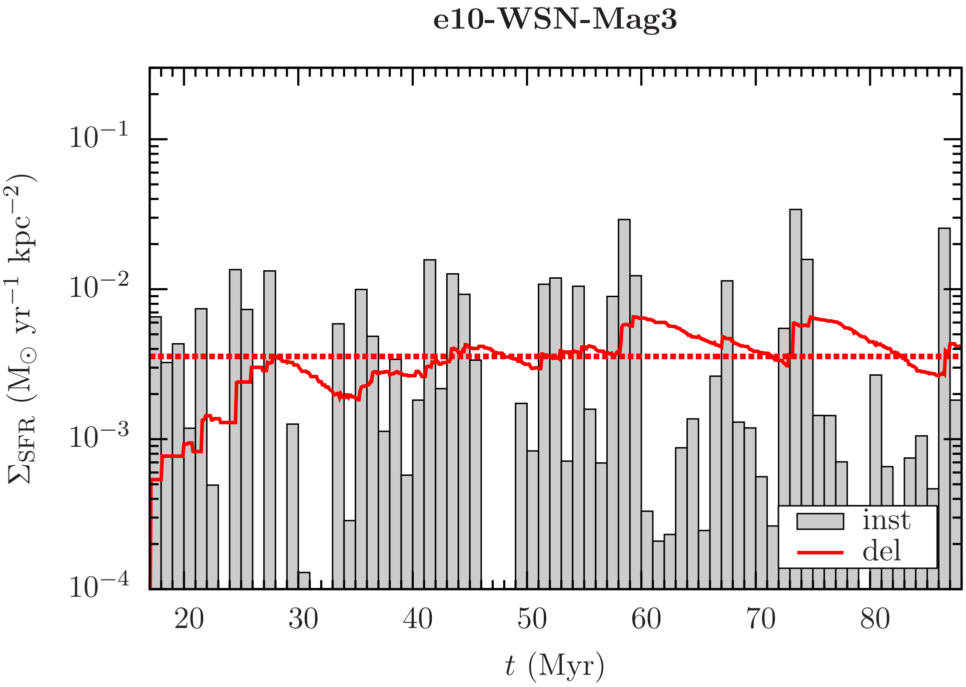

Figure 5.15: *Evolution of* $\Sigma_{\rm SFR}$ *(on the x-y plane) for different simulations. The grey bins represent* $\rm SFR_{inst}$ *(inst), while the red line is* $\rm SFR_{del}$ *(del). The red horizontal dashed line is the average* $\rm SFR_{del}$ *over 71 Myr of star formation activity.*

distribution of cold gas (as discussed in Sec. 5.3.2). At late times, the development of outflows in the e100-WSN simulations causes the SFR to drop towards low values due to the lack of gravitationally-unstable gas close to the mid-plane. On the other hand, the model with only stellar winds does not produce any outflows and a second burst of star formation occurs once feedback is no longer sufficient to provide pressure support for the disk. Magnetic fields do not play a major role on these time-scales, but delay the onset of star formation and therefore the development of outflows. Moreover, they increase the clustering of massive stars by creating fewer but more massive sink particles (see Table 5.2) due to additional pressure support of the cold and dense gas.

e10-SN-NoMag shows a more continuous SFH with respect to the same model with $\epsilon_{\rm SF} = 1$ as SNe alone at low $\epsilon_{\rm SF}$ do not efficiently counteract gravity both on local and global scales. The average SFR is 4.7 times smaller than the one recovered in e100-SN-NoMag. The SFH is similar to the one of e10-NoF-NoMag (i.e. e100-NoF-NoMag with all quantities rescaled by a factor of 0.1) and $\overline{\rm SFR}$ is 1.2 times smaller.

With both winds and SNe (e10-WSN-NoMag, e10-WSN-Mag3) the average SFR is 2 times smaller with respect to the case where only SNe are included, the same ratio found when comparing the same models with $\epsilon_{\rm SF} = 1$. Both runs do not produce outflows and have similar SFHs/$\overline{\rm SFR}$, with an average SFR around 5 times smaller with respect to the corresponding models with $\epsilon_{\rm SF} = 1$. This is also *at least* $\sim$ 24 times smaller than $\overline{\rm SFR}$ in the case of quasi-free-fall collapse (e100-NoF-NoMag).

5.3.4 Comparison with observations

We compare our models with observations of 23 (11 dwarfs and 12 large spirals) nearby "normal" star-forming galaxies by Leroy et al. (2008). These are composed by hundreds of radial profiles of $\Sigma_{\rm SFR}$, $\Sigma_{\rm H}$ and $\Sigma_{\rm H_2}$ (only for spirals) at 800 (spirals) and 400 (dwarf) pc resolution. We multiply their SFRs by a factor of 1.59 in order to rescale them from a Kroupa (2001) to a Salpeter (1955) IMF and we plot the corresponding data in the $\Sigma_{\rm SFR}$-$\Sigma_{\rm H+H_2}$ plane in Fig. 5.16. Each simulation point is shown at the characteristic time $t = t_{1/2}$, defined as the time at which half of the final total mass in stars has been formed (typically 20-40 Myr). The gas surface density is computed without (top) or with (bottom) the inclusion of the "sub-grid" H_2 for models with $\epsilon_{\rm SF} = 0.1$ (and including helium, as in Leroy et al., 2008). Moreover, we compare our SFRs with the ones predicted by the Kennicutt-Schmidt (KS) relation (Kennicutt, 1998, but see also e.g. Bigiel et al. 2008; Shetty et al. 2013, 2014),

$$\frac{\Sigma_{\rm SFR_{KS}}}{\rm M_\odot\, yr^{-1}\, kpc^{-2}} = 2.5 \times 10^{-4} \left(\frac{\Sigma_{\rm H+H_2}}{\rm M_\odot\, pc^{-2}} \right)^{1.4} . \tag{5.5}$$

Simulations with $\epsilon_{\rm SF} = 1$ are located at large $\Sigma_{\rm SFR}$ for their typical gas surface densities and do not agree with observations. This is particularly true for e100-NoF-NoMag, where $\Sigma_{\rm SFR}$ is about 100 times higher than the one predicted by the KS relation. Runs with stellar feedback (e100-SN-NoMag, e100-W-NoMag, e100-WSN-NoMag, e100-WSN-Mag3) are close to few observed profiles at $\Sigma_{\rm SFR} \gg 10^{-2}{\rm M_\odot}$ yr^{-1} kpc^{-2} for $\Sigma_{\rm H+H_2} = 7 - 10\,{\rm M_\odot}$ pc^{-2}. However, these data are mostly coming from observations of starburst dwarf irregular galaxies (in particular NGC 4449) for which measurements of $\Sigma_{\rm H_2}$ are missing. According to Leroy et al. (2008), we expect these galaxies to have $\Sigma_{\rm H_2} \approx 1-3 \times \Sigma_{\rm H}$. This would shift the profiles towards the right side, therefore making these simulations in disagreement with observations. We conclude that runs at $\epsilon_{\rm SF} = 1$ are more likely to represent starburst, rather than "normal", galaxies (see below).

Models with $\epsilon_{\rm SF} = 0.1$ are closer to both the KS relation and the bulk of the observed data points. Runs without stellar winds (e10-NoF-NoMag,

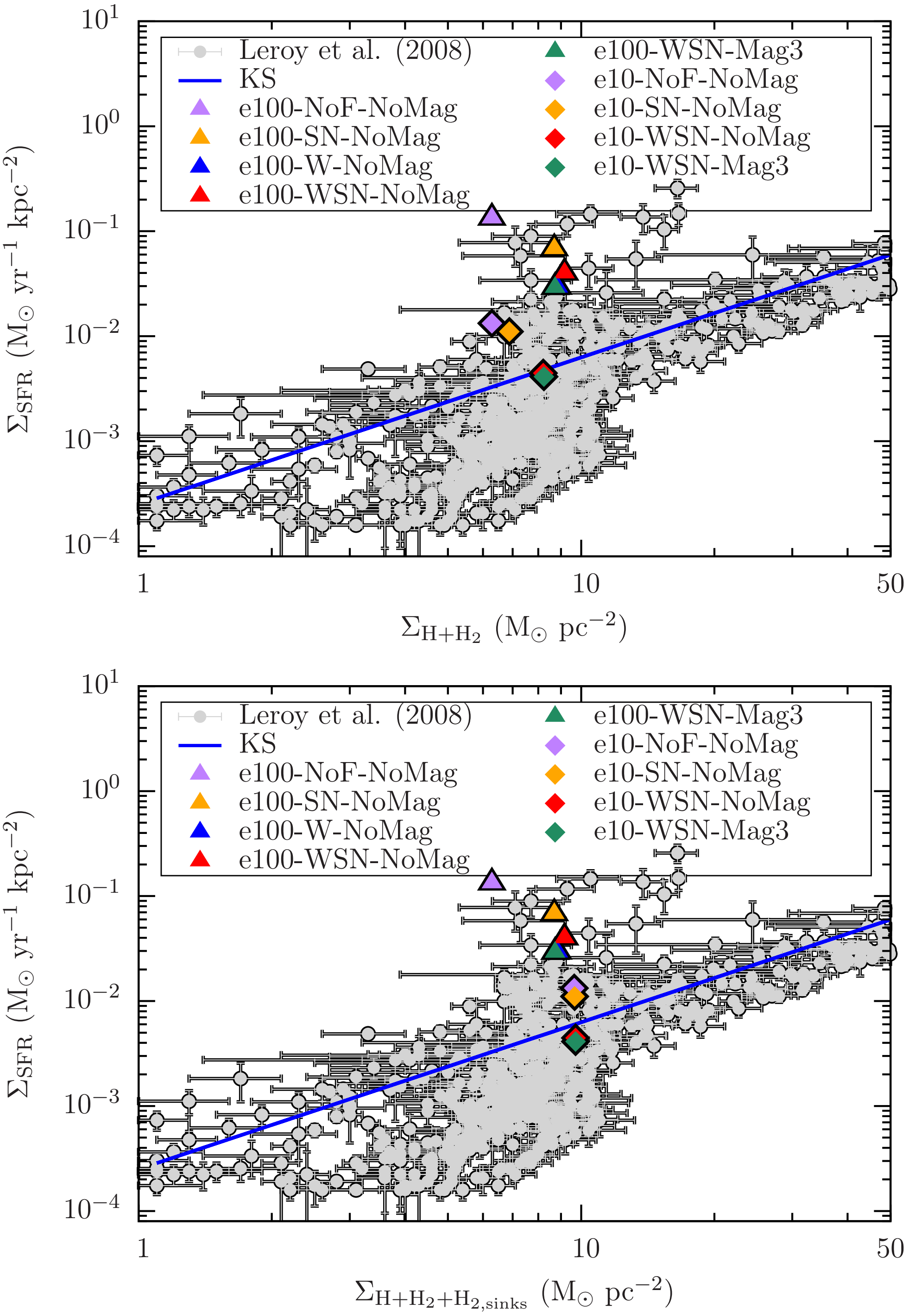

Figure 5.16: *SFR surface density vs.* H *plus* H_2 *surface density for different simulations at* $t = t_{1/2}$, *without (top) and with (bottom) the inclusion of "sub-grid"* H_2. *The grey points show the radial profiles from Leroy et al. (2008), while the blue line represents the KS relation.*

e10-SN-NoMag) show a better match with observations when the "sub-grid" H_2 is taken into account. When this is not included, the points shift towards lower gas surface densities and the models are at the edge of the observational dataset. Simulations with stellar winds (e10-WSN-NoMag, e10-WSN-Mag3) show a much better agreement with both the observed data and the KS relation, regardless of the inclusion of the "sub-grid" H_2.

As already shown in the previous sections, we find significantly different properties of the ISM depending on the assumed value of $\epsilon_{\rm SF}$. Models with $\epsilon_{\rm SF} = 1$ and including SNe produce vigorous outflows powered by the large thermal pressure of hot gas close to the mid-plane. The presence of large quantities of hot gas extending up to 1-2 kpc suggests that these simulations are representative of starbursting galaxies, such as NGC 253, where a diffuse (up to 10 kpc) thermal emission from very hot ($5 \times 10^7 \lesssim T \lesssim 10^8$ K) gas produced by stellar feedback and a consequent outflow in molecular, atomic and ionised gas has been observed by Cappi et al. (1999); Strickland et al. (2000, 2002); Bolatto et al. (2013); Lucero et al. (2015, but see also Strickland et al. 2004a,b). On the other hand, the same simulations with $\epsilon_{\rm SF} = 0.1$ do not produce outflows and are in agreement with observations of "normal" star-forming galaxies, especially when stellar winds are included. This implies that the small scale physics that sets $\epsilon_{\rm SF}$ at MCs-protostellar core scales is a key ingredient in regulating the ISM evolution on intermediate (pc-kpc) scales.

5.4 Conclusions

We study the impact of stellar winds and SNe on the three-phase ISM by running 3D, MHD, AMR simulations of a representative piece of a galactic disc with $\Sigma_{\rm gas} = 10\,{\rm M}_\odot\ {\rm pc}^{-2}$ and size $(500\,{\rm pc})^2 \times \pm\ 5\,{\rm kpc}$. We include an external, static stellar potential and self-gravity, radiative cooling and diffuse heating, magnetic fields, sink particles and stellar feedback in the form of stellar winds and SN explosions. We take into account dust and gas (self-)shielding and we track the distribution of molecular gas using a chemical network that allows us to follow the formation, evolution and destruction of five key chemical species: $\rm H, H^+, H_2, CO, C^+$. Star formation is modelled via sink particles' creation and accretion. We implement a simple sub-grid model to mimic the formation of massive stars within sink particles assuming star formation efficiencies of $\epsilon_{\rm SF} = 0.1$ and 1. We follow the evolution of each single massive star using the latest Geneva stellar tracks and we inject stellar feedback accordingly. We run simulations over a time-scale of 80-90 Myr with different combinations of star formation efficiency and feedback mechanism, with or without magnetic fields. We study the mutual dependence between stellar feedback, magnetic fields, and the multi-phase ISM.

We find:

- For a given stellar population, the energy injected by stellar winds is mostly dominated by short-lived very high-mass stars, while the majority of the energy injected as SNe comes from long-lived progenitors with lower masses. SNe dominate the total injected energy budget in the simulations. When both feedback processes are included, the total energy injected by SN explosions is ~ 5 times higher than the one from stellar winds.

- Stellar winds are the main star formation regulation mechanism at local scales, as they are able to stop accretion early on via energy injection from high-mass stars. SNe are still able to quench further star formation events but typically after $\approx 5-20\,\mathrm{Myr}$ due to the time delay between the formation and the explosion of massive stars.

- Stellar winds increase the energy transfer efficiency from SNe to the ISM via lowering the ambient medium density with which explosions interact. The stellar feedback energy transfer efficiency is a complex function of the SFR, the clustering of massive stars and the SFH of each simulation, which in turn depend on several factors. In general, the amount of energy transferred to the medium by SNe is higher for higher SFRs, clustering and presence of stellar winds. In the models with $\epsilon_{\mathrm{SF}} = 1$ including both stellar winds and SNe or SNe alone, we find an energy transfer efficiency between 1 and 10% at $t = 80 - 90\,\mathrm{Myr}$.

- SNe are mostly responsible for the conversion of warm, atomic and cold, atomic-molecular gas to a ionised, hot phase via shock-heating. Stellar winds are less energetic and convert most of the cold and warm gas into a warm and warm-hot phases via weak shock-heating and ram-pressure stripping.

- Stellar winds are the most efficient star formation regulation process on time-scales of $80 - 90\,\mathrm{Myr}$. Regardless of the presence of SNe and/or magnetic fields, the average SFR with stellar winds is at least $2 - 4$ times smaller than the one recovered when stellar feedback is not included, and ~ 2 times smaller than the models with SNe alone. This is also at least 24 times smaller with respect to the case where the disc goes in quasi-free-fall collapse. Magnetic fields do not play a major role in setting the global amount of gas converted into stars, but delay the star formation activity and increase the clustering of massive stars via additional pressure support of the cold gas.

- Simulations with $\epsilon_{\mathrm{SF}} = 1$ and SN feedback (with or without stellar winds) produce large VFFs of the hot phase close to the mid-plane. This over-pressurised gas launches powerful outflows that destroy the disc. When only stellar winds are included, the hot gas VFF drops to 20-50% and no outflows are present. Simulations with $\epsilon_{\mathrm{SF}} = 0.1$ including feedback do not produce any outflows and the disc stays bound, implying that powerful injection of energy by SNe is a necessary, but not sufficient, requirement for outflows driving.

- The thermodynamical properties of the gas strongly depend on the assumed value of ϵ_{SF}. This suggests that the small scale physics governing the star formation process is a key factor in the global evolution of the ISM at galactic scales.

- Models for $\epsilon_{\mathrm{SF}} = 0.1$ with stellar winds and SNe show the best agreement with observations of nearby "normal" star-forming galaxies. On the other hand, simulations with stellar winds and SNe or SNe alone at $\epsilon_{\mathrm{SF}} = 1$ appear to be more representative of starburst galaxies.

CHAPTER 6

Summary

In this thesis, we study the global impact of stellar winds and supernovae on the interstellar medium. We implement stellar winds and supernova feedback in the magneto-hydrodynamic code FLASH and we develop a subgrid model for star cluster sink particles.

We run simulations in a (256 pc)^3 periodic box to model the impact of supernova explosions on the multi-phase interstellar medium for different initial densities. For each initial density we drive supernovae at a fixed rate either at random positions, at density peaks, or both. We include radiative cooling and diffuse heating. We take into account dust and gas (self-)shielding and we track the distributions of $\mathrm{H}, \mathrm{H}^+, \mathrm{H}_2, \mathrm{CO}$, and C^+ using a chemical network. We show that supernovae located at random positions at high supernova rates result in hot gas filling a large fraction of the volume. This gas reaches high pressures due to the combination of explosions in the hot, low density medium and confinement in the periodic box. These pressures move the gas from a two-phase equilibrium to the single-phase, cold branch of the cooling curve. Molecular hydrogen dominates the mass, residing in small, dense clumps. Supernovae positioned in density peaks result in significant radiative losses, producing a filamentary interstellar medium with virtually no hot gas, and a small molecular hydrogen mass fraction. Varying the ratio of peak to random supernovae yields interstellar medium properties in between the two extremes, with a sharp transition for equal contributions.

We then take a step further and we model a representative piece of a galactic disc with size $(500\,\mathrm{pc})^2 \times \pm\, 5\,\mathrm{kpc}$ with self-consistent star formation. We include an external static galactic potential and self-gravity, radiative cooling and diffuse heating, dust and gas (self-)shielding, a chemical network, magnetic fields, sink particles and stellar winds and supernovae.

Star formation is modelled via sink particles creation, where each particle represents a star cluster or association. We mimic the formation of massive stars within clusters assuming different star formation efficiencies. We follow their evolution using the latest Geneva stellar tracks and we inject stellar feedback accordingly. We find that stellar winds are the most important star formation regulation mechanism over time-scales of $\lesssim 100\,\mathrm{Myr}$ as they further reduce the development of Jean-unstable gas at large scales and quench accretion onto sink particles at early times. The interstellar medium properties strongly depend on our assumed star formation efficiency in the dense gas, implying that the small scale physics governing the star formation process is crucial for the gas dynamics at galactic scales. For star formation efficiency of 100% we find large star formation rates. The inclusion of supernovae produces a hot, over-pressurised gas with high volume filling fraction that launches powerful outflows from the disc, similarly to starbursting galaxies. Simulations for 10% star formation efficiency with stellar winds and supernovae lead to a disc that is bound to the mid-plane and are in agreement with observations of “normal” star-forming galaxies.

Bibliography

Ackermann M., Ajello M., Allafort A., Baldini L., et al., 2013, Science, 339, 807

Agertz O., Kravtsov A. V., Leitner S. N., Gnedin N. Y., 2013, ApJ, 770, 25

Aggarwal K. M., 1983, MNRAS, 202, 15P

Anderson H., Ballance C. P., Badnell N. R., Summers H. P., 2000, Journal of Physics B Atomic Molecular Physics, 33, 1255

Anderson H., Ballance C. P., Badnell N. R., Summers H. P., 2002, Journal of Physics B Atomic Molecular Physics, 35, 1613

André P., Men'shchikov A., Bontemps S., Könyves V., Motte F., Schneider N., et al., 2010, A&A, 518, L102

Aumer M., Burkert A., Johansson P. H., Genzel R., 2010, ApJ, 719, 1230

Bagetakos I., Brinks E., Walter F., de Blok W. J. G., Usero A., Leroy A. K., Rich J. W., Kennicutt Jr. R. C., 2011, AJ, 141, 23

Bally J., Devine D., Alten V., Sutherland R. S., 1997, ApJ, 478, 603

Balsara D. S., Kim J., Mac Low M.-M., Mathews G. J., 2004, ApJ, 617, 339

Bate M. R., Bonnell I. A., Price N. M., 1995, MNRAS, 277, 362

Berghöfer T. W., Bowyer S., Lieu R., Knude J., 1998, ApJ, 500, 838

Bernstein R. A., Freedman W. L., Madore B. F., 2002, ApJ, 571, 107

Bigiel F., Leroy A., Walter F., Brinks E., de Blok W. J. G., Madore B., Thornley M. D., 2008, AJ, 136, 2846

Binney J., Merrifield M., 1998, Galactic Astronomy. Princeton University Press

Binney J., Nipoti C., Fraternali F., 2009, MNRAS, 397, 1804

Blaauw A., 1961, Bull. Astron. Inst. Netherlands, 15, 265

Black J. H., Dalgarno A., 1977, ApJS, 34, 405

Bleuler A., Teyssier R., 2014, MNRAS, 445, 4015

Blondin J. M., Wright E. B., Borkowski K. J., Reynolds S. P., 1998, ApJ, 500, 342

Bolatto A. D., Warren S. R., Leroy A. K., Walter F., Veilleux S., Ostriker E. C., Ott J., Zwaan M., Fisher D. B., Weiss A., Rosolowsky E., Hodge J., 2013, Nature, 499, 450

Boneberg D. M., Dale J. E., Girichidis P., Ercolano B., 2015, MNRAS, 447, 1341

Bouchut F., Klingenberg C., Waagan K., 2007, Numer. Math., 108, 7

Bouchut F., Klingenberg C., Waagan K., 2010, Numer. Math., 115, 647

Bowyer S., Lieu R., Sidher S. D., Lampton M., Knude J., 1995, Nature, 375, 212

Brighenti F., D'Ercole A., 1994, MNRAS, 270, 65

Caldú-Primo A., Schruba A., Walter F., Leroy A., Sandstrom K., de Blok W. J. G., Ianjamasimanana R., Mogotsi K. M., 2013, AJ, 146, 150

Cappi M., Persic M., Bassani L., Franceschini A., Hunt L. K., Molendi S., Palazzi E., Palumbo G. G. C., Rephaeli Y., Salucci P., 1999, A&A, 350, 777

Churchwell E., 2002, ARA&A, 40, 27

Cioffi D. F., McKee C. F., Bertschinger E., 1988, ApJ, 334, 252

Clark P. C., Glover S. C. O., Klessen R. S., 2012, MNRAS, 420, 745

Cox D. P., Smith B. W., 1974, ApJ, 189, L105

Creasey P., Theuns T., Bower R. G., 2013, MNRAS, 429, 1922

Creasey P., Theuns T., Bower R. G., Lacey C. G., 2011, MNRAS, 415, 3706

Crowther P. A., 2007, ARA&A, 45, 177

Crutcher R. M., 1999, ApJ, 520, 706

Dale J. E., Ercolano B., Bonnell I. A., 2012, MNRAS, 424, 377

Dale J. E., Ngoumou J., Ercolano B., Bonnell I. A., 2014, MNRAS, 442, 694

de Avillez M. A., 2000, MNRAS, 315, 479

de Avillez M. A., Breitschwerdt D., 2004, A&A, 425, 899

de Avillez M. A., Breitschwerdt D., 2007, ApJ, 665, L35

Dehnen W., Binney J., 1998, MNRAS, 294, 429

Dib S., Bell E., Burkert A., 2006, ApJ, 638, 797

Dijkstra M., Wyithe S., Haiman Z., Mesinger A., Pentericci L., 2014, MNRAS, 440, 3309

Dobbs C. L., Pringle J. E., 2013, MNRAS, 432, 653

Dong R., Draine B. T., 2011, ApJ, 727, 35

Downes D., Solomon P. M., 1998, ApJ, 507, 615

Draine B. T., 1978, ApJS, 36, 595

Draine B. T., 1990, in Blitz L., ed., The Evolution of the Interstellar Medium Vol. 12 of Astronomical Society of the Pacific Conference Series, Evolution of interstellar dust. pp 193–205

Draine B. T., 2011, Physics of the Interstellar and Intergalactic Medium

Draine B. T., Bertoldi F., 1996, ApJ, 468, 269

Dubey A., Antypas K., Calder A. C., Daley C., Fryxell B., Gallagher J. B., Lamb D. Q., Lee D., Olson K., Reid L. B., Rich P., Ricker P. M., Riley K. M., Rosner R., Siegel A., Taylor N. T., Weide K., Timmes F. X., Vladimirova N., ZuHone J., 2013, International J. High Perf. Comput. Appl., 551, L105

Dubey A., Fisher R., Graziani C., Jordan IV G. C., Lamb D. Q., Reid L. B., Rich P., Sheeler D., Townsley D., Weide K., 2008, in Pogorelov N. V., Audit E., Zank G. P., eds, Numerical Modeling of Space Plasma Flows Vol. 385 of Astronomical Society of the Pacific Conference Series, Challenges of Extreme Computing using the FLASH code. p. 145

Ekström S., Georgy C., Eggenberger P., Meynet G., Mowlavi N., Wyttenbach A., Granada A., Decressin T., Hirschi R., Frischknecht U., Charbonnel C., Maeder A., 2012, A&A, 537, A146

Eldridge J. J., Langer N., Tout C. A., 2011, MNRAS, 414, 3501

Elmegreen B. G., Burkert A., 2010, ApJ, 712, 294

Eswaran V., Pope S., 1988, Computers and Fluids, 16, 257

Federrath C., Banerjee R., Clark P. C., Klessen R. S., 2010, ApJ, 713, 269

Ferrière K. M., 2001, Rev. Mod. Phys., 73, 1031

Field G. B., Goldsmith D. W., Habing H. J., 1969, ApJ, 155, L149

Frank A., Ray T. P., Cabrit S., Hartigan P., Arce H. G., Bacciotti F., Bally J., Benisty M., Eislöffel J., Güdel M., Lebedev S., Nisini B., Raga A., 2014, Protostars and Planets VI, pp 451–474

Freyer T., Hensler G., Yorke H. W., 2003, ApJ, 594, 888

Freyer T., Hensler G., Yorke H. W., 2006, ApJ, 638, 262

Fryxell B., Olson K., Ricker P., Timmes F. X., Zingale M., Lamb D. Q., MacNeice P., Rosner R., Truran J. W., Tufo H., 2000, ApJS, 131, 273

Fujii M. S., Portegies Zwart S., 2011, Science, 334, 1380

Fukugita M., Peebles P. J. E., 2006, ApJ, 639, 590

Fukui Y., Moriguchi Y., Tamura K., Yamamoto H., Tawara Y., Mizuno N., Onishi T., Mizuno A., Uchiyama Y., Hiraga J., Takahashi T., Yamashita K., Ikeuchi S., 2003, PASJ, 55, L61

Gatto A., Fraternali F., Read J. I., Marinacci F., Lux H., Walch S., 2013, MNRAS, 433, 2749

Gatto A., Walch S., Low M.-M. M., Naab T., Girichidis P., Glover S. C. O., Wünsch R., Klessen R. S., Clark P. C., Baczynski C., Peters T., Ostriker J. P., Ibáñez-Mejía J. C., Haid S., 2015, MNRAS, 449, 1057

Gent F. A., Shukurov A., Fletcher A., Sarson G. R., Mantere M. J., 2013, MNRAS, 432, 1396

Genzel R., Tacconi L. J., Gracia-Carpio J., et al., 2010, MNRAS, 407, 2091

Georgy C., Ekström S., Meynet G., Massey P., Levesque E. M., Hirschi R., Eggenberger P., Maeder A., 2012, A&A, 542, A29

Gies D. R., 1987, ApJS, 64, 545

Gies D. R., Bolton C. T., 1986, ApJS, 61, 419

Girichidis P., Naab T., Walch S., Hanasz M., Mac Low M.-M., Ostriker J. P., Gatto A., Peters T., Wünsch R., Glover S. C. O., Klessen R. S., Clark P. C., Baczynski C., 2015, ArXiv e-prints

Girichidis P., Walch S., Naab T., Gatto A., Wünsch R., Glover S. C. O., Klessen R. S., Clark P. C., Peters T., Derigs D., Baczynski C., 2015, ArXiv e-prints

Glover S. C. O., Clark P. C., 2012a, MNRAS, 421, 116

Glover S. C. O., Clark P. C., 2012b, MNRAS, 421, 9

Glover S. C. O., Federrath C., Mac Low M.-M., Klessen R. S., 2010, MNRAS, 404, 2

Glover S. C. O., Mac Low M.-M., 2007a, ApJS, 169, 239

Glover S. C. O., Mac Low M.-M., 2007b, ApJ, 659, 1317

Gnat O., Ferland G. J., 2012, ApJS, 199, 20

Goodman A. A., Barranco J. A., Wilner D. J., Heyer M. H., 1998, ApJ, 504, 223

Gritschneder M., Naab T., Walch S., Burkert A., Heitsch F., 2009, ApJ, 694, L26

Gueth F., Guilloteau S., 1999, A&A, 343, 571

Habing H. J., 1968, Bull. Astron. Inst. Netherlands, 19, 421

Haffner L. M., Reynolds R. J., Tufte S. L., Madsen G. J., Jaehnig K. P., Percival J. W., 2003, ApJS, 149, 405

Hanasz M., Lesch H., Naab T., Gawryszczak A., Kowalik K., Wóltański D., 2013, ApJ, 777, L38

Heiles C., 1967, ApJS, 15, 97

Heiles C., 2001, ApJ, 551, L105

Heiles C., Troland T. H., 2003, ApJ, 586, 1067

Heitsch F., Mac Low M.-M., Klessen R. S., 2001, ApJ, 547, 280

Hennebelle P., Iffrig O., 2014, A&A, 570, A81

Hennebelle P., Pérault M., 1999, A&A, 351, 309

Hewitt J. W., Yusef-Zadeh F., 2009, ApJ, 694, L16

Hill A. S., Joung M. R., Mac Low M.-M., Benjamin R. A., Haffner L. M., Klingenberg C., Waagan K., 2012, ApJ, 750, 104

Hopkins P. F., Kereš D., Oñorbe J., Faucher-Giguère C.-A., Quataert E., Murray N., Bullock J. S., 2014, MNRAS, 445, 581

Hubber D. A., Walch S., Whitworth A. P., 2013, MNRAS, 430, 3261

Iffrig O., Hennebelle P., 2015, A&A, 576, A95

Jappsen A.-K., Klessen R. S., Larson R. B., Li Y., Mac Low M.-M., 2005, A&A, 435, 611

Jenkins E. B., Tripp T. M., 2011, ApJ, 734, 65

Joung M. K. R., Mac Low M.-M., 2006, ApJ, 653, 1266

Kalberla P. M. W., Burton W. B., Hartmann D., Arnal E. M., Bajaja E., Morras R., Pöppel W. G. L., 2005, A&A, 440, 775

Kalberla P. M. W., Dedes L., 2008, A&A, 487, 951

Kalberla P. M. W., Kerp J., 2009, ARA&A, 47, 27

Karl S. J., Naab T., Johansson P. H., Kotarba H., Boily C. M., Renaud F., Theis C., 2010, ApJ, 715, L88

Keller B. W., Wadsley J., Benincasa S. M., Couchman H. M. P., 2014, MNRAS, 442, 3013

Kennicutt Jr. R. C., 1998, ApJ, 498, 541

Kiewe M., Gal-Yam A., Arcavi I., Leonard D. C., Emilio Enriquez J., Cenko S. B., Fox D. B., Moon D.-S., Sand D. J., Soderberg A. M., CCCP T., 2012, ApJ, 744, 10

Kim C.-G., Kim W.-T., Ostriker E. C., 2011, ApJ, 743, 25

Kim C.-G., Ostriker E. C., 2015, ApJ, 802, 99

Kim C.-G., Ostriker E. C., Kim W.-T., 2013, ApJ, 776, 1

Kim J., 2004, Journal of Korean Astronomical Society, 37, 237

Kim J.-h., Krumholz M. R., Wise J. H., Turk M. J., Goldbaum N. J., Abel T., 2013, ApJ, 779, 8

Klessen R. S., Glover S. C. O., 2014, ArXiv e-prints

Klessen R. S., Hennebelle P., 2010, A&A, 520, A17

Krause M., Fierlinger K., Diehl R., Burkert A., Voss R., Ziegler U., 2013, A&A, 550, A49

Kritsuk A. G., Norman M. L., 2002, ApJ, 569, L127

Kroupa P., 2001, MNRAS, 322, 231

Krumholz M. R., Matzner C. D., 2009, ApJ, 703, 1352

Krumholz M. R., McKee C. F., Klein R. I., 2004, ApJ, 611, 399

Krumholz M. R., Thompson T. A., 2012, ApJ, 760, 155

Kudritzki R.-P., Puls J., 2000, ARA&A, 38, 613

Lada C. J., Lada E. A., 2003, ARA&A, 41, 57

Larson R. B., 1981, MNRAS, 194, 809

Leroy A. K., Walter F., Brinks E., Bigiel F., de Blok W. J. G., Madore B., Thornley M. D., 2008, AJ, 136, 2782

Lopez L. A., Krumholz M. R., Bolatto A. D., Prochaska J. X., Ramirez-Ruiz E., 2011, ApJ, 731, 91

Lucero D. M., Carignan C., Elson E. C., Randriamampandry T. H., Jarrett T. H., Oosterloo T. A., Heald G. H., 2015, MNRAS, 450, 3935

Mac Low M.-M., 1999, ApJ, 524, 169

Mac Low M.-M., Balsara D. S., Kim J., de Avillez M. A., 2005, ApJ, 626, 864

Mac Low M.-M., Klessen R. S., 2004, Reviews of Modern Physics, 76, 125

Mac Low M.-M., McCray R., 1988, ApJ, 324, 776

Marinacci F., Pakmor R., Springel V., Simpson C. M., 2014, MNRAS, 442, 3745

Markova N., Puls J., 2008, A&A, 478, 823

Martizzi D., Faucher-Giguère C.-A., Quataert E., 2015, MNRAS, 450, 504

Mathis J. S., Rumpl W., Nordsieck K. H., 1977, ApJ, 217, 425

Matzner C. D., 2007, ApJ, 659, 1394

McCray R., Kafatos M., 1987, ApJ, 317, 190

McKee C. F., Ostriker J. P., 1977, ApJ, 218, 148

Mestel L., Spitzer Jr. L., 1956, MNRAS, 116, 503

Micic M., Glover S. C. O., Banerjee R., Klessen R. S., 2013, MNRAS, 432, 626

Minkowski R., 1955, in Gas Dynamics of Cosmic Clouds Vol. 2 of IAU Symposium, The Observational Background of Cosmical Gasdynamics. p. 3

Murray N., Quataert E., Thompson T. A., 2010, ApJ, 709, 191

Nakanishi H., Sofue Y., 2006, PASJ, 58, 847

Oosterloo T., Fraternali F., Sancisi R., 2007, AJ, 134, 1019

Oppenheimer B. D., Davé R., Kereš D., Fardal M., Katz N., Kollmeier J. A., Weinberg D. H., 2010, MNRAS, 406, 2325

Ostriker E. C., McKee C. F., Leroy A. K., 2010, ApJ, 721, 975

Padoan P., Pan L., Haugboelle T., Nordlund A., 2015, ArXiv e-prints

Palouš J., Ehlerová S., 2000, New A Rev., 44, 369

Pellegrini E. W., Baldwin J. A., Ferland G. J., 2011, ApJ, 738, 34

Péquignot D., Tsamis Y. G., 2005, A&A, 430, 187

Perets H. B., Šubr L., 2012, ApJ, 751, 133

Petric A. O., Rupen M. P., 2007, AJ, 134, 1952

Pflamm-Altenburg J., Kroupa P., 2010, MNRAS, 404, 1564

Portegies Zwart S. F., 2000, ApJ, 544, 437

Pudritz R. E., Ouyed R., Fendt C., Brandenburg A., 2007, Protostars and Planets V, pp 277–294

Puls J., Kudritzki R.-P., Herrero A., Pauldrach A. W. A., Haser S. M., Lennon D. J., Gabler R., Voels S. A., Vilchez J. M., Wachter S., Feldmeier A., 1996, A&A, 305, 171

Puls J., Vink J. S., Najarro F., 2008, A&A Rev., 16, 209

Raymond J. C., Cox D. P., Smith B. W., 1976, ApJ, 204, 290

Rogers H., Pittard J. M., 2013, MNRAS, 431, 1337

Rohlfs K., Wilson T. L., 1996, Tools of Radio Astronomy

Rosolowsky E., Blitz L., 2005, ApJ, 623, 826

Salpeter E. E., 1955, ApJ, 121, 161

Saury E., Miville-Deschênes M.-A., Hennebelle P., Audit E., Schmidt W., 2014, A&A, 567, A16

Savage B. D., Sembach K. R., Wakker B. P., Richter P., Meade M., Jenkins E. B., Shull J. M., Moos H. W., Sonneborn G., 2003, ApJS, 146, 125

Scannapieco E., Gray W. J., Pan L., 2012, ApJ, 746, 57

Schmidt M., 1959, ApJ, 129, 243

Schruba A., Leroy A. K., Walter F., Bigiel F., Brinks E., de Blok W. J. G., Dumas G., Kramer C., Rosolowsky E., Sandstrom K., Schuster K., Usero A., Weiss A., Wiesemeyer H., 2011, AJ, 142, 37

Seifried D., Pudritz R. E., Banerjee R., Duffin D., Klessen R. S., 2012, MNRAS, 422, 347

Sellwood J. A., Balbus S. A., 1999, ApJ, 511, 660

Sembach K. R., Howk J. C., Ryans R. S. I., Keenan F. P., 2000, ApJ, 528, 310

Shapiro P. R., Field G. B., 1976, ApJ, 205, 762

Sharma P., Roy A., Nath B. B., Shchekinov Y., 2014, MNRAS, 443, 3463

Shetty R., Kelly B. C., Bigiel F., 2013, MNRAS, 430, 288

Shetty R., Kelly B. C., Rahman N., Bigiel F., Bolatto A. D., Clark P. C., Klessen R. S., Konstandin L. K., 2014, MNRAS, 437, L61

Shetty R., Ostriker E. C., 2012, ApJ, 754, 2

Shull J. M., Saken J. M., 1995, ApJ, 444, 663

Slavin J. D., Cox D. P., 1992, ApJ, 392, 131

Slyz A. D., Devriendt J. E. G., Bryan G., Silk J., 2005, MNRAS, 356, 737

Spitzer Jr. L., 1942, ApJ, 95, 329

Spitzer Jr. L., 1956, ApJ, 124, 20

Spitzer Jr. L., 1968, Dynamics of Interstellar Matter and the Formation of Stars. the University of Chicago Press, p. 1

Stinson G., Seth A., Katz N., Wadsley J., Governato F., Quinn T., 2006, MNRAS, 373, 1074

Stone J. M., Ostriker E. C., Gammie C. F., 1998, ApJ, 508, L99

Stone R. C., 1991, AJ, 102, 333

Strickland D. K., Heckman T. M., Colbert E. J. M., Hoopes C. G., Weaver K. A., 2004a, ApJS, 151, 193

Strickland D. K., Heckman T. M., Colbert E. J. M., Hoopes C. G., Weaver K. A., 2004b, ApJ, 606, 829

Strickland D. K., Heckman T. M., Weaver K. A., Dahlem M., 2000, AJ, 120, 2965

Strickland D. K., Heckman T. M., Weaver K. A., Hoopes C. G., Dahlem M., 2002, ApJ, 568, 689

Stutzki J., Bensch F., Heithausen A., Ossenkopf V., Zielinsky M., 1998, A&A, 336, 697

Sun K., Kramer C., Ossenkopf V., Bensch F., Stutzki J., Miller M., 2006, A&A, 451, 539

Swinbank A. M., Papadopoulos P. P., Cox P., Krips M., Ivison R. J., Smail I., Thomson A. P., Neri R., Richard J., Ebeling H., 2011, ApJ, 742, 11

Tacconi L. J., Genzel R., Neri R., Cox P., Cooper M. C., Shapiro K., Bolatto A., et al., 2010, Nature, 463, 781

Tacconi L. J., Neri R., Genzel R., Combes F., Bolatto A., Cooper M. C., Wuyts S., Bournaud F., Burkert A., Comerford J., et al., 2013, ApJ, 768, 74

Tamburro D., Rix H.-W., Leroy A. K., Mac Low M.-M., Walter F., Kennicutt R. C., Brinks E., de Blok W. J. G., 2009, AJ, 137, 4424

Tammann G. A., Loeffler W., Schroeder A., 1994, ApJS, 92, 487

Tenorio-Tagle G., Bodenheimer P., 1988, ARA&A, 26, 145

Tenorio-Tagle G., Bodenheimer P., Franco J., Rozyczka M., 1990, MNRAS, 244, 563

Tenorio-Tagle G., Rozyczka M., Franco J., Bodenheimer P., 1991, MNRAS, 251, 318

Teyssier R., Chapon D., Bournaud F., 2010, ApJ, 720, L149

Thacker R. J., Couchman H. M. P., 2000, ApJ, 545, 728

Tielens A. G. G. M., 2005, The Physics and Chemistry of the Interstellar Medium

Toalá J. A., Arthur S. J., 2011, ApJ, 737, 100

Troland T. H., Heiles C., 1986, ApJ, 301, 339

Truelove J. K., Klein R. I., McKee C. F., Holliman II J. H., Howell L. H., Greenough J. A., 1997, ApJ, 489, L179

van Loon J. T., 2006, in Lamers H. J. G. L. M., Langer N., Nugis T., Annuk K., eds, Stellar Evolution at Low Metallicity: Mass Loss, Explosions, Cosmology Vol. 353 of Astronomical Society of the Pacific Conference Series, On the metallicity dependence of the winds from red supergiants and Asymptotic Giant Branch stars. p. 211

Vázquez-Semadeni E., Gazol A., Scalo J., 2000, ApJ, 540, 271

Waagan K., 2009, Journal of Computational Physics, 228, 8609

Waagan K., Federrath C., Klingenberg C., 2011, Journal of Computational Physics, 230, 3331

Wada K., Meurer G., Norman C. A., 2002, ApJ, 577, 197

Walch S., Girichidis P., Naab T., Gatto A., Glover S. C. O., Wünsch R., Klessen R. S., Clark P. C., Peters T., Derigs D., Baczynski C., 2015, MNRAS, 454, 238

Walch S., Naab T., 2015, MNRAS, 451, 2757

Walch S., Whitworth A. P., Bisbas T. G., Wünsch R., Hubber D. A., 2013, MNRAS, 435, 917

Walch S., Wünsch R., Burkert A., Glover S., Whitworth A., 2011, ApJ, 733, 47

Walch S. K., Whitworth A. P., Bisbas T., Wünsch R., Hubber D., 2012, MNRAS, 427, 625

Weaver R., McCray R., Castor J., Shapiro P., Moore R., 1977, ApJ, 218, 377

Wilkinson M. I., Evans N. W., 1999, MNRAS, 310, 645

Wolfire M. G., Hollenbach D., McKee C. F., Tielens A. G. G. M., Bakes E. L. O., 1995, ApJ, 443, 152

Zhukovska S., Gail H.-P., Trieloff M., 2008, A&A, 479, 453

Zubko V., Dwek E., Arendt R. G., 2004, ApJS, 152, 211

Zuckerman B., Evans II N. J., 1974, ApJ, 192, L149

Acknowledgements

I would like to express my gratitude to Prof. Stefanie Walch, Dr. Thorsten Naab and Dr. Philipp Girichidis for their endless support and patience.

My sincere thanks also go to many collaborators with whom I have had the pleasure of working over these years, from the members of the SILCC collaboration to Mordecai-Mark Mac Low, Juan Ibáñez-Mejía, Alex Hill, Jana Grcevich, Andrew Emerick, Mohit Tanga, Patricia Shady and Joachim Puls.

Special thanks go to Sebastian Haid for his help in filling forms and for offering me a lot of beer.

I would also like to acknowledge the galaxy group at MPA.

Many thanks to my friends and colleagues in Germany and in Italy, in no particular order: Alessandro, Giulia, Matteo, Simone, Thomas, Lena, Elias, Eva, Nico, Chryssa, Elina, Alessio, Ghiggia, Tommaso, Pria, Tito, Giordi and many others.

I would also like to acknowledge my family, Ermanna, Pietro and Giovanni, for their constant support throughout these years.

Last but not least, super special thanks go to Lucrezia and Planck, they know why.

Erklaerung

Ich versichere, daß ich die von mir vorgelegte Dissertation selbständig angefertigt, die benutzten Quellen und Hilfsmittel vollständig angegeben und die Stellen der Arbeit – einschließlich Tabellen, Karten und Abbildungen –, die anderen Werken im Wortlaut oder dem Sinn nach entnommen sind, in jedem Einzelfall als Entlehnung kenntlich gemacht habe; daß diese Dissertation noch keiner anderen Fakultät oder Universität zur Prüfung vorgelegen hat; daß sie – abgesehen von unten angegebenen Teilpublikationen – noch nicht veröffentlicht worden ist sowie, daß ich eine solche Veröffentlichung vor Abschluß des Promotionsverfahrens nicht vornehmen werde. Die Bestimmungen dieser Promotionsordnung sind mir bekannt. Die von mir vorgelegte Dissertation ist von Prof. Dr. Stefanie K. Walch-Gassner betreut worden.

Publications

1. Peters, T.; Girichidis, P.; **Gatto, A.**; Naab, T.; Walch, S.; Wunsch, R.; Glover, S.; Clark, P.; Klessen, R.; Baczynski, C., *Impact of supernova and cosmic-ray driving on the surface brightness of the galactic halo in soft X-rays*, 2015, ApJL, 813, 27
2. Walch S.; Girichidis, P.; Naab, T.; **Gatto, A.**; Glover, S.; Wunsch, R.; Klessen, R.; Clark, P.; Peters, T.; Derigs, D.; Baczynski, C., *The SILCC (SImulating the LifeCycle of molecular Clouds) project: I. Chemical evolution of the supernova-driven ISM*, 2015, MNRAS, 454, 238
3. **Gatto, A.**; Walch, S.; Mac Low, M.-M.; Naab, T.; Girichidis, P.; Glover, S.; Wunsch, R.; Klessen, R.; Clark, P.; Baczynski, C.; Peters, T.; Ostriker, J.; Ibanez-Mejia, J.; Haid, S., *Modelling the supernova-driven ISM in different environments*, 2015, MNRAS, 449, 1057
4. **Gatto, A.**; Fraternali, F.; Read, J.; Marinacci, F.; Lux, H.; Walch, S., *Unveiling the corona of the Milky Way via ram-pressure stripping of dwarf satellites*, 2013, MNRAS, 433, 2749

Lebenslauf

Persönliche Angaben

Name: Andrea Gatto
Adresse: An der Mühle 1, 85716 Unterschleissheim
Geboren: am 9. Mai 1984 in Genua, Italien
Nationalität: Italienish

Schule & Studium

seit 06/2012: Ph.D.-Studenten, Max-Planck-Institut für Astrophysik, Garching bei München
Betreuer: Prof. Dr. S. K. Walch-Gassner

09-12/2014: Annette Kade fellow, American Museum of Natural History, New York City, USA
Gastgeber: Prof. Dr. M.-M. Mac Low

03/2012: *Laurea Magistrale*, Astrophysik und Kosmologie. Note: 110/110 *cum laude*

10/2008-03/2012: Astrophysik und Kosmologie, Universität zu Bologna

12/2008: *Laurea Triennale*, Astronomie. Note: 104/110

10/2004-12/2008: Astronomie, Universität zu Bologna

10/2003-03/2004: Ingenieurwissenschaften, Universität zu Genua

07/2003: *Diploma di scuola secondaria superiore, Liceo Scientifico.* Note: 80/100

09/1998-07/2003: *Liceo Scientifico* O. Grassi, Savona